The Impact of Solar Particle Events on Radiation Risk for Human Explorers of Mars

by

Camron Saul Gorguinpour

A dissertation submitted in partial satisfaction of the
requirements for the degree of

Joint Doctor of Philosophy

with University of California, San Francisco

in

Bioengineering

in the
Graduate Division
of the
University of California, Berkeley

Committee in Charge:
Professor Thomas Budinger, Chair
Professor Thomas Lang
Professor Robert Lin

Spring 2010

Abstract

The Impact of Solar Particle Events on Radiation Risk for Human Explorers of Mars

by

Camron Saul Gorguinpour

Joint Doctor of Philosophy

with University of California, San Francisco

in Bioengineering

University of California, Berkeley

Professor Thomas Budinger, Chair

This project has examined one specific issue facing human explorers at Mars – radiation dose from solar particle events (SPEs). While the issue is specific, the work involved in carrying out this study has been truly multidisciplinary. From space physics to modeling the Martian atmosphere to assessing radiation risk to humans, a lot of ground is covered. At each point along the way, efforts were made to clarify the science and assumptions used to derive quantitative estimates and draw meaningful conclusions. The data and analyses provided in this project represent the most comprehensive study of SPE's at a planetary body other than Earth. The analysis includes dose estimates from galactic cosmic radiation.

The specific aims of this project are to:

1. Establish a methodology for estimating the fluence of energetic particles at Mars from SPEs;
2. Establish a predictive model to estimate the frequency of SPE occurrence and cumulative SPE fluence received at Mars, as a function of the Solar Cycle;
3. Develop a model to estimate the fluence of energetic particles from SPEs on the Martian surface;

4. Estimate and assess the radiation dose on the Martian surface from SPEs, as compared to galactic cosmic radiation (GCR); and
5. Assess the viability of various types of shielding and mission profiles to mitigate the radiation risk to human explorers on the Martian surface.

Some of the conclusions drawn from this study include:

- The MCP detector onboard MGS ER (and presumably other spacecraft) can serve as an effective detector for high-energy ionizing radiation.
- Though more work is necessary, it is possible to estimate future solar activity at Earth and Mars based on current solar observations.
- Spectral information from SPE's at Mars is required to thoroughly assess the radiation environment on the Martian surface.
- An unshielded astronaut on the Martian surface may face long-term and acute radiation risk from SPE's, depending on the likelihood of their occurrence.
- Various mitigation strategies can be employed to minimize the radiation risk to human explorers on Mars, though shielding is limited for astronauts outside of a fixed habitat.

Table of Contents

List of Figures

List of Tables

Chapter 1
Introduction

1.1 Overview

Radiation exposure is a critical concern for astronaut safety during long-duration missions, such as missions to Mars. The Mars Exploration Program Analysis Group (MEPAG) is a multi-institutional panel that has been tasked by NASA to "work with the scientific community to establish consensus priorities for the future scientific exploration of Mars." MEPAG establishes goals for future robotic missions but also addresses priorities in preparation for human exploration. Among this group's proposed investigations in preparation of human space exploration is the following:

> ***Goal IV. Objective B. Investigation 5.***
> *Characterize in detail the ionizing radiation environment at the Martian surface, distinguishing contributions from the energetic charged particles that penetrate the atmosphere, secondary neutrons produced in the atmosphere, and secondary charged particles and neutrons produced in the regolith.*
> *Measurements:*
> *a. Measurement of charged particles with directionality. Identify particles by species and energy from protons to iron nuclei in the energy range 20-1000 MeV/nucleon.*
> *b. Measurement of neutrons with directionality. Energy range from 1 keV (or lower) to 100MeV (or higher).*
> *c. Simultaneous with surface measurements, a detector should be placed in orbit to measure energy spectra in Solar Energetic Particle events.*

The project outlined in this chapter utilizes Earth- and Mars-based data to address each of the key radiation measurements outlined by MEPAG, as related to large-scale solar events. Specifically, this study examines the radiation impact of Solar Particle Events (SPEs), which are typically caused by coronal mass ejections (CMEs). These wide-ranging magnetic disturbances originate in the solar corona and permeate throughout the Solar System. Through accelerative processes, CME's can generate large fluxes of particle radiation that impact both human and robotic space explorers. However, not every CME results in an SPE.

The specific aims of this project are to:

1. Establish a methodology for estimating the fluence of energetic particles from SPEs arriving at Mars;
2. Establish a predictive model to estimate the frequency of SPE occurrence and cumulative SPE fluence received at Mars, as a function of the Solar Cycle;
3. Develop a computer simulation to estimate the fluence of energetic particles from SPEs on the Martian surface;
4. Estimate and assess the radiation dose on the Martian surface from SPEs, as compared to galactic cosmic radiation (GCR); and
5. Assess the viability of various types of shielding and mission profiles to mitigate the radiation risk to human explorers on the Martian surface.

Unlike the pervasive GCR, SPEs originate from the Sun and occur sporadically and with great intensity. Using satellite data from Earth and Mars and existing radiation transport codes, it is possible to estimate the radiation exposure from SPEs delivered to an astronaut on the Martian surface. For the purposes of this analysis, the accelerated particles and the particles within the magnetic disturbance of a CME will be termed "solar energetic particles (SEPs)."

SPEs pose a significant radiation hazard to all human and robotic space missions. The Japanese Nozomi spacecraft failed as a result of a SPE, as did the Mars Radiation Environment Experiment (MARIE) instrument onboard the Mars Odyssey satellite. In both cases, the instruments' electronics were permanently damaged by the intense radiation exposure. Dosimeters onboard the Mir Space Station confirmed that on one day, in 1989, a single SPE delivered three months worth of radiation exposure to cosmonauts (Badhwar 2002).

On Mars, unprotected human space explorers face increased risk of long-term and acute physiological damage. The majority of published research related to radiation health risks at Mars deals with the impact of Galactic Cosmic Radiation (GCR). This study will provide a comparison of the relative importance of GCR and solar activity. Figure 1-1 depicts a process for tracking a CME propagating through space as it is detected by a variety of Earth- and Mars-based instruments. The SOHO satellite provides continuous coronal imaging to determine the timing and direction of CME onset. ACE and Wind satellites include high-energy particle detectors that determine the fluxes, fluences, and spectra of SPE's at Earth induced by CMEs. Mars Global Surveyor (MGS) includes instruments that can be used to detect SPEs at Mars, as described below.

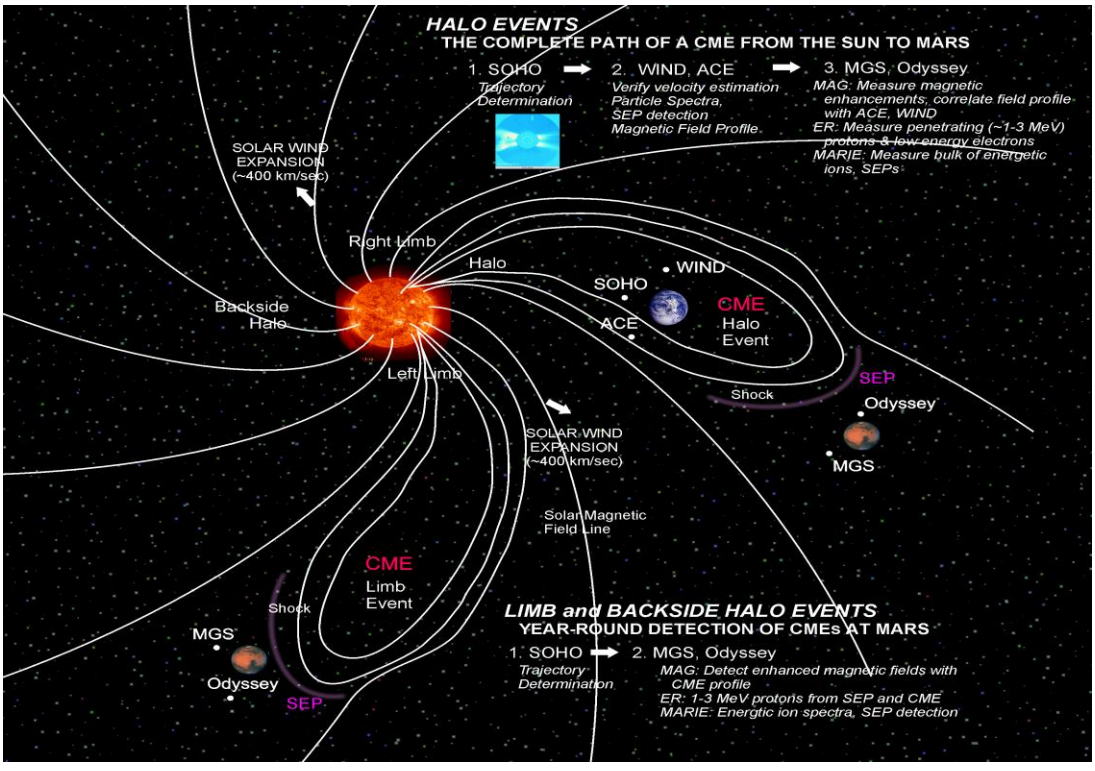

Figure 1-1. Propagation of an interplanetary shock from the Sun to Mars. (Delory et al. 2004)

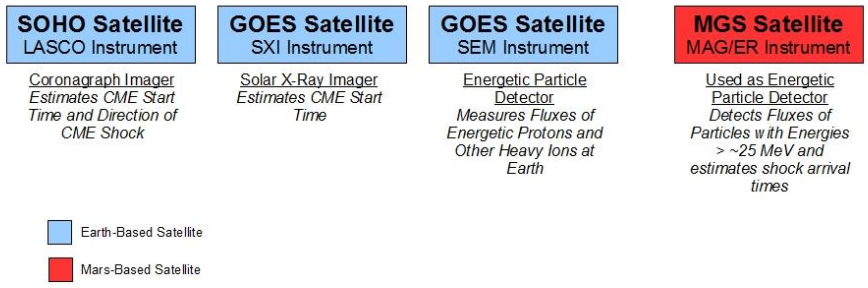

Figure 1-2. Summary of Earth- and Mars-based satellites used in this study.

1.2 Description of Dissertation Chapters

Figure 1-3 provides a graphical description of this project. The chapters of this text address the following topics:

Chapter 1: Introduction – A summary of the overall project with relevant background information.

Chapter 2: Detection and Analysis of Solar Energetic Particles at Mars – There have been no instruments at Mars for an extended period of time that are capable of detecting solar energetic particles. However, the Electron Reflectometer (ER) onboard the Mars Global Surveyor (MGS) satellite was capable of indirect detection of high-energy ions. This chapter describes the process by which MGS ER data are interpreted to estimate the fluence of energetic particles arriving at Mars during SPEs. A physical argument is made that the microchannel plate (MCP) detector onboard MGS ER detects energetic ions with a high efficiency (~90%). This argument is confirmed in a variety of ways, including comparison to comparable data from the MARIE instrument onboard the Mars Odyssey satellite.

Chapter 3: Characteristics of Solar Particle Events at Mars – The relevant instruments onboard MGS operated from January 1999 through October 2006. During this time dozens of SPEs were detected. This chapter presents a methodology for identifying the duration and frequency of SPEs over time. An analysis of the statistical features of SPEs at Mars is presented, including peak fluxes, fluences, and frequency of SPE occurrence. A methodology is also presented for predicting the relative frequency of SPE occurrences, based on sunspot data. Predictive models for estimating the interplanetary shock arrival times are also examined to determine the viability of using Earth-based data to estimate the impact of SPEs at Mars.

Chapter 4: Impact of Solar Particle Events on the Radiation Environment at the Martian Surface – Data from MGS ER only describe the radiation environment in orbit around Mars. In order to determine the radiation environment on the Martian surface, the Particle and Heavy Ion Transport Code System (PHITS) is used to estimate the interaction of energetic particles through the Martian atmosphere and with the Martian regolith. An additional limitation of the MGS ER data is an inability to determine the energetic particle spectra for SPEs. A power law spectrum is applied to the SPE data with an average spectral index that was determined from Earth-based data taken over the same timeframe as MGS ER operation.

Chapter 5: Radiation Dose on the Martian Surface from Solar Particle Events – Using information derived in the previous chapters, this chapter provides a radiation dose estimate for human explorers on the Martian surface. The estimated dose is compared to lifetime radiation dose limits established by NASA, as well as information related to acute physiological effects of large doses. An assessment is also made of the ability to mitigate radiation risk by selecting appropriate timing, locations, and shielding for a Mars mission.

Chapter 6: Conclusion – This chapter reviews information provided in the previous chapters and provides a discussion of areas for future study.

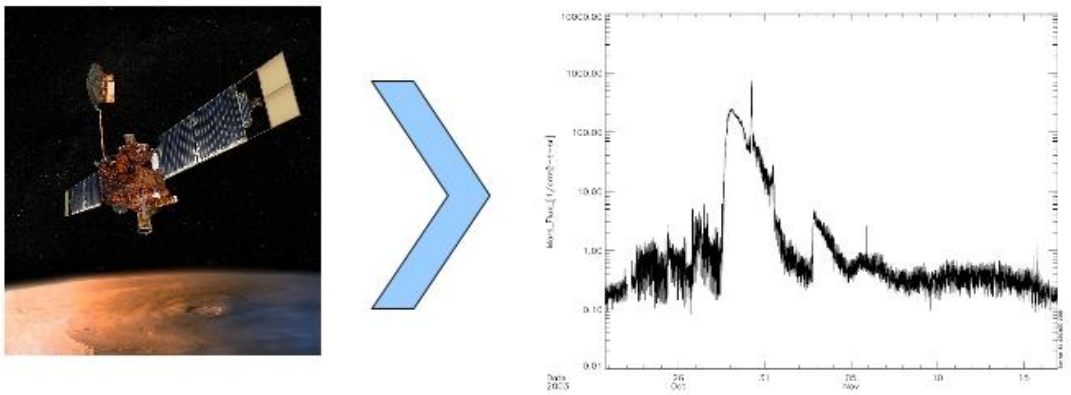

Chapter 2 used raw SPE data from MGS ER to generate high-energy particle fluence estimates.

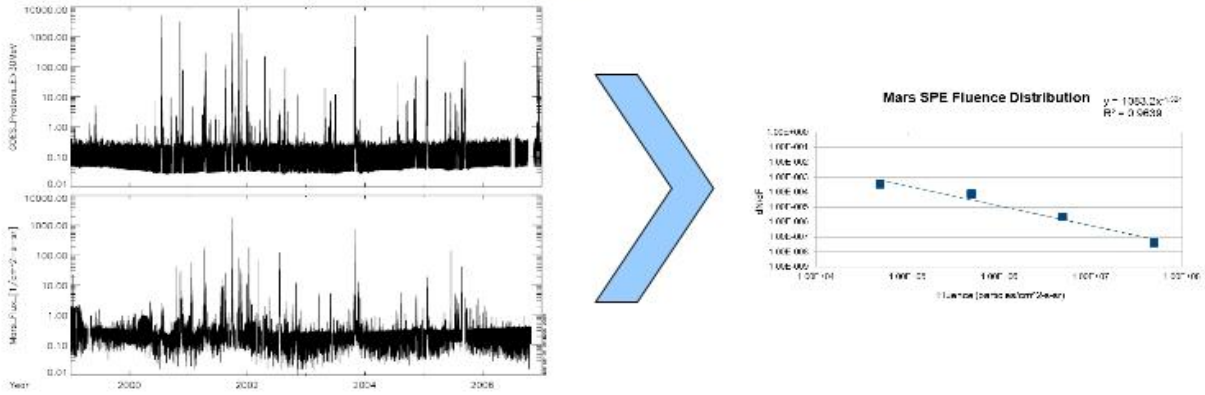

Chapter 3 examined the statistical properties of SPE's arriving at Mars, using the full MGS ER data set.

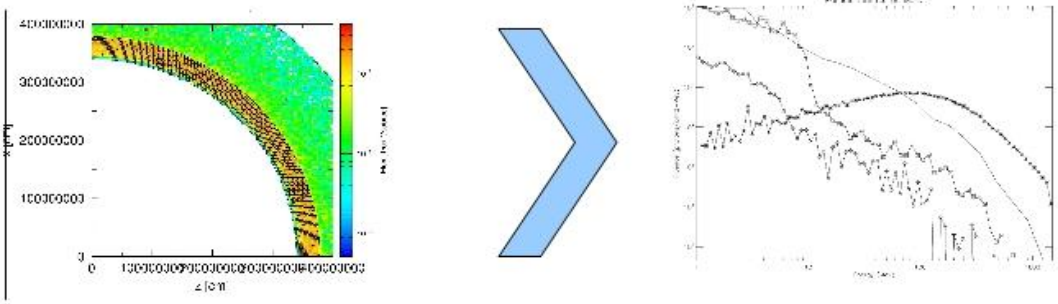

Chapter 4 used the PHITS radiation transport code to estimate the fluence of particles on the surface of Mars, due to SPE's.

Chapter 5 calculates the cumulative effective dose delivered to human explorers on the surface of Mars, based on the estimated surface fluence of particles caused by SPE's

Figure 1-3. Progression of information included in chapters of this dissertation.

1.3 Sources of High Energy Particle Radiation in Interplanetary Space

For the purposes of this paper, "high energy particle radiation" refers to any particle with energy above approximately 20 MeV. Interplanetary space is populated by such particles. The two primary categories for these particles are:

1. Solar Energetic Particles
2. Galactic Cosmic Radiation (GCR)

While this project deals strictly with solar energetic particles that originate from CMEs, these particles can also originate from solar flares and the so-called Co-rotating Interaction Regions of the solar wind. CMEs deliver a much higher flux of particles than GCR but at much lower energies [~10-1000/(s-m^2-sr-MeV/nucleon) for particles with energies >10 Mev/nucleon]. CMEs are also transient events that last over periods of hours to days (Zapp et al 2002).

GCR originates from the supernovae of distant starts and provides a relatively low flux of very high energy particles [~10^{-3}/(day-m^2-sr-MeV/nucleon) for particles with energies ~1000 MeV/nucleon]. Figure 1-4 presents modeled integral spectra for various GCR particles. It is evident that the flux of GCR is negligible at energies lower than ~200MeV/nucleon. The GCR spectrum is modulated by the 11-year solar cycle. At maximum solar activity, the magnetic field strength of the heliosphere – the Sun's "global" magnetic field – increases. This tends to shield the solar system from GCR. The modulation of GCR flux is also presented in Figure 1-4.

Figure 1-5 presents proton spectral data for several large CMEs that occurred between October and November 2003 and spectral data for various charged particles during a CME in January 2005. The variation in spectra between several events is evident. While the proton spectra tend to follow a double-power-law form, the spectral indices for the high and low energy particles are notably different for each event. In its simplest form, a double power law spectrum takes the following form:

$$\Phi(E) = A \times E^{\alpha} \qquad [E < E_c] \text{ (Equations 1-1)}$$

$$\Phi(E) = B \times E^{\beta} \qquad [E > E_c]$$

Here, Φ is the particle flux or fluence, A and B are scaling constants, α and β are the low- and high-energy spectral indexes, respectively, and E_c is the cutoff energy between the low- and high-energy spectra.

This is evidenced in the left panel of Figure 1-5, where low energy protons (E < ~10 MeV) have an average spectral index of approximately 1.2 for the five observed events. For the same events, high energy protons (E > ~10 MeV) have an average spectral index of 4.2. Moreover, the spectral indices between different particle species tend to vary. For the purposes of this study, a single power law spectrum is assumed for solar energetic particles, because the relevant energy range is about approximately 20 MeV.

During maximum solar activity, CMEs can occur several times per day. At minimal solar activity, fewer CMEs occur a few times per week. While the magnitudes of solar events tend to increase

at solar maximum, very large events also occur near solar minimum. For example, several large CMEs occurred in October/November 2003 after maximum solar activity.

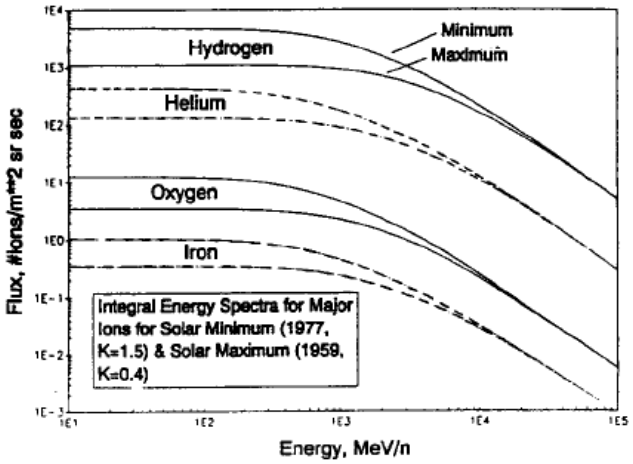

Figure 1-4. Modeled integral flux spectra for various GCR particles at solar minimum and solar maximum. (Badhwar and O'Neill 1994)

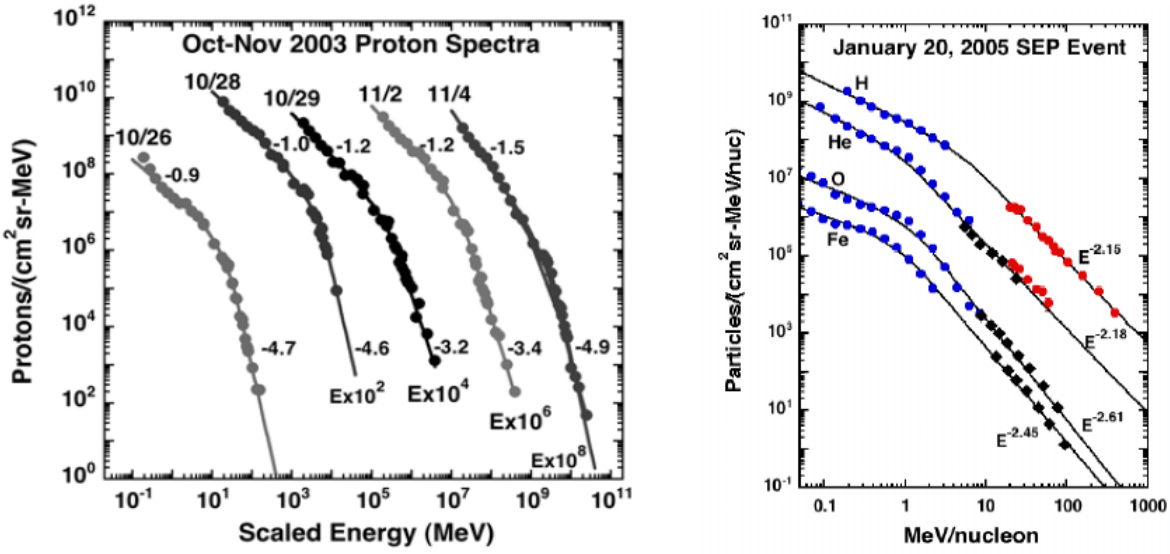

Figure 1-5. (Left) Proton spectra for five events in October/November 2003. Both power law indices are listed. (Right) Particle spectra for H, He, O, and Fe for CME in January 2005. (Mewaldt et al. 2005)

1.4 Instruments for Assessing the Radiation Environment at Mars

There are no instruments at Mars that are designed to measure solar energetic particle spectra. The MARIE instrument onboard the Mars Odyssey satellite detected energetic particles but was specifically designed to examine GCR. However, the Electron Reflectometer (ER) onboard the Mars Global Surveyor (MGS) satellite provides an opportunity to indirectly measure the total particle flux from CMEs and GCR. The ER is designed to measure low energy (< 16 keV) electrons from the solar wind and photoelectrons from the Martian atmosphere. Figure 1-6 displays the structure of the ER, which consists primarily of an electrostatic analyzer, a microchannel plate (MCP), and a position-sensitive resistive anode. Particles enter the ER through the aperture and are guided to the MCP by an oscillating potential within the electrostatic analyzer. If a particle is outside the desired energy range, it will be deflected into the instrument housing rather than reach the MCP. Particles that reach the MCP generate an "electron cloud" in the MCP that is detected by the anode. The signal generated by the anode is noted for both its position and intensity. By noting the position of the affected anode, directional information can be deduced regarding the incident electron. (Mitchell et al. 2001)

While the ER is designed to detect electrons with energies less than 16 keV, particles with energies greater than approximately 25 MeV are able to penetrate the aluminum shielding of the ER instrument and register a count. It is not possible to obtain spectral information for these "penetrating particles," but a particle count rate can be determined. The process of identifying and counting penetrating particles is presented in Chapter 2.

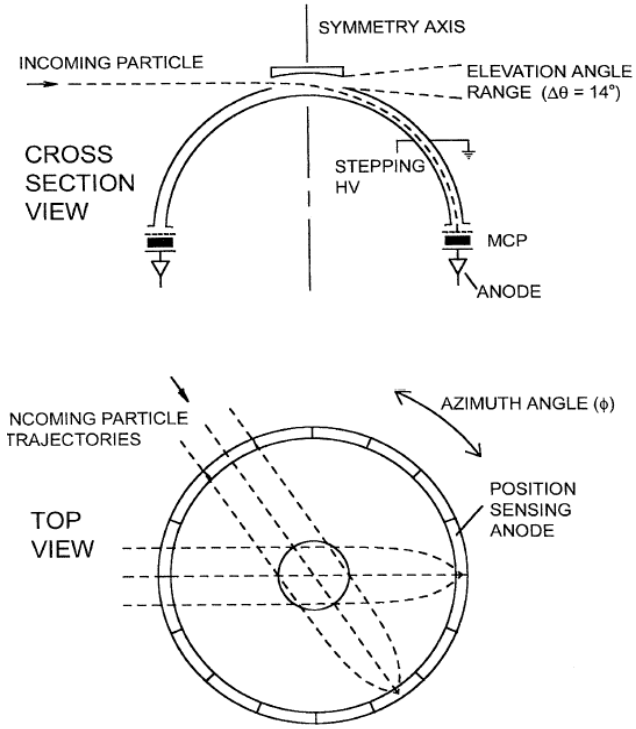

Figure 1-6. Schematic of Mars Global Surveyor (MGS) Electron Reflectometer (ER). (Mitchell et al. 2001)

The most common current method of assessing the impact of CMEs at Mars is to extrapolate Earth-based data. Primary instruments used to assess the near-Earth solar energetic particle environment include: the EPACT instrument onboard the Wind Satellite, the Space Environment Monitor (SEM) onboard the GOES Satellites [GOES-11 is the primary data collection satellite], and the Solar Isotope Spectrometer (SIS) onboard the ACE Satellite. A comparison of these instruments is provided in Table 1. The LASCO instrument onboard the SOHO Satellite is also critical for assessing the timing, location, and magnitude of CMEs. Figure 1-7 presents a comparison of Earth-based data to MGS ER data.

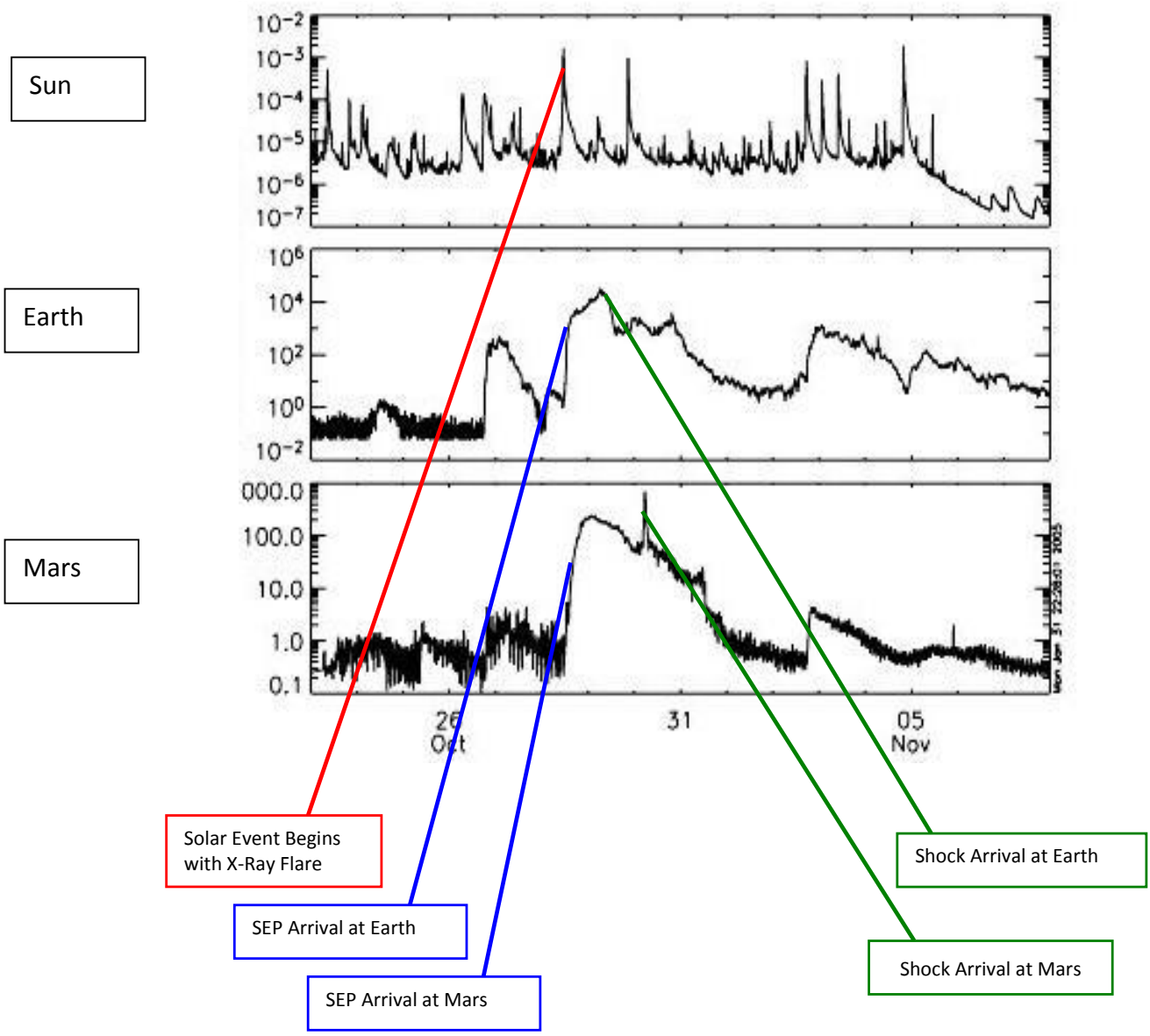

Figure 1-7. Comparison plot of Sun, Earth, and Mars data during a period of intense solar activity. *Top Panel.* X-ray flux measurements made by a GOES satellite. *Middle Panel.* Proton Flux measurements for protons with energies > 10 MeV, measurements made by a GOES satellite. *Bottom Panel.* Particle Flux measurements for particles with energies > 20 MeV, measurements made by Mars Global Surveyor (MGS) Electron Reflectometer (ER).

As presented in Chapter 3, there were 85 SPE's observed by MGS ER during the period of its operation from January 1999 to October 2006. Of the events observed during this timeframe, 22% were observed at Earth but not Mars, and 18% were observed at Mars but not Earth. This restricts the ability to use Earth-based data to assess SPE's on the Martian surface. While predictive models require further advancement, it is currently possible to estimate the relative frequency of SPE's during future solar cycles. This allows some predictive capability in selecting the optimal times for travel to Mars. Moreover, the relative occurrence of SPE's at different flux and fluence levels can be adequately modeled with a power law.

The primary limitation of the MGS ER dataset is the absence of spectral information for each SPE. Typically, SPE fluxes and fluences are described by a double-power law spectrum. There is a low-energy power function that is applicable to energies below ~10 MeV and a high-energy power function for all energies higher than that. For the purposes of this study, a single-power law function is applied, because all of the observed energies are above ~25 MeV. However, the value of the exponent for the power law function, called the spectral index, varies widely between events and is indistinguishable for MGS ER data.

To resolve the lack of spectral information at Mars, a survey of events observed at Earth is conducted and an average spectral index determined. The average spectral index is sufficient when examining the impact of many events, but the wide variation in indexes between events makes it difficult to draw strong conclusions regarding specific SPE's. Analyses in this study used the average spectral index in most cases, but discussions are also provided to present the effects of the full range of spectra.

1.5 Assessing the Radiation Environment on the Martian Surface

Solar particle interactions with the Martian atmosphere dictate not only the flux of solar particles at the surface but also the flux of secondary particles. Moreover, the particle interaction with the Martian regolith produces secondary particles that may be hazardous to biological organisms. The dose delivered at the Martian surface by solar energetic protons alone may overshadow the cumulative dose received from galactic cosmic radiation (Wilson et al 1999). The influence of solar energetic protons is compounded by the production of secondary neutrons from both the Martian atmosphere and regolith (Clowdsley et al 2001).

Chapter 4 of this report describes the process by which the energetic particle flux on the surface of Mars is estimated. Several SPE spectra were used as inputs to a model of the Martian atmosphere and regolith that was developed, using the Particle and Heavy Ion Transport code System (PHITS). A simple atmospheric model of concentric spheres of CO_2 with exponentially decreasing density was used, and the surface model assumed a composition of O, Si, and Fe with a density of 3.27 g/cm^3. Both forward- and back-scattered fluxes and fluences were estimated at an average surface altitude. The fluences and peak fluxes of protons, neutrons, electrons, and gamma rays created by SPE's were estimated for each year of MGS ER operation.

The results of this study are similar to those of other reports in the literature. One of the most significant findings is that back-scattered neutrons account for approximately 50% of the

neutron flux on the Martian surface. This is similar to results from other studies that used different radiation transport codes, such as HZETRN and Geant-4.

1.6 Biological Impact of Solar Energetic Particles

The outputs from the simulated SPE interaction with the Martian atmosphere and regolith are the peak fluxes and fluences of particles on the Martian surface. This information is used in Chapter 5 to assess the annual radiation dose from SPE's. This is compared to the GCR dose, as well as annual and lifetime dose limits established by NASA and NCRP. A discussion of mitigation strategies is also presented by analyzing mission timing, radiation conditions at various altitudes on the Martian surface, and shielding strategies.

Protons contribute approximately 90% of the total SPE dose on the Martian surface. Of the proton dose, only about 20% is caused by primary particles (energies greater than ~200 MeV). In fact, 50% of the dose comes from secondary protons with energies less than 80 MeV. Neutrons contribute the bulk of the remaining dose. Electrons and gamma rays contribute a negligible dose to human explorers on the Martian surface.

Unlike orbital, lunar, or deep space missions, Mars has an atmosphere that provides some protection from harmful radiation. By moving to lower altitudes more atmosphere is placed between the explorer and the particle environment. Additionally, the Martian regolith provides an in-situ shielding source that can limit the need to carry shielding from Earth. Of course, modeling the solar environment allows mission planners to predict times when harmful radiation is minimized. In practice, these mitigation strategies are likely to be used in concert to enable human exploration of Mars.

References

G.D. Badhwar et al, “Radiation Measurements Onboard the Mir Orbital Station”, *Rad. Measurements*, 35, 2002.

Badhwar G.D. and P.M. O’Neill, “Long-Term Modulation of Galactic Cosmic Radiation and its Model for Space Exploration”, *Adv. Space Res.,* Vol. 14, No. 10, 1994.

M.S. Clowdsley et al, “Neutron Environments on the Martian Surface”, *Physica Media*, 17, 2001.

F.A. Cucinotta et al, “Analysis of Radiation Risk from Alpha Particle Component of Solar Particle Events”, *Adv. Space Res.*, Vol. 14, No. 10, 1994.

M.Y. Kim et al, “Contribution of High Charge and Energy (HZE) Ions During Solar-Particle Event of September 29, 1989” , NASA/TP-1999-209320, May 1999.

F. Leblanc et al, “Some Expected Impacts of a Solar Particle Event at Mars”, *J. Geo. Res.*, Vol. 107, No. A5, 2002.

R.A. Mewaldt et al, “Solar-Particle Energy Spectra during the Large Events of October-November 2003 and January 2005”, *29th Annual Cosmic Ray Conference Pune*, 2005, 00, 101-104.

D.L. Mitchel et al, “Intense Solar Activity of Oct-Nov 2003 Observed at Mars with the MGS Magnetometer/Electron Reflectometer”, 2003 American Geophysical Union Conference, San Francisco, California. December 8-12, 2003.

G.J. Taylor et al, “Scientific Goals, Objectives, and Investigations: 2003”, *Mars Exploration Program Analysis Group*, October 2003.

Townsend L.W. and E.N. Zapp, “Dose Uncertainties for Large Solar Particle Events: Input Spectra Variability and Human Geometry Approximations”, *Rad. Measurements*, 30, 1999.

Tylka A.J. and W.F. Dietrich, “IMP-8 Observations of the Spectra, Composition, and Variability of Solar Heavy Ions at High Energies Relevant to Manned Space Missions”, *Rad. Measurements*, 30, 1999.

J.W. Wilson et al, “Mars Surface Ionizing Radiation Environment: Need for Validation”, *MARS 2001 Workshop*, Houston, Texas, October 2-4, 1999.

N. Zapp et al, “A Comparison of Quality Factors and Weighting Factors for Characterizing Astronaut Radiation Exposures”, *Adv. Space Res,*, Vol. 30, No. 4, 2002.

Chapter 2
Detection & Analysis of Solar Energetic Particles at Mars

Abstract

This chapter presents a methodology for evaluating the energetic particle environment at Mars during solar particle events, using data from the Electron Reflectometer (ER) onboard the Mars Global Surveyor (MGS) satellite. While the instrument was not designed for this purpose, it is shown that MGS ER can be used to estimate the flux of solar energetic particles with energies greater than ~ 25 MeV/n. Flux estimates derived from this methodology are validated by comparison to four independent measurements:

1. The radial gradient of solar energetic particle fluences, as measured by MGS ER and the SEM instrument onboard GOES-10, fall as $R^{-2.2}$, where R is the radial distance from the Sun. This is well aligned with prior theoretical and empirical studies.
2. The radial gradient of solar energetic particle fluxes, as measured by MGS ER and the SEM instrument onboard GOES-10, fall as $R^{-3.5}$, where R is the radial distance from the Sun. This is well aligned with prior theoretical and empirical studies.
3. Galactic Cosmic Background (GCR) flux measurements made by MGS ER are well-aligned with measurements made by the MARIE instrument onboard the Mars Odyssey satellite.
4. Solar Energetic Particle (SEP) flux measurements made by MGS ER are aligned with measurements made by the MARIE instrument within 7.8%.

2.1 Introduction

The Electron Reflectometer (ER) instrument onboard the Mars Global Surveyor (MGS) satellite collected data in low-Mars orbit from January 1999 through October 2006. This instrument was specifically designed to detect low-energy electrons (E < ~19keV) from the solar wind and photoelectrons ejected from the upper ionosphere of Mars. An unanticipated benefit of the ER is the direct detection of solar energetic particles (SEP's) over the eight year period of the instrument's operation. Comparison of count rate data from ER to Earth-based energetic particle detectors makes clear that ER, in fact, detected SEP's from dozens of solar particle events.

Energetic particles (E > ~ 25MeV/n) are capable of penetrating the ER instrument housing and can register a signal within the detector. The term "penetrating particle" is used for any energetic particle that passes through the ER instrument housing. If the "penetrating particle" count rates can be translated to a particle flux, the ER will provide one of the most comprehensive data sets for solar particle events at a planetary body other than Earth. However, the process of estimating a particle flux from the ER count rates is not trivial. This chapter describes a strategy for effectively deriving flux estimates from the ER data during solar particle events.

Of primary importance is the lack of experimental data to determine the ER detector efficiency for particles in the energy ranges of "penetrating particles." ER utilizes micro-channel plate (MCP) detectors to register count rates of incident particles. MCP response is well-known for electrons and ions with energies less than ~ 500keV, and there is limited experimental data for ions with energies up to 8 MeV/n. There are no direct experimental data for the MCP response to 25 MeV protons or particles of greater energy. Thus, the interpretation that a "penetrating particle" count in the detector correlates directly to a single solar energetic particle must be justified, as is done in this chapter. In fact, it was initially posited that primary "penetrating particles" could not register a count in the detector and that secondary electrons produced within the ER housing were being detected. Further analysis shows that MCP detectors are highly efficient for energetic ions. This analysis is presented in Section 2.4. Subsequent radiation transport modeling also indicates that secondary electrons are produced with such low frequency that they are unlikely to be generating the observed signal.

Another chief concern is establishing a geometric factor for "penetrating particles" reaching the ER detector. A geometric factor is a normalization factor that allows a detector's count rate to be converted to a flux, using detailed information regarding the detector's field of view and operation. The ER geometric factor is known for low energy electrons, which must enter the normal optics of the ER to be detected. On the contrary, "penetrating particles" can enter the instrument from any angle. Moreover, there is non-uniform thickness in the instrument housing. So, certain angles of incidence require more or less energy than others to reach the detector. Furthermore, the ER detectors lay at the back of the instrument – shielded from the rear by the full mass of the MGS satellite. Part of the MGS mass is an unknown amount of propellant, which contributes to the uncertainty of energies required for particles to reach the ER from the rear.

Despite these challenges, a methodology is for deriving SEP flux estimates from MGS ER has been developed and validated. Three independent measurements from the Earth-based GOES-10 satellite and the Mars Odyssey satellite have been compared to MGS ER. It is demonstrated that these independent measurements provide strong validation for the methodology described in this chapter. These findings provide the framework for further analysis of the SEP environment at Mars and are used throughout this dissertation.

2.2 Electron Reflectometer (ER) Onboard Mars Global Surveyor (MGS)

MGS ER is an electrostatic analyzer, designed to measure fluxes of electrons from the solar wind and photoelectrons from the upper-ionosphere of Mars. Figure 2-1 displays the structure of the ER, which consists primarily of an electrostatic analyzer, a micro-channel plate (MCP), and a position-sensitive resistive anode. Particles enter the ER through the aperture and are guided to the MCP by an oscillating potential within the electrostatic analyzer. If a particle is outside the desired energy range, it will be deflected into the instrument housing rather than reach the MCP. Particles that reach the MCP generate an "electron cloud" that is detected by the anode. These particles are binned into one of 19 energy bins, based on the voltage present in the electrostatic analyzer. The signal generated by the anode is noted for both its position and intensity. By noting the position of the affected anode, directional information can be deduced regarding the incident electron. (Mitchell et al. 2001)

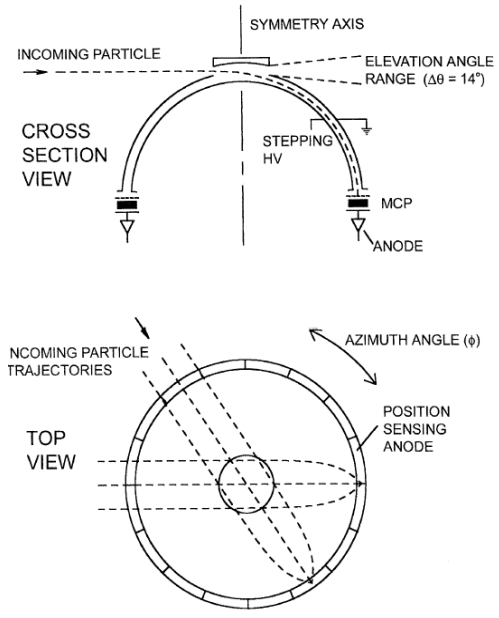

Figure 2-1. Schematic of Mars Global Surveyor (MGS) Electron Reflectometer (ER). (Mitchell et al. 2001)

2.2.1 MGS ER Shielding

The micro-channel plate detectors inside MGS ER experience vastly different levels of shielding on the front side of the detectors from the back-side. On the front-side, the detectors are shielded from the outside space environment by the aluminum housing of the ER instrument. By design, the front-side of the detectors always point toward nadir. The back-side of the detectors point toward zenith and is shielded by the full mass of the MGS spacecraft.

MGS ER is housed inside an aluminum frame, which includes an electrostatic analyzer and the structural support for the instrument. Aluminum thickness varies along different ray angles through the housing to the MCP. The average thickness of aluminum housing surrounding the MCP detectors is 3mm. For analysis in this chapter, it is assumed that there is uniform 3mm thickness of aluminum shielding.

The back-side shielding for MGS ER is much more complex than the front side. There is significant uncertainty in the mass of the MGS spacecraft. Upon launch, the total mass – including fuel – was 1391kg. The initial propellant mass was 216.5kg of hydrazine and 144kg of N_2O_4. It is not known how much of the propellant was expended in flight to Mars. The bulk of the remaining mass (1030.5kg) for MGS is a rectangular box of dimensions 1.7m x 1.17m x 1.17m. While the spacecraft also consists of a long boom and two solar panels, this study assumes that all of the non-propellant spacecraft mass resides within the previously-described box. For further simplicity, it is assumed that the spacecraft mass consists entirely of uniformly distributed aluminum. This creates an aluminum box of density 0.443 g/cm^3. The issue of propellant mass will be addressed later in this chapter when "penetrating particles" are discussed. Graphical representations of the MGS spacecraft and instrument deck are provided in Figure 2-2.

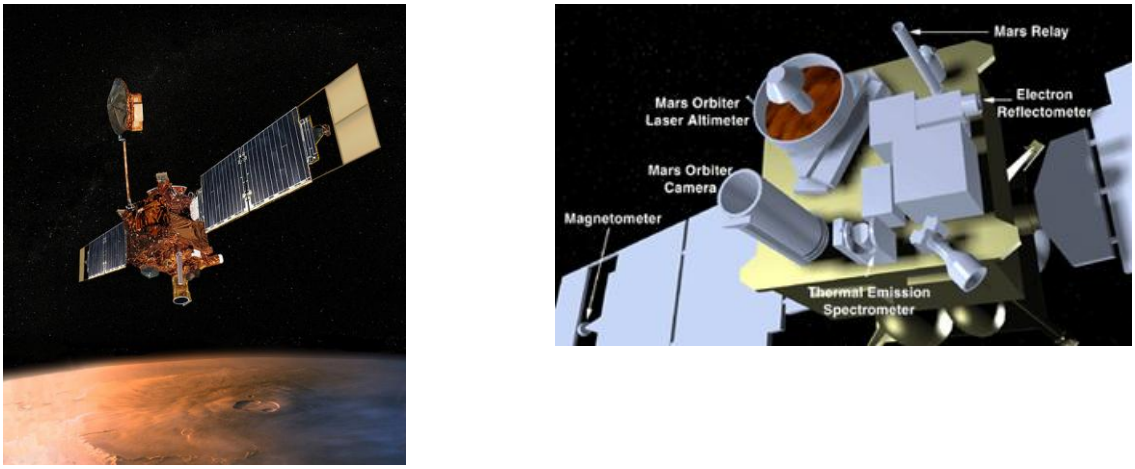

Figure 2-2. Mars Global Surveyor spacecraft (left) and instrument deck (right).
(Left image from: http:// nssdc.gsfc.nasa.gov/planetary/image/mars_global_surveyor.jpg)
(Right image from: http:// http://burro.astr.cwru.edu/stu/media/missions/mgs_diagram.jpg)

2.2.2 Micro-Channel Plate (MCP) Detectors

For more than three decades, micro-channel plate detectors have been used for the detection of photons, electrons, and ions. MCP detectors demonstrate relatively high efficiencies over a broad range of energies and a variety of incident particles.

The principal operation of the MCP is similar to most electron multiplier devices. That is, an incident particle or photon initiates a cascade of secondary electrons that are detected as a current in a nearby anode. The use of micro-channels provides increased efficiency, because electron cascades can occur in multiple channels. This results gains as high as 10^8 for each incident particle or photon.

Micro-channel walls are typically hexagonal in shape and oriented at ~8° angle to the normal of the micro-channel plate. Channel walls are etched into the micro-channel glass, and both the walls and glass are designed to promote secondary electron production. Figure 2-3 presents the typical structure of an MCP detector. It is common for MCP devices to employ a "chevron configuration" in which two MCP's are stacked on top of each other such that the micro-channels form a v-shape (See Figure 2-4). This configuration increases the detector gain while limiting the effects of ions generated within the detector.

The detector used on MGS ER is a Phillips brand MCP with a chevron configuration. Each micro-channel plate in the chevron is 1mm thick. The channels are 12.5µm thick oriented at a 13° angle to the normal of the micro-channel plate (Curtis 2009). Unfortunately, material composition and efficiency information for the specific detector used by MGS ER is not available. However, general MCP efficiency information was obtained from the manufacturer. Material composition information for standard MCP glass is provided by Wiza 1979. These efficiency and materials information are provided in Figure 2-5 and Table 1, respectively. Efficiency data for energies greater than 1 MeV/n will be presented elsewhere in this chapter.

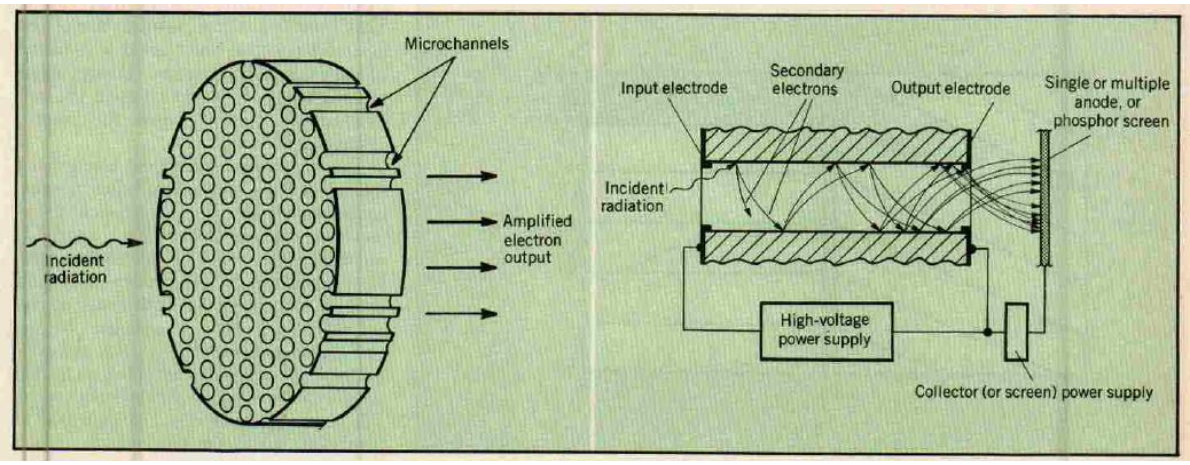

Figure 2-3. Operation of a typical MCP detector. (Leskovar 1977)

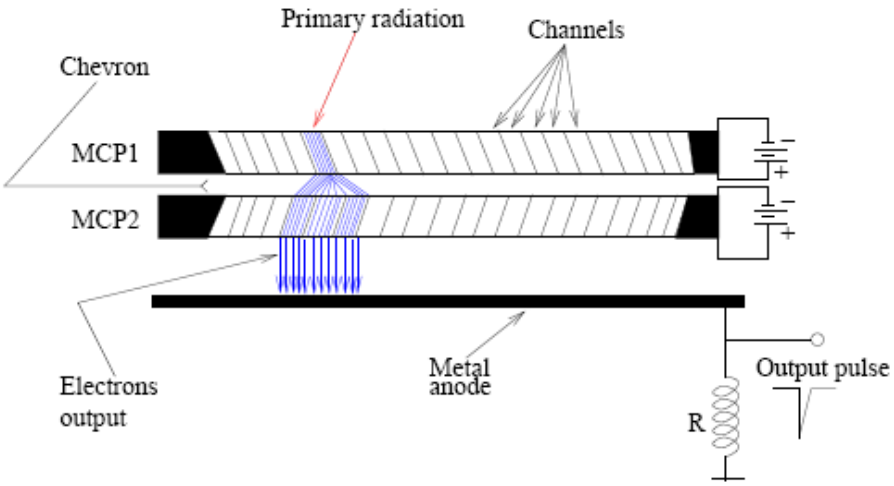

Figure 2-4. Chevron Configuration for MCP Detectors. (Kosev 2007)

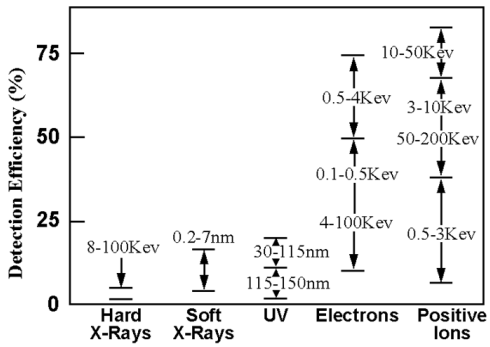

Figure 2-5. Detection Efficiency of Charged Particles and Electromagnetic radiation in MCP detectors. (Netolicky 2009)

Z	Element	Weight(%)
82	Pb	47.8
8	O	25.8
14	Si	18.2
19	K	4.2
37	Rb	1.8
56	Ba	1.3
33	As	0.4
55	Cs	0.2
11	Na	0.1

Table 2-1. Elemental Composition of MCP Glass (Wiza 1979)

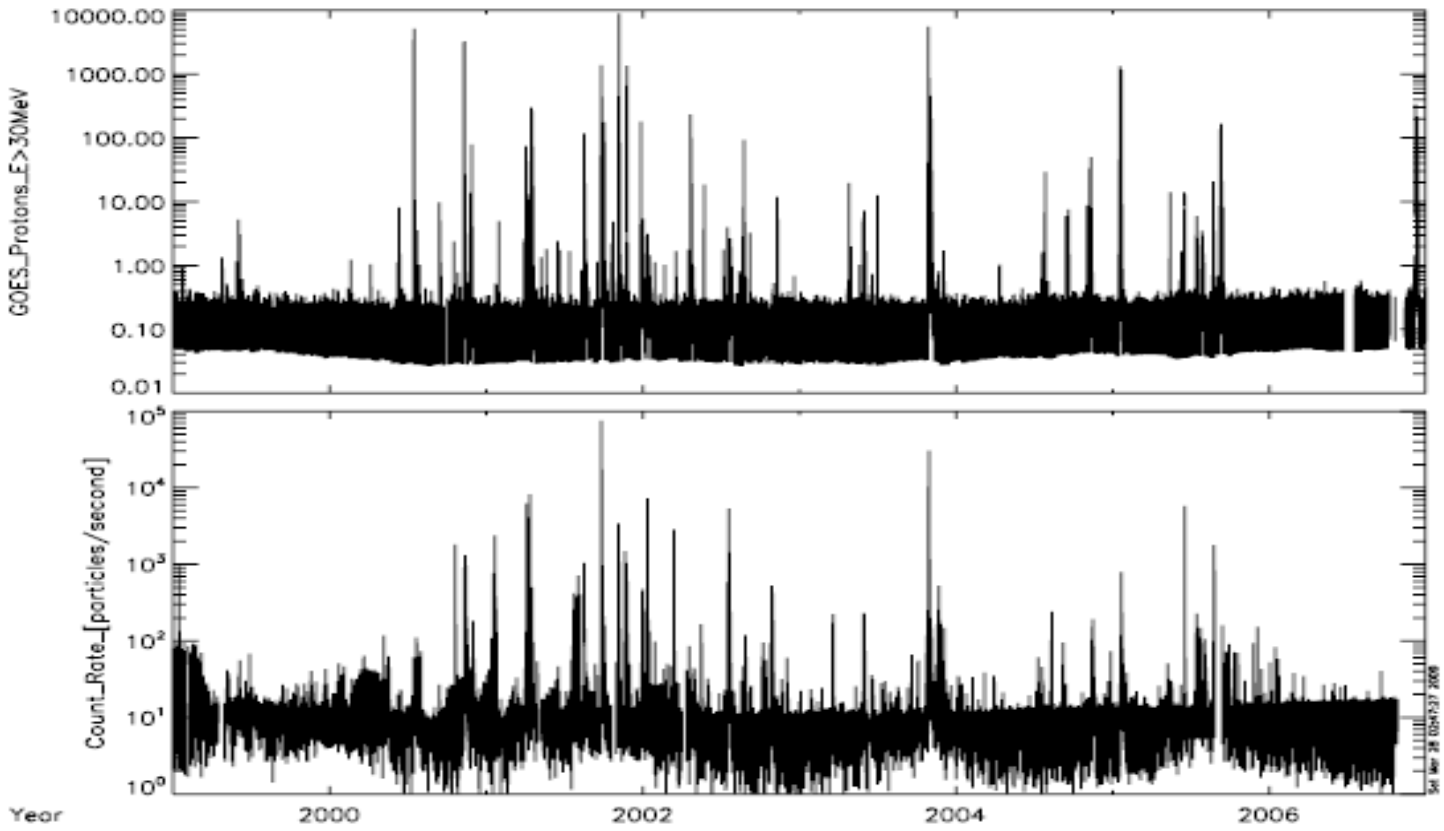

Figure 2-6. (Top Panel) Integral flux for protons with energies greater than 30 MeV, as measured at Earth by the SEM instrument onboard the GOES-10 satellite. Flux is measured in Particles/cm^2-s-sr. (Bottom Panel) Penetrating particle count rate observed the Electron Reflectometer (ER) instrument onboard the Mars Global Surveyor Satellite.

2.3 Detection of "Penetrating Particles"

MGS ER was not designed to observed solar energetic particles (SEP's). Therefore, it is important to verify that that observed increases in particle count rates are, in fact, SEP's produced during coronal mass ejections (CME's).

The first evidence of solar particle events onboard MGS did not occur with the ER but rather the Magnetometer (MAG). Upon arrival at Mars, in 1997, MGS entered "aerobraking" orbit, which is a highly elliptical orbit designed to use the Martian atmosphere to gradually slow the satellite into its permanent "mapping" orbit. During aerobraking, the Magnetometer was activated near apoapsis – the point in the satellite's orbit that is farthest from the planet. While the ER was not active to deduce the presence of SEPs, the MAG showed clear enhancements in the magnetic environment near Mars during times of known solar activity. Comparisons of coronal mass ejection (CME) shock arrival times at Earth to the observed magnetic enhancements at Mars made clear that the MAG was in fact observing CME shocks passing the near-Mars environment.

At a 378km circular orbit (termed "mapping orbit"), MGS is located within the ionosphere-induced magnetic field that enshrouds Mars. It was initially unclear whether or not the ER detector would be able to observe SEP's in "mapping" orbit. Moreover, it was unclear whether the ambient fluxes of electrons would overshadow the presence of solar energetic particles. It was soon determined that the field strength of the induced magnetic field is far too weak to limit access of SEP's to low-Mars orbit. Further, ambient fluxes of electrons at the highest energy channels are very low, which allows for the potential detection of "penetrating particles."

2.3.1 Penetrating Ions

Particles that entered MGS ER by penetrating the instrument's aluminum housing were initially identified by comparing count rates in the 3 highest energy channels (kinetic energy of ~1keV – 16keV). When multiple energy channels exhibited concurrent uniform increases in count rates, it was presumed that the particles being counted did not enter the normal optics of the instrument. This presumption is justified, because it is highly unlikely that such an increase would occur uniformly with ambient electrons over such great range of energies. Later analyses of the highest ER energy channel determined that the flux of ambient electrons of that energy range falls below the background rate. Thus, the highest energy channel alone can be used to determine the count rate and (with some additional analysis) the flux of penetrating particles.

On several occasions, the increase in particle count rates lasted several days. The time-intensity profiles of these prolonged count rate enhancements appear visually similar to observations of solar particle events observed by high energy ion detectors near Earth. A comparison of particle enhancements at Mars to those observed at Earth between 1999 and 2007 is presented in Figure 2-6. As will be presented in Chapter 3, nearly 91% of SPE's observed at Mars are also observed at Earth when the planets are near opposition. The close correlation in the occurrence of coronal mass ejections arriving at Earth to count rate enhancements observed with MGS ER further substantiates that MGS ER is detecting SEP's produced during coronal mass ejections.

Based on the shielding assumptions noted in the previous section, it is possible to estimate the energy range of particles that can penetrate the ER instrument housing and MGS spacecraft structure to reach the ER detector. Assuming a uniform 3mm shielding thickness on the front-side of the detector, ions with energies greater than ~25 MeV/n can penetrate the shielding and reach the MCP. This projected stopping range can be verified by the NIST online table of stopping rages (http://physics.nist.gov/PhysRefData/Star/Text/contents.html). Figure 2-7 presents the ranges of protons and electrons in aluminum over a wide range of energies.

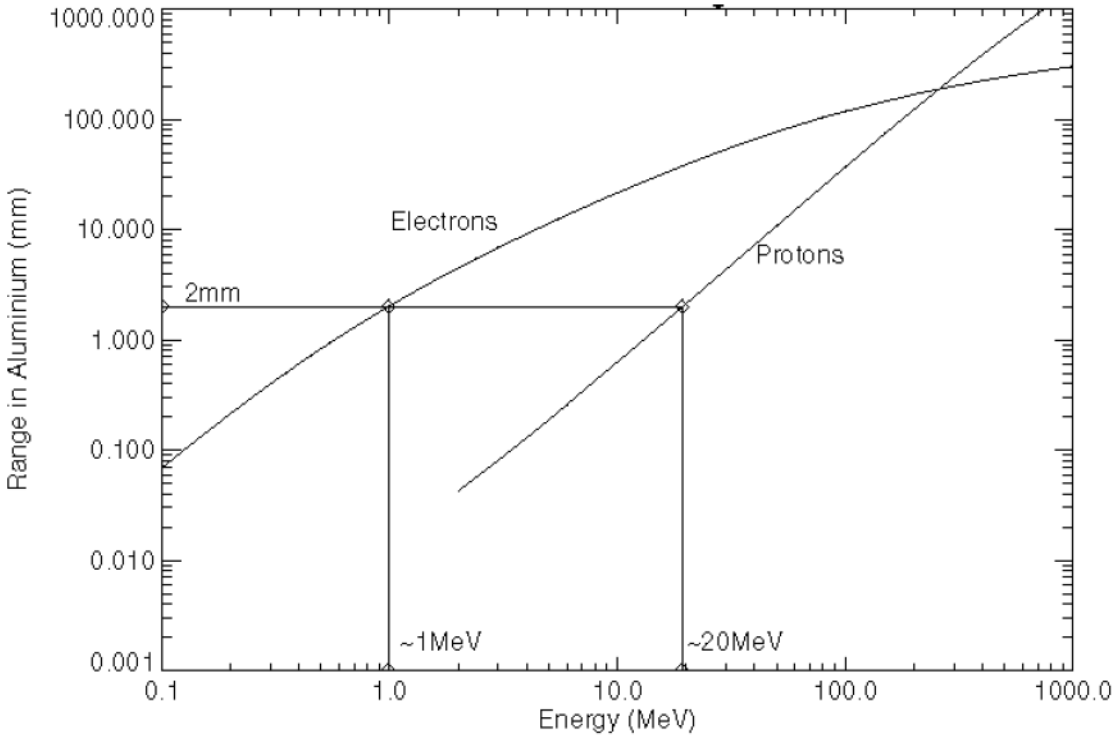

Figure 2-7. Ranges of electrons and protons in aluminum. (Daly et. al. 1996)

From the back-side of the detector, the minimum energy to penetrate the shielding depends on the angle of incidence. The minimum distance a particle must travel through the MGS spacecraft to reach the MCP is 58.5cm, and the maximum distance is ~180cm. It is assumed that no propellant remains in the spacecraft in order to establish a minimum energy required to reach the back-side of the MCP. So, it should be noted that actual penetration energies are likely to be substantially higher than those reported here. The radiation transport software, TRIM, was used to assess the stopping range of ions at the minimum and maximum distances. The minimum energy for a back-entry particle to reach the MCP is ~175 MeV/n. At the maximum traversal distance the penetration energy is ~330 MeV/n.

A simple form for determining the high energy spectra for SEPs is provided by Ellison and Ramaty (1985) and is as follows:

$$\text{Flux} \sim E^{-x} \qquad \text{(Equation 2-1)}$$

The "x-factor" – typically referred to as the power-law exponent - in Equation 2-1 is a constant that defines the hardness of the spectrum for a given event. Typically a more-complex double power law is used to describe SEP spectra. However, the double power law spectra are primarily useful in examining data over a broad energy range. For the purposes of this study, only high energy particle data (>1MeV) are examined. Thus, the simpler form is used. A survey was conducted of 31 SEP proton spectra between January 1, 1999 and January 1, 2007. Integral flux data were measured with the SEM instrument onboard the Earth-based GOES-10 satellite, using energy channels ranging from 1 MeV to 60 MeV. The average "x-factor" was 2.1 +/- 0.1.

The front-side flux of protons with energies greater than 25 MeV was compared to the back-side flux, assuming back-side penetration energy of 250 MeV. Based on this comparison, particles capable of back-entry typically constitute less than 8% of the total particle flux reaching MGS. Again, it is important to note that the estimates provided here do not take into account the presence of propellant, which will further reduce the relative significance of back-entry particles.

2.3.2 Secondary Particles

Production of secondary particles in the ER instrument housing and MGS structure was considered to determine if such particles contribute significantly to the MCP count rate. Emphasis was placed on examining the production of secondary electrons and neutrons, as these are the most common particle species to be produced. Secondary particle production was examined for both front-entry and back-entry particles.

Penetrating particles reaching the front-side of the MCP must pass through the ~3mm of aluminum that constitutes the ER instrument housing. While it is possible that these particles could generate secondary particles, the rate of secondary production is very low. Secondary electron and neutron production from energetic protons passing through 3mm of aluminum was modeled with the radiation transport code, PHITS. Particle and Heavy Ion Transport code System (PHITS) is a Monte Carlo-based code developed by the Japanese Atomic Energy Institute and Tohoku University. The model - presented in greater detail in Chapter 4 – is a combination of several independent transport programs that give PHITS a broad range of applicability to photons and particles across a wide range of energies. Figure 2-8 provides a graphical representation of the structure and applicability of PHITS.

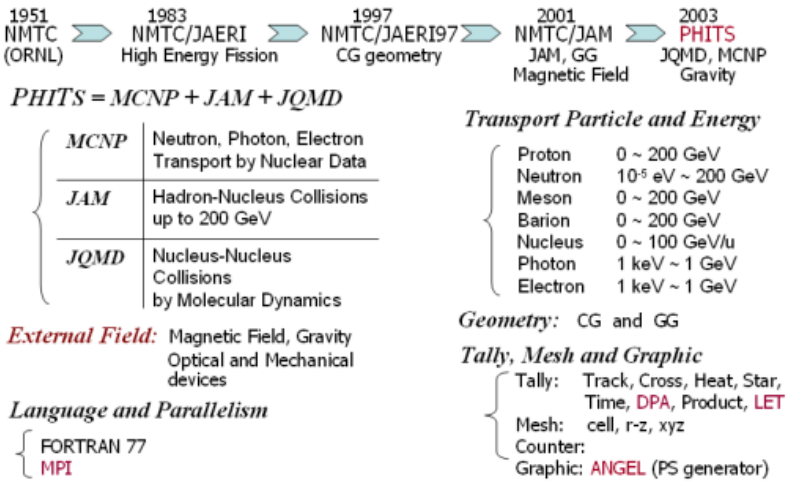

Figure 2-8. Graphical representation of the structure an applicability of the PHITS radiation transport code. (http://phits.jaea.go.jp/Overview.html)

Figure 2-9 presents the basic geometric arrangement used to assess secondary particle production from SEP's traversing 3mm of aluminum. The geometry consists of a pencil beam passing through a 3mm-wide sheet of aluminum with a planar detector positioned 1mm behind the aluminum sheet. A SEP energy spectrum of the form $E^{-2.5}$ was used to model the transport 1.0×10^6 protons of energies between 10 and 1500 MeV. Figures 2-10 and 2-11 present the fluxes of protons and secondary electrons and neutrons through the 3mm aluminum sheet. From this model, it is revealed that secondary electrons and neutrons each contribute less than ~1% of the particle flux emerging from the aluminum sheet.

It is possible that back-entry particles could generate secondary particles that reach the MCP. However, it is unlikely that these secondary particles are readily detected. This can be understood by noting that particle detection in an MCP requires the production of an electron avalanche. For this to occur, back-entry secondary particles (primarily electrons) must be able to penetrate the full length (2mm) of the MCP detector and strike front-side of one of the micro-channel walls. It is highly unlikely that a substantial flux of secondary particles with sufficient energy to generate an electron shower will occur.

The energy required for a secondary electron to traverse the full length of the MCP detector can be determined with the following formula (Katz and Penfold 1952):

$$R = 0.412 \times E^S \qquad \text{(Equation 2-2)}$$

R is the maximum electron range (g/cm^2), E is the kinetic energy of the electron (MeV), and $S \sim 1.265 - 0.0954 \times \ln(E)$.

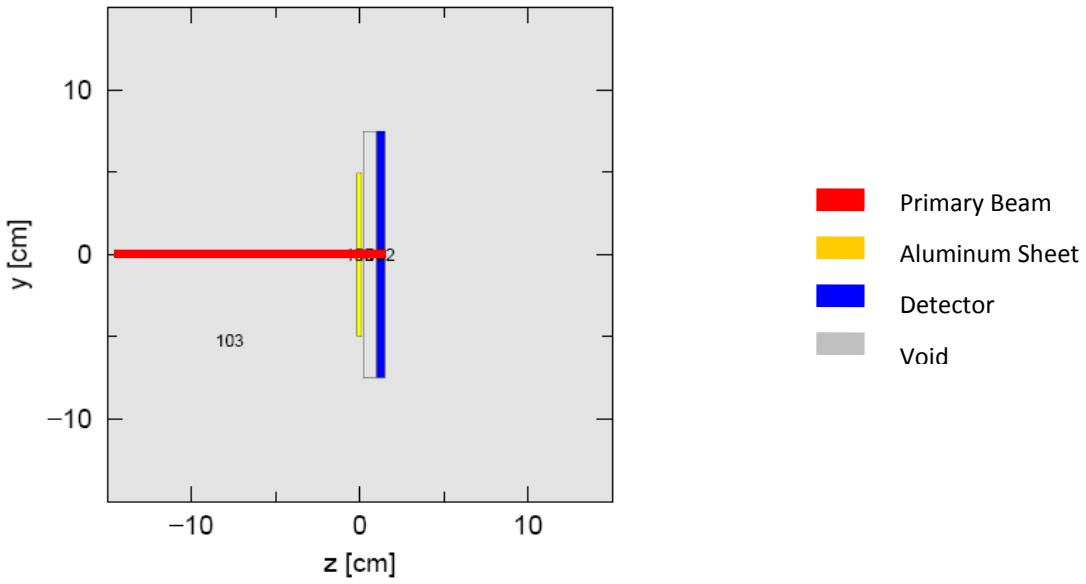

Figure 2-9. Geometric model used in PHITS to determine the flux of secondary particles from SEP's traversing 3mm of aluminum. (Image generated by PHITS)

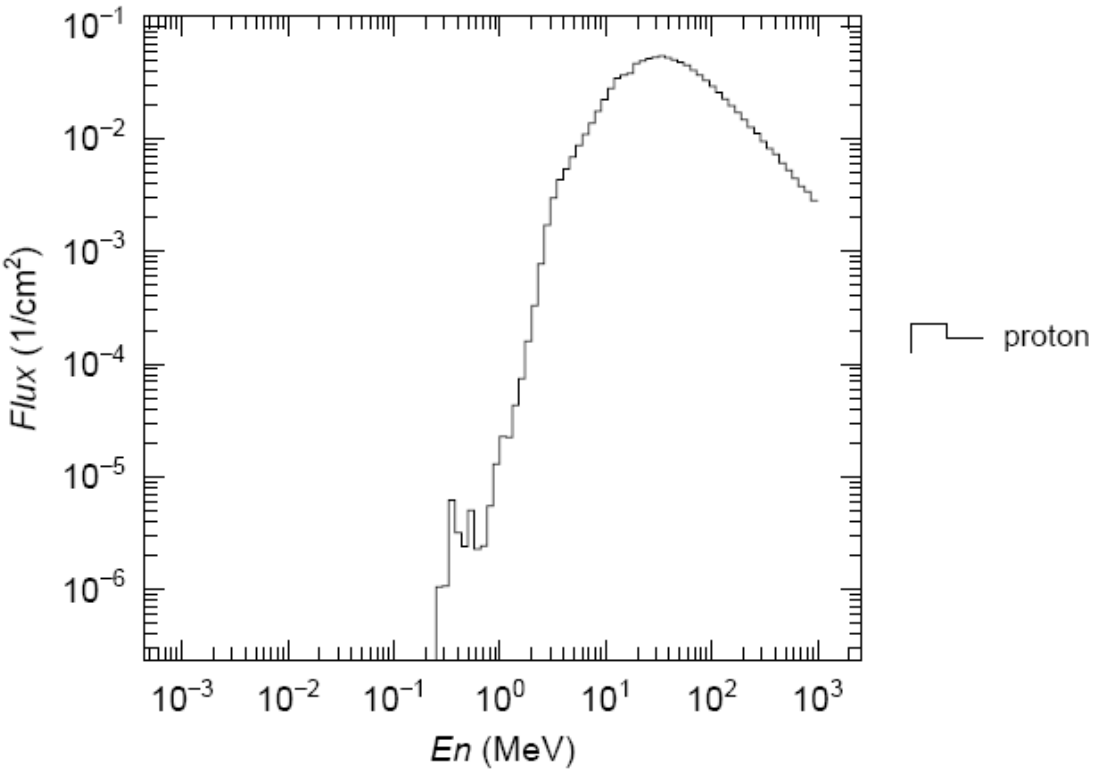

Figure 2-10. Proton spectrum for SEP's passing through 3mm of aluminium. (Plot generated by PHITS)

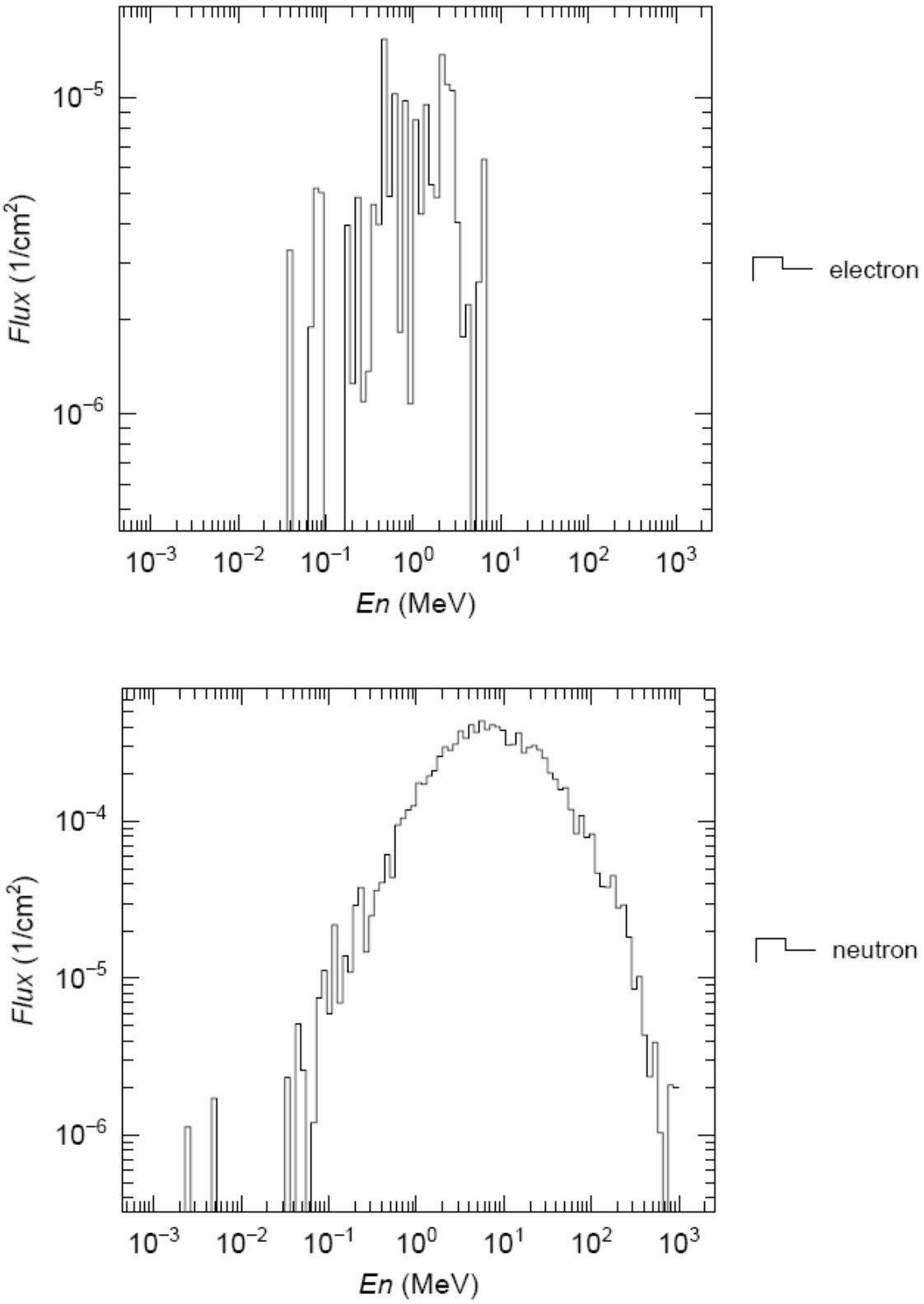

Figure 2-11. Secondary electrons (Top Panel) and neutrons (Bottom Panel) produced by SEP's traversing 3mm of aluminum. (Plot generated by PHITS)

The range of the electron is equal to:

$$R = \textit{Thickness / Density} = 0.2 \text{ (cm)} / 4.0 \text{ (g/cm}^3\text{)} = 0.8 \text{ g/cm}^2$$

Inserting this value into Equation 2-2 and solving for E reveals that a secondary electron must have energy greater than ~1.7 MeV to reach the front of the MCP and trigger an electron avalanche. Very few secondary electrons will be produced in this energy range.

Secondary neutrons face the opposite problem, in that their energies are likely too high to allow an interaction with the MCP. Neutrons produced in collisions of high-energy (> 175 MeV) protons with aluminum have typical energies in the MeV range. The collision lengths for neutrons of these energies on an MCP range from a few centimeters to several meters. This is well beyond the 2mm thickness of the MCP.

Based on this analysis, it is concluded that secondary particles generated within the MGS spacecraft or the ER housing do not contribute significantly to the flux of particles detected by the MCP. Rather, the count rates detected by the MCP must be the result of direct interaction with primary particles.

2.3.3 Penetrating Electrons and Heavy Ions

Using Equation 2-2, it is evident that electrons with energies greater than 3 MeV can penetrate the aluminum shielding of the ER instrument. To better interpret the meaning of the ER count rate during solar particle events, it is important to estimate the relative contribution of penetrating electrons to the observed count rate.

Mewaldt, et al. (2005) derives spectra for energetic protons, alpha particles, oxygen ions, and electrons during the large series of solar events that occurred in October – November 2003. Spectra for protons and electrons during one event are presented in Figure 2-12. The parameters listed in Mewaldt, et al. (2005) were used to determine the ratios of penetrating ions and electrons to protons in each of the events studied. For this analysis, electrons with energies greater than 3 MeV and ions with energies greater than 25 MeV were considered.

From this analysis, it is clear that penetrating electrons contribute the most to the overall flux with an average of 3.6% of the total penetrating particle flux. However, electrons demonstrate the greatest variation as well. On average, alpha particles contribute 1.3% of the total penetrating particle flux. Heavy ions contribute very little to the penetrating particle flux, as is evidenced by the low contribution of oxygen – approximately one hundredth of a percent.

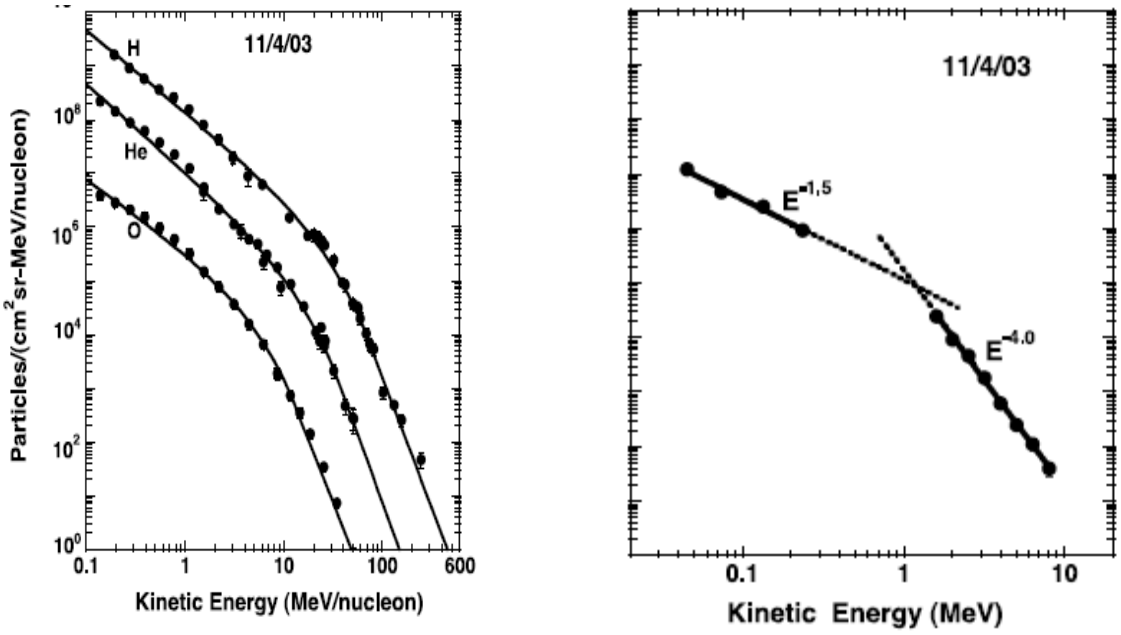

Figure 2-12. Ion (left) and Electron (right) Spectra for Solar Particle Event. (Mewaldt et al 2005)

	Oct. 26	*Oct. 28*	*Oct. 29*	*Nov. 02*	*Nov. 4*	***Average***
He / H	0.011	0.017	0.013	0.013	0.012	**0.013**
O / H	1.5×10^{-4}	1.6×10^{-4}	8.8×10^{-5}	1.1×10^{-4}	5.1×10^{-5}	**1.1×10^{-4}**
e- / H	0.027	0.0046	NA	0.056	0.057	**0.036**

Table 2-2. Ratios of He, O, and electron fluxes to protons fluxes at energies capable of penetrating MGS ER aluminum housing. Data derived from Mewaldt et al (2005)

2.4 Estimating Flux from Penetrating Particle Count Rates

Complete analysis of the ER penetrating particle data requires an adequate methodology for estimating the particle flux from raw count rate data. This is not a trivial process, as there are significant challenges in determining the ER detector efficiency for penetrating particles. Some consideration must also be given for the presence of energetic heavy ions and electrons. This section describes a strategy to provide an accurate for the SEP flux at Mars, based on penetrating particle count rates observed by MGS ER.

2.4.1 Efficiency of Micro-Channel Plate Detectors for High-Energy Ions

As mentioned previously, MGS ER was designed for detection of low-energy electrons. The MCP detector response for high-energy ions is unknown. Furthermore, the literature is sparse regarding MCP efficiencies for ions with energies greater than a few hundred keV. Mosher, et al. (2001) measured MCP efficiencies for ions with energies up to 8.25 MeV for alpha particles. It was found that 8.2 MeV alpha particles were detected with 80% efficiency, and that efficiency

increased with energy for ions between 357 keV to 8.25 MeV. Mosher, et al. (2001) attribute the high efficiency of energetic ions to the particles' ability to penetrate and excite multiple ion channels. Hence, this analysis considers both the ability of various particles to ionize MCP material and the number of channels that each incident particle traverses.

The radiation transport software TRIM (Transport of Ions in Matter) was used to examine energy deposition and ion paths for 8 MeV alpha particles and 25 MeV protons. TRIM is a package within the Stopping Range in Matter (SRIM) software set, which is available online at http://www.srim.org. Of the SRIM software packages, TRIM is the most comprehensive and is capable of providing visual displays of ion paths for a wide range of energies through an equally wide range of target materials. TRIM is also capable of determining target damage, ionization, sputtering, and phonon production (http://www.srim.org/SRIM/SRIMINTRO.htm). While TRIM does not provide as extensive information as PHITS regarding secondary particle production and transport, it is far more efficient at determining ionization tracks through a variety of media. Thus, it was used in this study to explore a variety of scenarios for mono-energetic protons traversing a sample MCP material.

A summary of results is presented in Table 2-3. The TRIM simulations used a 2mm target of MCP material with channel diameters of 12.5µm and center-to-center channel distance of 15.5µm. The elemental composition of the MCP is described in Table 2-1 (Wiza 1979). An average ionization potential of 9 eV is assumed for MCP material, which takes into account the ionization potentials of each constituent element and their relative mass contributions. Figure 2-13 provides a graphical representation of the physical analysis described here.

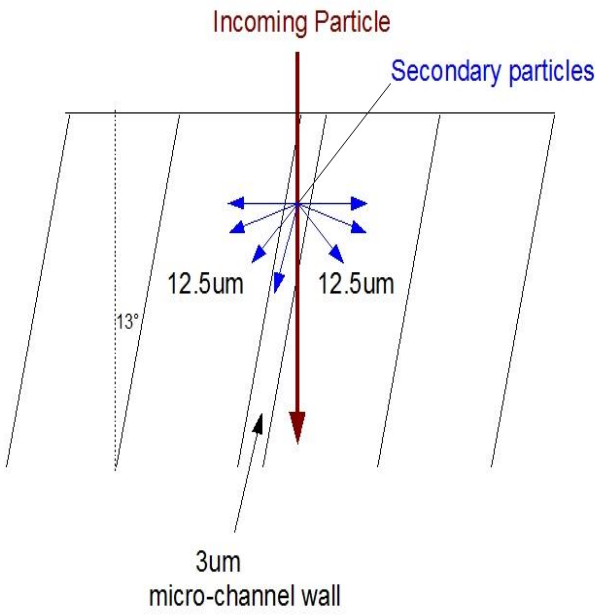

Figure 2-13. Energetic Ion Interaction with MCP.

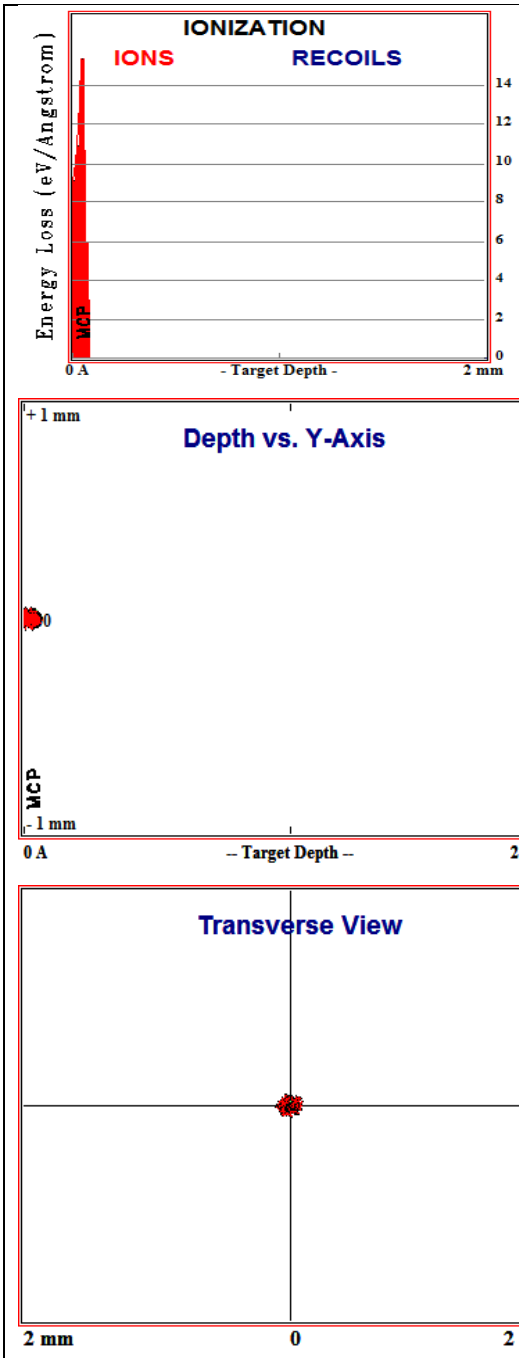

Figure 2-14. 8.25 MeV Helium Interaction with MCP.(Top Panel) Energy Loss vs. Depth. (Middle Panel) Ion Tracks vs. Depth – Cross Section. (Bottom Panel) Transverse – "Anode View" – of Ionization Tracks in MCP.

(Plots generated by TRIM.)

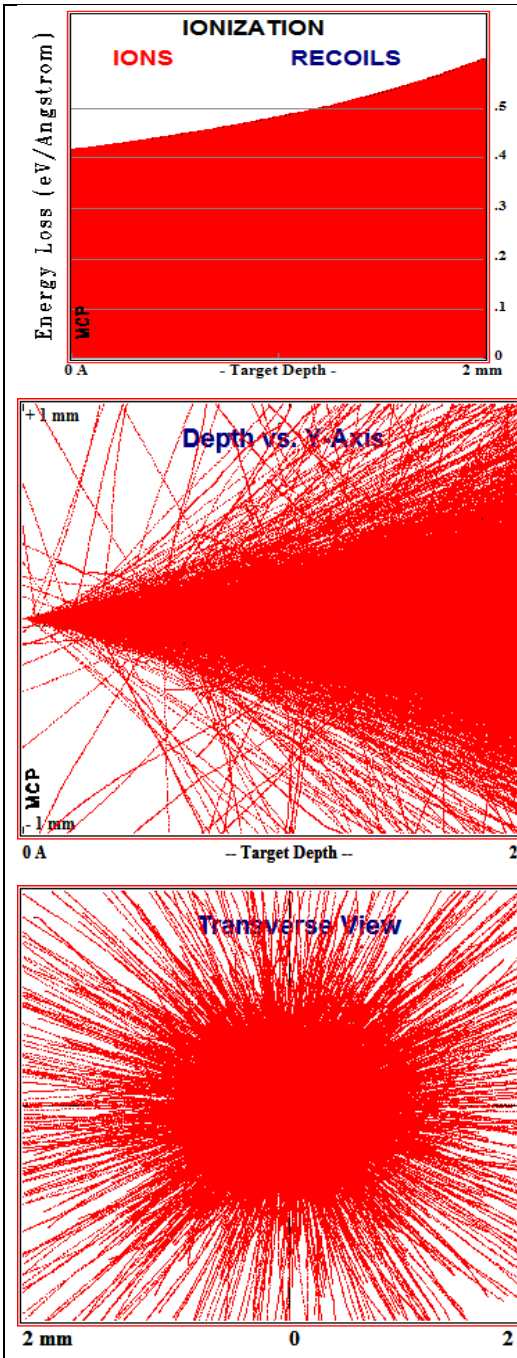

Figure 2-15. 25 MeV Proton Interaction with MCP. (Top Panel) Energy Loss vs. Depth. (Middle Panel) Ion Tracks vs. Depth – Cross Section. (Bottom Panel) Transverse – "Anode View" – of Ionization Tracks in MCP.

(Plots generated by TRIM.)

An 8 MeV alpha particle has a stopping range of ~50µm in a typical MCP – sufficient to cross at least 4 micro-channels. Figure 2-14 presents the energy loss characteristics and ionization tracks of 8 MeV alpha particles in MCP material, as determined by TRIM. The particle deposits all of its energy in the MCP material with a peak energy loss of ~160 keV/µm. This has the potential to directly generate as many as ~9 x 10^5 electrons, each of which are accelerated toward the anode by the voltage bias across the MCP plates. Not only can the electrons interact directly with the anode, but they can also strike the micro-channel walls to generate electron avalanches.

The stopping range of a 25 MeV proton in an MCP lies beyond 2mm. However, this particle has the potential to deposit more energy and generate more electrons than an 8 MeV alpha particle. As the proton traverses the MCP, it loses an average of ~5 keV/µm. Over the 2mm of MCP material, the total energy deposited is ~10 MeV. This is enough energy to produce as many as ~ 1.1 x 10^6 electrons. If the proton traverses the MCP in a straight line, it will interact with a minimum of 30 micro-channels. However, the 25 MeV proton has a substantial chance of deviating from its incident path and transmitting secondary ions, as displayed in Figure 2-15. This dramatically increases the potential for interaction with micro-channel walls and increases the capacity to produce detectable electrons.

Of course, electron production in micro-channel walls does not necessary result in an electron avalanche in the micro-channel itself. Secondary electrons must have sufficient energy to escape the micro-channel walls. Moreover, the electrons must escape the walls toward the front-end of the MCP in order to produce a sufficient gain to be detected by the detector anode. A quantitative rationale will be shown here to demonstrate that a 25 MeV proton will cause at least one electron to enter the micro-channel on the front-side of the MCP with near certainty.

As mentioned previously, the micro-channel walls are estimated to be 3µm thick. Here, we assume that all electrons are produced in the center of the micro-channel walls and must traverse 1.5µm in order to enter the micro-channel. Equation 2-2 presents a method to determine the practical range of an electron for a given energy. Using 1.5µm as the range, Equation 2-2 can be solved for electron energy. Doing so reveals that an electron must have a kinetic energy of ~19keV to escape the micro-channel wall.

The following formula can be used to determine the probability of an energetic proton to generate an electron of a given energy (Leroy and Rancoita 2004):

$$\text{Probability} = 0.1535 \times B \times \rho/\beta^2 \times Z/A \times 1/E \qquad \text{(Equation 2-3)}$$

B is the distanced traversed by the proton; ρ is the target material density; β = v/c for the incoming proton; Z/A is the proton-to-atomic mass ratio for the target material; E is the kinetic energy of the produced electrons.

Using the material properties for an MCP detector (see Table 2-1) and proton energy of 25MeV, Equation 2-3 demonstrates that there is a 7.4% chance of a 19keV electron being produced in each traversed channel wall.

As mentioned previously, each 25 MeV proton traverses a minimum of 30 micro-channel walls throughout the MCP – 15 walls on the front-side and 15 walls on the back-side of the MCP. With a 7.4% chance of producing an escapable electron (E > 19keV) per wall, the probability of an electron not being released ($P = (1-0.07)^{30}$) into the micro-channel on the front-side of the MCP is ~11%. It was also noted previously that 25 MeV protons deviate significantly from a linear path through the MCP (See Figure 2-11). Hence, these protons are likely to traverse far more than 15 micro-channel walls on the front-side of the detector. Based on this analysis, it is concluded that 25 MeV protons are very likely to produce an electron avalanche in the MCP detector.

Qualitatively, it makes good sense that 25 MeV protons would have a higher efficiency than low-energy electrons (for which the ER was designed to detect). The track structures for energetic protons are denser and thicker than that for low-energy electrons. Thus, more energetic electrons are produced and should be detected. So, if low-energy electrons are detected by the MCP with high efficiency, 25 MeV protons should be detected with a much higher efficiency.

In addition to being more efficiently detected than low-energy electrons, 25 MeV protons must also be more efficiently detected than 8 MeV alpha particles in an MCP detector. Protons with energies of 25 MeV interact with substantially more micro-channel walls and deposit more energy over 2mm of MCP material than 8 MeV alpha particles. Hence, it is expected that the efficiency of 25 MeV protons should be much greater than the reported 80% efficiency of 8 MeV alpha particles for MCP detectors. Given the range of 80 – 100%, this study uses an estimate of 90% efficiency for 25 MeV protons.

It is not expected that this efficiency will change significantly with increasing particle energy. While the average energy deposited decreases with increasing energy, the incoming particles will traverse and interact with many more micro-channel walls than an 8 MeV alpha particle. Hence, it is estimated that the MCP is 90% efficient for ions with energies *greater than* 25 MeV.

Back-entry particles face a greater challenge in being detected. When a particle interacts with the MCP from behind, the secondary electrons will tend to move in a direction away from the anode. Thus, an electron avalanche produced by a back-entry particle would likely move in a direction away from the anode and toward the front-side of the MCP. These avalanche electrons would not be detected.

Moreover, the voltage bias placed over the MCP will act to slow the particles as they emerge from the micro-channel walls. As a result, the likelihood of an electron avalanche occurring is very low, and the efficiency of MCP detectors for back-entry particles must be equally low. Based on their relatively low efficiency and low flux, back-entry particles will no longer be considered in this study.

	8.25 MeV Alpha Particle	25 MeV Proton
Range (μm)	~50	NA
Peak Energy Loss per Distance (keV/μm)	16	6
Total Energy Deposited (MeV)	8.25	~10.0
Potential # Electrons Produced	~9 x 10^5	~1.2 x 10^6
Minimum Micro-Channel Crossings	4	30
MCP Efficiency	80%	90%*

Table 2-3. Summary of data regarding penetration and ionization in 2mm of standard MCP material *(Wiza 1979)* by 8.25 MeV alpha particles and 25 MeV protons.
*Estimate based on available data.

2.4.2 MGS ER Geometric Factor for Penetrating Particles

With the exclusion of back-entry particles, calculating the geometric factor for penetrating particles becomes a far simpler process. The fundamental equation for calculating the geometric factor of a detector (assuming there is no angular dependence on the range of incident energies) is:

$$G = \iiint d\mathbf{A} \sin\theta \, d\boldsymbol{\theta} \, d\boldsymbol{\phi} \qquad \text{Equation 2-4}$$

$d\mathbf{A}$ represents the differential area of the detector, θ is the angular displacement of the incident particle from the vertical axis, and ϕ is the angular displacement of the incident particle from the horizontal axis. It is assumed that the incident particle flux is isotropic.

While front-entry particles may enter from any angle the ER instrument from any forward angle, the particle must strike the MCP at an angle that traces through the anode. By taking into account the surface area of the detector, solid angle, and the angles of incidence, Equation 2-5 can be reduced to the following form *(Delory 2009)*:

$$G = \pi \times \text{Area} \qquad \text{Equation 2-5}$$

As displayed in Figure 2-1, MGS ER utilizes ring-shaped MCP detector. The outer diameter of the ring is 8.7cm and the inner diameter is 6.6cm. Thus, the total area is 25.2cm^2. However, there are portions of the detectors that are not responsive. Taking the inactive areas into account, the usable area of the MCP detector ring is 15.2 cm^2 (Delory 2009).

A geometric factor of 47.8 is found by inserting the usable detector area into Equation 2-5.

2.4.3 Conversion of MGS ER Count Rate Measurements to Flux Estimates

In three basic steps, the count rates observed by MGS ER can be converted to a flux estimate:

1. Adjust the count rate to account for detector efficiency.
2. Adjust the count rate to account for counts that are not penetrating protons (i.e., electrons and alpha particles).
3. Divide the count rate by the geometric factor for penetrating particles.

As discussed previously, the estimated efficiency for penetrating particles is 90%. This study assumes that 5% of the count rate measured by MGS ER is due to penetrating electrons and alpha particles (4% electrons and 1% alpha particles). It is necessary to remove these particles from the count rate in order to more effectively compare proton fluxes at Mars to those at Earth. Finally, the geometric factor of 47.8 – established in the previous section – will be applied to convert the ER count rates to a flux value.

$$\text{Flux} = (C - 0.05C) / (0.9 \times 47.8) \qquad \text{Equation 2-6}$$

C represents the count rate measurements. Figure 2-16 presents the flux estimates for MGS ER during the duration of the instrument's operation.

2.5 Validation of MGS ER Penetrating Particle Flux Estimates

The application of Equation 2-6 to count rate data collected from MGS ER has been validated by comparison two independent instruments – one at Earth and another at Mars. Three independent comparisons have been used to validate the analysis described in this chapter:

1. Flux measurements at Earth and Mars;
2. Fluence measurements at Earth and Mars; and
3. Galactic Cosmic Ray flux measurements by two independent detectors in Mars orbit.
4. Solar Energetic Particle flux measurements by two independent detectors in Mars orbit.

GOES-10 utilizes the SEM instrument to collect energetic particle data for protons with energies from 1 - ~200 MeV. While the bulk of comparisons between MGS ER and SEM will be presented in Chapter 3, this section demonstrates that the estimated flux at MGS ER is in very close agreement with theoretical predictions and empirical observations regarding the radial gradient of solar energetic particle flux between Earth and Mars.

The MARIE instrument, onboard the Mars Odyssey satellite, collected energetic particle data continuously from July 2002 – October 2003. MARIE data are not reliable during solar particle events due to an exceedingly long dead time. However, a comparison of quiet time flux at MARIE to flux estimates with MGS ER shows that the instruments are in close agreement.

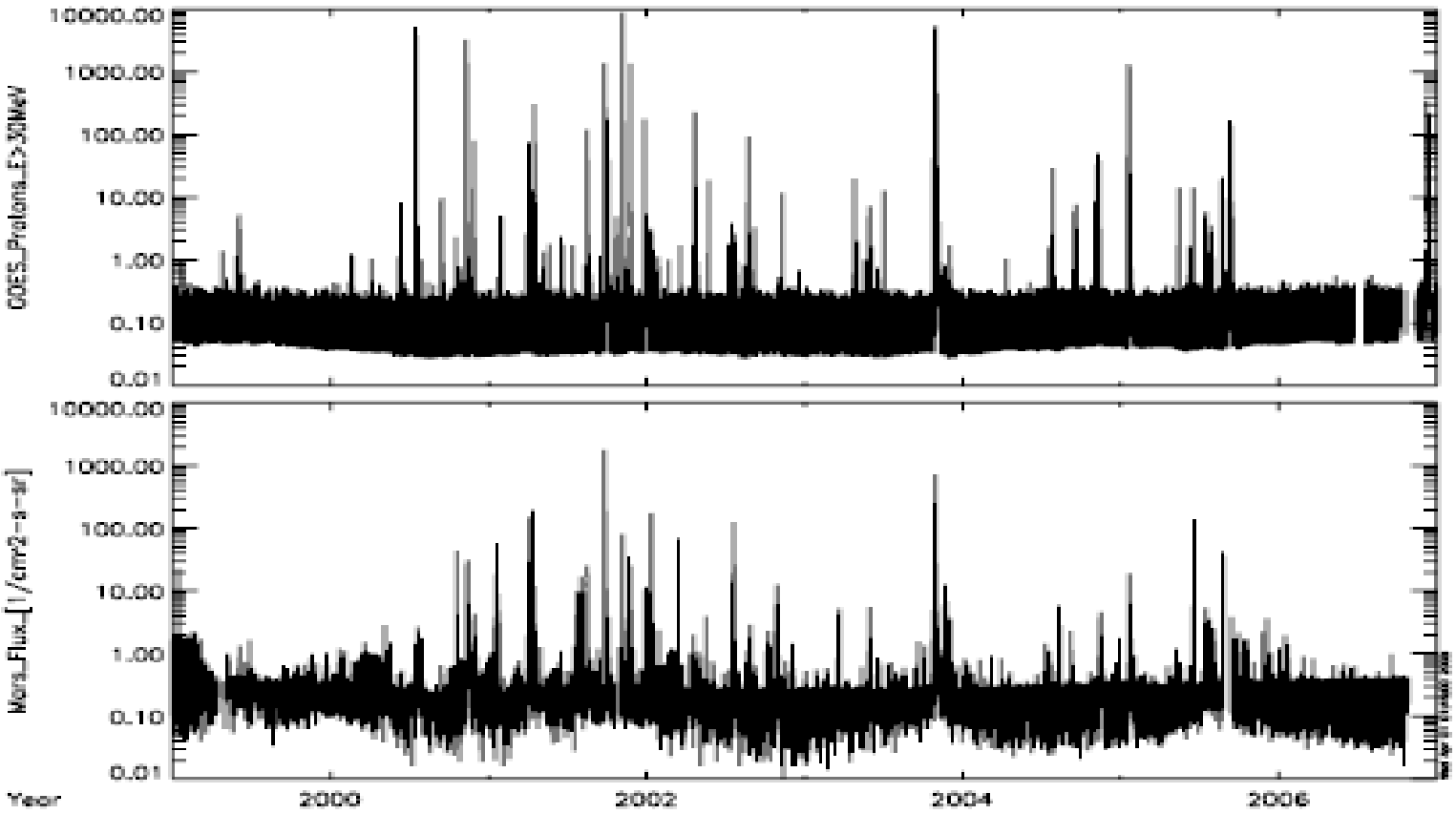

Figure 2-16. (Top Panel) Integral flux for protons with energies greater than 30 MeV, as measured at Earth by the SEM instrument onboard the GOES-10 satellite. Flux is measured in Particles/cm^2-s-sr. (Bottom Panel) Penetrating particle flux estimate observed the Electron Reflectometer (ER) instrument onboard the Mars Global Surveyor Satellite. Flux is measured in Particles/cm^2-s-sr

2.5.1 Radial Gradient of Solar Energetic Particle Flux and Fluence

It is typical for studies of the radiation environment at Mars to extrapolate Earth-based data to Mars distance by scaling down Earth data as $1/R^y$. Here, R is the radial distance from the Sun and y is a scaling factor. As originally reported by Feynman and Gabriel (1989) and nicely summarized by Smart and Shea (2002), the "y-factor" falls within the following ranges:

- Typical y-factors for flux extrapolations for radial distances beyond 1 AU are between 3 and 4, with a common value of 3.4.
- Fluence extrapolations vary between 2 and 3, with a typical value of 2.5.

To establish a viable validation of the MGS ER flux estimate, a survey was conducted to find solar particle events that met the following criteria:

1. The event was detected by GOES-10 and MGS ER.
2. The event did not overlap with any prior or succeeding event.
3. Earth and Mars were within 30° of opposition at the time of the event.

By constraining the analysis in this manner, extraneous factors (e.g., longitudinal variations) that may affect the propagation of SEP's through space are limited. For example, Smart and Shea (2002) suggest that overlapping solar particle events dramatically alter the radial gradient of observed SEP's. The criteria listed above would limit any such effects. Between 1999 and 2007, 58 events were observed. Five of the observed events met all of the above criteria. The fluences and peak fluxes were measured at GOES-10 and MGS ER for each of the five selected events.

A minor modification was necessary for the GOES-10 SEM data. To adequately compare SEM data to MGS ER, the SEM data needed to represent protons with energies greater than 25 MeV. However, the SEM integral energy channels are energies greater than 1, 5, 10, 30, 50, 60, and 100 MeV. To account for the energy difference, a spectrum was modeled for each of the events in the form: Flux ~ E^{-a}. The 30 MeV channel was scaled to 25 MeV using the modeled spectrum.

Comparison of peak fluxes between SEM and MGS ER is straightforward. Maximum flux values for each instrument were obtained, and the Earth-to-Mars flux ratio was calculated. The following formula was used to calculate the "y-factor" for each event:

$$y = \ln(\Phi) / \ln(1.5) \qquad \text{Equation 2-7}$$

Φ is the Earth-to-Mars peak flux ratio, and 1.5 is the ratio of the distance of Earth from the Sun to that of Mars. The average "y-factor" for peak fluxes in the five selected events is 3.5 +/- 0.3. This is very close to the value predicted by Feynman and Gabriel (1989). Full results of this analysis are presented in Table 2-4.

Event Start Date/Time	Φ	y
1999-05-27/12:55:28	3.0	2.7
2001-03-29/20:09:36	5.7	4.3
2001-05-20/10:49:36	4.4	3.6
2001-06-15/17:34:56	2.8	2.5
2001-08-16/03:45:04	5.4	4.2
Average	4.2	3.5

Table 2-4. Peak flux comparison data.

It is somewhat more complicated to compare fluence measurements between SEM and MGS ER, because such comparisons require clear and consistent determination of the start and end times for an event at Mars and Earth. This was accomplished by establishing annual background fluxes at each instrument for every year between 1999 and 2007. Background fluxes were calculated by average the flux over twenty quiet-time days at various points throughout the year. A particular solar particle event is said to begin when the flux exceeds 3σ of the annual background flux for more than one hour. Similarly, the event is said to end when the flux drops below 3σ of the annual background flux for more than one hour. This methodology for determining event start and end times was found to have the greatest consistency between events, though there were instances where estimates were necessary. Once the start and end times are established, the average flux for the event is calculated and multiplied by the duration to determine the total particle fluence. As with the peak flux calculations, the following formula was used to calculate the "z-factor" for each event:

$$z = \ln(\Psi) / \ln(1.5) \qquad \text{Equation 2-8}$$

Ψ is the Earth-to-Mars fluence ratio, and 1.5 is the ratio of the distance of Earth from the Sun to that of Mars. The average "z-factor" fluences in the five selected events is 2.2 +/- 0.4. Again, this is entirely consistent with the value predicted by Feynman and Gabriel (1989). Full results of this analysis are presented in Table 2-5.

The clear consistency between predicted flux and fluence gradients and those derived from analysis of MGS ER data provides another validation for the analysis described in this chapter. At the very least, this analysis demonstrates that the flux estimates for energetic particle data with MGS ER are no less accurate than those provided for in empirical models.

Event Start Date/Time	Ψ	z
1999-05-27/12:55:28	1.5	1.0
2001-03-29/20:09:36	3.2	2.8
2001-05-20/10:49:36	2.8	2.5
2001-06-15/17:34:56	1.7	1.2
2001-08-16/03:45:04	4.1	3.5
Average	2.6	2.2

Table 2-5. Fluence comparison data.

2.5.2 Galactic Cosmic Radiation Flux Measurements at Mars

The MARIE instrument, onboard the Mars Odyssey satellite, entered orbit around Mars in 2001. Due to errors in the instrument electronics, it was not able to provide consistent data coverage until March 2002. At that time, it began collecting energetic ion data for particles with energies greater than ~30MeV/n. MARIE operated through October 2003, when a series of powerful solar particle events caused a permanent malfunction in the instrument's electronics. During its time of operation, MARIE provides a direct comparison of energetic particle data to MGS ER.

However, the comparison of MARIE data to MGS ER is most easily accomplished during quiet times. MARIE has a long dead time that causes the instrument to saturate at relatively low fluxes. So, there are few solar particle event data to compare.

MARIE utilizes a silicon detector stack to detect the incidence of particles, their energies, and their composition. The instrument was designed to detect particles entering the front aperture or from behind (See Figure 2-17). A Cerenkov detector was placed at the back end of the instrument to trigger when back-entry particles arrived. However, the Cerenkov detector ceased to function early on in the mission, leaving the instrument unable to distinguish between front- and back-entry particles.

The situation is made more complicated by the fact that the back-side of MARIE rests against the Mars Odyssey spacecraft. There is an unknown mass of propellant remaining in Mars Odyssey, which makes it difficult to know the energy range of particles entering from behind. Without this knowledge, it is difficult to determine the correct geometric factor for MARIE.

This analysis presents a range of fluxes for MARIE. The upper limit of this range utilizes a geometric factor that assumes no back-entry particles are counted – geometric factor of 3.2cm^2-sr (Lee 2009). The lower limit assumes that the back of the detector is equally accessible as the front – geometric factor of 6.4cm^2-sr.

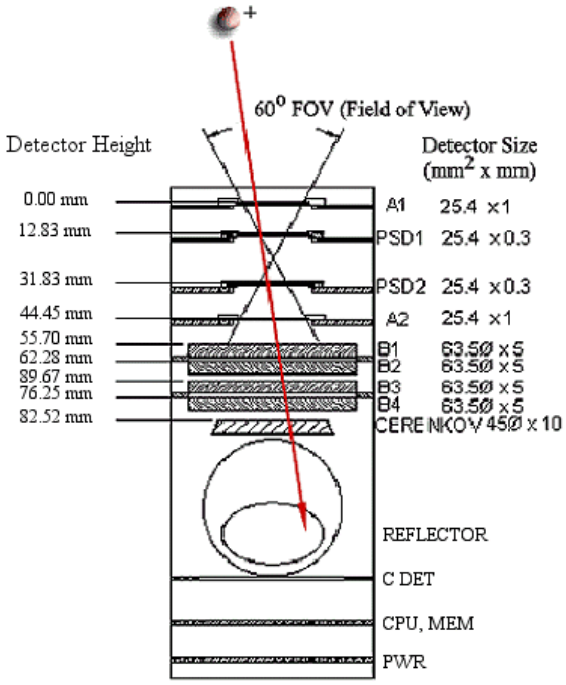

Figure 2-17. Schematic of MARIE detector stack. (Pinsky and Wilson 2002)

Data for MARIE are stored as event records, which describe the time, position, and energy deposition in each of the stack detectors. An event is recorded any time there is a coincident detection in the A1 and A2 detectors. The comparison of MARIE data to MGS ER data does not require detailed energy or position information. Rather, only the total particle fluxes are relevant.

Event records from MARIE were binned into five minute intervals and averaged to create an initial count rate. A dead time correction of 23% was applied to the count rates to account for the time required to reset the device after each record. Low- and high-limit fluxes were then calculated by dividing corrected counts rates by the appropriate geometric factor.

The full MARIE data set was compared to MGS ER to identify extended periods of quiet time. Five days were selected for comparison based on the following criteria:

- There were no prolonged gaps in MARIE or MGS ER data;
- There were no known solar events during the given timeframe; and
- Days were selected that span the full timeframe of MARIE operation at Mars.

Over the five days, the average lower limit flux measured by MARIE was 0.116 particles/cm^2-s-sr. High limit flux measurements with MARIE are simply twice the lower limit for an average of 0.234 particles/cm^2-s-sr. For comparison to the MGS ER, the correction factor for the alpha particle contribution was removed from the MGS ER flux estimate. An average flux of 0.178particles/cm^2-s-sr was measured for MGS ER during the five quiet time days. This is almost

exactly in the middle of MARIE's flux range and reflects the detection of some (but not all) back-entry particles by MARIE. The results of this analysis are summarized in Table 2-6.

Strong consistency with MARIE measurements further validates the MGS ER flux estimates described in this chapter.

	6/13/02	*09/13/02*	*11/24/02*	*05/04/03*	*10/11/03*	**Average**
MARIE High Flux Estimate	0.24	0.22	0.24	0.23	0.24	0.234
MGS ER	0.17	0.17	0.17	0.18	0.2	0.178
MARIE Low Flux Estimate	0.12	0.11	0.12	0.11	0.12	0.116

Table 2-6. Comparison of high- and low-limit background flux measurements with MARIE to MGS ER flux estimate. Units are: Particles / cm^2-s-sr.

2.5.3 Comparison of Solar Particle Event Measurements at MARIE and MGS ER

During its time of operation MARIE experienced serious limitations in its ability to detect solar particle events. As discussed previously, a long dead time caused MARIE to saturate at relatively low particle count rates. Several techniques have been employed to derive measurements from various counters in the MARIE detector stack by making certain assumptions regarding the detector and satellite housing. However, those techniques are wrought with instrument-specific errors that make a comparison to MGS ER less than useful.

For the purposes of this study, a single solar particle event was identified that was observed by MGS ER and was also small enough that there was not significant saturation at MARIE. Figure 2-18 presents the data from October 2002 for MARIE and MGS ER. The event to be compared is identified in Figure 2-18 for clarity. A broader timeframe is displayed in order to better present the challenges of overcoming saturation in the MARIE detector.

The start time for the comparison event was set at 7:00am on October 25, 2002; the end time was set at 8:00am on October 27, 2002. These times were chosen to encompass the full range of the event, while avoiding gaps in the data. As in other analyses presented in this chapter, the average flux value was calculated for each instrument and used for comparison. It should also be noted that the MARIE data are somewhat underestimated here due to a few brief drops in flux that are clearly caused by instrumental errors.

MGS ER observed and average flux of 0.97particles/cm^2-s-sr for this event, whereas the average flux observed by MARIE was 0.90particles/cm^2-s-sr. It is expected that the observed average flux at MGS ER is somewhat higher (7.8%) than MARIE due to the issues in MARIE data noted previously. Regardless, the two instruments are in very close agreement when examining the same event.

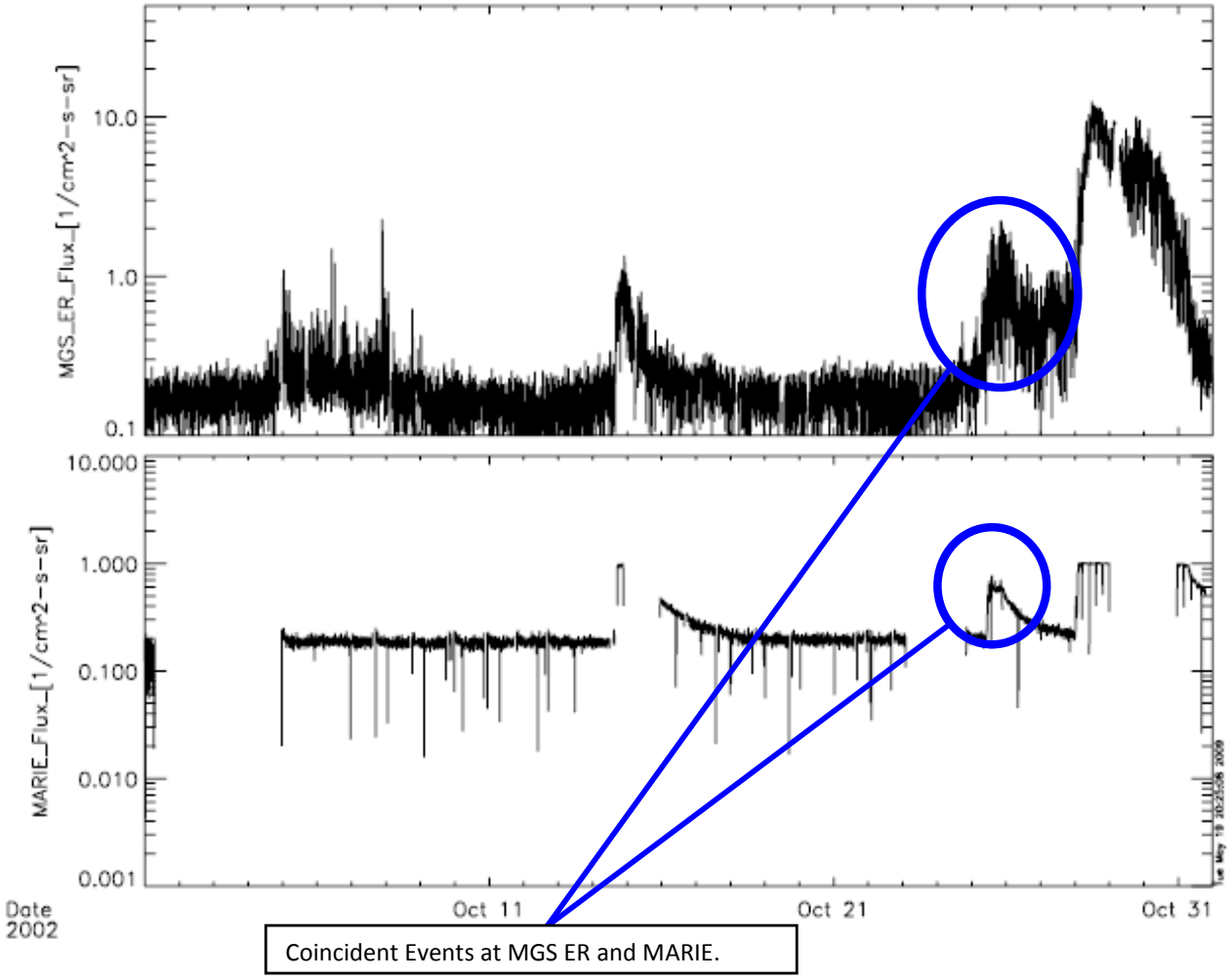

Figure 2-18. Comparison of MGS ER and MARIE data during October 2002.

An alternate technique for converting the MGS ER count rate to a particle flux is to use MARIE data as a metric to scale the ER data. The average count rate at ER for the solar particle event described above could be measured and scaled to the average flux at Marie. As is evidenced by the analysis above, this alternate technique for estimating the ER particle flux yields nearly the same result as the methodology described in this chapter. Hence, the two techniques are virtually equivalent. The primary reason that the scaling of ER data to MARIE was not emphasized in this chapter is that there were too few events where MARIE did not saturate. There are methods to extrapolate data from MARIE when it saturated, but these methods are not well-proven and are less consistent than the physical approach taken in this chapter.

2.6 Conclusion

This chapter has described a methodology for deriving energetic particle flux measurements from the Electron Reflectometer (ER) onboard the Mars Global Surveyor (MGS) satellite. The methodology takes into account physical parameters of the satellite and instrument structure and composition, all known information regarding the operation of micro-channel plate (MCP) detectors, and the spectral features of solar energetic particle (SEP's). It is found that the penetrating particle count rates measured by ER are due primarily to protons with energies greater than 25 MeV, with a minor contribution (~5%) from energetic electrons and alpha particles. At these energies, an MCP efficiency of 90% can be expected. It has also been shown that particles entering the ER detector from the back-side are unlikely to contribute significantly to the overall penetrating particle count rate. With knowledge of the spectral features of penetrating particles, the geometric factors, and the detection efficiency, ER count rates can be easily converted to a flux estimate.

Results of this estimate have been validated by four independent measurements at other satellites: SEP flux and fluence measurements by the Earth-based GOES-10 satellite and galactic cosmic background flux and SEP flux measurements by the Mars Odyssey satellite. The close correlation of these data sets to MGS ER flux estimates confirms that the methodology described in this chapter is useful in assessing the impact of solar particle events on the Mars environment.

Acknowledgements

The following individuals provided vital information, data, and advising toward the completion of this chapter:

Dr. Stephen Blattnig, NASA Langley Research Center

Dr. Martha Clowdsley, NASA Langley Research Center

Dr. Greg Delory, University of California, Berkeley

Dr. Lawrence Heilbronn, University of Tennessee

Dr. Christian Iliadis, University of North Carolina

Dr. Kerry Lee, NASA Johnson Space Center

Mr. Bill Netolicky, Photonis USA, Inc.

Dr. Cary Zeitlin, Southwest Research Institute

References

D. Curtis. Personal Correspondence. 2009.

E.J. Daly et. al. "Space Environment Analysis: Experience and Trends." ESA 1996 Symposium on Environment Modelling for Space-based Applications, Sept. 18-20, 1996, ESTEC, Noordwijk, The Netherlands.

G. Delory. Personal Correspondence. 2009.

D.C. Ellison and R. Ramaty. “Shock Acceleration of Electrons and Ions in Solar Flares”. Astrophysical Journal, vol. 298, pages 400-408. 1985.

J. Feynman and S. Gabriel (Eds.). Interplanetary Particle Environment. JPL Publication 88-28, Jet Propulsion Laboratory, California Institute of Technology, Pasadena, CA, 1988.

http://burro.astr.cwru.edu/stu/media/missions/mgs_diagram.jpg

http://nssdc.gsfc.nasa.gov/planetary/image/mars_global_surveyor.jpg

http://phits.jaea.go.jp/Overview.html

http://physics.nist.gov/PhysRefData/Star/Text/contents.html

http://www.srim.org/SRIM/SRIMINTRO.htm

L. Katz and A.S. Penfold. “Range-Energy Relations for Electrons and the Determination of Beta-Ray End-Point Energies by Absorption”. Reviews of Modern Physics, vol. 24, pages 28-44. 1952.

K.M. Kosev. A High-Resolution Time-of-Flight Spectrometer for Fission Fragments and Ion Beams. Dissertation, Technical University of Dresden. 2007.

K. Lee. Personal Correspondence. 2009.

C. Leroy and P. Rancoita. Principles of Radiation Interaction and Matter and Detection. World Scientific Publishing Company. 2004.

B. Leskovar. “Microchannel Plates”. Physics Today, pages 42-49. November 1977

R.A. Mewaldt, et al. “Proton, Helium, and Electron Spectra During the Large Solar Events of October – November 2003”. Journal of Geophysical Research, vol. 110. 2005.

D.L. Mitchell et al. “Probing Mars’ Crustal Magnetic Field and Ionosphere with the MGS Electron Reflectometer”. Journal of Geophysical Research, vol. 106, no. E10, pages: 23, 403-423, 417. 2001.

J. Mosher, et al. “Nuclear Recoil Detection with Microchannel Plates.” Nuclear Instruments and Methods in Physics Research, A 459, pages 532-542. 2001.

B. Netolicky. Personal Correspondence. 2009.

L.S. Pinsky and T.L. Wilson. “Analysis of the Mars Odyessey MARIE Experiment Data”. ISSO Annual Report, Y2002, pages 97-100. University of Houston, Clear Lake. 2002.

D.F. Smart and M.A. Shea. “Comment on Estimating the Solar Proton Environment that May Affect Mars Missions”. Advances in Space Research, vol. 31, no. 1, pages 45-50. 2002.

J.L. Wiza. “Microchannel Plate Detectors”. Nuclear Instruments and Methods, Vol. 162, pages 587-601. 1979.

Chapter 3
Characteristics of Solar Particle Events at Mars

Abstract

The primary goal of this chapter is to provide – as well as possible – a comprehensive review of physical properties of solar particle events (SPE's) at Mars. These properties include time-intensity profiles, frequency of events, fluences, peak fluxes, and interplanetary shock arrival times. Data collected from the Electron Reflectometer (ER) onboard the Mars Global Surveyor (MGS) satellite were compared to Earth-based data from the SEM instrument onboard the GOES-10 satellite. These comparisons assist in the interpretation of Mars-based data and determine the viability of predictive models for various SPE statistics. A summary of key findings follows:

- Approximately 22% of SPE's that occurred during the period of MGS ER's operation (1999- 2006) were observed at Earth but not Mars. Similarly, 18% of SPE's were observed at Mars but not Earth. This significantly limits the ability to exclusively use Earth-based data to predict the occurrence and impact of SPE"s at Mars.
- Time-intensity profiles at Earth and Mars match predictions provided in the literature, based on the physical location of the detector with respect to the motion of the interplanetary shock wave.
- The probability of an SPE occurrence at Earth increases exponentially with the daily sunspot area. However, Earth-based measurements of sunspot area are not reliable to determine the probability of an SPE occurrence at Mars.
- Predictive models for sunspot activity were used to estimate the number of SPE's at Mars, during the period of MGS ER operation. The model was accurate within 22%, though much more work is necessary for these models to be viable.
- SPE fluence and peak flux distributions were modeled to a power law function with a high degree of reliability. These models correlate well with similar efforts in the literature and can be used to predict the magnitudes of SPE's arriving at Mars.
- Empirical models to predict interplanetary shock arrival times at Earth are not reliable at Mars. This is likely due to spatial differences in the measured initial shock speed between the two planets.

While a significant part of this chapter deals with predictive models, this study is not intended to provide definitive space weather forecasting. Rather, the goal is to provide an overview of the measurements made with MGS ER and to demonstrate which predictive models may or may not be feasible.

3.1 Introduction

The methodology described in Chapter 2 for estimating solar energetic particle fluxes at Mars enables a thorough analysis of solar particle events (SPE's). This chapter provides such an analysis by examining the frequency of SPE occurrences at Mars, as well as their peak fluxes, fluences, time-intensity profiles, and shock arrival times. The intent of this chapter is to fully describe the dataset of SPE's observed at Mars. Comparison of Earth- and Mars-based data clarifies the potential for developing statistical predictions of the future impact of SPE's at Mars, though it is understood that more work is required to make viable predictions.

Mars Global Surveyor's (MGS) Electron Reflectometer (ER) instrument collected energetic particle data at Mars for nearly eight years, from January 1999 to October 2006. Figures 2-6 and 2-12 demonstrate that dozens of SPE's were observed during the lifespan of MGS ER. In order to distinguish between SPE's and spurious increases in particle flux, a set of well-defined criteria are employed to define the occurrence of an SPE. These criteria are presented in Section 3.2 and consider the peak flux and duration of a particle enhancement in the ER data. Based on these criteria, it is determined that 85 SPE's were detected by ER during its lifetime. However, many of the SPE's identified in this study are constituent parts of a series of two or more overlapping events. The occurrence of overlapping events creates some ambiguity in determining SPE frequencies and particle fluences. To resolve this ambiguity, overlapping SPE's are identified by alternate criteria. Of the 85 observed SPE's, 43 were the result of overlapping SPE's.

SPE occurrence frequencies are analyzed versus the solar cycle and the Earth-Sun-Mars (ESM) angle. The former analysis allows for the prediction of the number of SPE's to reach Mars at a given point in time. The latter analysis is used subsequently to understand the predictive capability of Earth-based data to determine the radiation environment at Mars. An important discovery from this analysis is that 18.8% of events observed at Mars were not observed at Earth and 22.4% of events observed at Earth were not seen at Mars. These results have significant relevance in determining the predictability of SPE's at Mars, using Earth-based data.

Analyses of particle fluxes in this study focus primarily on the peak flux for a given event. For many cases the peak particle flux for an SPE represents the arrival of an interplanetary shockwave, which has particular importance in understanding the propagation of SPE's through the Solar System. It is found that the peak flux at Mars is greater than that at Earth for 18% of SPE's observed at both locations. The radial gradient of solar energetic particle fluxes is often discussed in the literature. This chapter expands on the analyses presented in Chapter 2 regarding the drop-off in flux between Earth and Mars.

Measurements of SPE fluences are somewhat complicated by ambiguities in the start and end times for an event. Strategies outlined in Chapter 2 for identifying event start and end times are elaborated on here. Average background flux measurements were calculated for each year from 1999 through 2006, using a twenty-day sample of days throughout each year when an SPE did not occur. An event's start time is marked when the flux increases beyond 3σ of the annual background flux rate for more than one hour. The event ends when the flux decreases below 3σ of the annual background flux rate for more than one hour. In a few cases, the background flux

near the start or end of an event exceeds the 3σ limit. For these events, the start and/or end times are estimated. As with the flux measurements, fluences measured by MGS ER are compared to Earth-based data. Based on this comparison, it is found that the fluence observed at Mars were greater than that at Earth for 14% of events observed at both locations.

This study also examines the variations in time-intensity profiles for distinct SPE's that are observed both at Earth and Mars. Prior studies suggest that the time-intensity profiles of SPE's vary based on the solar longitudinal position of the observer. Comparative data between MGS ER and Earth-based data validate these prior studies and provide useful information in predicting the impact of SPE's on Mars.

While the analysis of MGS ER data in this chapter is vital for understanding the energetic particle environment at Mars, it is not entirely comprehensive. Spectral data are not available through MGS ER and will not be considered in this chapter. A methodology for extrapolating Earth-based spectral data to Mars is presented in Chapter 4 as part of the determination of the energetic particle environment on the Martian surface.

3.2 General Observations of Solar Particle Events at Earth and Mars

The Solar Particle Events (SPE's) presented in this study are caused by coronal mass ejections (CME's), which are large-scale magnetic disturbances that originate in the solar corona and travel through interplanetary space. Other phenomena, such as solar flares and co-rotating interaction regions also contribute to the energetic particle environment. These other phenomena present only short-term increases in energetic particles and are not believed to pose a significant threat to human space explorers. Figure 3-1 presents MGS ER flux estimates from 2003 for particles with energies greater than 25MeV. There are several large-scale and long-duration increases in energetic particle flux that clearly present the typical time-intensity profile for a CME, but there are many smaller increases in the particle flux that may not be due to CME's. Thus, uniform criteria are established to define a CME-induced SPE:

1. The peak flux must be greater than 1 particle/cm^2-s-sr.
2. The flux must exceed 3σ of the annual background flux for more than one hour.
3. There must be a clear start time and end time, which are determined in two ways:
    a) For singular events, the start time takes place when Criterion #2 is first satisfied and the end time takes place when the flux drops below 3σ of the annual background flux rate for more than one hour.
    b) For overlapping series of events, the first event of the series begins when Criterion #2 is satisfied and ends at the lowest point between the first and second peaks of the series. However, the lowest point must be at least one order of magnitude smaller than the two peaks in order to be considered a transition between two separate events. The end time of the first event is considered the start time of the second event. This process continues for as many events are

part of the series, until the flux drops below 3σ of the annual background flux rate for more than one hour. (See Figure 3-2)

Criterion #1 filters out small events that may or may not be due to coronal mass ejections. It is presumed that phenomena resulting in such low increases in energetic particle flux do not substantially contribute to the radiation environment on the Martian surface or the radiation dose received by a potential human explorer. Criterion #2 filters out sporadic increases in particle flux, which may be due to non-SPE phenomena or instrumental anomalies. Table 3-1 presents the annual background flux rates for 1999 through 2006. These values were calculated by taking twenty day-long averages of the background flux at various times throughout each year. Earth data were collected with the SEM instrument on board the GOES-10 satellite, and Mars data were collected with MGS ER. It is important to note that the Galactic Cosmic Ray (GCR) background flux is subtracted from the SEM dataset. So, the background flux does not represent the number of real GCR particles present at Earth.

One of the primary challenges in interpreting these data is establishing rigorous criteria for the start and end times of each event. This information necessary to determine total fluences for each event, as well as generally counting the number of observed events. Criterion #3 lays out a consistent process for determining the start and end times for events, both in the case of a singular event and in an overlapping series of events. Figure 3-2 presents a step-by-step description of how Criterion #3 is used to identify the start and end times for a distinct event within an overlapping series of SPE's. This process limits the degree of inherent uncertainty in examining overlapping events.

Analyses of the full data set, using these criteria, produced consistent, replicable results.

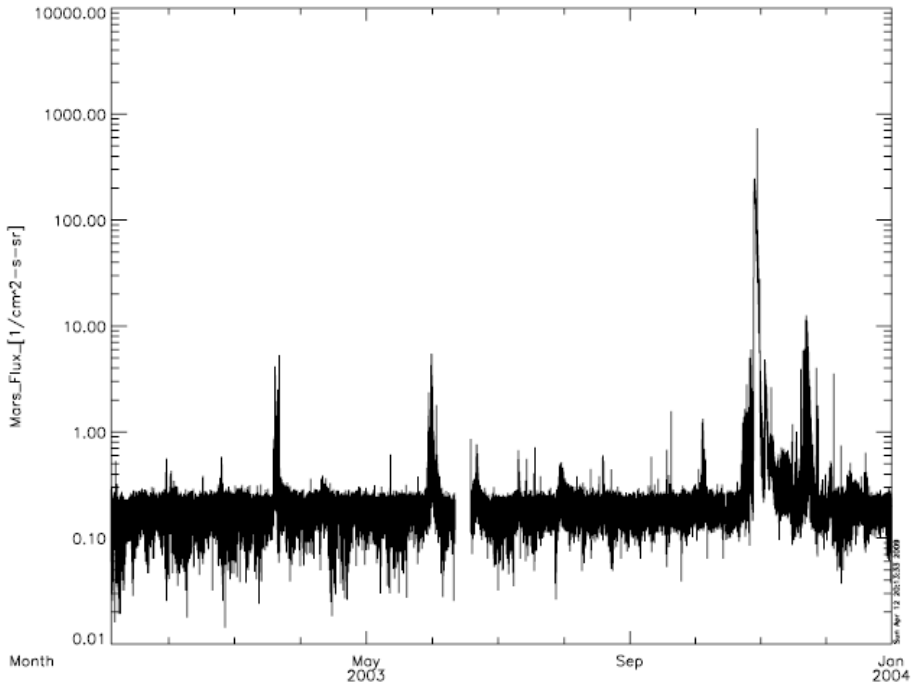

Figure 3-1. Energetic particle flux (energies > 25MeV/n) detected by MGS ER in 2003.

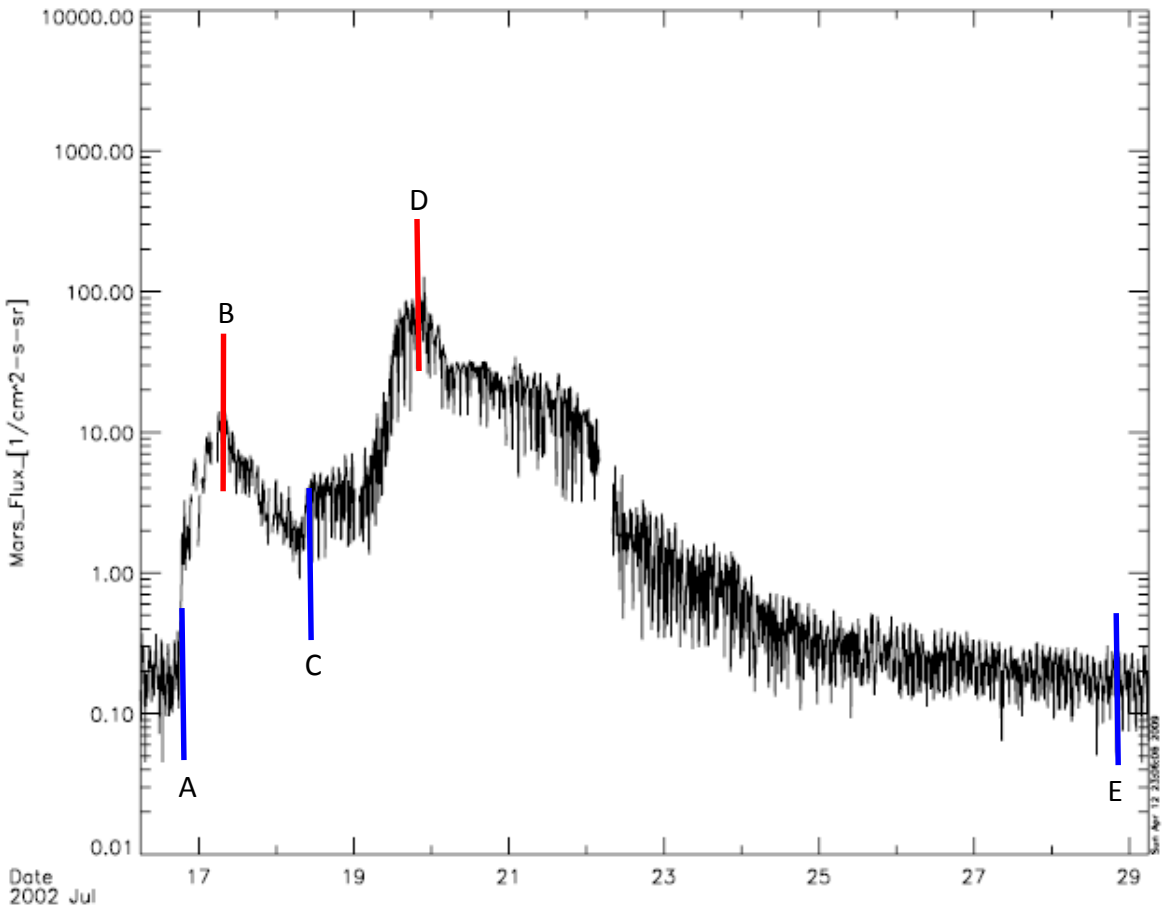

Figure 3-2. Criteria for Identifying Start and End Times for an Overlapping Series of SPE's.

A. The flux exceeds 3σ of the annual background flux for more than one hour, which satisfies Criterion #2. This signifies the start time of both the series of SPE's and the first event within the series.

B. The peak flux of the first event exceeds 1 particle/cm^2-s-sr, which satisfies Criterion #1.

C. The flux decreases by more than one order of magnitude after the first peak and subsequently increases more than one order of magnitude to reach the second peak. This satisfies Criterion #3b and signifies the end of the first event and the beginning of the second event.

D. The peak flux of the second event exceeds 1 particle/ cm^2-s-sr.

E. The flux is smaller than 3σ of the annual background flux for more than one hour. This signifies the end time of both the series of SPE's and the second event within the series.

Some overlapping series of events consist of more than two constituent SPE's. In those cases, the process described above is carried out exactly the same but with Step C repeated between constituent events.

Year	Dates	Average Earth Flux	Earth σ	Average Mars Flux	Mars σ
1999	*4/10 – 4/12; 5/24 – 5/26; 7/16 – 7/21; 9/1 – 9/6; 12/5 – 12/11*	.095	.016	.24	.020
2000	*1/15 – 1/18; 5/21 – 5/25; 8/8 – 8/12; 8/19 – 8/23; 9/8 – 9/12; 12/12 – 12/13*	.064	.0076	.16	.020
2001	*2/10 – 2/15; 3/15 – 3/17; 6/26 – 7/1; 9/17 – 9/20; 12/6 – 12/11*	.069	.0022	.17	.019
2002	*2/6 – 2/11; 3/27 – 4/1; 6/13 – 6/18; 9/13 – 9/16; 12/21 – 12/23*	.075	.0043	.16	.012
2003	*1/14 – 1/18; 4/6 – 4/10; 7/22 – 7/27; 10/8 – 10/12; 12/26 – 12/29*	.07	.0065	.18	.0049
2004	*1/17 – 1/21; 3/10 – 3/14; 6/1 – 6/5; 8/18 – 8/22; 12/13 – 12/17*	.089	.013	.20	.016
2005	*2/12 – 2/16; 4/13 – 4/17; 6/4 – 6/8; 10/13 – 10/17; 11/09 – 11/13*	.093	.012	.22	.014
2006	*1/9 – 1/13; 4/14 – 4/18; 7/26 – 7/30; 8/20 – 8/24; 9/29 – 10/3*	.13	.023	.26	.016

Table 3-1. Average background fluxes and standard deviations (σ) of particles with energies greater than 25MeV at Earth and Mars. Flux is presented in units of particles/cm^2-s-sr. Earth-based data are collected with the SEM instrument onboard the GOES-10 satellite. Mars data are collected with MGS ER.

3.2.1 Occurrence of Solar Particle Events at Various Earth-Sun-Mars Angles

For the purpose of comparison, it is important to examine the relative positions of the Earth, Sun, and Mars during each observed SPE. A top-down view of the Solar System is used to divide space into six even sectors. The position of Mars is determined by the Earth-Sun-Mars (ESM) angle, with increasing angle moving clockwise from the Earth-Sun line (See Figure 3-3 and Table 3-2). The frequency of SPE occurrences in each sector is purely random, and no correlation between SPE occurrence and ESM angle is suggested. However, the categorization of SPE occurrences into spatial sectors provides a context for understanding observational differences between Earth and Mars.

Beyond the spatial orientation, SPE's are further divided into three categories: Coincident events, Mars-only events, and Earth-only events. As the names imply, coincident events produced observations at both Earth and Mars, while Earth- and Mars-only events were observed exclusively at one planet or the other. There were 50 coincident events observed by MGS ER and GOES-10 between January 1999 and November 2006. During this same time frame, 19 Earth-only events and 16 Mars-only events were observed. Thus, a total of 85 events were observed. Of these, 43 events were part of an overlapping series of consecutive events.

The occurrence of Earth- and Mars-only events is clearly significant, because it suggests a possible limitation in the ability to use Earth-based data to provide SPE warnings to Mars explorers. Table 3-3 provides a breakdown of coincident, Earth-, and Mars-only events based on the Sector in which Mars is present during each occurrence. Figure 3-4 is a graphical representation of the data presented in Table 3-3. While the information provided in Table 3-3 is limited by the number of events, certain trends are evident. Foremost, it is clear that Mars-only events occur nearly as frequently as Earth-only events. In fact, nearly 1 in 5 events will be only observed at Mars. It is particularly noteworthy that Mars- and Earth-only events are observed even when the planets are closely aligned (i.e., Sectors 1 and 2). This places serious restrictions on the ability to forecast SPE's at Mars using Earth-based data.

Another evident trend from Table 3-3 is that Coincident SPE's are most likely to occur in Sectors 1 and 2. This makes sense, because in these sectors Earth and Mars are much more likely to be magnetically connected to the Sun along the same or adjacent field lines. Figure 3-5 presents a schematic of the interplanetary magnetic field lines as they project from the Sun outward into the Solar System. These magnetic field lines form a Parker Spiral, and Coincident SPE's are much more likely to occur when Earth and Mars reside on or near the same field line. This occurs most frequently in Sectors 1 and 2, as observed in Table 3-3. Not surprisingly, the lowest occurrence of Coincident SPE's is in Sector 6, where it is physically impossible for Earth and Mars to reside on the same magnetic field line. It is also not surprising that the occurrence of Coincident events is low in Sector 3, because Earth and Mars are on opposite sides of the Sun.

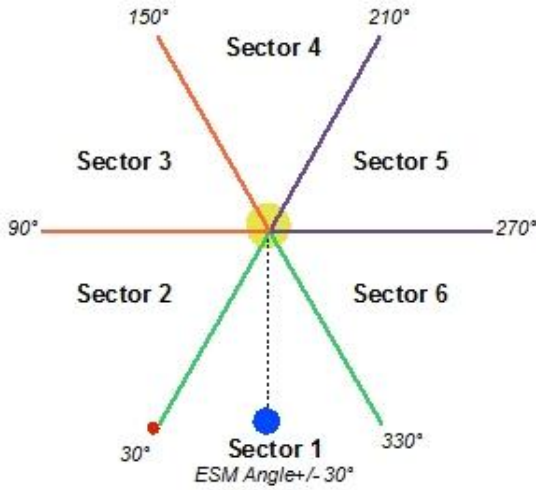

Figure 3-3. Top-down view of the Solar System, divided into six sectors based on the Earth-Sun-Mars (ESM) angle.

Sector #	ESM
1	+/ 30°
2	30°-90°
3	90°-150°
4	150°-210°
5	210°-270°
6	270°-330°

Table 3-2. Angular range of sectors used to define the location of Mars, relative to the Earth and Sun.

Sector #	Total # SPE's	# Mars-Only SPE's [% of Total]	# Earth-Only SPE's [% of Total]	# Coincident SPE's [% of Total]
1	23	1 [4.3%]	2 [8.7%]	20 [87.0%]
2	16	2 [12.5%]	3 [18.8%]	11 [68.8%]
3	11	3 [27.2%]	4 [36.4%]	4 [36.4%]
4	18	5 [27.7%]	4 [22.2%]	9 [50.0%]
5	10	2 [20.0%]	5 [50.0%]	3 [30.0%]
6	7	3 [42.9%]	1 [14.3%]	3 [42.9%]
Total	85	16 [18.8%]	19 [22.4%]	50 [58.8%]

Table 3-3. Summary of the occurrences of coincident, Earth-, and Mars-based SPE's by Sector.

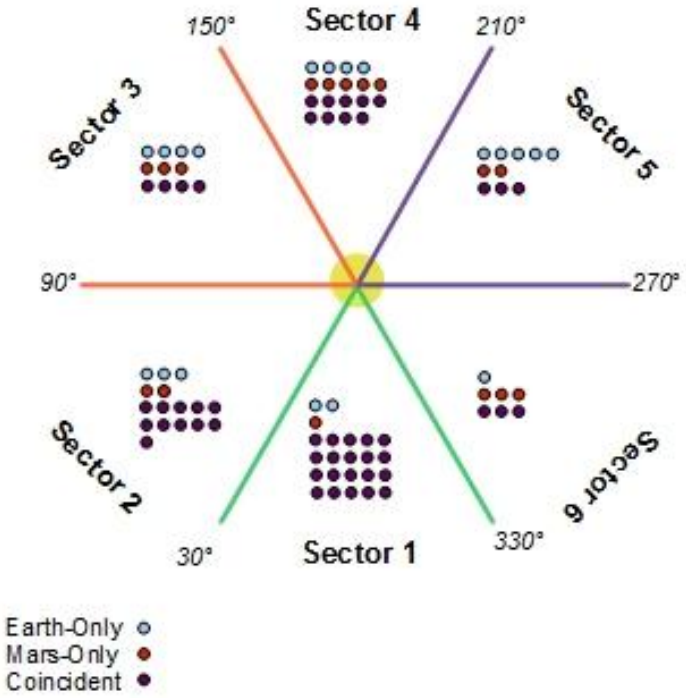

Figure 3-4. Distribution of Coincident, Earth-Only, and Mars-Only SPE's by Earth-Sun-Mars angle (ESM).

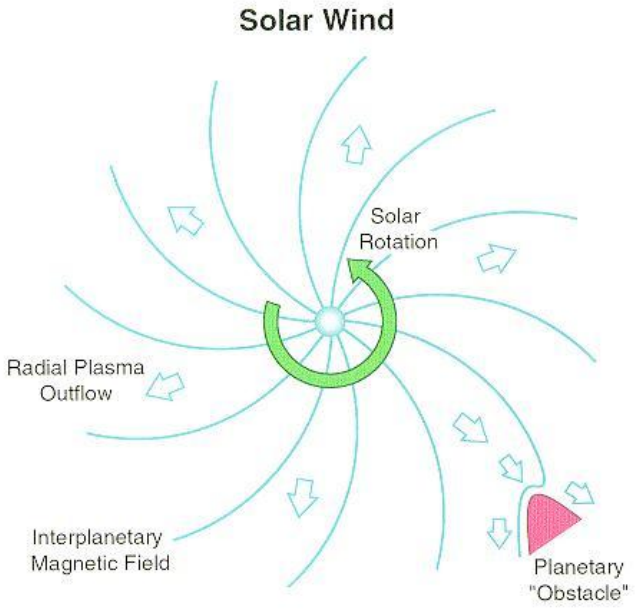

Figure 3-5. Schematic of the Solar Wind & Interplanetary Magnetic Field. (From http://www.igpp.ucla.edu/)

3.2.2 Time-Intensity Profiles of SPE's at Earth and Mars

As a coronal mass ejection (CME) emerges into interplanetary space, it is typically moving at a speed faster than the ambient solar wind. The shockwave created by this interaction accelerates particles that may be subsequently detected as a solar particle event (SPE). As the accelerated particles arrive at the detector, an initial increase is detected in energetic particle flux. This flux increase is maintained throughout the duration of the event. It is also possible that the shock itsjelf may be detected as it arrives. Interplanetary shockwaves can travel with a speed of a few hundred kilometers per second to over 2,000 km/s. Thus, the shock is typically detected much after the initial onset of energetic particles. Despite the delay in its arrival, the interplanetary shock typically carries a substantial flux of energetic particles with it. In fact, a shock is commonly observed as an impulsive spike in energetic particle flux within the SPE. However, a shock is not always observed during an SPE. Depending on the location of the detector (relative to the direction of the CME's propagation), it is common to observe the shock-accelerated particles without observing the shock itself. Thus, the time-intensity profiles for various SPE's can look dramatically different from one another.

Reames (1999) provides the most commonly cited explanation for variations in time-intensity profiles for SPE's (See Figure 3-6). According to Reames, an observer on the eastern edge of the shock will see a spike in energetic particles that peaks rapidly and gradually tapers off. This due to the fact that the eastern observer will be magnetically well-connected to the event as it emerges from the Sun, which provides an easy path for initial shock-accelerated particles to reach the observer. As the shock propagates through space, it becomes less-and-less well-connected to the eastern observer. Thus, a fairly rapid drop in energetic particle flux is expected. If detected, the shock appears as an impulsive spike on the downward slope of the time-intensity profile.

In contrast, a western observer should not readily detect the initial shock-accelerated particles, because it is not well-connected magnetically to the event. As the shock moves through space, it moves closer to the western observer and gradually increases the number of detected energetic particles. The energetic particle flux increases until the shock passes the observer or terminates.

An observer located near the nose of the shock is likely to see a rapid and sustained increase in energetic particle flux throughout the duration of the event. If observed, the shock will likely appear as an impulsive spike in energetic particle flux prior to the event's drop-off. Comparisons of time-intensity profiles are presented in Figures 3-7, 3-8, and 3-9 for SPE's that were observed at Earth and Mars in various spatial orientations.

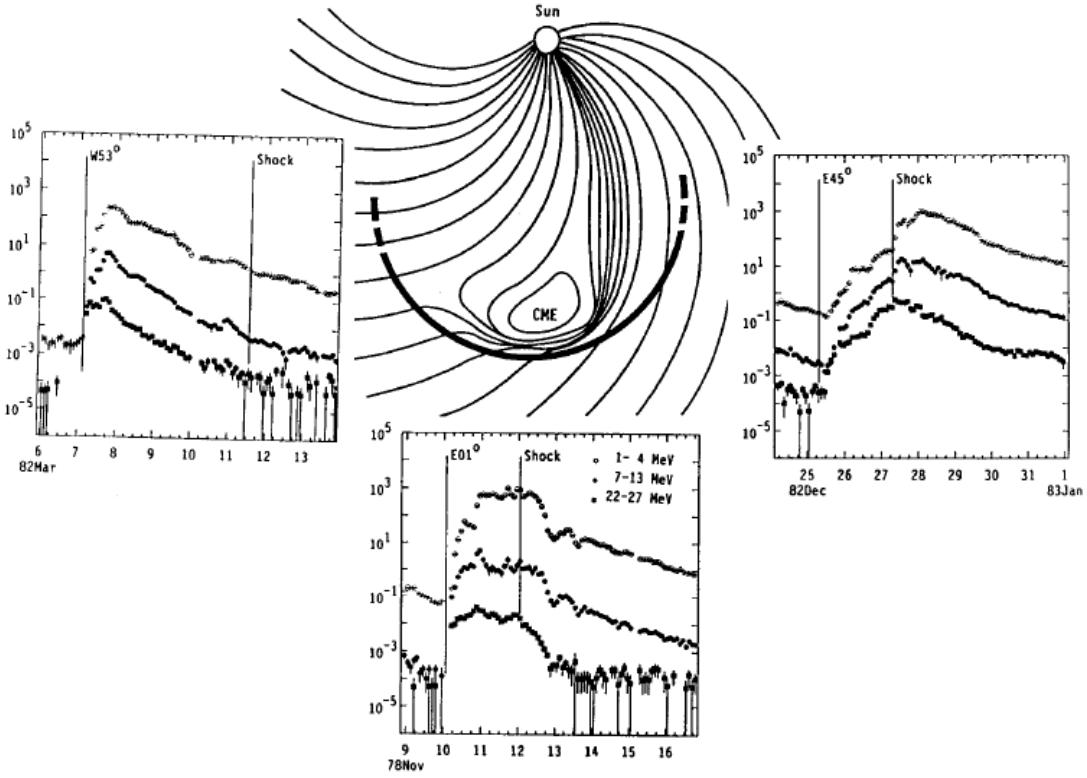

Figure 3-6. Intensity profiles are shown for protons in 3 energy intervals for observers viewing an evolving CME and shock from 3 different solar longitudes. [Image and caption from Reames (1999)]

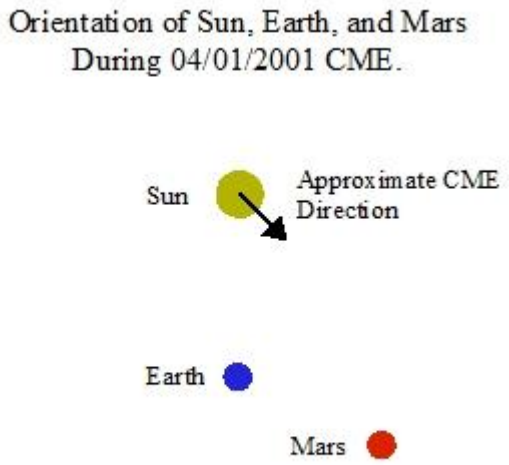

In Figure 3-7, Earth and Mars are near opposition, but Mars is approximately 30° west of Earth. The causal CME was a westward pointing "partial halo," which means some component of the CME's motion was directed toward Earth though there was significant motion in the westward direction. Based on this orientation, it can be expected that Earth would experience a rapid increase in energetic flux with a gradual decline, because it is east of the motion of the CME. Mars is expected to observe a more gradual increase in energetic particles with a distinct plateau, because it is more directly aligned with the CME's motion. In fact, this is what was observed at both planets.

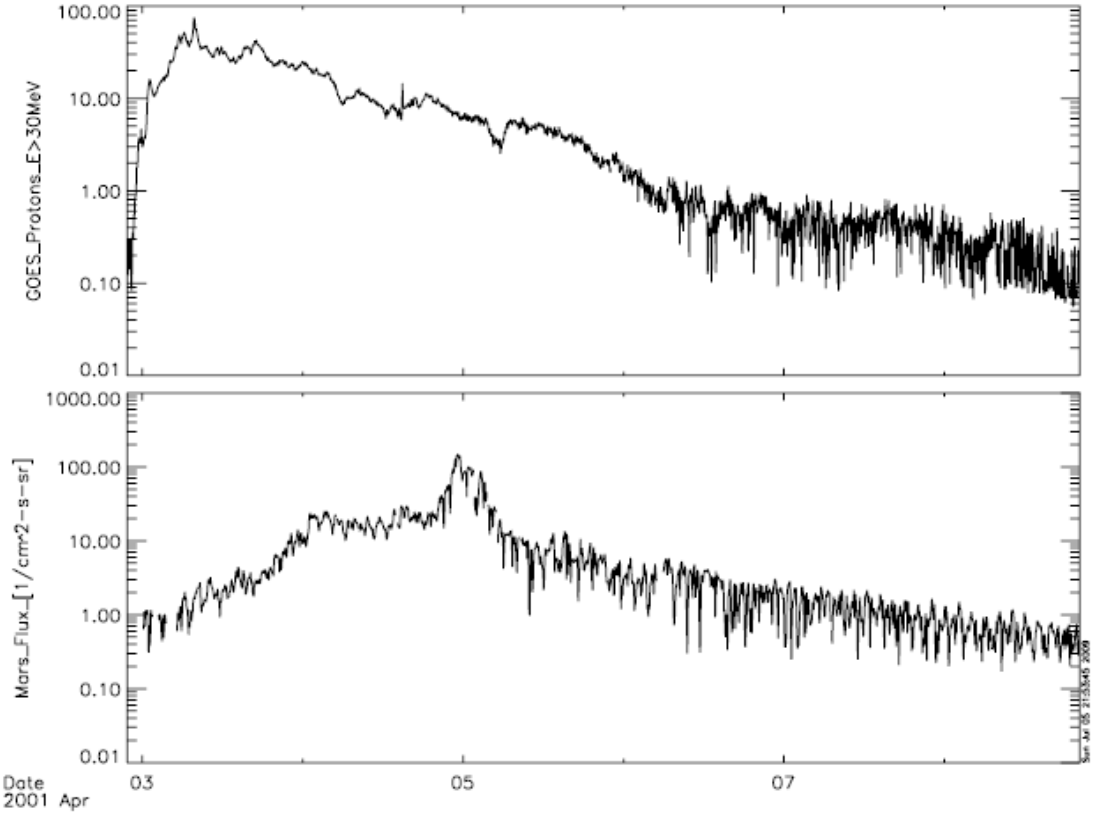

Figure 3-7. (Top Panel) Relative orientation of Earth, Mars, the Sun, and the estimated direction of CME propagation for an event in April 2001. (Bottom Panel) Comparison of time-intensity profiles at Earth and Mars.

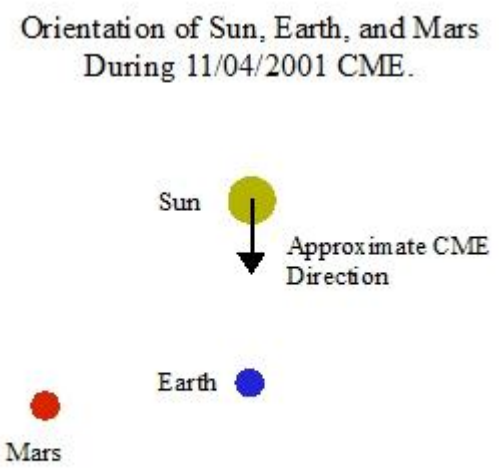

In Figure 3-8, Earth and Mars are again near opposition, but Mars is approximately 45° east of Earth. The causal CME was a "halo" event, which means the primary component of the CME's motion was directed toward Earth. Based on this orientation, it can be expected that Earth would observe a gradual and sustained increase in energetic particles with a secondary rise in energetic particle flux when the shock arrives. Mars is expected to observe a rapid initial rise in energetic particles with a gradual fall-off, because the event is initially well-connected to Mars but the shock does not necessarily arrive.

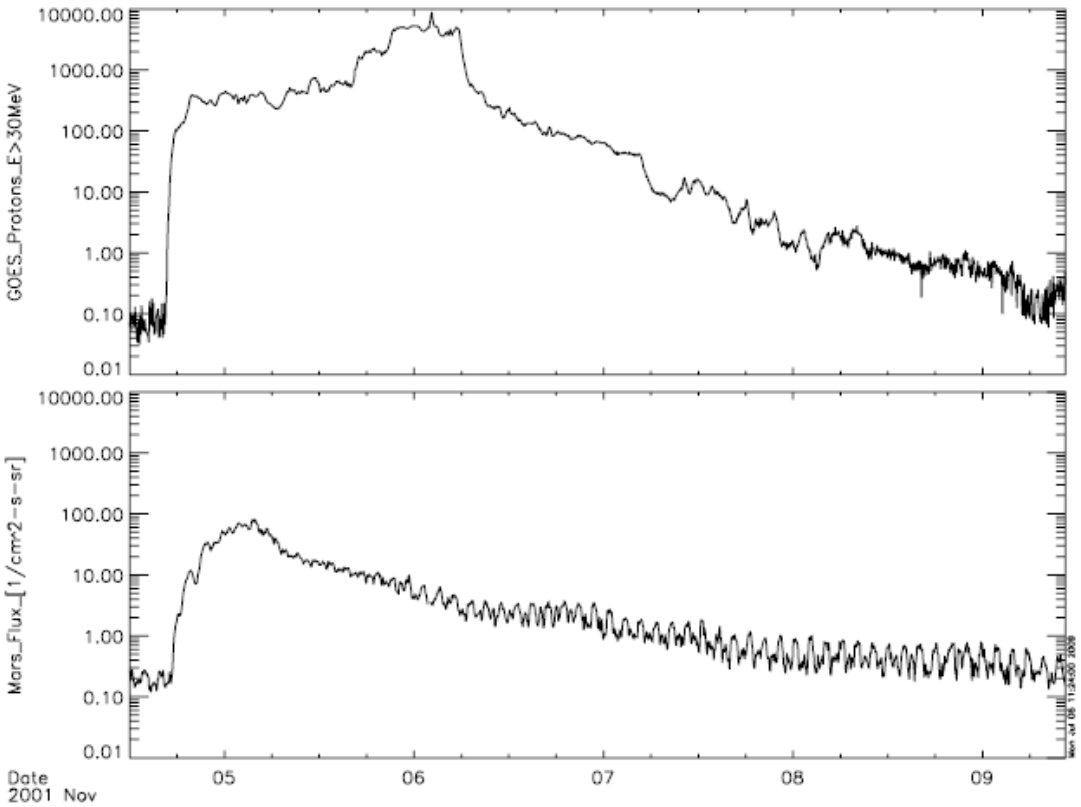

Figure 3-8. (Top Panel) Relative orientation of Earth, Mars, the Sun, and the estimated direction of CME propagation for an event in November 2001. (Bottom Panel) Comparison of time-intensity profiles at Earth and Mars.

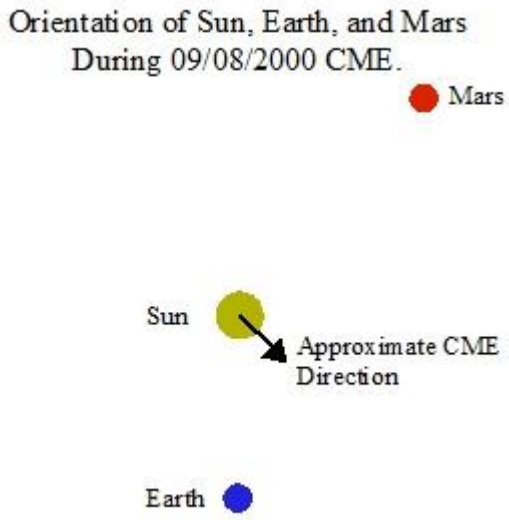

Earth and Mars are near conjunction in Figure 3-9. The causal CME was again a "partial halo" event with a strong westward component of motion. The time-intensity profiles are similar to those in Figure 3-7, particularly at Earth. Data at Mars demonstrate a gradual increase and there is no distinct plateau in the energetic particle data. This is indicative of an event that is detected from a western observer. It also appears that a shock was detected at Mars on November 12, 2000. In contrast, the detector at Earth demonstrates an expected time-intensity profile from an eastern observer, i.e. a rapid increase followed by a precipitous drop-off in energetic particles. No shock is visually apparent in the Earth-based data.

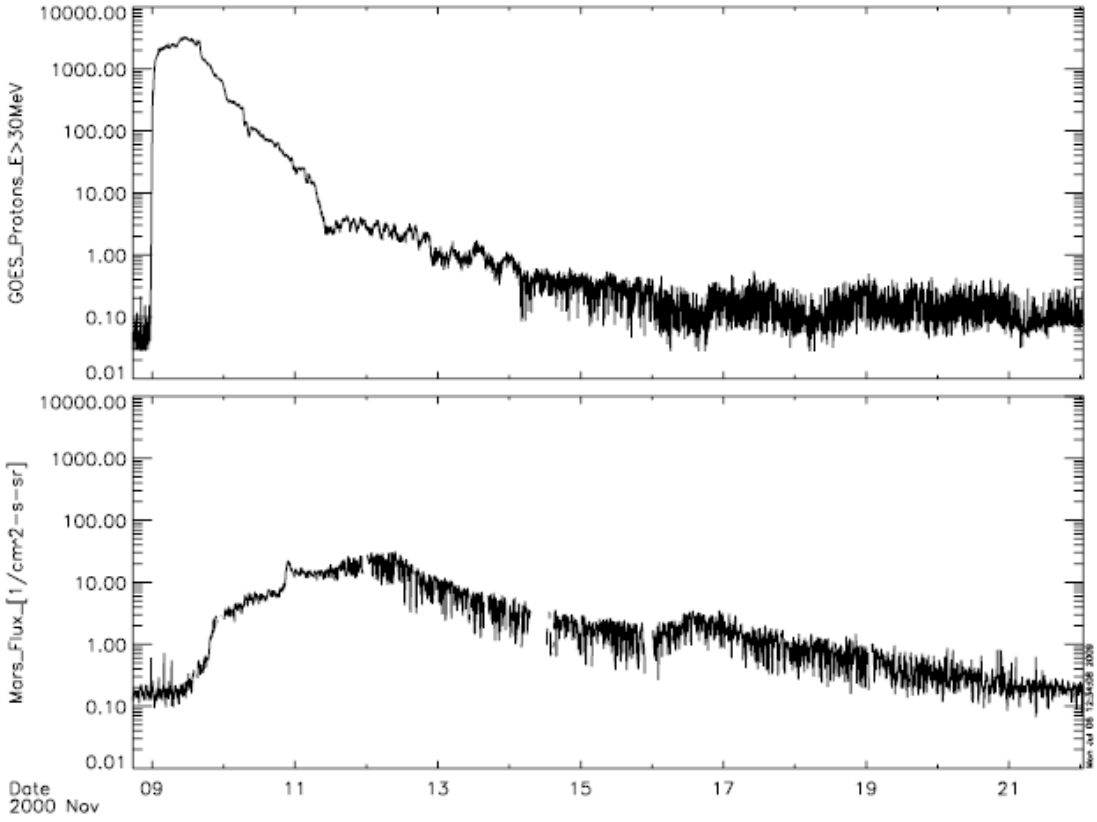

Figure 3-9. (Top Panel) Relative orientation of Earth, Mars, the Sun, and the estimated direction of CME propagation for an event in November 2000. (Bottom Panel) Comparison of time-intensity profiles at Earth and Mars.

3.3 Frequency of Solar Particle Events

Sunspots are large-scale magnetic enhancements that occur near the surface of the Sun. They are observed as distinct dark regions on the solar surface. It is assumed that the frequency of SPE's increase with the number of observed sunspots, because SPE's are typically associated with large-scale magnetic enhancements in the Interplanetary Magnetic Field. Sunspot counts have been measured daily since May of 1874. Originally, these counts were collected by the Royal Greenwich Observatory (RGO) but were later collected by the United States Air Force (USAF) and the National Oceanic and Atmospheric Administration (NOAA). (Hathaway 2009)

Hathaway (2009) compared RGO, USAF, and NOAA data to resolve discrepancies between data sets. Based on this comparison, daily sunspot activity is accessible from May 1874 to present. In order to reduce uncertainties in the sunspot number, Hathaway (2009) recorded sunspot activity in terms of a cumulative area of sunspots relative to the total hemispheric area of the Sun. The units for sunspot area (SSA) are recorded as millionths of a hemisphere.

The feasibility of using Earth-based sunspot measurements to assess the probability of an SPE arriving at Mars is presented here. During the period of MGS ER operation, the SSA was noted at the starting day for each observed SPE. The SSA for each event was then compared to the total number of times that SSA occurred during the period of MGS ER operation. For the purposes of this analysis, SSA values were binned into ranges of 500 millionths of a hemisphere. In this way, a probability of SPE occurrence was determined over a range of SSA values. This analysis was conducted for Coincident, Earth-only, and Mars-only SPE's to determine if there are discrepancies between these classes of event.

Figures 3-10 through 3-12 present the relative probability of an SPE occurrence for Coincident, Earth-only, and Mars-only events. From this analysis, it is clear that the occurrence of an SPE increases exponentially with increase SSA. However, it is important to note that data are limited for very large SSA values (greater than ~3000 millionths of a hemisphere), because relatively few days occurred during the MGS ER operation period with very large SSA values. SPE data for SSA values greater than 3000 millionths of a hemisphere were included in this analysis, but it should be noted that much more data are necessary to develop an accurate model. However, it should also be noted that when SSA values greater than 3000 millionths of a hemisphere were removed from the analysis, the curve fit did not change. This model can also be applied to Earth-only events, but there is a much higher degree of error. Unfortunately, the use of this model breaks down for Mars-only events. The errors are much too high to reliably predict the occurrence of a Mars-only event. This is likely due to the fact that the majority of Mars-only events occur when Earth and Mars are on opposite sides of the Sun. At these times, the SSA is unreliable because it only applies to the hemisphere of the Sun that faces Earth.

The consistency between the Coincident and Earth-only SPE data suggests that an exponential model is reasonably reliable for predicting the occurrence of SPE's at Earth, based on sunspot area. It can also be assumed that this model would be equally reliable at Mars if viable Mars-based sunspot data were available. For the purposes of this study, the exponential form determined for Coincident SPE probabilities will be used to model the likelihood of occurrence of SPE's at Mars over time:

P = .006 * 1.001^SSA (Equation 3-1)

Here, P is the probability of an SPE occurrence and SSA is the measured sunspot area for a given day.

The development of this model could be useful for providing real-time warnings to astronauts at Mars, though this would likely require a Mars-based solar imager to better-determine the relevant sunspot area.

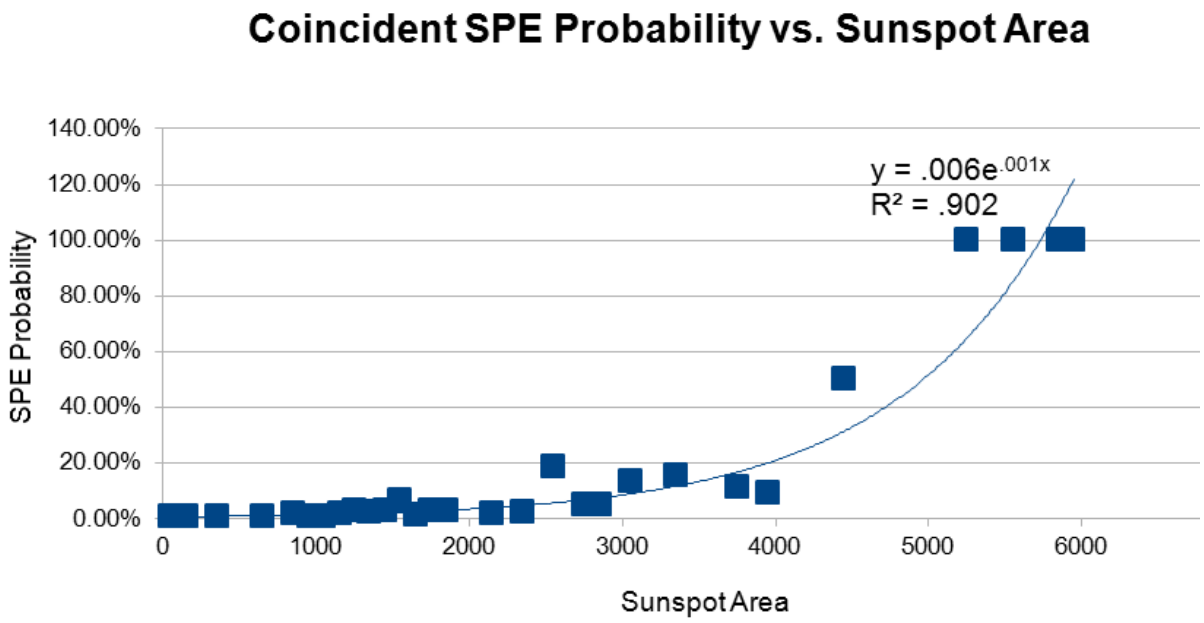

Figure 3-10. Probability of a Coincident SPE based on observed sunspot area (in millionths of a solar hemisphere). The data follow an exponential curve, though there is significant error around this curve. The fitted curve equation and R2 value are provided in the upper-right hand corner of the graph.

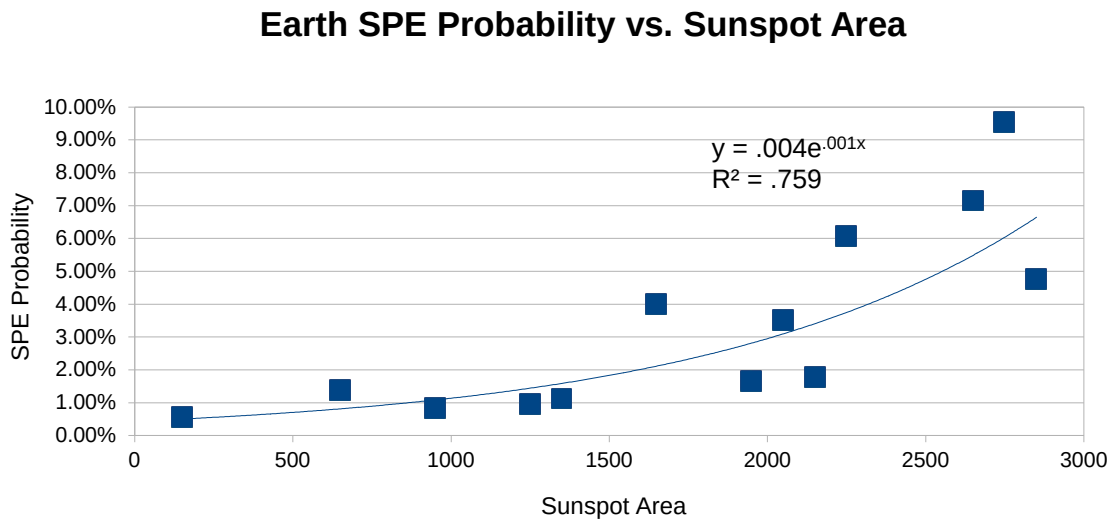

Figure 3-11. Probability of an Earth-only SPE based on observed sunspot area (in millionths of a solar hemisphere). The data follow an exponential curve, though there is significant error around this curve. The fitted curve equation and R2 value are provided in the upper-right hand corner of the graph. Despite the large error, the curve equation and relative uncertainty closely match that of the Coincident SPE probability noted in Figure 3-9.

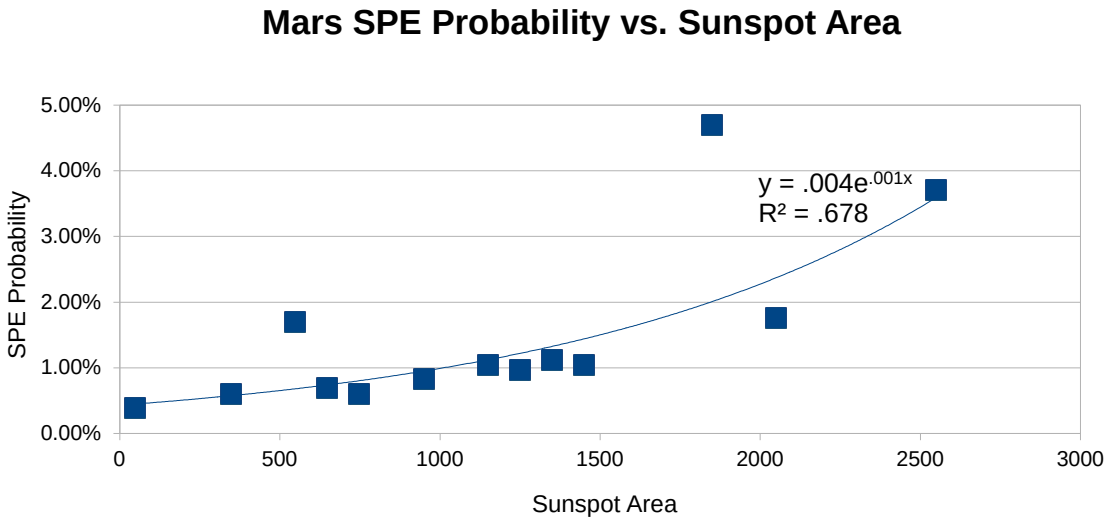

Figure 3-12. Probability of an Earth-only SPE based on observed sunspot area (in millionths of a solar hemisphere). The data most closely follow an exponential curve, but there is too much uncertainty to consider this model reliable. The fitted curve equation and R^2 value are provided in the upper-right hand corner of the graph.

3.3.1 Prediction of Future Sunspot Area Measurements

It is well-established that solar activity (and, by extension, sunspot area measurements) roughly follows an 11-year cycle, which includes a minimum and maximum period of activity. It is of substantial importance to all space missions that reliable predictions be generated for future solar cycle durations and amplitudes. Several models have been developed to provide such predictions, but – as might be expected – these models are fraught with error and uncertainty. Despite their shortcomings, predictive models of solar activity provide a basis for examining the relative intensities of future, past, and current solar cycles. The analysis provided here utilizes a predictive model to generate a rough estimate for the number of solar particle events that will reach Mars in the current solar cycle. This estimate is not intended to provide a crystal ball look into the future but rather a relative look at what one might expect to see at Mars compared to the current solar cycle. Obviously, the quality of this estimate is directly dependent on the quality of the predictive model.

Prior studies have used current solar cycle data to feed regression and curve fitting models, while other studies have utilized Earth-based geomagnetic data to predict the amplitudes of future solar cycles. Hathaway et al. (1999) provides a review of various techniques in predicting sunspot activity and describes an integrative method for merging various techniques into a single predictive value for the monthly sunspot number. In this model, the general form of the sunspot number over time is as follows:

$$R(t) = R_{max}(t - t_0)^3/[e^{(t-t0)\text{^}2/b\text{^}2} - 0.71] \qquad \text{(Equation 3-2)}$$

R(t) is the sunspot number at time, t is the duration from the cycle start time (noted as t_0), R_{max} is the amplitude of the cycle, an b is given by:

$$b(R_{max}) = 27.12 + 25.15/(R_{max} \times 1000)^{1/4} \qquad \text{(Equation 3-3)}$$

Equations 3-2 and 3-3 were developed from regression techniques, and are highly dependent on an accurate prediction of R_{max}. Hathaway et al (1999) combined their regression technique with a more accurate predictor of R_{max}, which has the following form:

$$R_{max}(n) = 12.4 + 5.72\ aa_{Imax}(n) + 0.173DD(n-1) - 0.382\ R_{max}(n-1) \pm 10.7 \qquad \text{(Equation 3-4)}$$

Here, n is the solar cycle number for the cycle to be predicted, aa_{Imax} is the maximum of the "interplanetary" component of the geomagnetic index, and DD(n-1) is the number of geomagnetically disturbed days during the n-1 solar cycle.

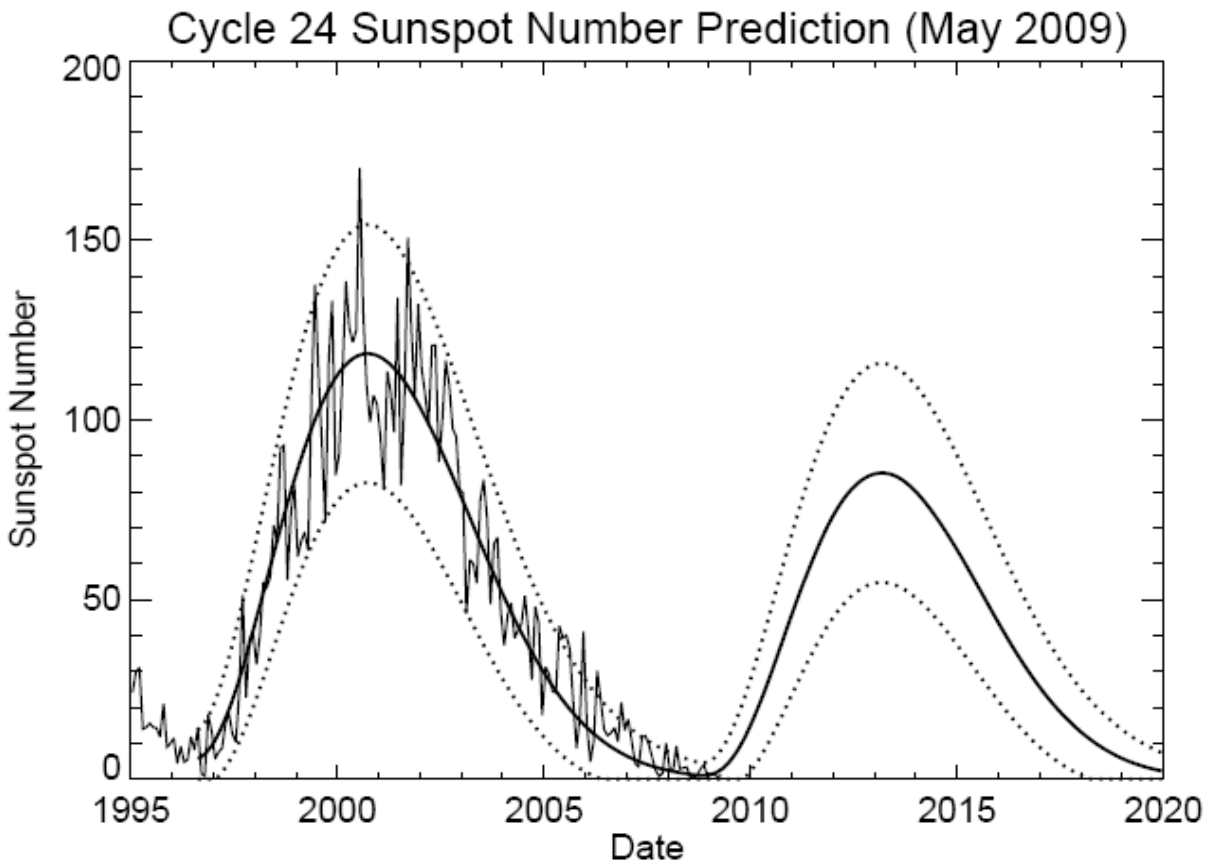

Figure 3-13. Hathaway et. al. (2009) prediction of sunspot number compared to sunspot data for the prior solar cycle. (http://solarscience.msfc.nasa.gov/images/ssn_predict_l.gif)

Despite the complexities of this model, it was generally reliable at predicting the overall form and amplitude of the four previous solar cycles. Hence, it can be reasonably applied to future solar cycles. However, the fluctuations in solar activity over time are not reliably predicted. Figure 3-13 (http://solarscience.msfc.nasa.gov/images/ssn_predict_l.gif) presents the prediction for the prior and current solar cycles. The three curves shown in Figure 3-13 represent (from bottom to top) the 5%, 50%, and 95% confidence levels for the sunspot number to fall below the predicted value. Actual sunspot number measurements are placed over the predicted curves to demonstrate the model's viability for predicting future sunspot activity. For the purposes of this study, the 95% confidence level (the top curve in Figure 3-13) is used.

In order to convert the sunspot number predictions to an anticipated sunspot area, the average area per sunspot was calculated for all days from May 1, 1874 to June 1, 2009. Based on this analysis, it is found that on average each sunspot constitutes 13.2 millionths of a solar hemisphere. Hence, the predicted sunspot numbers in Figure 3-14 are scaled by a factor of 13.3.

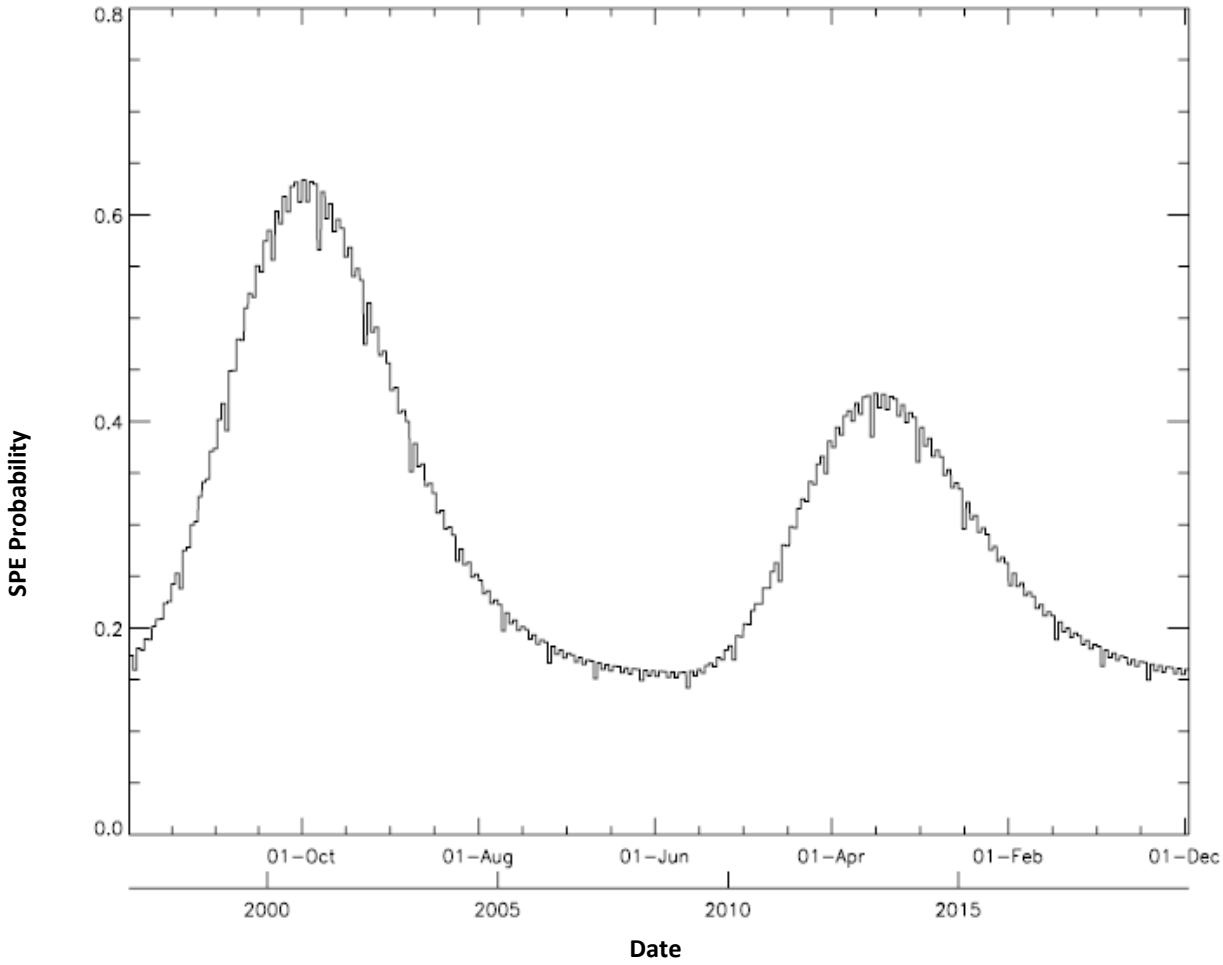

Figure 3-14. Predicted probability of an SPE occurrence, based on predictive model for sunspot activity and modeled relationship between sunspot area and SPE occurrence

3.3.2 Prediction of Future SPE Occurrences at Earth and Mars

The predictive sunspot number model described in the previous section can be used to estimate the probability of an SPE occurrence in future solar cycles. By converting the sunspot number prediction into a sunspot area, Equation 3-1 can be used to determine the probability of an SPE occurrence at a future month. Figure 3-14 displays the predicted probability for an SPE to occur in each month from 1997 to 2020.

In order to validate the probability predictions presented in Figure 3-14, the number of SPE's actually observed at Earth by the GOES-10 satellite was compared to the predicted value from January 1999 – December 2006. During this period of time, 69 SPE's were observed at Earth. The model described in this analysis predicts (at the 95% confidence level) that 54 SPE's would have been detected, which is a difference of 22% compared to actual observations. While this is far from perfect, it does provide a reasonable estimate for the number of SPE's to occur at Earth.

Based on this model, it is estimated that approximately 46 SPE's will be detected at Earth during the full duration of the current solar cycle – ranging from January 2009 to December 2020. So, SPE activity is expected be much less than in the previous solar cycle. The comparative data between Earth and Mars, presented in Table 3-1, suggests that the occurrence of SPE's at Mars will be ~4% less than that at Earth. Hence, it is expected that approximately 44 SPE's will be observed at Mars during the full duration of the current solar cycle. Of course, the 4% difference in SPE occurrences is well-within the margin of error for both the data and the models.

While these estimates pertain to observations during the full solar cycle, a more developed predictive model could allow for estimates at a smaller timescale. Thus, it may possible to compare estimates of the number of expected SPE's during solar minimum and maximum. This capability could be useful to understand the expected radiation dose delivered to human space explorers and electronics at different phases of a particular mission. Chapters 4 and 5 address this issue in greater detail.

3.4 Fluences for Solar Particle Events at Earth and Mars

One of the most significant measurements of SPE's for human space exploration is the total event fluence of energetic particles. Several attempts have been made to model and predict solar energetic particles fluences for Earth-based missions, though little has been done in relation to Mars. This study aims to determine the applicability of Earth-based models to MGS ER data. Unfortunately, there are a number of factors that limit the ability for Mars data to be directly compared to Earth-based models. These factors include location, energy ranges, and criteria for defining the start and end times for an SPE. However, it is possible to compare the relative forms of the probability distributions to identify similarities or differences between Earth and Mars. Three SPE fluence models were examined to determine the most appropriate comparison to MGS ER data: Feynman et al. (1993), Nymmik (1999), and Xapsos (1999). Each of these models has its benefits and shortcomings, which will be addressed here.

The Feynman et al. (1993) model, known as the JPL Proton Fluence Model (JPFM), utilizes a log-normal distribution function to describe the likelihood of an SPE occurring within a given range of fluences. JPFM is valid for protons with energies between approximately 10 and 100MeV and for "large events" with fluences greater than ~10^6 particles/cm^2. The start time for an event is defined as the day that the proton flux exceeds a background threshold, and the end time is defined as when the flux returns to the background level for two days. Another restriction on the JPFM model is that it assumes SPE's only occur during "solar active" years, which is the seven-year period surrounding the solar maximum. It also assumes a zero probability for an SPE occurrence in years near solar minimum. A fundamental limitation of this model is its inability to adequately describe smaller events (Feynman et al. 1993). However, the authors determine that low-fluence SPE's contribute minimally to the overall mission risk in low-Earth orbit *(Feynman et al. 2002)*.

Nymmik (1999) proposes a simple power-law distribution to describe the occurrence of SPE's with various fluences. The same general criteria as JPFM are used to describe the start and end

times for SPE's, but the range of fluences is somewhat broadened to include all SPE's with fluence greater than ~10^5 particles/cm^2. The proton energy range is also broadened to include all protons with energies greater than 30MeV. Moreover, Nymmik does not restrict his model to "solar active" times. Rather, he asserts that there is a significant probability of an SPE occurrence near solar minimum and that the fluences of such SPE's can exceed that of the galactic cosmic radiation. The power-law form of this model adequately describes low-fluence SPE's, but overestimates the probability of a high-fluence SPE (Gabriel and Feynman 1996).

Xapsos et al. (1999) employ the maximum entropy principle to establish a reliable model for the SPE fluence distribution. The maximum entropy principle states that the most reliable distribution for a set of testable information is that which maximizes the information entropy (J.N. Kapur 1989). Based on this analysis, Xapsos et al. (1999) find a truncated power law distribution to be the most reliable model for SPE fluences over a broad range of SPE fluences. The range of proton energies used in this model is 1 to >100MeV, and the modeled fluence range is for SPE's with fluences greater than ~10^6 particles/cm^2. As with JPFM, this model only considers events during "solar active" times and results are given as the annual proton fluence per active year.

For the purposes of this study, the exclusion of "solar quiet" times from JPFM and the Xapsos et al. (1999) model is a critical shortcoming. While such exclusion is reasonable for long duration missions (one or more solar cycle), it is an unacceptable exclusion for the 2-3 year mission durations that are likely for human exploration of Mars. It is obviously deficient if such a human mission takes place near solar minimum. Therefore, the Nymmik (1999) model is selected for use in this study. While the Nymmik model is somewhat unreliable for high-fluence SPE's, it is expected that such large SPE's will be more rarely observed at Mars than at Earth due to the additional distance from the Sun. Moreover, the energy range of protons used in the Nymmik model more closely matches that of the MGS ER data then either of the other models.

The power-law distribution described by Nymmik (1999) is of the form:

$$\psi(\phi) = (1/N)\,(dN/d\phi) = C\,\phi^{-1.41} \qquad \text{(Equation 3-5)}$$

ψ is the probability of an SPE having a fluence, ϕ, within a range $d\phi$. N is the total number of events in the data set, dN is the number of events within the $d\phi$, and C is a constant.

Figure 3-15 presents data from Nymmik (1999) with the author's power-law fit for the fluence distribution. The distribution coefficient, -1.41, provides a reliable fit to the experimental data. In order to determine the applicability of this model to the data set used in this paper, a power-law fit was applied to the 59 SPE's detected at Earth with the GOES-10 satellite from January 1999 through December 2007. The power-law fit provides an equally good fit to these data, with a distribution coefficient of -1.17. This is within 19% of the value determined by Nymmik, which is reasonable given the variation in event criteria and the significantly smaller data set used in this study.

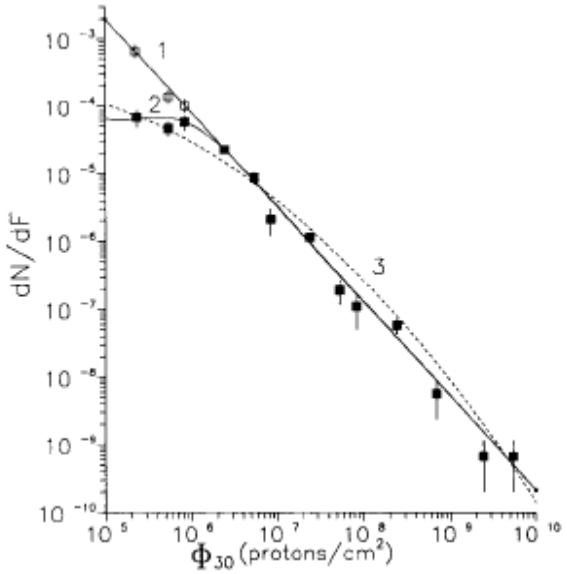

Figure 3-15. The SEP event fluence distribution. The black squares are experimental data from Gabriel and Feynman *(1996)*. The light squares are experimental data corrected for the threshold effect. Curve 1 is the distribution in terms of Eq. (3-5). Curve 2 is the distribution allowing for the threshold effect in terms of the selection conditions of SEP events. Curve 3 is the best log-normal distribution for the given set of experimental dots. (Figure and caption from Nymmik (1999))

Further comparison was conducted with the 56 SPE's observed at Mars with the MGS ER instrument. The power-law fit was reliable with the Mars-based data as well. A distribution coefficient of -1.32 was determined with the MGS ER data. Based on the consistency between datasets and instrument locations, it is concluded that a power-law fit is sufficient to predict the distribution of SPE fluences at Earth and Mars. The Earth- and Mars-based fits are presented in Figures 3-16 and 3-17, respectively.

From the formulae presented in Figures 3-16 and 3-17, it is clear that there are differences in the anticipated SPE fluences between Earth and Mars. In general, it can be expected that SPE's observed at Mars are more likely to have lower fluences ($10^4 – 10^6$ particles/cm^2) than those observed at Earth, because of the greater distance from the Sun. Conversely, observations at Earth are more likely to have large fluences (>10^6 particles/cm^2) than those observed at Mars. This is consistent with findings presented in Chapter 2 that the fluence between Earth and Mars for coincident events falls as $1/R^{2.2}$, where R is radial distance from the Sun.

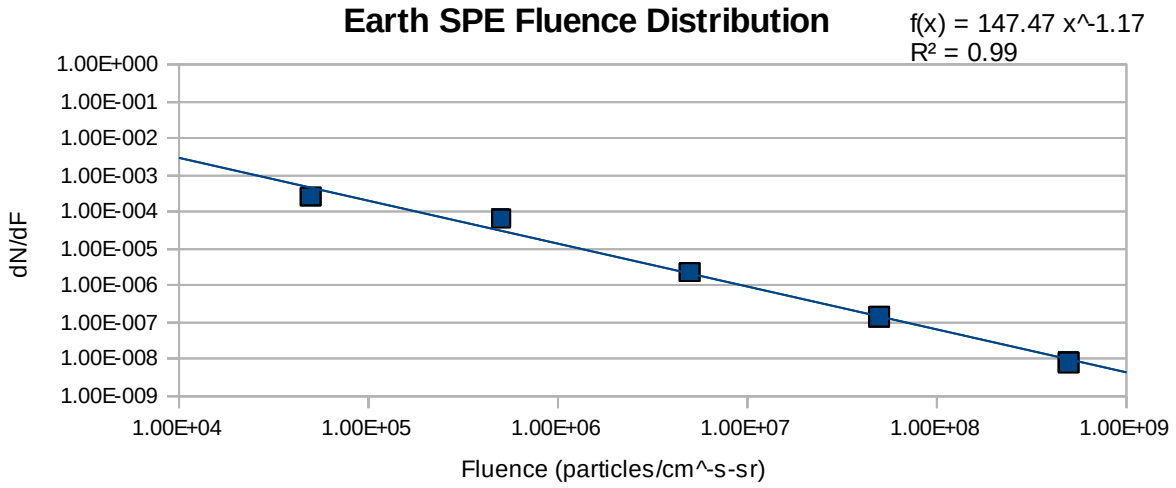

Figure 3-16. Fluence distribution for Earth-based data for protons with E > ~25MeV collected at the GOES-10 satellite between January 1999 and December 2007. A power-law fit was applied, in accordance with the model proposed by Nymmik (1999). The fitted curve equation and R^2 value are provided in the upper-right hand corner of the graph.

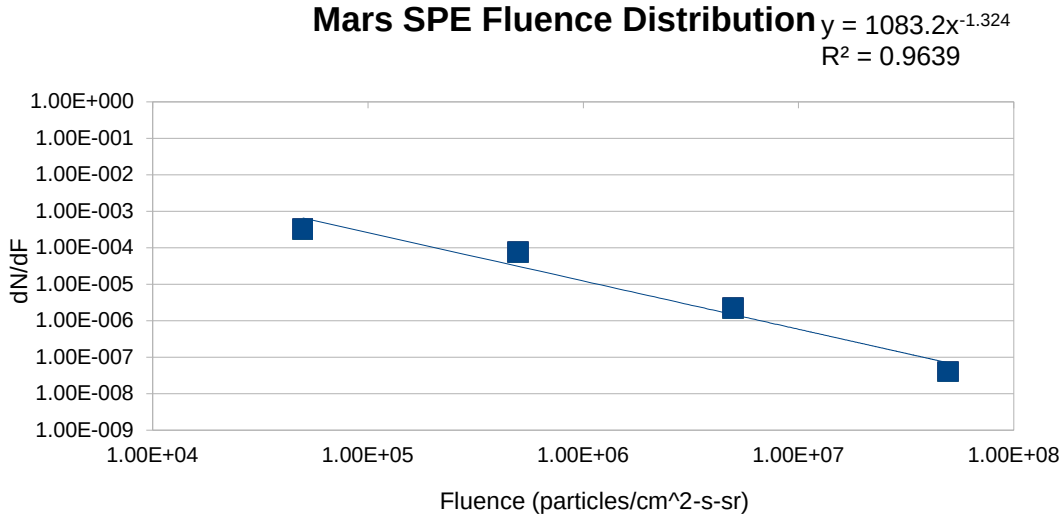

Figure 3-17. Fluence distribution for Mars-based data for protons with E > ~25MeV collected by MGS ER between January 1999 and December 2007. A power-law fit was applied, in accordance with the model proposed by Nymmik *(1999)*. The fitted curve equation and R^2 value are provided in the upper-right hand corner of the graph.

It is also noteworthy that the fluence at Mars is occasionally greater than that at Earth for the same event. While this is expected for times that Earth and Mars are near conjunction, it also occurs at times when Earth and Mars are near opposition. During times when Earth and Mars are closely aligned with the Sun (Sectors 1 and 2 in Figure 3-3), the fluence is only greater at Mars when there are overlapping series of events. This is likely caused by one or more of the overlapping events being better-connected magnetically to Mars than Earth. In other cases, it is likely due to longitudinal variations in SPE's as they propagate through space. As mentioned previously, there are also events that are observed at Mars only.

3.5 Peak Fluxes and Shock Arrival Times for SPE's at Earth and Mars

Another key factor in predicting the impact of SPE's at Mars is the peak flux for a given event. This measurement is often used to assess the acute radiation risk to electronics and biological organisms. Peak flux is also often indicative of the interplanetary shock arrival from the initial solar event. Shock arrival times are important, because they indicate the speed at which an SPE propagates through space and thus reflect the warning time available to protect crewmembers and instruments. This section provides information on the distribution of peak fluxes for SPE's observed at Earth and Mars. Information is also presented on the shock arrival times for coincident SPE's that occurred when Earth and Mars were near opposition. However, it should be noted that there is no direct way to measure the arrival time of shocks at Mars. Strategies for estimating the arrival times for some events are provided here.

3.5.1 Distribution of Peak Fluxes for SPE's at Earth and Mars

As with the fluence model described in the previous section, a power-law model is used to describe the distribution of peak fluxes for SPE's. This form has been validated by Xapsos et al. (1998) who found good agreement with experimental data. Xapsos et al. examined SPE data for protons with energies greater than 10MeV and focused on events with peak fluxes above a few hundred particles/cm^2-s-sr. The data used by Xapsos et al. was also restricted to SPE's that occurred in solar active years. In contrast, the data used in this study are for SPE's with peak fluxes above 1 particle/cm^2-s-sr, for energies greater than 30 MeV, and for all years during the solar cycle.

Despite these differences, the power-law form still provides a good fit to both Mars and Earth-based data used in this study. The power-law coefficient deduced by Xapsos et al. for Earth-based observations is -.68. This differs substantially from the coefficient found for the Earth-based data used in this study, -1.13. Figures 3-18 and 3-19 present the data fit from Xapsos et al. and the Earth-based data from this study, respectively.

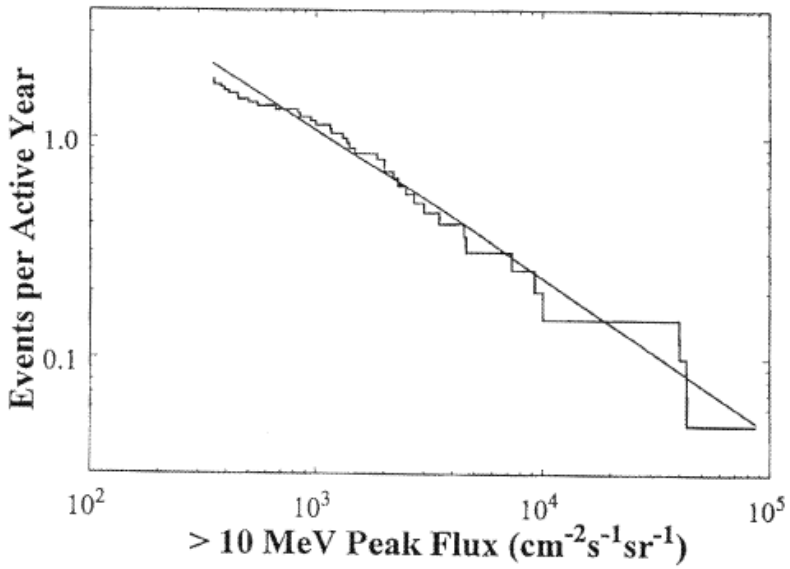

Figure 3-18. Initial distribution of large solar proton event peak fluxes. The ordinate represents the number of events per solar active year having a peak value that exceeds that shown on the abscissa. The histogram shows the activity for the last 20 solar active years. The straight line is the predicted value from the power-law model. (Figure and parts of caption from Xapsos et al. (1998))

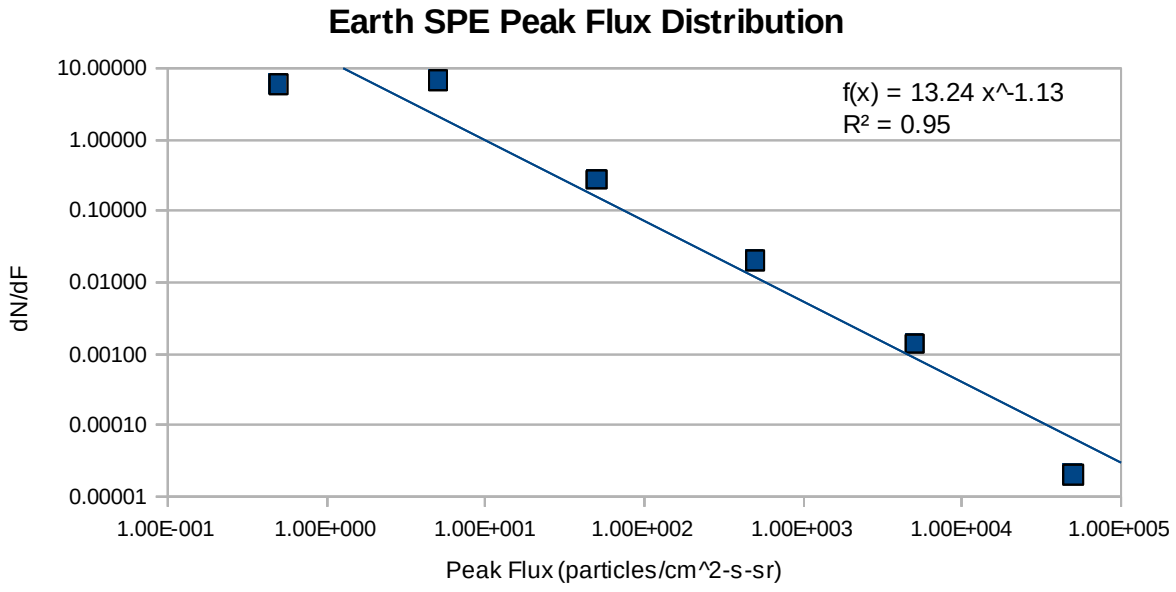

Figure 3-19. Peak flux distribution for Earth-based data for protons with E > ~25MeV collected by GOES-10 between January 1999 and December 2007. A power-law fit was applied, in accordance with the model proposed by Xapsos et al. (1998). The fitted curve equation and R^2 value are provided in the upper-right hand corner of the graph.

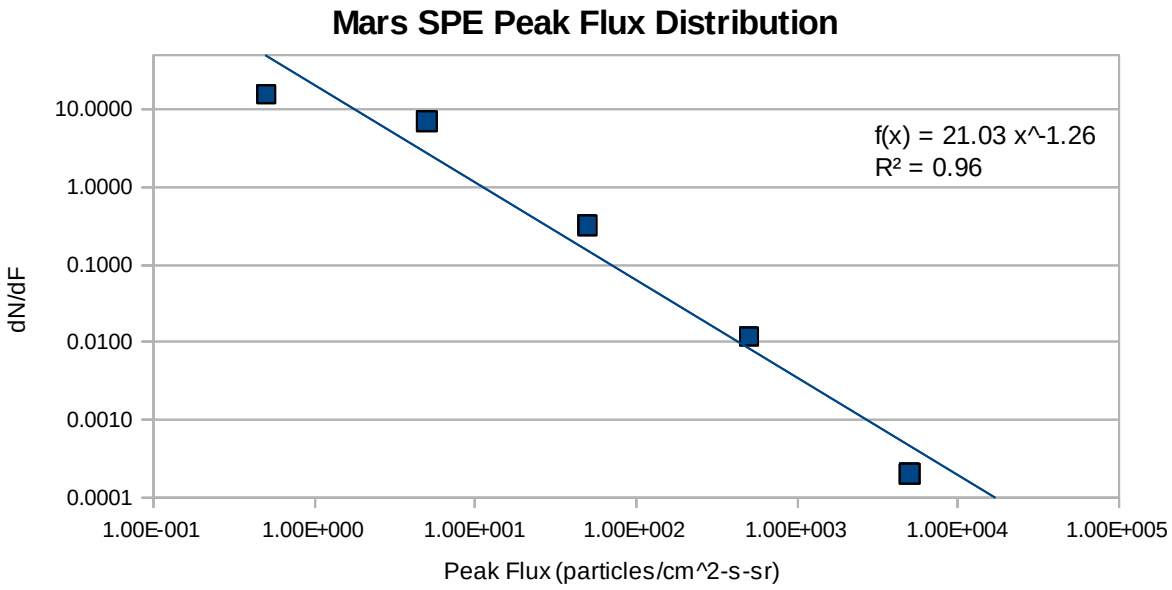

Figure 3-20. Peak flux distribution for Mars-based data for protons with E > ~25MeV collected by MGS ER between January 1999 and December 2007. A power-law fit was applied, in accordance with the model proposed by Xapsos et al. (1998). The fitted curve equation and R^2 value are provided in the upper-right hand corner of the graph.

As one might expect, the power-law coefficient is smaller at Mars than Earth. Thus, it is far less likely to observe a large peak flux at Mars. This is also consistent with findings presented in Chapter 2 that the peak flux between Earth and Mars for coincident events falls as $1/R^{3.5}$, where R is radial distance from the Sun. As with the analysis of SPE fluences, there are occasionally events where the peak flux at Mars is greater than that at Earth. However, incidents of higher peak flux at Mars occur as often for singular events as overlapping events. This is most likely due to longitudinal variations in the solar particle events as they propagate through space.

3.5.2 Shock Time of Arrival at Earth and Mars

As mentioned previously, the peak flux from an SPE is often caused by the arrival of an interplanetary shockwave that is produced during the onset of a coronal mass ejection (CME). Therefore, the shock arrival time can be a critical parameter in determining the time available to mitigate harm from an SPE. Several models have been developed to predict shock arrival times. These models fall into two primary categories: empirical and magnetohydrodynamic (MHD). Empirical models compare CME starting time and speed measurements to magnetometer data near Earth. MHD models use elaborate computer-based simulations that apply a variety of physical parameters to predict the propagation of interplanetary shockwaves through the Solar System.

While MHD models are useful in understanding the physical complexities of the propagation of interplanetary shockwaves, long processing and preparation times make them less useful for real time assessment. Two empirical models were examined in this study – Lindsay et al. (1999)

and Gopalswamy et al. (2002). Both models use the initial CME speed and ambient solar wind speed to predict the acceleration or deceleration of the shock in interplanetary space. This allows for a prediction of the shock arrival times at various distances from the Sun. The Gopalswamy et al (2001) model assumes that the shock speed will match the solar wind speed at approximately .75 AU, while the Lindsay et al (1999) model does not terminate the acceleration or deceleration of the shock. Both models are in good agreement with observations, though the Gopalswamy model uses a broader sample of observed events in deriving its results.

Lindsay et al. (1999) used a model of the following form:

$$V_{ip} = (0.25 \pm 0.04)\, V_c + 360 \pm 23 \qquad \text{(Equation 3-6)}$$

V_{ip} is the interplanetary shock speed and V_c is the CME speed as measured by coronagraph images taken by the LASCO instrument onboard the SOHO satellite. This form is based on the assumption that the ambient solar wind speed is 400 km/s. Based on Equation 3-6, the shock time of arrival can be easily determined by:

$$T_L = d / V_{ip} \qquad \text{(Equation 3-7)}$$

Here, T_L is the shock time of arrival based on the Lindsay et al. (1999) model and d is the radial distance from the Sun.

Gopalswamy et al. (2002) assumes that the shock will accelerate to a certain point in space then maintain a constant speed beyond that point. Acceleration is given by the following equation:

$$a = 2.193 - 0.0054\, u \qquad \text{(Equation 3-8)}$$

a is the acceleration of the shock and u is the initial CME speed. This assumes an ambient solar wind speed of 400 km/s. The time for the shock to reach the point where it no longer accelerates is given by:

$$t_1 = [-u + (u^2 + 2ad_1)^{1/2}] / a \qquad \text{(Equation 3-9)}$$

u and a are described in Equation 3-8, t_1 is the shock time of arrival at the acceleration cessation point, and d_1 is the radial distance from the Sun to the acceleration cessation point. The time for the shock to reach a point beyond the acceleration cessation distance is given by:

$$t_2 = d_2 / (u^2 + 2ad_1)^{1/2} \qquad \text{(Equation 3-10)}$$

u, a, and d_1 are described in Equation 3-9. The shock travel time from d_1 to a further distance, d_2, is given by t_2. The total expected travel time from the Sun to a distance, d_2, is given by the sum of t_1 and t_2:

$$T_G = t_1 + t_2 \qquad \text{(Equation 3-11)}$$

Here, T_G is the shock time of arrival based on the Gopalswamy et al. (2002) model and t_1 and t_2 are described in Equations 3-9 and 3-10, respectively.

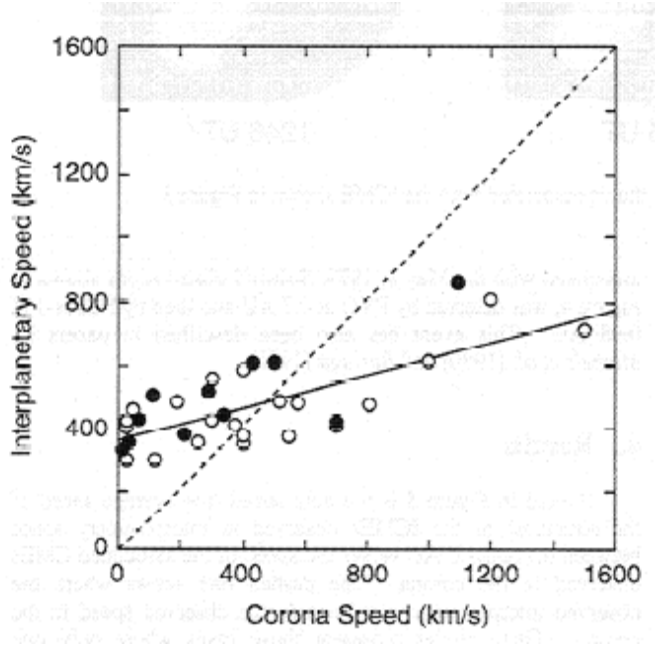

Figure 3-21. Speed of an interplanetary shock plotted as a function of the associated CME speed in the solar corona. Open circles represent high-confidence cases. Closed circles represent moderate-confidence cases. The formula describing the line fitted to the data is given by Equation 3-6. (Image and caption from Lindsay et al. (1999))

Figures 3-21 and 3-22 compare the relative fits of shock arrival time data for the Lindsay et al. (1999) and Gopalswamy et al. (2002) models, respectively. Neither model is perfect but each presents a rough prediction of the shock arrival time at Earth's distance.

Both models are used in this study to estimate the shock arrival times at Mars for coincident SPE's when Earth and Mars were near opposition. Two methods were combined to estimate the shock arrival time at Mars: the Mars solar wind pressure proxy (Criders et al. 2003) and visual cues. These methods are described in greater detail below. The estimated shock arrival time at Mars was also compared to the Lindsay et al. (1999) and Gopalswamy et al. (2002) models.

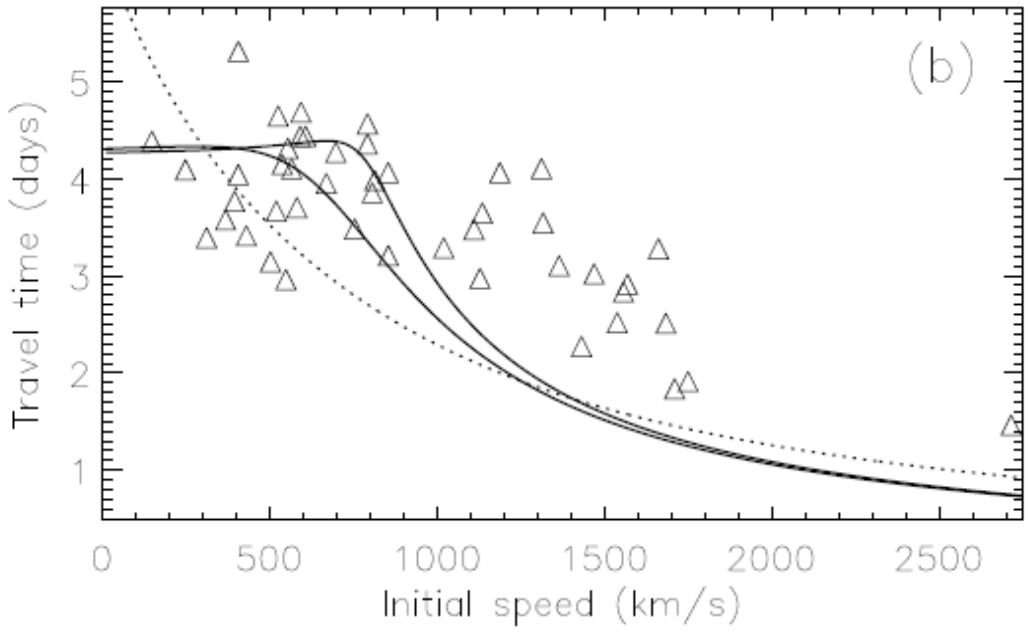

Figure 3-22. Comparison between predicted and observed travel times based on the acceleration profile described in Gopalswamy et al. *(2002)*. Both linear (solid curves) and quadratic (dotted curve) acceleration cases are shown. The solid curves show the effect of the acceleration-cessation distance (lower – 0.76AU, upper – 0.95 AU). (Image and caption from Gopalswamy et al. (2002))

Establishing the shock time of arrival at Mars can be somewhat subjective. Magnetometer data onboard the Mars Global Surveyor (MGS) satellite are typically an unreliable sources of information in determining the presence of an interplanetary shock. The ionospheric magnetic field strength at MGS altitude is greater than that of the shockwave, which makes it particularly difficult to isolate which part of the magnetometer data is ambient as opposed to shock-related.

Crider et al. (2003) developed a methodology to determine the magnetic field pressure induced by the solar wind on the Martian ionosphere. During shock arrival times, this pressure can be expected to dramatically increase. The pressure proxy determination assumes a Newtonian pressure balance occurs between the solar wind's magnetic field pressure and that of an obstacle, in this case the induced magnetic field in the Martian ionosphere. The component of the magnetic field that is parallel to the obstacle boundary is the relevant parameter in determining magnetic field pressure. Crider et al. (2003) determined that the magnetic field is typically parallel to the boundary in the magnetic pileup region (MPR), which is a region of nearly direct interaction between the solar wind and Mars' magnetic field (See Figure 3-23). Hence, the following formula can be used to calculate the solar wind pressure observed by MGS:

$$P_{MGS} = B^2_{mpr} / (2\mu_o k \cos\theta) \qquad \text{(Equation 3-12)}$$

B_{mpr} is the magnetic field at the magnetic pileup region, μ_o is the permeability of free space, k is a proportionality constant, and θ is the angle between the direction of ram pressure and the normal to the obstacle surface. Unfortunately, this method of determining shock arrival times through a magnetic pressure proxy is limited, because B_{mpr} can only be measured once during each orbit (approximately 90 minutes). So, the pressure proxy can only be used to identify a broad timeframe in which a shock may arrive. Figure 3-24 compares the Mars pressure proxy to direct Earth-based measurements from the Wind satellite during solar quiet times. It is shown that there is excellent agreement between the two datasets when Mars is near opposition.

While the Mars pressure proxy is not independently sufficient to determine a shock arrival time, it can be used in concert with energetic particle data to establish a far more accurate estimate. The correlation of an increase in magnetic pressure at Mars and an impulsive increase in energetic particle flux is a strong indicator of a shock arrival. Independently, an impulsive increase in energetic particle flux would not necessarily indicate the arrival of an interplanetary shock. The Mars pressure proxy provides important confirmation for features that can be visually observed in the particle data. It may also be possible to observe shock arrival time from low-energy electron measurements.

For the purposes of this study, the start time and initial CME velocity for an event is based on coronagraph images from the LASCO instrument onboard the Earth-based SOHO satellite. An online database is available that presents these data (http://cdaw.gsfc.nasa.gov/CME_list/). Shock arrival times are established as the time of a peak flux in MGS penetrating particles where there is a coincident increase in magnetic pressure.

Shock arrival times determined in this manner were compared to the predicted shock arrival times for the Gopalswamy et al. (2002) and Lindsay et al. (1999) models to determine which provides the best predictive capability. In order to limit the effects of longitudinal variations in the shock speed, it was necessary to restrict the comparison in this study to those events that occurred when Earth and Mars were near opposition (Sectors 1 and 2).

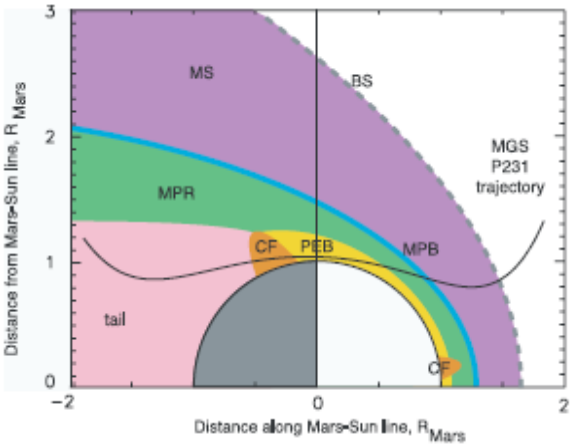

Figure 3-23. Cylindrical projection of the trajectory of MGS pass 231 to show the locations of the different regimes. The shaded areas represent the bow shock (dashed line), magnetosheath (purple), MPB (blue), magnetic pileup region (green), photoelectron boundary (yellow), a crustal field (orange), and the tail (pink). (Figure and Caption from Crider et al. (2003))

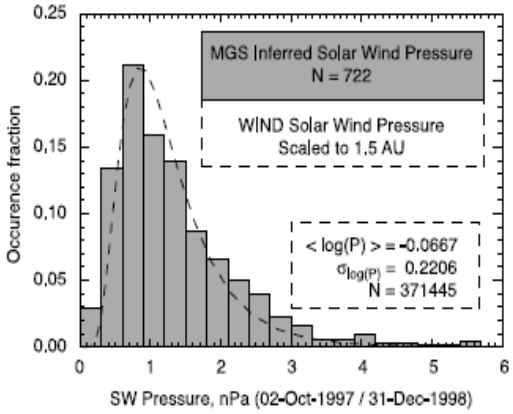

Figure 3-24. Comparison of the solar wind pressure distribution obtained by this proxy at Mars with the solar wind pressure measured by Wind at Earth during the same time period. (Figure and Caption from Crider et al. (2003))

Unfortunately, only six events occurred near Earth-Mars opposition, demonstrated a clear magnetic shock at Mars, and could be traced to a specific CME observation at the Sun. Despite this shortcoming, a comparison was made between the measured shock arrival time at Mars and predictions from Gopalswamy et al. (2002) and Lindsay et al. (1999) models. For the six relevant events, the Lindsay model had an average error of 28% and the Gopalswamy model had an average error of 47%.

From this analysis, it is clear that the Lindsay model is much more reliable than the Gopalswamy model, though neither model is particularly accurate at Mars. Both models are dependent on measurements of CME speed near the solar corona. Currently, these measurements are made from the vantage point of the Earth-based SOHO satellite. It is likely that the inaccuracy of the Gopalswamy and Lindsay models is due largely to the difference in relative CME speed between Earth and Mars. Mars-based measurements of CME speeds may yield better results for shock time of arrival models.

The full dataset of events was analyzed to determine the average shock arrival time at Mars compared to Earth. On average, the shock arrival at Earth is 37 ± 3 hours, whereas the average arrival time at Mars is 71 ± 6 hours. While it is expected that the shock arrival time will be longer at Mars than at Earth, the average arrival time at Mars is nearly twice that at Earth. This cannot be explained solely by the extra distance traveled between the Sun and Mars. Rather, the shock must continue to decelerate beyond 1 AU. This is in agreement with the Lindsay et al. (1999) model but contradicts the Gopalswamy et al. (2002) model, which terminates the shock

deceleration at approximately .75 AU. Additional Mars-based data are required to develop a useful model for the shock arrival times at Mars.

3.6 Conclusion

The availability of SPE data from MGS ER allows for a thorough analysis of the features, frequency, and magnitudes of these events at Mars. A comparison of these data to Earth-based observations provides perspective on the possibilities of predicting the impact of SPE's on Mars in the current and future solar cycles.

Among the most basic and most important findings in this chapter is that events are sometimes seen at Mars but not Earth, even in cases where the two planets are closely aligned. The implication of this finding is that Earth-based instruments are not alone sufficient to predict the occurrence of SPE's at Mars. Moreover, Earth-based instruments are insufficient to provide warning systems to Mars-based missions.

However, SPE fluence and peak flux comparisons between Earth and Mars are helpful in assessing the relative likelihood of events to occur with different scales. In fact, flux and fluence measurements made by MGS ER are well-aligned with predictive models that have been developed for Earth-based missions. These findings provide the basis for the development of Mars-based predictive models, though additional data are required.

In order to develop predictive models for SPE frequencies and shock times of arrival at Mars, additional Mars-based instruments are required. In particular, a Mars-based coronagraph imager would support the development of these models. Of course, a Mars-based energetic ion detector is also important to expand the current data set and to improve the accuracy of analysis.

Acknowledgments

Special thanks to Dr. Stephen Blattnig, NASA Langley Research Center, for taking time to review several iterations of this chapter and for providing a wide range of good advice on the topics herein.

References

D.H. Crider et al. “A Proxy for Determining Solar Wind Dynamic Pressure at Mars using Mars Global Surveyor Data.” *Journal of Geophysical Research,* vol. 108, no. A12. 2003.

J. Feynman et al. “Interplanetary proton Fuence Model: JPL 1991.” *Journal of Geophysical Research* vol. 98, pgs. 13,281–13,294. 1993.

N. Gopalswamy et al. “Predicting the 1-AU Arrival Times of Coronal Mass Ejections.” *Journal of Geophysical Research.* 2002.

D. Hathaway et al. “A Synthesis of Solar Cycle Prediction Techniques.” *Journal of Geophysical Research,* vol. 104, no. A10, pgs. 22,375 – 22,388. 1999.

J.N. Kapur. *Maximum Entropy Models in Science and Engineering*. John Wiley & Sons, Inc. New York. 1989.

G.M. Lindsay et al. “Relationships between Coronal Mass Ejection Speeds from Coronagraph Images and Interplanetary Characteristics of Associated Interplanetary Coronal Mass Ejections.” *Journal of Geophysical Research,* vol. 104, no. A6, pgs. 12,515 – 12,523. 1999.

R.A. Nymmik. “Probabilistic Model for Fluences and Peak Fluxes of Solar Energetic Particles.” *Radiation Measurements,* vol. 30, pgs. 287-296. 1999.

D. Reames. “Solar Energetic Particles: Is there Time to Hide?” *Radiation Measurements,* vol. 30, pgs. 297-308. 1999.

http://www.igpp.ucla.edu/

http://solarscience.msfc.nasa.gov/images/ssn_predict_l.gif

M.A. Xapsos et al. “Space Environment Effects : Model for Emission of Solar Protons (ESP) – Cumulative and Worst-Case Event Fluences.” *NASA Technical Paper 1999-209763*. 1999.

M.A. Xapsos et al. “Extreme Value Analysis of Solar Energetic Proton Peak Fluxes.” *Solar Physics,* vol. 183, pgs. 157-164. 1998.

Chapter 4
Impact of Solar Particle Events on the Radiation Environment at the Martian Surface

Abstract

This chapter presents the process of modeling the radiation field at the surface of Mars, due to solar particle events (SPE's). The lack of spectral information at Mars is a significant hindrance to understanding the surface radiation environment, but certain spectral information is gleaned from Earth-based data. In particular, the average spectral index (3.2) was determined for high energy proton data from 58 SPE's observed at Earth. Spectral indexes were also determined for typical hard (1.3) and soft (4.3) SPE spectra. This range of spectral indexes was combined with a model of the Martian atmosphere and surface to create a radiation model for the Particle and Heavy Ion Transport code System (PHITS). The surface fluxes and fluences of protons, electrons, neutrons, and photons were examined.

Based on the output of the PHITS model, it is determined that the presence of particles back-scattered from the Martian surface compose a significant portion of the overall surface fluence. Most notably, front- and back-scattered neutrons dominate the radiation environment up to approximately 100 MeV. Beyond that energy, primary protons that fully penetrate the Martian atmosphere dominate the total surface radiation flux. These findings match those of similar studies that used HZETRN and Geant4 radiation transport codes. Unfortunately, the range of spectral indexes is so broad that the potential surface fluences span 2-3 orders of magnitude. However, the average spectral index allows for the estimation of surface fluence caused by several SPE's over time. This information will be applied in Chapter 5 to estimate the radiation dose for a human on the surface of Mars.

4.1 Introduction

In an effort to characterize the occurrences of solar particle events (SPE's) at Mars, Chapter 3 presented the fluence and peak flux distributions for SPE's arriving at Mars orbit from January 1999 through December 2006. While this is important and useful information, it is alone insufficient to assess the impact of SPE's on the Martian surface. In order to determine the fluence and peak flux distributions of SPE's on the surface of Mars, two items are necessary:

1. Characterization of the spectral properties of SPE's arriving at Mars' orbit; and
2. A radiation transport code to simulate the interaction of solar energetic particles with the Martian atmosphere and regolith.

This chapter addresses both of these items. Unlike Chapter 3, this chapter does not attempt to predict future activity on Mars. Rather, if focuses on existing data during the time of operation of the Mars Global Surveyor (MGS) Electron Reflectometer (ER).

Unfortunately, spectral information for SPE's at Mars is very limited. In fact, the only information available is that detected particles must have an energy greater than approximately 25 MeV (See Chapter 2). Earth-based spectral information is available from the SEM instrument, on board the GOES-10 satellite. While it is not possible to directly apply Earth-based spectra to Mars data, the distribution of spectral indices was determined at Earth and applied to MGS ER data. Average, hard, and soft spectra at Earth were applied to a sample SPE observed at Mars for use in a radiation transport model designed to estimate the radiation field on the Martian surface.

A computer model of the Martian atmosphere and surface was created for the Particle and Heavy Ion Transport code System (PHITS). The average, hard, and soft Martian SPE spectra were used as inputs into the model, which generated fluence and peak flux estimates on the Martian surface. PHITS is a Monte Carlo-based code that is capable of analyzing a broad range of nuclear interactions over a wide range of energies. Fluence and flux estimates are available for protons, neutrons, electrons, and gamma rays from a few keV to several hundred MeV.

The following comparisons were made regarding the estimated particle fluxes and fluences on the Martian surface:

- The overall fluences and peak fluxes of protons, neutrons, electrons, and gamma rays.
- The relative contributions of particles generated through forward-scattering in the Martian atmosphere and back-scattered from the Martian surface.
- The relative fluences and fluxes of protons, neutrons, electrons, and gamma rays, based on average, hard, and soft incident SPE spectra.

The results of these analyses are consistent with results published in the literature, using alternate radiation transport codes. In general, the surface fluence and peak flux are highly dependent on the hardness of the incident SPE spectrum. Back-scattered particles provide a substantial contribution to the overall surface radiation field. Data produced from these

analyses will be used in Chapter 5 to estimate the radiation dose a human will receive on the surface of Mars for a variety of individual SPE's, as well as the cumulative dose over time.

4.2 Solar Particle Event Spectra at Earth and Mars

4.2.1 Solar Particle Event Spectra at Earth

The SEM instrument onboard the GOES-10 satellite collected solar energetic proton data in integral energy bins of energies greater than 1, 5, 10, 30, 50, 60, and 100 MeV. To create energy spectra for each event, the difference in total event fluence for each energy channel and the next highest energy channel was calculated for the 10, 30, 50, and 60 MeV energy channels. This created energy bins of varying widths. The fluence of each bin is estimated to be the exact fluence at the energy midpoint of each bin (See Table 4-1). A power-law fit was applied to the resulting data. As explained in Chapter 2, SPE spectra typically follow a double-power-law form, which applies separate high- and low-energy spectral indexes. Because this study is only concerned with high energy particles, a single power law spectrum is sufficient for each SPE. Hence, each spectrum is of the form:

$$\partial F(E)/\partial E = A \times E^{b} \qquad \text{Equation 4-1}$$

$\partial F(E)$ is the differential energy-dependent fluence or flux from an SPE, E is the energy of interest, A is a scaling constant, and b is the spectral index. Figure 4-1 presents a sample spectrum.

The distribution of spectral indexes for 58 Earth-based events is presented in Figure 4-2. A low spectral index implies that high energy particle fluences drop off at a relatively low rate, whereas a high spectral index implies that high energy particle fluences drop off rapidly with increasing energy. Hence, an SPE with low fluence can be more damaging than a high-fluence SPE, if low-fluence SPE has a significantly lower spectral index. A low spectral index is referred to as a "hard" spectrum, and a high spectral index is referred to as a "soft" spectrum.

As can be seen in Figure 4-2, SPE spectral indexes occur over a wide range, between 1.22 and 4.69, with an average spectral index of 3.1. The distribution of spectral indexes does not follow a clear mathematical form. However, nearly 75% of events have a spectral index between 2.0 and 4.0. For the purposes of this study, an average spectral index of 3.2 was used. A spectral index of 1.3 was used to represent a hard spectrum, and a spectral index of 4.3 was used to represent a soft spectrum. The impact of spectral indexes on the surface fluence and peak flux at Mars are presented here, and their relative biological importance is presented in Chapter 5.

Energy Bin Range (MeV)	Estimated Energy (MeV)
10.0 – 30.0 MeV	20.0 MeV
30.0 – 50.0 MeV	40.0 MeV
50.0 – 60.0 MeV	55.0 MeV
60.0 – 100.0 MeV	80.0 MeV

Table 4-1. Energy bins and estimated energies used for calculation of Earth-based SPE Spectra.

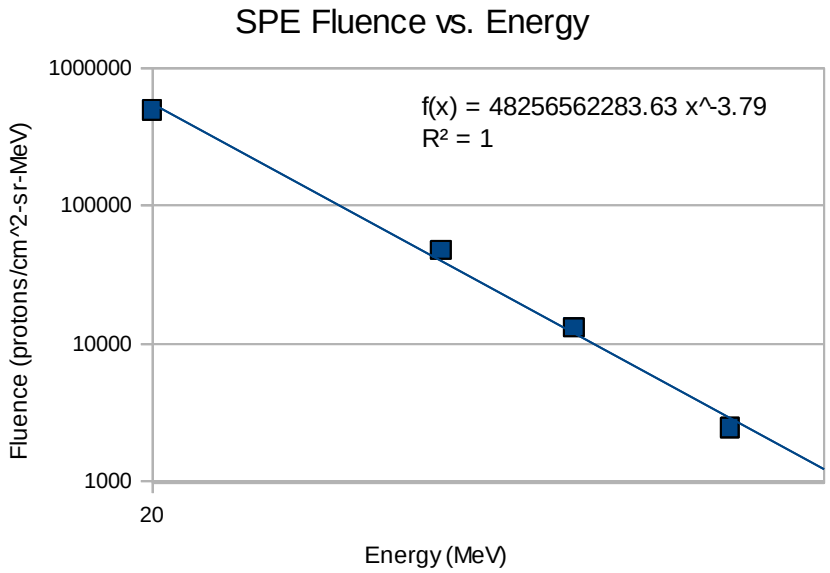

Figure 4-1. Calculated proton spectrum for a Solar Particle Event (SPE). The spectral index in this case is 3.79.

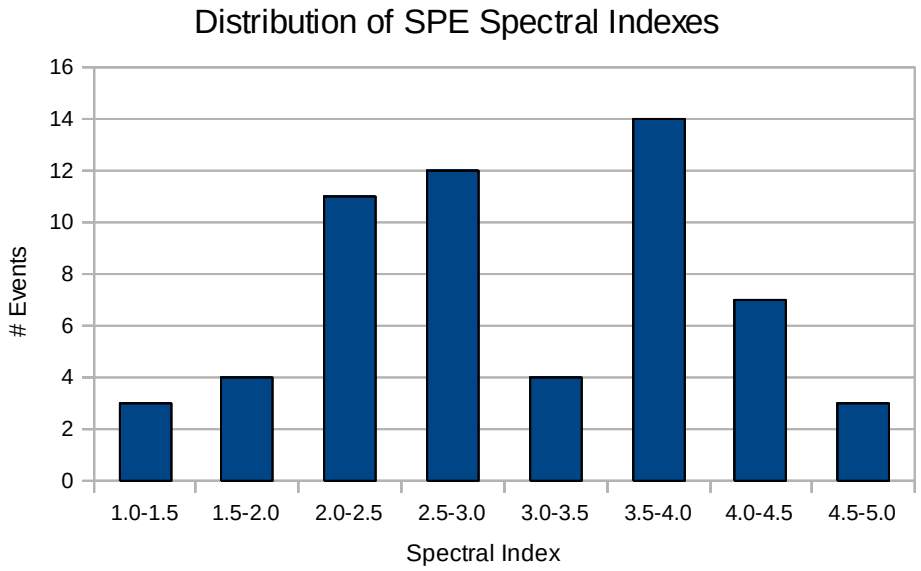

Figure 4-2. Spectral indexes for 58 solar particle events observed at Earth.

4.2.2 Solar Particle Event Spectra at Mars

SPE's are complex events that demonstrate significant spatial variability. Hence, the particle spectrum measured at Earth does not necessarily apply to that at Mars – even when the planets are magnetically aligned. Rather than attempting to infer particle spectra at Mars, this study assumes that the distribution of spectral indexes at Earth and Mars are equivalent.

The average spectral index is used to assess the cumulative impact for a series of events on the surface of Mars. Hard and soft spectra are used to evaluate the range particle fluences on the Martian surface for individual SPE's. While the use of proxy spectra is far from perfect, it represents the best strategy possible, given the absence of spectral data at Mars. Moreover, the analyses presented in this study are sufficient to draw meaningful, quantitative estimates of the impact of SPE radiation on the Martian surface.

4.3 Energetic Particle Transport in the Martian Atmosphere and Regolith

4.3.1 PHITS Overview

Modeling the transport of energetic particles through the Martian atmosphere and regolith is not a trivial process, and several radiation transport codes are available for this purpose. The Particle and Heavy Ion Transport code System (PHITS) is a Monte Carlo-based radiation transport code, developed by the Japan Atomic Energy Institute (JAERI), in collaboration with Tohoku University and the Research Organization for Information Science & Technology (RIST). PHITS combines a variety of existing software to create a single transport code with applicability to a wide range of energies, forms of radiation, and target materials. Figure 4-3 presents the constituent programs that constitute the full PHITS radiation transport code, as well as its progression, structure, and applicability.

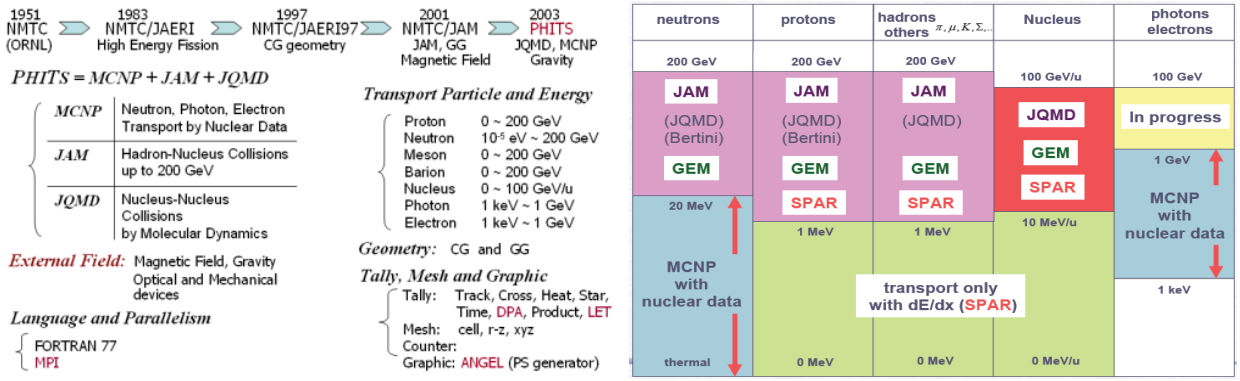

a) b)

Figure 4-3. a) Overview of the development of PHITS, as well as the complete range of particle energies available. b) Map of constituent programs within PHITS that are responsible for processing particles at different energy levels. (http://phits.jaea.go.jp/Overview.html)

Several transport codes were considered in the development of this study, including HZETRN, FLUKA, and Geant4. In fact, Mars radiation studies have been conducted using HZETRN and Geant4. These studies are discussed below. However, PHITS provided the broadest range of energies and radiation types, as well as a straightforward user interface. The PHITS code itself was readily accessible, and it has been validated in a variety of planetary studies (for example, Sato and Niita 2006, Sato et al. 2008). PHITS has been used extensively to model energetic particle transport through atmospheres and is used in the EXPACS program, which allows users to identify the cosmic radiation dose at any point on Earth (http://phits.jaea.go.jp/expacs/). Moreover, PHITS uses a standard MCNP format for its inputs. Software is available to convert CAD drawings to MCNP input format, which creates great potential to easily develop complex geometric models for radiative sources and targets. While this capability was not employed for the current study, its potential is compelling for future use. Computing resources for this study were provided by the Department of Mathematics at James Madison University. A 24-core processing cluster was utilized and was more than sufficient to carry out runs of 10^7 particles within 2 hours or less.

4.3.2 Model Inputs

The complete PHITS input code used in this study is available in Appendix A. A detailed description of the inputs is provided here. It is important to note that the model input was reviewed by PHITS developers prior to use in this study and was found to be sufficiently assembled (Niita 2009). In fact, test results were similar to those generated by the PHITS developers in a similar Mars model.

4.3.2.1 General Parameters

PHITS requires a variety of general inputs to establish basic parameters of the radiation transport model. The most significant of these parameters are described here.

In each simulation conducted in this study, 10^7 test particles were injected into the modeled Martian environment. Nuclear libraries were used to evaluate each of these particles and their byproducts, so long as their energies remained with the limits presented in Table 4-2. Below the minimum values, nuclear reactions are no longer considered. Other computational methods are used to evaluate interactions of particles exceeding the energy threshold. However, very few particles exceed the maximum energy limit.

Several inputs were set to describe the range of nuclear reactions to be considered, such as gamma emission, electron transport, and Coulomb diffusion. Other inputs identified specific nuclear cross section models to be used, such as the Tripathi formula for calculation nucleon-nucleon cross sections. Full details of each model are not included here, but Niita (2008) provides a comprehensive description of the models available with PHITS and their physical bases. Appendix A provides more details regarding the specific input choices in this study.

Radiation Type	Minimum Energy (MeV)	Maximum Energy (MeV)
Proton	10^{-6}	150
Neutron	10^{-11}	150
Electron	1	500
Positron	1	500
Photon	1	1000
Deuteron*	1	-
Triton*	1	-
^{3}He*	1	-
Alpha Particle*	1	-
Heavy Ion*	1	-

** No definable maximum energy limit.*

Table 4-2. Energy ranges used for various radiation types as input parameters for PHITS simulations of SPE interaction with a modeled Mars environment.

4.3.2.2 Source Description

The model used in this study employs a spherical shell source, with a radius of 3,780 km (approximately 385 km above the Martian surface). Particles are emitted isotropically inward toward the planet. Only protons were used as source particles, with an energy range between 25 and 1,500 MeV. As described previously, three particle spectra were used, corresponding to hard, average, and soft spectra. Separate simulations were conducted for each of the spectral forms presented in Equations 4-2.

a) $F(E) = E^{-1.3}$

b) $F(E) = E^{-3.2}$ Equations 4-2

c) $F(E) = E^{-4.3}$

4.3.2.3 Mars Model

A series of concentric spheres is used to describe the Martian surface and atmosphere. The innermost sphere represents the planetary body and has a radius of 3396 km. There are 23 larger concentric spheres, each representing a layer of Martian atmosphere. The outermost layer of atmosphere is approximately 285 km above the surface. Figure 4-4 displays a quadrant of the complete Mars model.

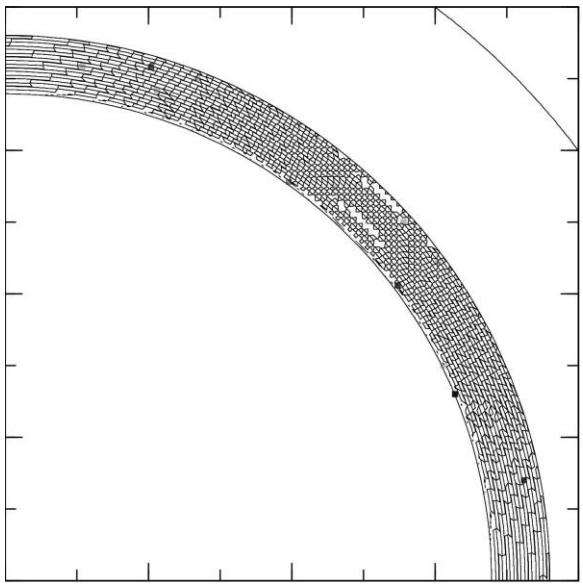

Figure 4-4. Model of Mars, using concentric spheres. The innermost sphere is the Martian surface, and each subsequent sphere is a layer of atmosphere.

The true atmosphere of Mars consists of 95% CO_2, with 5% of other trace elements. For the purposes of this study, it is assumed that the Martian atmosphere consists entirely of CO_2. An exponential decline in atmospheric density with altitude was assumed. The first 10 layers of atmosphere closest to the planet were divided such that the density of each layer represented a 10% decline in atmospheric density from the surface level of 1.64×10^{-5} g/cm^3. Beyond the 10th layer of atmosphere (1.64×10^{-5} g/cm^3), the layers were spaced to reflect an order of magnitude decrease in density from the previous layer. The outermost layer of atmosphere has a density of 1.64×10^{-19} g/cm^3. Figure 4-5 and Table 4-3 display the modeled change in atmospheric density with altitude.

The composition of the Martian surface is less certain and more complex than that of the atmosphere. Data from Mars Pathfinder indicate that the surface is primarily composed of SiO_2, FeO, and Al_2O_3. Approximately 80% of the Martian surface is composed of O (~43%), Si (~22%), and Fe (~15%). The remainder of the surface composition consists of trace elements. [http://marsprogram.jpl.nasa.gov/MPF/science/apxs_elemental.html]

This study assumes that the Martian surface has a density of 3.37 g/cm^3 and has a composition solely of O, Si, and Fe. Table 4-4 presents the breakdown of relative densities for each consituent element in the modeled Martian surface.

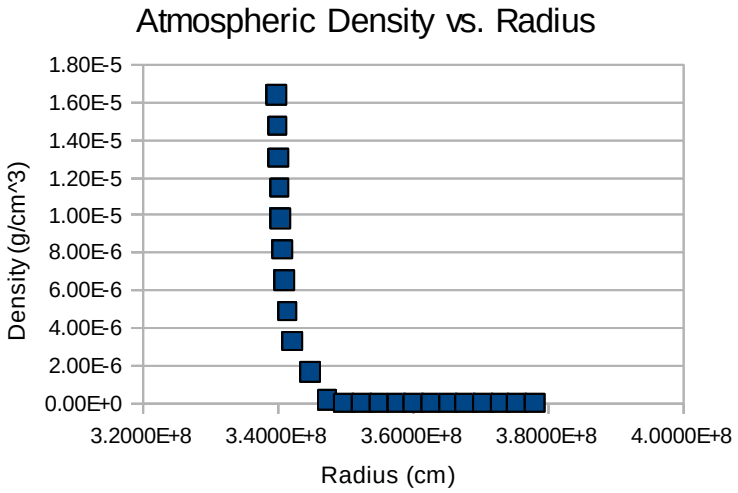

Radius (cm)	Density (g/cm^3)
3.3972E+8	1.64E-5
3.3985E+8	1.48E-5
3.4000E+8	1.31E-5
3.4017E+8	1.15E-5
3.4037E+8	9.84E-6
3.4062E+8	8.20E-6
3.4094E+8	6.56E-6
3.4139E+8	4.92E-6
3.4216E+8	3.28E-6
3.4472E+8	1.64E-6
3.4728E+8	1.64E-7
3.4984E+8	1.64E-8
3.5240E+8	1.64E-9
3.5495E+8	1.64E-10
3.5751E+8	1.64E-11
3.6007E+8	1.64E-12
3.6263E+8	1.64E-13
3.6519E+8	1.64E-14
3.6775E+8	1.64E-15
3.7031E+8	1.64E-16
3.7287E+8	1.64E-17
3.7543E+8	1.64E-18
3.7799E+8	1.64E-19

Figure 4-5. (Left) Atmospheric density vs. radius of each layer of simulated Martian atmosphere used in this study. An exponential decrease in density with distance was assumed.

Table 4-3. (Right) Raw data corresponding to the plot presented in Figure 4-5.

Element	Density (g/cm^3)
Fe	1.48
O	1.2
Si	0.69
Total	3.37

Table 4-4. Elemental composition and relative density for simulated Martian surface.

4.3.3 Model Outputs

Given the inputs described above, PHITS provides a tally of particles crossing a thin detector shield encapsulating the Martian surface. For this study, a tally was recorded for protons, neutrons, electrons, and photons crossing the model detector. Energy ranges for each type of radiation are presented in Table 4-5. These energy ranges were selected to assess the flux of particles at the Martian surface with energies relevant to human exploration.

Radiation Type	Energy Range (MeV)
Proton	1.0 – 5000.0
Neutron	$1.0x10^{-10}$ – $1.0x10^{4}$
Electon	0.1 – 1000.0
Photon	0.01 – 1000.0

Table 4-5. Energy ranges of radiation types tallied by PHITS at the modeled Martian surface.

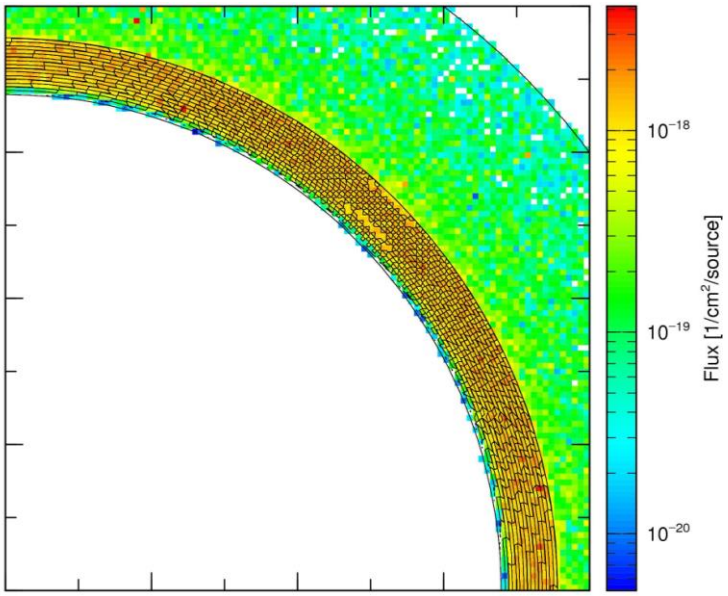

Figure 4-6. Uncalibrated graphical output of PHITS simulation of proton transport through the Martian atmosphere. This simulation assumed 10^7 test particles entering the Martian atmosphere, whereas typical events can have up to 10^{26} protons enter.

PHITS tallies were divided by the total area of the detector – in this case, the surface area of the Martian surface. They were also divided by the number of test particles used in the simulation, which an important normalization that allows for future scaling to real flux and fluence data. Thus, the PHITS output is given in particles/cm^2/# of sources, where every particle entering the

model environment is considered an individual source. Separate tallies are carried out for particles reaching the detector from the atmosphere and from the Martian surface. This allows for important analyses of the relative influence of front- and back-scattered particles on the surface radiation environment. Figure 4-6 present an uncalibrated graphical output for protons traversing the Martian atmosphere. The calibration process is described below.

PHITS output data are divided into 100 energy bins of various sizes. The PHITS output file provides the lower- and upper-limit energies for each bin, as well as the corresponding flux within each energy bin. A typical PHITS output file is provided in Appendix B.

4.3.4 Process for Analyzing Model Outputs

For PHITS output data to be useful, they must be normalized and scaled to appropriate dimensions and to real data. This is accomplished in two steps:

- Normalize the PHITS output data by energy to account for different energy bin sizes.
- Scale the PHITS output data to the measured flux of particles entering the Martian atmosphere.

Energy normalization is a straightforward process. The PHITS output flux is divided by the bin size (in MeV) of each energy bin. For graphing purposes, each data point of normalized flux is plotted against the midpoint of its corresponding energy bin. This normalized flux has units of particles/cm^2-MeV-# of sources.

Flux data collected by MGS ER are in units of particles/cm^2-s-sr. In order to scale the PHITS output data to the measured values, it is necessary to determine the total number of measured particles entering the Martian atmosphere. This is accomplished in two steps:

1. Multiply the measured flux by the total surface area of the outermost layer of Martian atmosphere (~1.8×10^{19} cm^2). This accounts for the full flux of particles into the Martian atmosphere, as opposed to the flux through a single point.
2. Multiply the total flux by 2π steradians, which accounts for the portion of space accessible by a point on the Martian atmosphere that does not include any part of the Martian atmosphere. Hence, any particle reaching a point on the outermost layer of atmosphere from beyond 2π steradians must be from within the atmosphere itself and is already accounted for as part of the modeled system.

The process is completed by multiplying the total number of particles entering the system by the energy-normalized PHITS output data. This results in flux units of particles/cm^2-s-MeV at the Martian surface. To calculate fluence at the Martian surface, the exact same process is used as described above. The only difference is that the measured data are in units of fluence, which results in final units of particles/cm^2-s-MeV.

4.4 Results

The data analysis procedure described above was used to assess fluxes and fluences of particles on the surface of Mars from three perspectives:

1. Radiation Type: Surface protons, neutrons, electrons, and photons were analyzed.
2. Spectral Index: Hard, soft, and average spectral indexes were used.
3. Directionality: Forward- and back-scattered particles were examined.

4.4.1 Analysis by Radiation Type

Figure 4-7 presents the fluences of protons, neutrons, electrons, and photons at the surface of Mars, based on an input spectral index of 3.2 and an incident fluence of 3.0×10^7 protons/cm^2-sr for protons with energies greater than 25 MeV. These input parameters represent an average spectral index applied to the largest solar particle event (SPE) observed during between January 1999 and December 2006.

Neutrons (the solid line in Figure 4-7) and photons (squares) dominate the low energy radiation environment from 1 – 10 MeV. At approximately 10 MeV, photon fluence drops off and neutrons dominate the radiation environment through approximately 70 MeV. Protons (stars) dominate the radiation environment at energies above 70 MeV. The peak proton fluence occurs at approximately 100 MeV, with a fluence of approximately 10^5 protons/cm^2-MeV. The strong representation of protons at high energies is likely due to the fact that protons above ~100 MeV are able to penetrate directly through the Martian atmosphere. Thus, the high energy protons observed at the Martian surface are primary particles directly from the SPE.

Electrons (diamonds) represent the smallest contribution to the radiation environment and have fluences typically 1 – 2 orders of magnitude smaller than any other form of radiation.

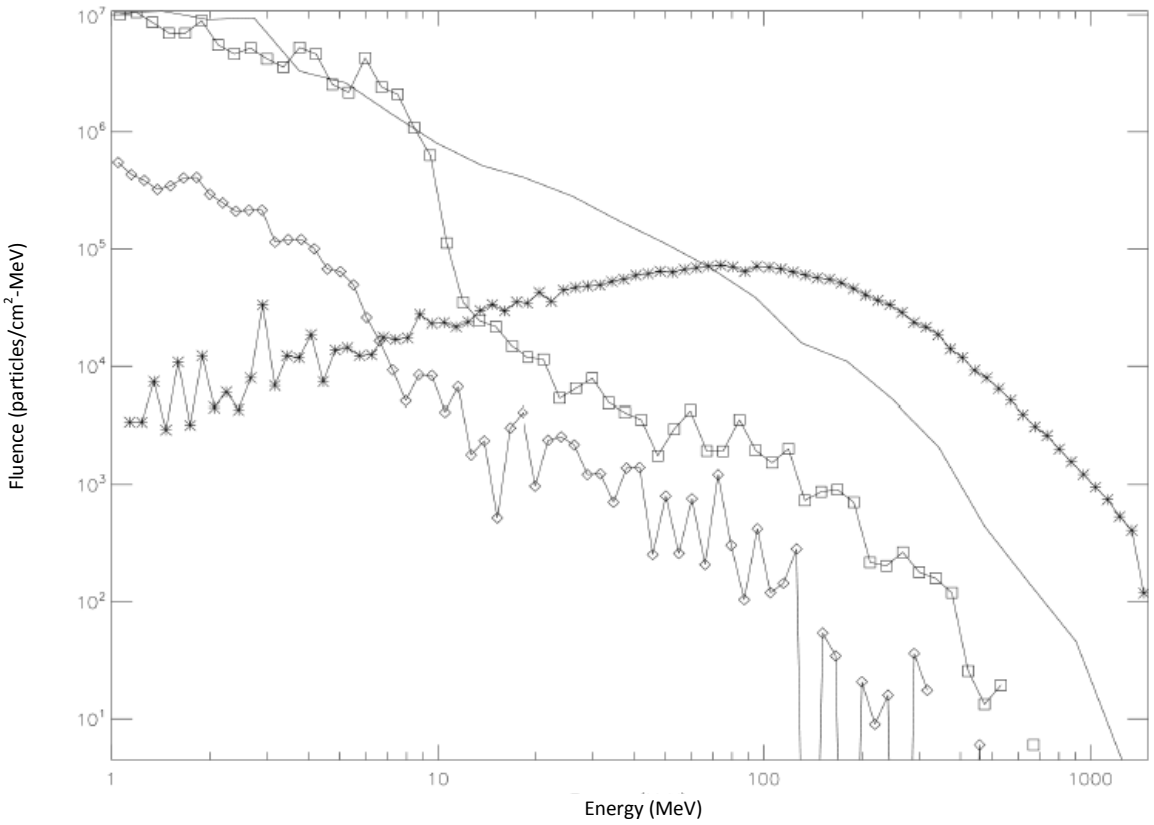

Figure 4-7. Fluence of neutrons (solid line), protons (stars), electrons (diamonds), and photons (squares) at the Martian surface for an incident SEP with flux of 3.0×10^7 protons/cm^2-sr and a spectral index of 3.2.

4.4.2 Analysis by Spectral Index

As discussed previously, the spectral index of each SPE plays a pivotal role in its ultimate impact of the surface of Mars. Figures 4-8 through 4-11 present the difference in fluences at the Martian surface for different radiation types at different spectral indexes. In accordance with Equations 4-2, three spectral indexes were compared: 1.3, (solid line in Figure 4-8) 3.2 (stars), and 4.3 (diamonds). These indexes represent the range of SPE spectra observed at Earth between January 1999 and December 2006.

As anticipated, the fluence at the surface of Mars varies substantially between hard and soft input spectra. A hard spectrum produces a surface fluence of about two orders of magnitude greater than a soft spectrum for protons, electrons, and photons. The difference is approximately three orders of magnitude for neutrons. During SPE's with softer spectra, there is a precipitous drop in photon fluence at approximately 10 MeV. This does not occur for harder spectra, which demonstrate a more gradual decline in photon fluence.

The biological consequences of these spectral differences will be addressed in Chapter 5 but are presented here simply to demonstrate some of the features of the surface particle spectra.

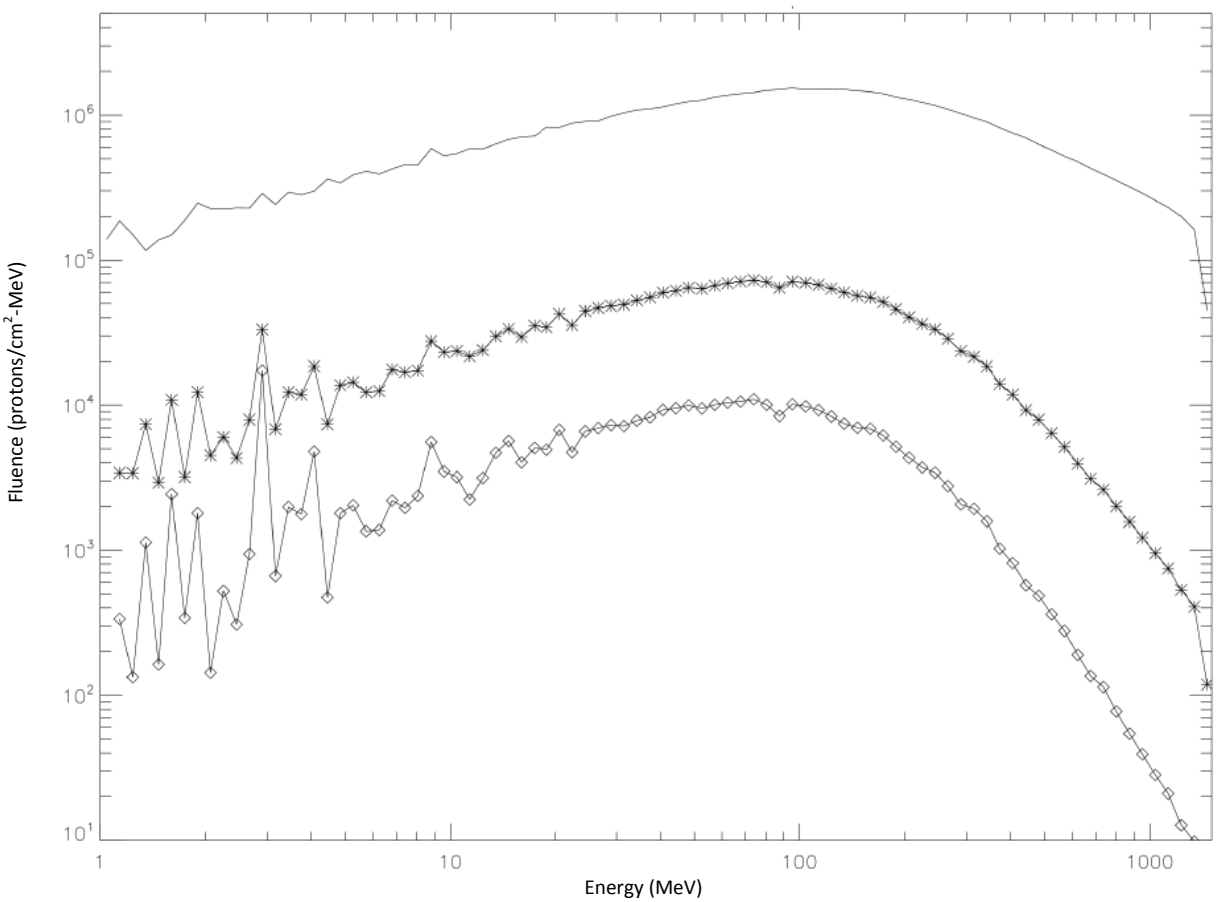

Figure 4-8. Proton fluence on Mars at various spectral indexes. Spectral index of 1.3 (solid line), 3.2 (stars), and 4.3 (diamonds) are presented. Fluences are based on an incident SEP with flux of 3.0×10^7 protons/cm^2-sr.

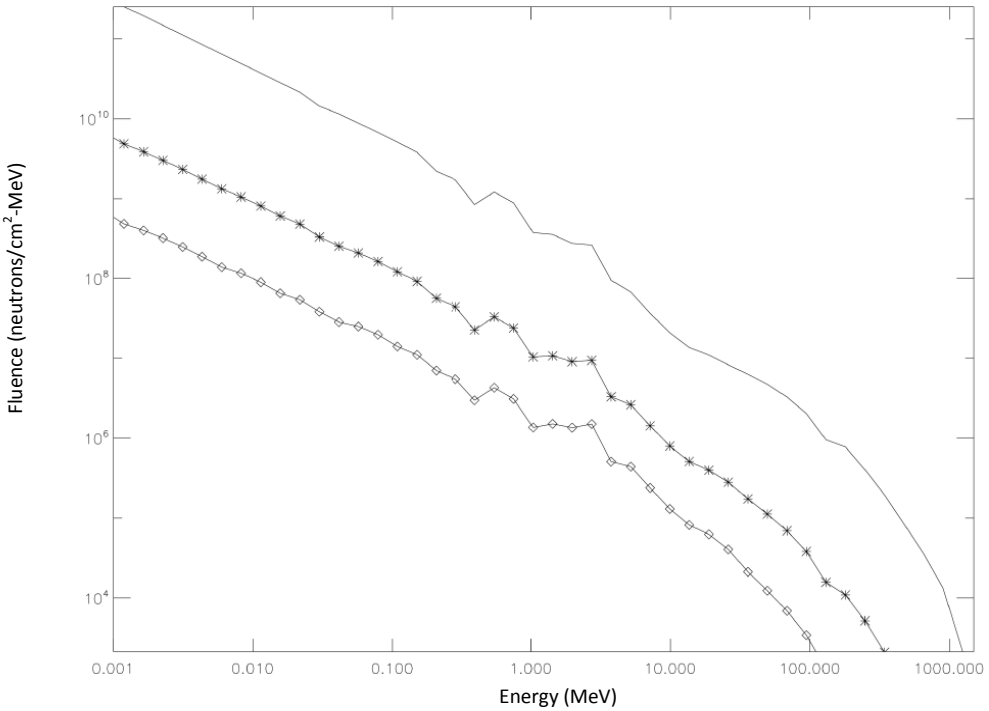

Figure 4-9. Neutron fluence on Mars at various spectral indices. Spectral index of 1.3 (solid line), 3.2 (stars), and 4.3 (diamonds) are presented. Fluences are based on incident SEP with flux of 3.0×10^7 protons/cm^2-sr.

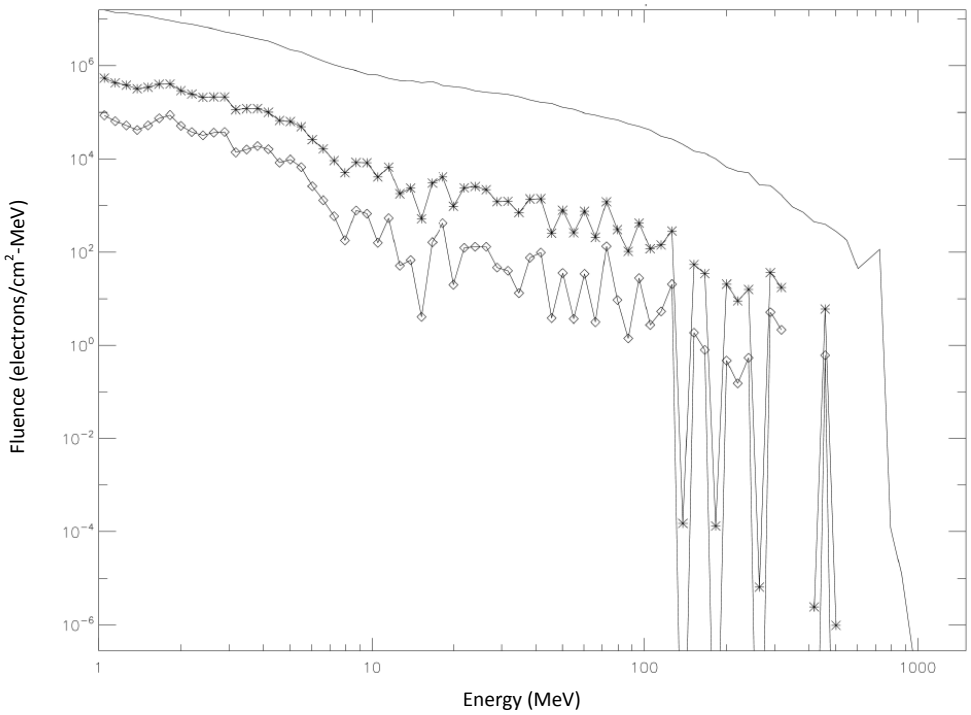

Figure 4-10. Electron fluence on Mars at various spectral indexes. Spectral index of 1.3 (solid line), 3.2 (stars), and 4.3 (diamonds) are presented. Fluences are based on an incident SEP with flux of 3.0×10^7 protons/cm^2-sr.

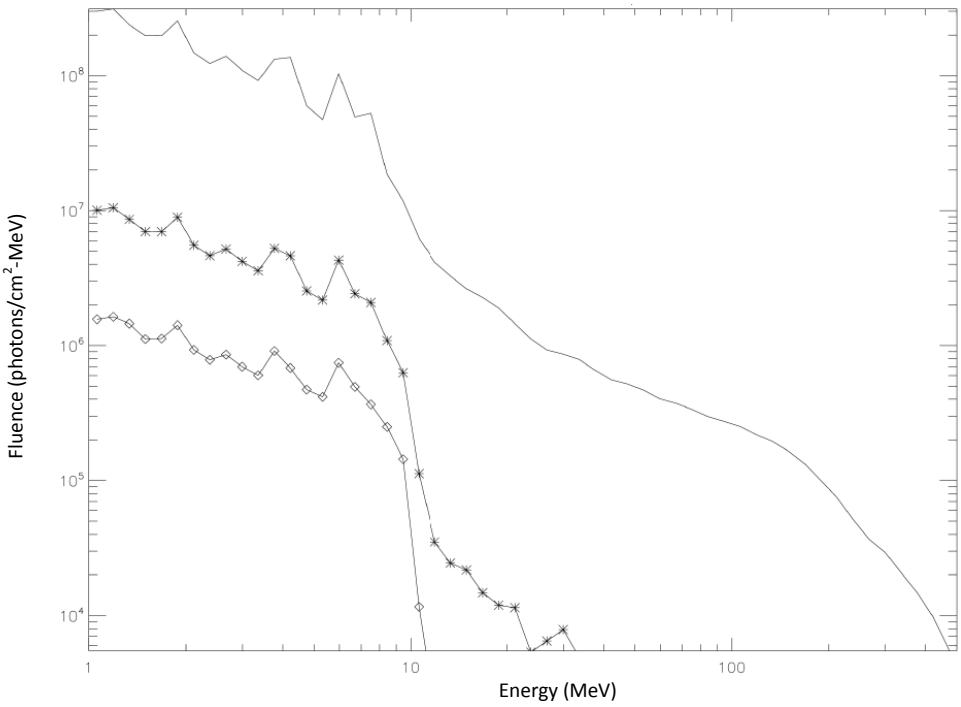

Figure 4-11. Photon fluence on Mars at various spectral indexes. Spectral index of 1.3 (solid line), 3.2 (stars), and 4.3 (diamonds) are presented. Fluences are based on an incident SEP with flux of 3.0×10^7 protons/cm^2-sr.

4.4.3 Analysis of Front- and Back-Scattered Spectra

Nuclear interactions of energetic particles with the Martian atmosphere and regolith create a potential for exposure to both forward- and back-scattered radiation at the Martian surface. The presence of back-scattered radiation increases the potential radiation dose to a human explorer but also suggests potential strategies to mitigate the radiation dose through properly-placed shielding. Figures 4-12 through 4-15 compare the forward- and back-scattered fluences of protons, neutrons, electrons, and photons for an SPE arriving at Mars with a spectral index of 3.2 and a fluence of 3.0×10^7 protons/cm^2-sr for protons with energies greater than 25 MeV.

Of the forms of radiation examined in this study, only protons do not have a significant fluence from back-scattered particles. At energies below 10 MeV, the fluence of forward-scattered protons is approximately one order of magnitude greater than back-scattered protons. The difference increases to 2-3 orders of magnitude for energies greater than 10 MeV.

Surface fluences of back-scattered photons and electrons are within an order of magnitude of forward-scattered photons and electrons, respectively. Below approximately 5 MeV, back-scattered neutrons have a slightly greater fluence than forward-scattered neutrons. Even above 5 MeV, back-scattered neutrons remain within an order of magnitude of the forward-scattered fluence.

These results are in agreement with those of similar studies conducted by Clowdsley et al (2000) and Gurtner et al (2005). The Clowdley study used HZETRN to examine neutron fluence on the Martian surface, and the Gurtner study used Geant4 to examine the fluences of multiple particles. Figures 4-16 and 4-17 present their results.

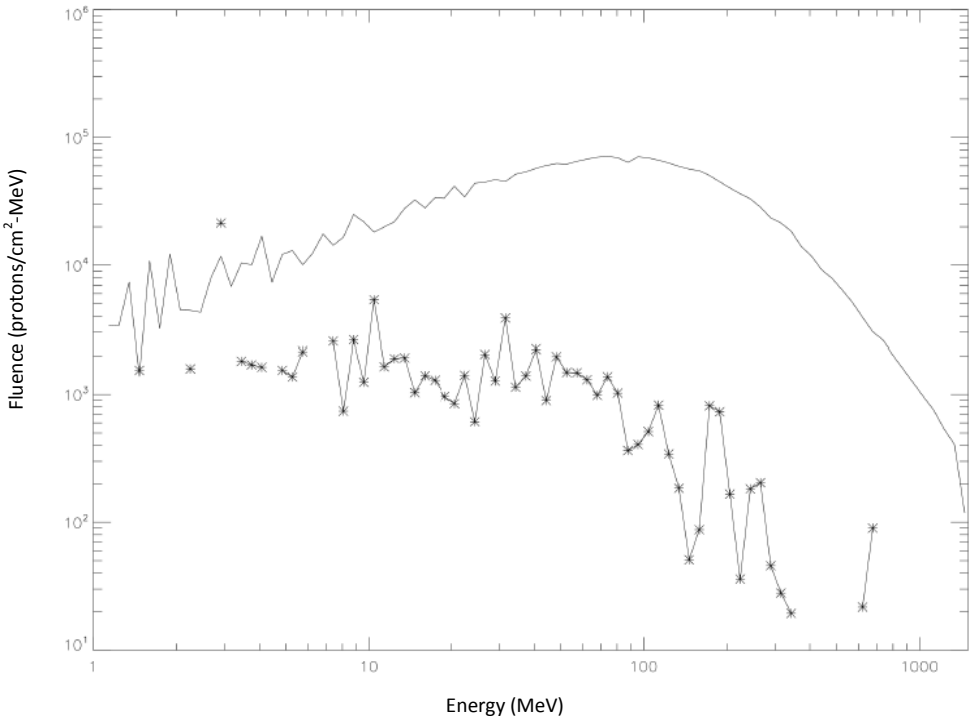

Figure 4-12. Forward-scattered (solid line) and back-scattered (stars) proton fluence on Mars. Fluences are based on an incident SEP with flux of 3.0×10^7 protons/cm^2-sr.

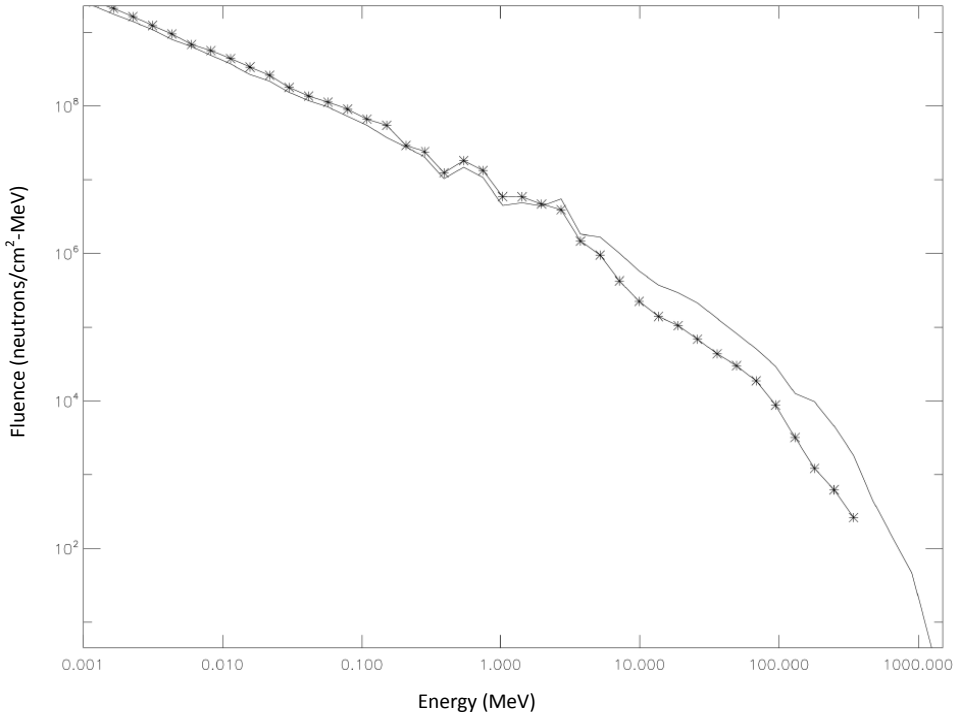

Figure 4-13. Forward-scattered (solid line) and back-scattered (stars) neutron fluence on Mars. Fluences are based on an incident SEP with flux of 3.0×10^7 protons/cm^2-sr.

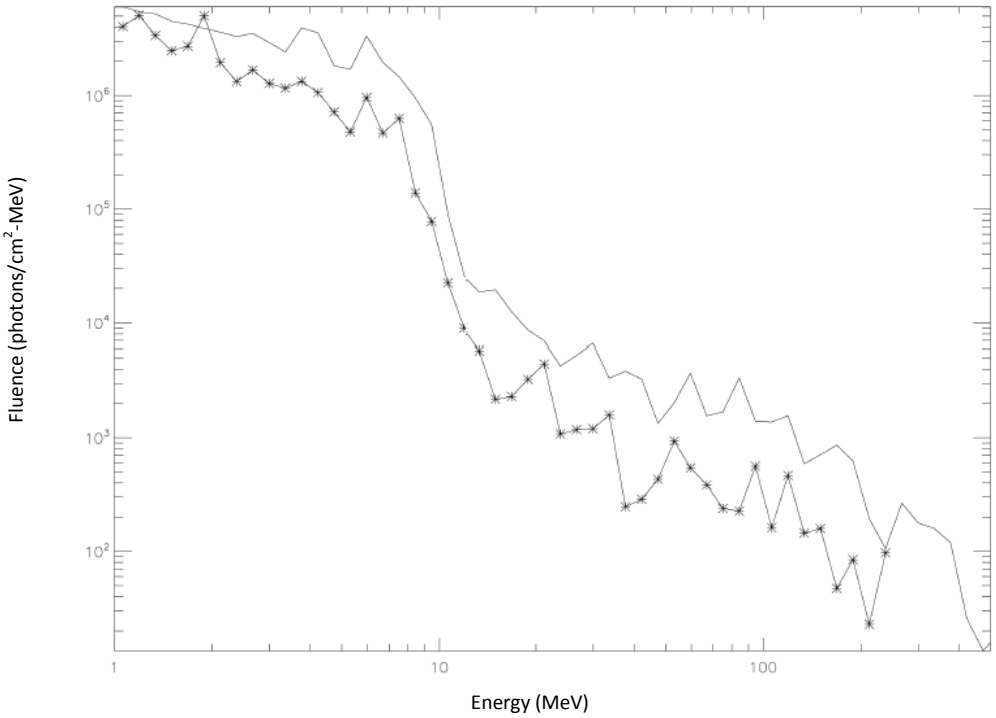

Figure 4-14. Forward-scattered (solid line) and back-scattered (stars) photon fluence on Mars. Fluences are based on an incident SEP with flux of 3.0×10^7 protons/cm^2-sr.

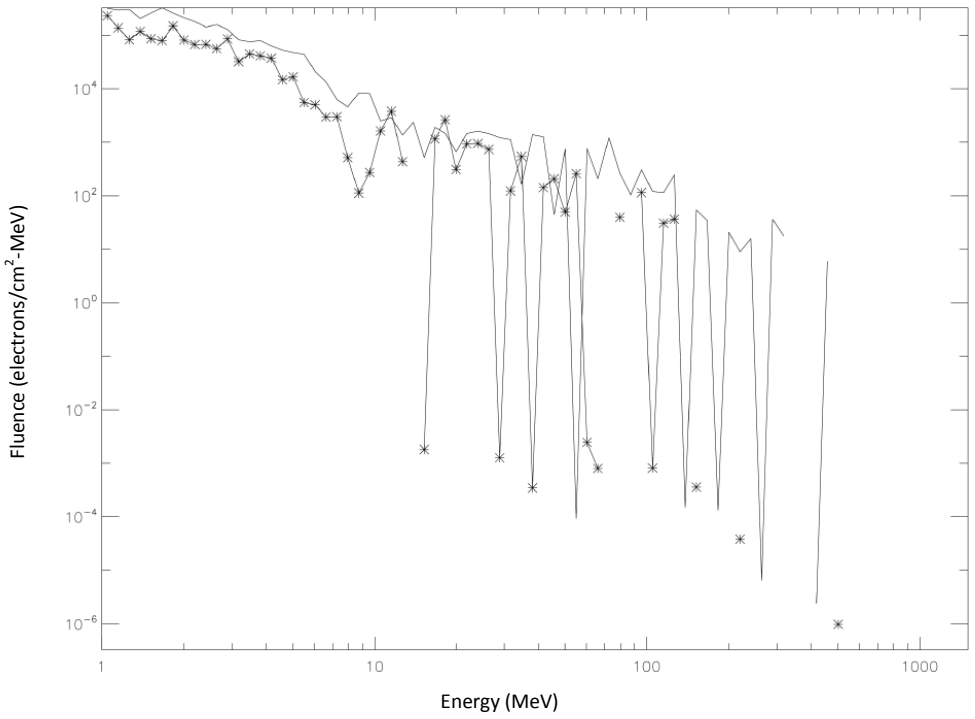

Figure 4-15. Forward-scattered (solid line) and ack-scattered (stars) electron fluence on Mars. Fluences are based on an incident SEP with flux of 3.0×10^7 protons/cm^2-sr.

Clowdsley et al (2000) used the spectrum from the SPE observed on February 23, 1956 to assess the neutron fluence on the surface of Mars. It was found that the back-scattered component of the neutron fluence was comparable to that of the forward-scattered component. Moreover, the overall shape of the neutron spectrum from the Clowdsley study is similar to that found in this report, including a plateau in neutron fluence near 1 MeV with a subsequent rapid drop-off. The Clowdsley study also compared the neutron environment caused by an SPE to that caused by the nominal Galactic Cosmic Radiation (GCR). The Badhwar-O'Neill model (Badhwar et al. 1994) for the GCR spectrum was used. These results are overlayed in Figure 4-16 and provide an interesting comparison.

Gurtner et al (2005) similarly examined the relative impact of SPE's and GCR on the surface radiation environment of Mars, but they also included analyses of protons, electrons, and photons. The sample SPE used in the Gurtner study was that of the September 29, 1989 event. They used direct GCR measurements from the MARIE instrument onboard the Mars Odyssey satellite for their model environment. As with this report and the Clowdsley study, the Gurtner study concluded that back-scattered neutrons provide a substantial fluence to the surface of Mars. Overall trends in protons, neutrons, photons were similar to those found in this report. However, there are significant discrepancies in the high-energy electron environment. Above 10 MeV, the electron fluence modeled in this report demonstrates strong fluctuations of several orders of magnitude. The electron environment modeled by the Gurtner study showed no such fluctuations but rather a smooth decline in fluence with increasing energy. While the

cause of these differences ought to be examined, it likely has little impact on the radiation risk to humans on the Martian surface because the total fluences are quite low.

4.5 Conclusion

The use of PHITS to model the radiation environment on the surface of Mars demonstrates similar results to other studies with the same purpose. It is clear that the high energy environment (> 100 MeV) is dominated by primary protons that have fully penetrated the Martian atmosphere. However, there is a significant contribution of lower energy neutrons that may also pose a significant radiation risk to human explorers. Of particular note is the presence of a substantial population of neutrons that are back-scattered from the Martian surface.

The true importance of these fluences is presented in Chapter 5 when dose estimates are calculated. Regardless of the quality of the PHITS code and Mars model, there is a substantial uncertainty caused by the lack of spectral information at Mars. Order of magnitude differences exist between the fluences for all particles determined from different SPE spectral indexes. Use of an average spectral index limits some uncertainty in results over several events, but analysis of specific SPE's is not likely to produce valid results other than to provide a range of potential fluences.

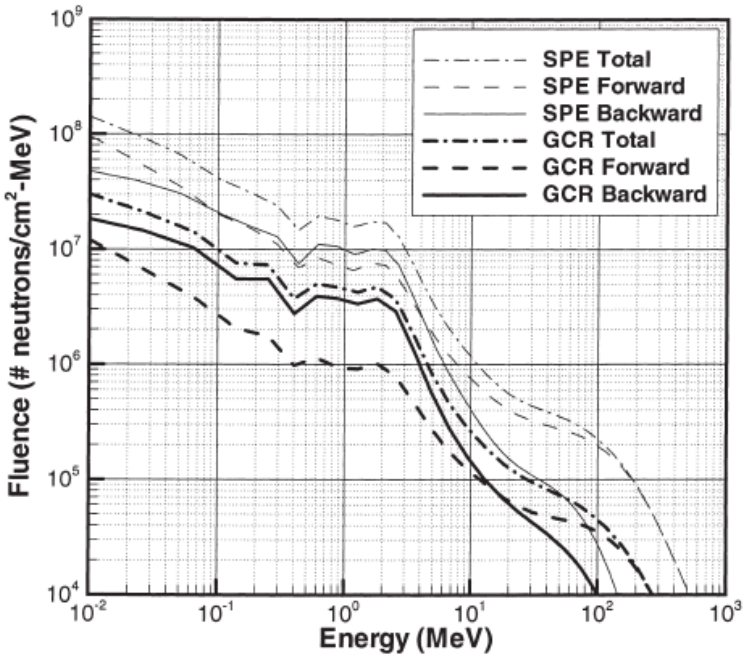

Figure 4-16. The neutron environment on Mars, based on an HZETRN simulation, using the Badhwar-O'Neill model for GCR fluence and the spectrum of the February 23, 1956 SPE. (Figure and parts of caption from Clowdsley et al. (2000))

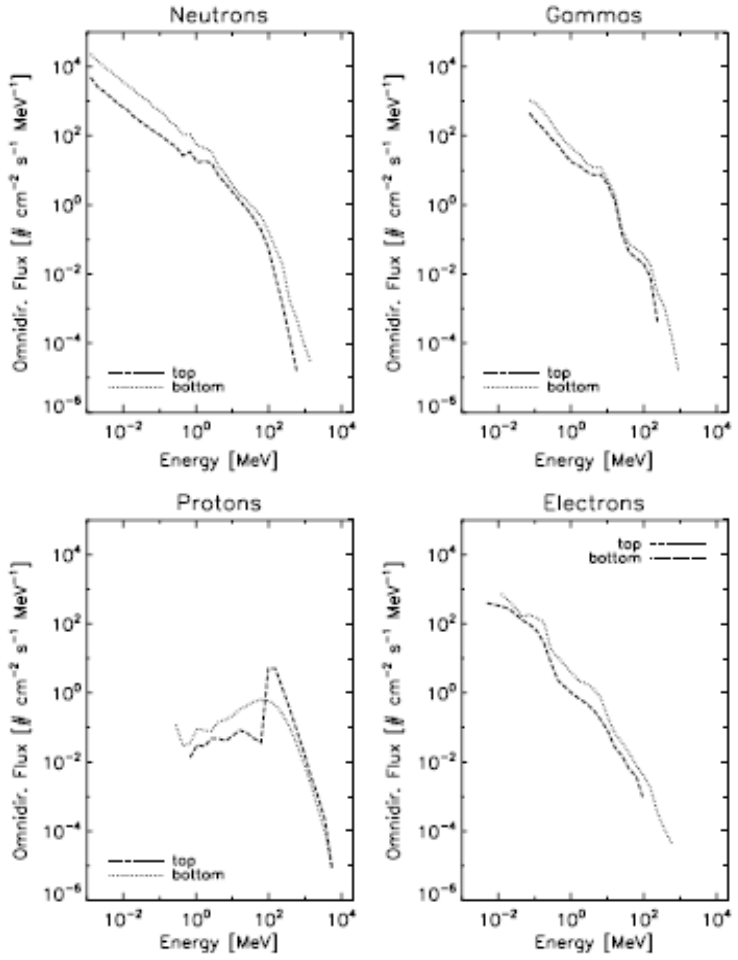

Figure 4-17. Computed omnidirectional radiation flux at the top of the Martian atmosphere and at surface level, assuming the proton spectrum of the 09/29/1989 solar particle event. (Figure and Caption from Gurtner et al (2005))

Acknowledgments

The following individuals provided vital information, data, and advising toward the completion of this chapter:

Dr. Sukesh Aghara, Texas A&M University, Prairie View

Dr. Stephen Blattnig, NASA Langley Research Center

Dr. Thomas Budinger, Lawrence Berkeley National Laboratory

Dr. Lawrence Heilbronn, University of Tennessee

Dr. Koji Niita, RIST, Japan

Dr. Roger Thelwell, James Madison University

Special thanks to the Department of Mathematics at James Madison University for their generous support of this project and for providing access to their 24-core processing cluster, which was essential to carry out the data analysis presented in this chapter. The computing resources were funded by NSF grant DMS – 0821309.

References

Badhwar G.D. and P.M. O'Neill, "Long-Term Modulation of Galactic Cosmic Radiation and its Model for Space Exploration", *Adv. Space Res.,* Vol. 14, No. 10, 1994.

M.S. Clowdsley et al, "Neutron Environments on the Martian Surface", *Physica Media*, 17, 2001.

M. Gurtner et al. "Simulation of the Interaction of Space Radiation with the Martian Atmosphere and Surface", *Advances in Space Research,* 36, 2176-2181, 2005.

http://phits.jaea.go.jp/expacs/

http://phits.jaea.go.jp/Overview.html

http://marsprogram.jpl.nasa.gov/MPF/science/apxs_elemental.html

T. Sato and K. Niita, "Analytical Functions of Predict Cosmic-Ray Neutron Spectra in the Atomsphere," *Radiation Research*, 166, 544. 2006.

T. Sato et al. "Development of PARMA: PHITS-based analytical radiation model in the atmosphere," *Radiation Research*, 170, 244-259, 2008.

K. Niita. *Personal Correspondence.* 2009

K. Niita. "Nuclear Reaction Models in Particle and Heavy Ion Transport code System PHITS", *1st Workshop on Accelerator Radiation Induced Activation*, Paul Scherrer Institut, Switzerland, October 13-17, 2008.

T. Sato and K. Niita, "Analytical Functions of Predict Cosmic-Ray Neutron Spectra in the Atomsphere," *Radiation Research*, 166, 544. 2006.

T. Sato et al. "Development of PARMA: PHITS-based analytical radiation model in the atmosphere," *Radiation Research*, 170, 244-259, 2008.

Chapter 5
Radiation Dose on the Martian Surface from Solar Particle Events

Abstract

Using fluence information from Chapter 4, this chapter describes the expected effective radiation dose from solar particle events (SPE's) to a human explorer on the surface of Mars. Assuming an average spectrum for all SPE's arriving at Mars, the following results were determined:

- The annual dose from SPE's on Mars range from 0.7 Sv at solar maximum to 0.0 Sv near solar minimum (no SPE's were detected near solar minimum).
- The dose from the largest single event (September 24, 2001) was approximately 0.49 Sv, which is high enough to cause deleterious physiological effects.
- Protons dominate the dose delivered to human explorers on the surface of Mars, contributing approximately 91% of the overall dose. Neutrons contribute nearly the entire remaining dose. Electrons and gamma rays contribute a negligible dose.
- Approximately 19% of the proton dose is due to primary protons of energies greater than about 200 MeV that penetrate the full depth of the Martian atmosphere.
- A slightly harder-than-average spectrum can result in a dose of several Sieverts, which is potentially lethal.

Data from the literature demonstrate the annual GCR dose on the Martian surface ranges from 0.15 Sv during solar maximum to 0.32 Sv during solar minimum. NASA career dose limits for astronauts range from 1.0 Sv to 4.0 Sv, depending on gender and the age at the time of first radiation exposure.

These results suggest that SPE's pose a serious threat to human explorers on Mars. Proper shielding, careful selection of the surface location, and appropriate timing of human mission to Mars can mitigate some of the anticipated radiation dose. However, shielding options are limited for activities outside a Mars habitat.

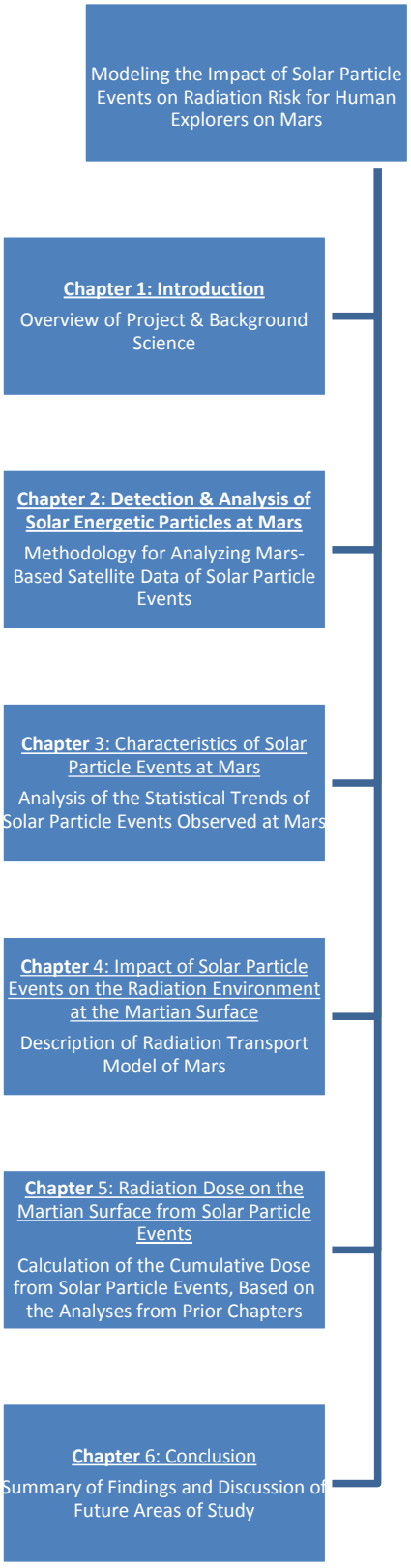

Figure 5-1. Progression of information from this project by chapter.

5.1 Introduction

Fluence estimates presented in Chapter 4 provide an opportunity to assess the radiation dose delivered to humans on the surface of Mars. While other studies have examined the impact of specific solar particle events (SPE's) on the Martian surface, this is the first time Mars-based data are used to determine the cumulative dose from multiple SPE's. As a result, a true comparison can be made to annual dose estimates from galactic cosmic radiation (GCR) on Mars, as well as Earth-based metrics for radiation dose.

As with Chapter 4, this chapter does not intend to predict future doses on the Martian surface. Rather, it examines data from 1999 – 2006 to determine what the dose would have been had a human been present. It is also important to note that there is a critical absence of spectral data at Mars. As in Chapter 4, this chapter presents information for a range of spectral shapes. The doses at the limits of this range differ by orders of magnitude, which makes it difficult to assess the real impact of any specific SPE. To address this shortcoming, an average spectral shape is employed, which provides a best estimate of the dose delivered to a human on Mars over several SPE's. For the purposes of this study, annual doses were calculated for each year of SPE observations at Mars.

In any study that presents dose calculations, the choice of radiation weighting factors plays a significant role in the final result. Weighting factors are constant scaling values that are applied to dose calculations to account for the relative biological harm of different types of radiation. Unfortunately, some of these weighting factors vary over time and between research organizations. For example, the Nation Council on Radiation Protection and Measurements (NCRP) states a weighting factor of 2 for high-energy protons. In contrast, the International Commission on Radiation Protections (ICRP) uses a weighting factor of 5. Weighting factors for neutrons are binned within different energy ranges and have changed multiple times over the last three decades. The selection of weighting factors is somewhat arbitrary, but the quality factors used in this study were chosen to match the most current values determined by NCRP.

Four radiation types were examined in this study: protons, neutrons, electrons, and photons. For each type of radiation, the effective dose was determined. The fundamental physical processes for determining energy deposition in matter were considered for each radiation type. For proton equivalent dose calculation purposes, energy deposition was determined with the Bethe-Bloch Equation, and weighting factors found in the literature were used. Equivalent doses for neutrons, electrons, and photons were determined by comparison to experimental data and weighting factors found in the literature. While comparisons to experimental data formed the bases of dose calculations for these radiation types, the physical properties of energy deposition were considered and are presented in this report.

Typical dose estimates on Earth and in space were compared to estimates of Mars surface dose, as well as GCR estimates on the surface of Mars. These estimates provide a basis for comparison with the SPE dose estimates determined in this study. Dose estimates were also compared with NASA's established career dose limits for human space explorers.

Radiation mitigation strategies are also considered here for a variety of mission scenarios, including the timing of the mission relative to solar cycle, surface locations on Mars, and shielding both inside and outside of a habitat.

5.2 Fundamental Units and Terminology in Radiation Biology

The basic measurement of radiation interaction in matter for biological purposes is the absorbed dose, which is commonly given in SI units of Gray (Gy).

$$1\ \text{Gy} = 1\ \text{Joule/kilogram} \qquad \text{(Equation 5-1)}$$

Different types of radiation impart different amounts of energy to a target material even if radiation types possess the same kinetic energy. For example, a 1 MeV proton deposits significantly more energy to an absorbing material than a 1 MeV electron. The difference is primarily due to the different linear energy transfers (LET) for each particle. A particle's LET is the amount of energy locally imparted to a material per unit path length through the material.

$$\text{LET} = -dE/dx \qquad \text{(Equation 5-2)}$$

The exact determination of LET depends on the nature of interactions between the incident radiation and the absorbing material. These interactions are related to both the type of incident radiation and its energy. Given an LET and fluence of particles, the absorbed dose in water can be calculated as follows (Alpen 1998):

$$D(E) = 0.16\ L(E)\ \Phi(E) \qquad \text{(Equation 5-3)}$$

D(E) is the absorbed dose in units of Gy, L(E) is the LET of the incident particles in units of keV/μm, Φ(E) is the fluence of particles in units of particles/ μm^2, and E is the energy, in MeV, of the particles in question. In this report, the target material for radiation interaction is water (ρ = 1.0 g/cm3), which is a common proxy for human tissue.

While absorbed dose is an important quantity, it does not fully describe the degree of radiation damage to a target material. The mechanism for deposition of energy in a target material influences its degree of radiation damage. However, it is difficult to quantify these differences between impacts of various radiation types and energies. So, a radiation weighting factor is often applied to the absorbed dose, which results in a quantity called "equivalent dose". While the radiation weighting factor is a unitless multiplier, the absorbed dose unit of Gray is changed to the equivalent dose unit of Sievert (Sv) – an older unit is the rem (1 rem = 0.01 Sv).

$$H(E) = w_R\ D(E) \qquad \text{(Equation 5-4)}$$

H is the equivalent dose, w_R is the radiation weighting factor, and D(E) is the absorbed dose for a specific radiation type at a given energy, E. Depending on the radiation type, the radiation weighting factor may also be dependent on energy – as is the case with neutrons. The total equivalent dose is determined by summing H over all energies and radiation types.

Unfortunately, the radiation weighting factors assigned to different radiation types and energies have varied over time. Moreover, different studies suggest weighting factors that disagree with one another. In this study, a radiation weighting factor of 1 was used for all gamma rays and photons, which is consistent with both current NCRP and ICRP recommendations. For protons, a radiation weighting factor of 2 was chosen, which corresponds to the current NCRP recommendation – though ICRP recommends a factor of 5 (Turner 2007). Recommended radiation weighting factors (ICRP and NCRP) for neutrons are dependent on energy. These factors are presented in Table 5-1.

Neutron Energy Range	$\mathbf{w_R}$
< 10 keV	5
10 keV < E < 100 keV	10
100 keV < E < 2 MeV	20
2 MeV < E < 20 MeV	10
> 20 MeV	5

Table 5-1. NCRP and ICRP recommended radiation weighting factors for neutrons at various energy ranges. (NCRP Report No. 116)

Different bodily tissues and organs respond to radiation damage in different ways. Thus, an additional tissue weighting factor is often applied to the equivalent dose to account for the various levels of response. The term “effective dose” is used to describe the quantity determined when a tissue weighting factor is applied to the equivalent dose. Like other quantities that attempt to quantify radiation damage, effective dose is commonly described in units of Sieverts.

$$Ef = \Sigma w_T H_T \qquad \text{(Equation 5-5)}$$

Ef is the effective dose, w_T is the tissue weighting factor, and H_T is the equivalent dose delivered to a specific organ, T. To determine the effective dose, the equivalent dose must be multiplied by the appropriate weighting factor in each tissue. However, this study assumes SPE’s deliver a uniform, whole-body dose to human explorers on the surface of Mars. Under this assumption, all bodily tissues and organs receive the same equivalent dose. This makes the tissue weighting factors irrelevant, because the weighting factor for each organ is equivalent (Turner 2007). Hence, equivalent dose and effective dose are assumed to be numerically equivalent in this study. The term “dose” is used to describe these quantities henceforth.

5.3 Radiation Doses from Solar Particle Events on the Surface of Mars

Particle fluences and energy spectra on the surface of Mars for protons, neutrons, electrons, and photons were determined through the modeling techniques described in Chapter 4. The total annual fluence of each radiation type was determined from 1999 through 2006. Table 5-2 presents the annual fluence of SPE protons reaching Mars.

An average SPE spectral index of 3.2 was used for all events, and a discussion of the impact of modifying the spectral index is presented below. The spectral index is discussed in Chapter 4 and refers to the exponent of the power law function that describes the particle spectrum of an SPE. Various methods were used to determine the LET for each particle type. Once determined, the LET was used in conjunction with Equations 5-3, Equation 5-4, and the aforementioned radiation weighting factors to determine the cumulative radiation dose.

This section presents the methodology and results from radiation dose calculations for each radiation type. A more comprehensive discussion of the biological impact of these doses is provided in Section 5-4, which includes a comparison of SPE doses on the surface of Mars to Earth-based doses and other space missions.

Year	*1999*	*2000*	*2001*	*2002*	*2003*	*2004*	*2005*	*2006*
# Events	3	10	16	14	12	2	9	0
Fluence (cm^{-2})	$2.7x10^5$	$5.9x10^6$	$4.8x10^7$	$1.5x10^7$	$2.7x10^7$	$2.4x10^5$	$5.2x10^6$	0

Table 5-2. Breakdown of annual SPE fluences above ~25 MeV in Mars orbit

5.3.1 Radiation Dose from Protons

Protons contribute the largest portion of the SPE dose on the surface of Mars. The LET (in units of keV/μm) for protons traversing water was calculated using the relativistic form of the Bethe Equation:

$$L = .307\ (Z_t\ \rho/A_t)\ (Z_p^2/\beta^2)\ (\ln(2\ m_e\ \beta^2/(I\ (1. - \beta^2))) - \beta^2) \qquad \text{(Equation 5-6)}$$

Z_t – Atomic Number of the Target Material: 10
A_t – Mass Number of the Target Material: 18
ρ – Target Material Density: 1 g/cm^3
Z_p – Atomic Number of Incident Particle: 1
β – (particle velocity)/(speed of light)
m_e – Electron Mass: .511 MeV
I – Mean Excitation Potential: $74.9x10^{-6}$ MeV

Using a radiation weighting factor of 2.0 and assuming a uniform, whole-body radiation field, the annual dose from SPE's was calculated. These annual doses are presented in Table 5-3. The peak annual dose is 0.70 Sv, which occurred in 2001 – near solar maximum. Once again, it is important to note that the dose estimates established in this study are strongly dependent on the use of an average spectral index to characterize the incident SPE.

Even slight changes in the spectral index for a large event can dramatically affect the overall dose. This is particularly important for large events where the spectrum is harder than average. In these cases, the single event dose can reach several Sieverts. For example, the largest event observed at Mars took place on September 24, 2001. Assuming the average spectral index of 3.2, the surface dose is approximately 0.42 Sv. With a spectral index of 2.7, the dose would be approximately 3.4 Sv – a potentially lethal dose. Of course, a softer spectrum would render the same SPE relatively harmless. Over the course of several events, the use of an average spectrum provides a reasonable estimate for the cumulative dose from SPE's on the surface of Mars. However, there remains a significant chance that a single SPE can deliver a lethal dose. During solar minimum, it is possible (as in 2006) that no SPE's are observed and there is no corresponding dose on the surface of Mars.

Year	*1999*	*2000*	*2001*	*2002*	*2003*	*2004*	*2005*	*2006*
Proton Dose (Sv)	0.004	0.086	0.70	0.22	0.40	0.0035	0.075	0

Table 5-3. Proton annual effective dose (Sv) on the surface of Mars from SPE's.

For shielding purposes, it is important to assess the dose delivered by different segments of the particle spectrum. Figure 5-2 presents the proton dose delivered versus proton energy, using three incident SPE proton spectra. Regardless of the shape of the spectrum, protons with energies greater than approximately 200 MeV are able to penetrate directly through the Martian atmosphere. These primary protons contribute approximately 19% of the total surface radiation dose. Approximately 50% of the dose is delivered by protons with energies less than 80 MeV.

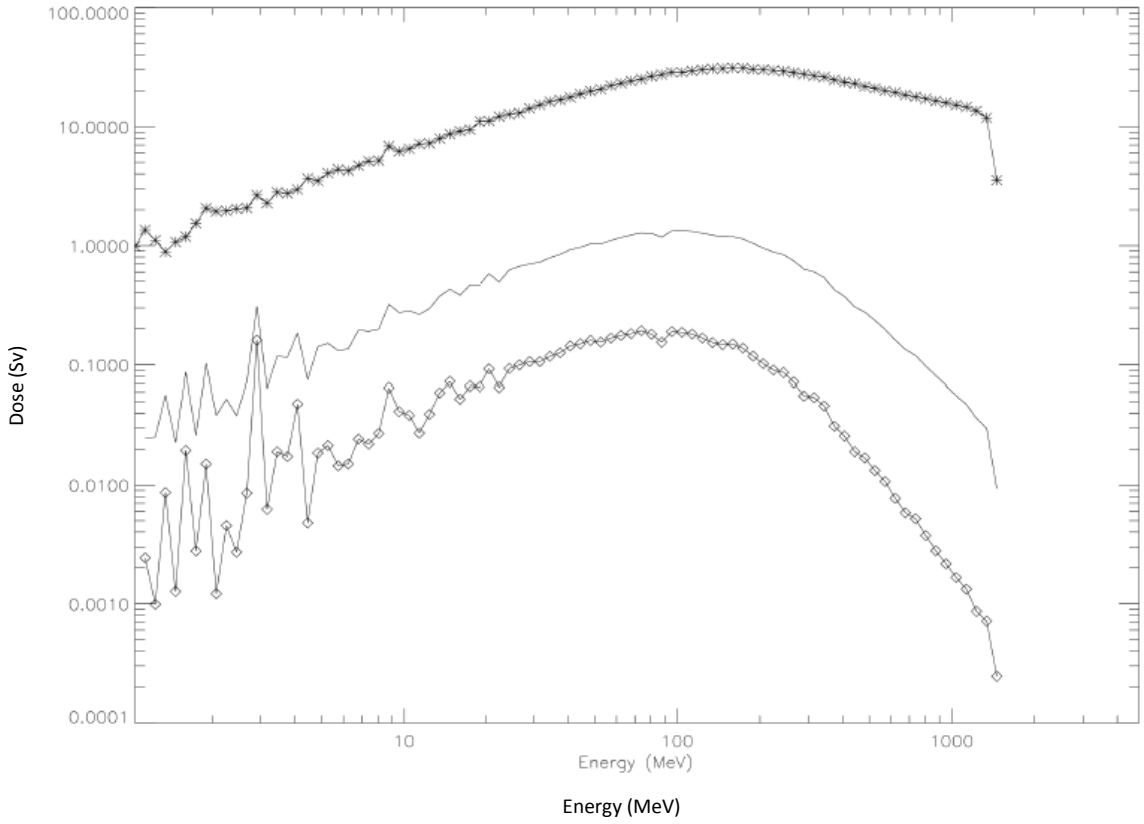

Figure 5-2. Proton annual effective dose (Sv) on the surface of Mars versus proton energy (MeV) at three incident SPE spectral indexes: 1.3 (stars), 3.2 (solid), 4.3 (diamonds).

5.3.2 Radiation Dose from Neutrons

NCRP (1971) reported experimental neutron dose measurements, using a 30-cm phantom target. In this study, the neutron flux density required to deposit 1 mSv in the 30-cm target over a 40 hour period was measured. These data make it possible to extrapolate the effective doses for energies ranging from 1 eV to 400 MeV. Table 5-4 presents the data from this study.

In order to derive a useful quantity from the data presented in Table 5-4, five steps were followed for each energy value:

1. Convert neutron flux to fluence by multiplying flux by 40 hours (144000 seconds).
2. Create a “dose per fluence” value by dividing 1 mSv by the measured neutron fluence.
3. Factor out the obsolete quality factors by dividing the “dose per fluence” by those factors.
4. Multiply the resulting value by the modern radiation weighting factors.
5. Multiply the revised “dose per fluence” by the modeled fluence of neutrons on the Martian surface.

This process allows one to determine the dose from neutrons, using the most current radiation weighting factors. For reference, Table 5-1 presents the radiation weighting factors used in this study. Using the process described above, it is determined that the large event on September 24, 2001 would result in a neutron dose of approximately 0.07 Sv – assuming an average incident SPE spectrum. While this is a much lower dose than that received from protons, it is biologically significant. As with the proton dose, a slightly harder incident SPE spectrum results in a much greater dose. A spectral index of 2.7 would result in a neutron dose of approximately 0.65 Sv.

Neutron Energy	$\overline{QF}$	Neutron Flux Density
MeV		$cm^{-2}\ s^{-1}$
2.5×10^{-8} (thermal)	2	680
1×10^{-7}	2	680
1×10^{-6}	2	560
1×10^{-5}	2	560
1×10^{-4}	2	580
1×10^{-3}	2	680
1×10^{-2}	2.5	700
1×10^{-1}	7.5	115
5×10^{-1}	11	27
1	11	19
2.5	9	20
5	8	16
7	7	17
10	6.5	17
14	7.5	12
20	8	11
40	7	10
60	5.5	11
1×10^{2}	4	14
2×10^{2}	3.5	13
3×10^{2}	3.5	11
4×10^{2}	3.5	10

Table 5-4. Mean quality Factor, QF, and values of neutron flux density which, in a period of 40 hours, results in a maximum dose equivalent of 40 hours. QF represents the maximum average quality factor for neutrons passing through the phantom. (NCRP 1971)

Year	*1999*	*2000*	*2001*	*2002*	*2003*	*2004*	*2005*	*2006*
Neutron Dose (Sv)	0.00039	0.0086	0.070	0.022	0.040	0.00035	0.0075	0

Table 5-5. Neutron annual effective dose (Sv) on the surface of Mars from SPE's.

The annual dose from neutrons created by SPE's is presented in Table 5-5. In general, the neutron dose is a tenth of the proton dose in each year with a peak of 0.07 Sv at solar maximum. An interesting note regarding the neutron dose is that half of the surface fluence

(and correspondingly half the dose) is the result of back-scattered particles from the Martian surface. By preventing the forward-scattered and primary particles from reaching the surface, it is likely possible to significantly reduce exposure to back-scattered neutrons.

5.3.3 Radiation Dose from Electrons and Gamma Rays

As might be expected, the contribution of electrons and gamma rays to the overall dose on the Martian surface is negligible. A radiation weighting factor of 1.0 is used for electrons and gamma rays. The LET (-dE/dx) of electrons in water was determined by summing the radiative and collisional stopping powers. This is summarized in Table 5-6 for energy ranges relevant to this study. For energies not listed in Table 5-6, linear interpolation was used to estimate the LET at intermediate energies. Equations 5-3 and 5-4 are used to calculate a dose based on the LET values presented in Table 5-9.

The dose imparted by gamma rays is dependent on the mass energy-absorption coefficient (μ_{en}/ρ) and the energy flux density, ψ, using on Equation 5-7. Table 5-7 presents μ_{en}/ρ for various energies of relevance.

$$D(E) = \psi(E)\, \mu_{en}/\rho \qquad \text{(Equation 5-7)}$$

Mass energy-absorption coefficients at energies between those listed in Table 5-7 were estimated through linear interpolation. The mass energy-absorptions coefficients at energies greater than 100 MeV were estimated as the 100 MeV value. Table 5-8 presents the annual doses from SPE-induced electrons and gamma rays on the surface of Mars. The doses for these radiation types are similar. For example the peak dose is 0.64 mSv and 0.67 mSv for electrons and gamma rays, respectively. These doses are not biologically significant. Even with the largest event in the data set with an extremely hard spectrum (spectral index of 1.3), the total dose from electrons and gamma rays only reaches 0.04 Sv.

Energy (MeV)	$-dE_{col}/dx$ (keV/µm)	$-dE_{rad}/dx$ (keV/ µm)	$-dE_{total}/dx$ (keV/ µm)
1	0.187	0.0017	0.189
4	0.191	0.0065	0.198
7	0.193	0.0084	0.202
10	0.200	0.0183	0.218
100	0.220	0.240	0.460
1000	0.240	2.63	2.87

Table 5-6. LET (-dE/dx) of electrons in water due to collisional, radiative, and total energy absorption. (Turner 2007)

Energy (MeV)	1	10	100
μ_{en}/ρ (cm^2/g)	0.0310	0.0157	0.0122

Table 5-7. Mass Energy-Absorption Coefficients (μ_{en}/ρ) for photons in water at various energies. (Turner 2007)

Year	*1999*	*2000*	*2001*	*2002*	*2003*	*2004*	*2005*	*2006*
Electron Dose (Sv)	$3.6x10^{-6}$	$7.8x10^{-5}$	$6.4x10^{-4}$	$2.0x10^{-4}$	$3.6x10^{-4}$	$3.2x10^{-6}$	$6.8x10^{-5}$	0
Gamma Ray Dose (Sv)	$3.8x10^{-6}$	$8.2x10^{-5}$	$6.7x10^{-4}$	$2.1x10^{-4}$	$3.8x10^{-4}$	$3.4x10^{-6}$	$7.1x10^{-5}$	0

Table 5-8. Electron and gamma ray annual effective dose (Sv) on the surface of Mars from SPE's.

5.3.4 Total Dose on the Surface of Mars from SPE-Induced Primary and Secondary Radiation

It is straightforward to determine the total surface radiation dose from SPE's by summing the surface doses of each radiation type. Clearly, the proton dose dominates the overall radiation impact on the Martian surface. The overall annual dose near solar maximum is approximately 0.77 Sv, which accounts for the total proton and neutron doses on the Martian surface. Total annual dose estimates for each year of observations at Mars are provided in Table 5-9.

Year	*1999*	*2000*	*2001*	*2002*	*2003*	*2004*	*2005*	*2006*
Total Dose (Sv)	0.0044	0.095	0.77	0.242	0.44	0.0039	0.083	0

Table 5-9. Total annual effective dose (Sv) on the surface of Mars from SPE's.

For the large SPE on September 24, 2001, the total dose is approximately 0.49 Sv – assuming an average SPE spectral index of 3.2. With a slightly harder spectrum of 2.7, this total dose increases to approximately 4.1 Sv.

5.4 Typical Radiation Doses and Dose Limits

The effects of radiation on humans depend on the absorbed dose and duration of exposure. Acute effects from doses in the range of a few Sieverts include vomiting, hair loss, bleeding ulcers, and death within a few weeks or months. Late effects from non-lethal doses, such as cataracts and cancer, are observed over time as an increased likelihood of occurrence relative to the general population. Due to the very small sample size of human space explorers, it is difficult to assess the risk of long-term effects from space radiation. Thus, estimates of long-term radiation risk for human space explorers should be taken skeptically, though they do provide useful metrics to understand the relative significance of different levels of radiation exposure.

Table 5-10 presents the anticipated acute and late effects of whole-body irradiation at various effective doses. In general, acute effects from radiation begin at about 0.5 Sv, and risk of death begins at a few Sieverts. The National Research Council's Committee on Biological Effects of Ionizing Radiation (BEIR) has produced general guidelines for late-term radiation risk. The BEIR V Report (1990) suggests that a continuous lifetime exposure of 10 mSv/year during adulthood results in about 3,000 excess fatal cancers per 100,000 people. Letaw (1997) used the BEIR V data to estimate a 2% - 5% increase in the chance of cancer fatality for each 0.5 Sv received by a human space explorer. ICRP presents similar results, with an estimate of a 4% excess risk of cancer fatality per 0.5 Sv of high dose, high dose rate radiation (Hall and Giaccia 2006).

Radiation effects		
Chronic dose	Risk	
~0.4 Sv	First evidence of increased cancer risk as late effect from protracted radiation	
2–4 Sv/year	Chronic radiation syndrome with complex clinical symptoms	
Acute Single Dose	Effect	Outcome
~0.2 Sv	First evidence of increased cancer risk as late effect	
<0.25 Sv	No obvious direct clinical effects	
>0.5 Sv	Nausea, vomiting	No early death anticipated
(>0.7) 3–5 Sv	*Bone marrow syndrome*: Symptoms include internal bleeding, fatigue, bacterial infections, and fever.	Death rate for this syndrome peaks at 30 days, but continues out to 60 days. Death occurs from sepsis
5–12 Sv	*Gastrointestinal tract syndrome*: Symptoms include nausea, vomiting, diarrhea, dehydration, electrolytic imbalance, loss of digestion ability, bleeding ulcers	Deaths from this syndrome occur between 3 and 10 days post exposure. Death occurs from sepsis
>20 Sv	*Central nervous system syndrome*: Symptoms include loss of coordination, confusion, coma, convulsions, shock, and the symptoms of the blood forming organ and gastrointestinal tract syndromes	No survivors expected

Table 5-10. Radiation effects in humans after whole body irradiation. (Hellweg and Baumstark-Khan 2007)

To fully understand the significance of radiation doses on the surface of Mars, it is useful to examine common doses received on Earth, in Low-Earth Orbit (LEO), and from galactic cosmic radiation (GCR) on Mars.

5.4.1 Radiation Doses and Dose Limits on the Surface of Earth

Figure 5-3 breaks down the general sources of radiation background on Earth, and Figure 5-4 provides some specific examples of effective doses for different activities. As seen in Figure 5-3, the average annual effective dose to a person in the United States is approximately 363 mrem, or 3.63 mSv (1 rem = 0.01 Sv). The dominant source of Earth-based radiation is natural radon gas, which is an alpha-emitter that exists in varying quantities throughout the globe. For workers that interact with radioactive elements, dose limits are set to minimize the risk for deleterious effects. These general limits are displayed in Figure 5-5. The whole-body effective dose limit is .05 Sv/year.

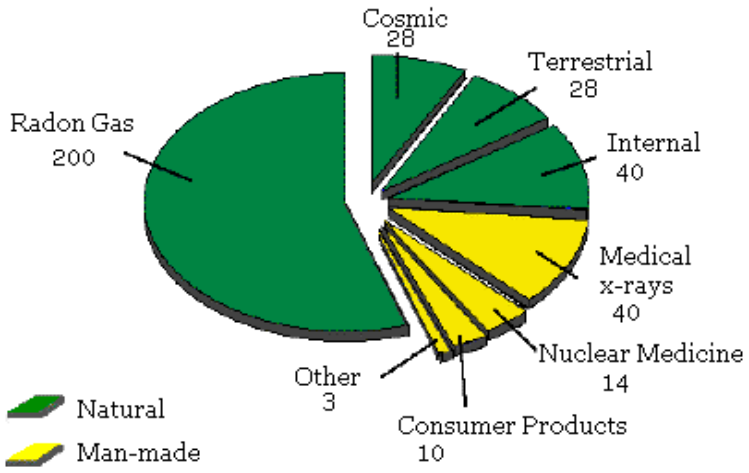

Figure 5-3. Average radiation dose on Earth, in mrem (1 rem = .01 Sv). (http://www.aps.anl.gov/Users/Become_A_User/Before_You_Arrive/Study_Guides/GERT/)

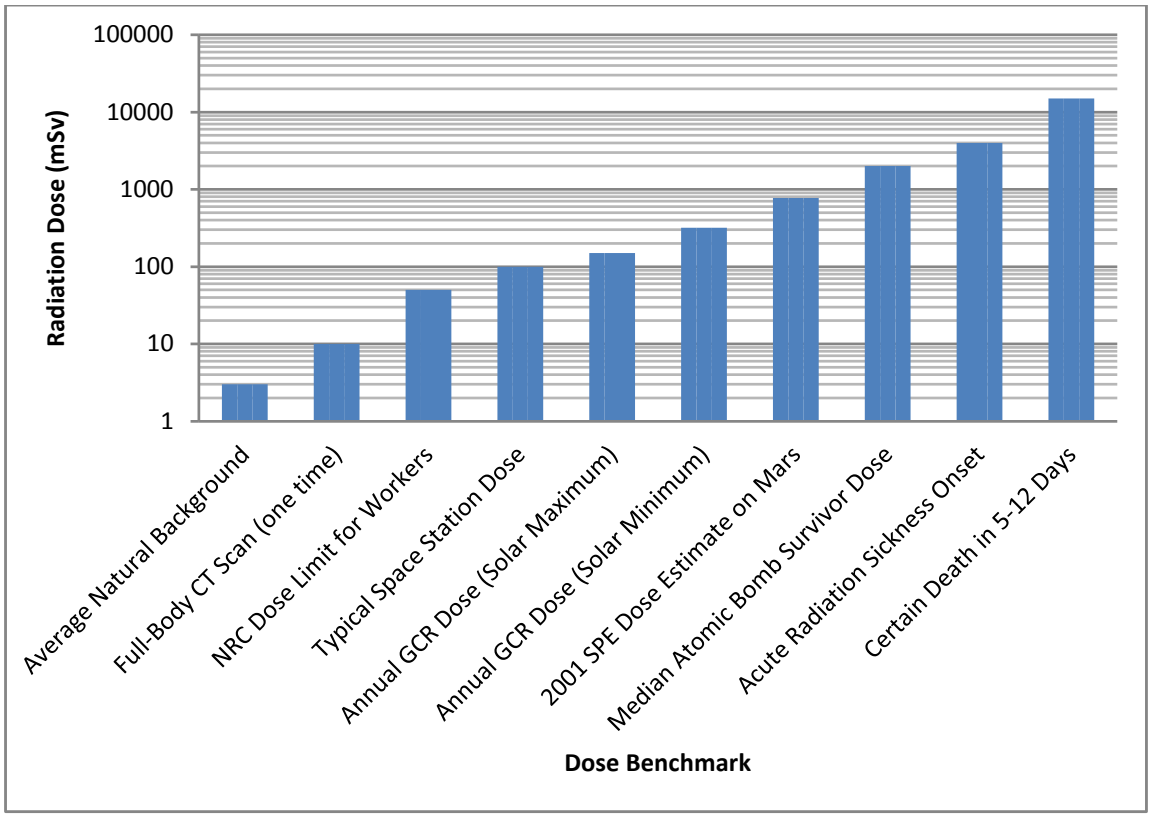

Figure 5-4. Effective doses (mSv) for various benchmarks.

Annual Dose Limits for Occupationally Exposed Adults

Body Parts	*Effective Dose Equivalent (Sv)*
Eyes	0.15
Skin	0.5
Bone Marrow, Gonads & Other Internal Organs	0.5
Elbows to Hands	0.5
Knees to Feet	0.5
Total Effective Dose Equivalent	0.05

Table 5-11. Dose limits for radiation workers.
(http://www.nrc.gov/reading-rm/doc-collections/nuregs/staff/sr1556/v21/1556vol21final/1556vol21final7.gif)

5.4.2 Radiation Doses and Dose Limits for Human Space Missions

Current lifetime dose limits for human space explorers are established by NASA and are dependent on gender and the crew member's age at the time of first radiation exposure. Table 5-12 presents NASA's current radiation dose limits. In general, younger crew members and women have a higher likelihood of radiation-induced cancer. So, their dose limits are set lower than other populations.

Age at First Exposure	Male Dose Limit (Sv)	Female Dose Limit (Sv)
25	1.50	1.00
35	2.50	1.75
45	3.25	2.50
55	4.00	3.00

Table 5-12. NASA radiation dose limits (Sv) by gender and age of first exposure. (Letaw 1997)

Average doses to humans in Low Earth Orbit (LEO) depend on the altitude and inclination of the specific orbit. Table 5-13 presents the annualized average doses to human space explorers for a variety of orbital profiles, including estimates of the lunar surface and transit to Mars. Of course, the vast majority of human space explorers spend far less than one year in orbit – typical missions last for about two weeks and few last more than 6 months. The average annual dose on the International Space Station (ISS) is 0.16 Sv during solar maximum and 0.32 Sv during solar minimum (NASA 2002). Solar Particle Events (SPE's) can also contribute substantially to the radiation dose in LEO. Unshielded doses from SPE's in LEO can reach 10 Sv, which is potentially lethal (Letaw 1997).

Mission Type	Annualized Average Dose (Sv)*
278 km, 28.5° circular orbit	0.0353
278 km, 57° circular orbit	0.0706
278 km, 90° circular orbit	0.0950
463 km, 28.5° circular orbit	0.3040
648 km, 28.5° circular orbit	1.5200
ISS (~400 km, 51.2° circular orbit), solar min.	0.3200
ISS (~400 km, 51.2° circular orbit), solar max.	0.1600
Surface of Moon	0.2500
Flight to Mars	0.5000

* Unless otherwise noted, doses were determined for solar minimum.

Table 5-13. Annualized average doses for various mission profiles. (Adapted from Letaw (1997) with data included from NASA (2002))

5.4.3 Radiation Doses from Galactic Cosmic Radiation (GCR) on the Martian Surface

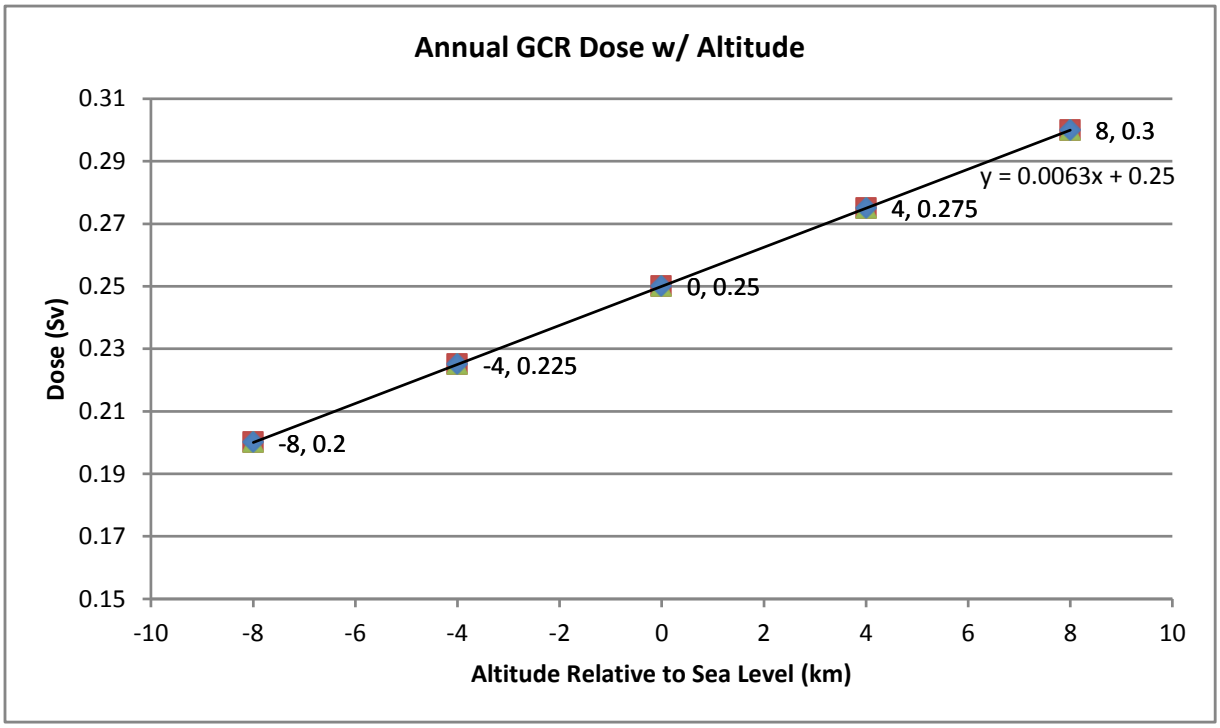

Figure 5-5. Annual GCR dose with altitude (relative to sea level) of Mars at solar minimum. (Based on Cucinotta et al (2001))

The radiation dose from galactic cosmic radiation (GCR) on the surface of Mars has been modeled and reported on extensively in the literature. Cucinotta et al. (2001) used detailed topographical data from Mars to model the GCR radiation dose with altitude. The annual GCR dose ranges from 0.2 – 0.3 Sv during solar minimum, depending on altitude. Figure 5-5 displays the variation of GCR annual dose during solar minimum with altitude (relative to sea level). Simonsen (1997) reported similar results, with an estimate of 0.32 Sv/year at solar minimum and 0.15 Sv/year at solar maximum. These estimates closely match the measured annual GCR dose received on the International Space Station (ISS). For future reference, it is important to note that GCR fluences are relatively straightforward to model. This is starkly different from the process of modeling the doses from SPE's, as presented in Chapter 3.

It is also important to note the altitude variations in GCR-induced radiation dose on the Martian surface. The atmospheric density differences at various altitudes results in approximately ± 20% variations in the GCR surface dose relative to the mean altitude. As previously discussed, only ~20% of the surface dose from SPE's results from primary particles with energies greater than 200 MeV – energetic enough to penetrate the average depth of the Martian atmosphere. Thus, it is expected that these variations will be far more pronounced for SPE's, because the energy ranges are much lower than for GCR. This is discussed in greater detail below.

Altitude variations aside, a cumulative radiation dose estimate can be determined for both GCR and SPE radiation. The SPE dose at solar maximum was calculated at 0.77 Sv. In combination with the GCR dose estimate at solar maximum, a cumulative annual dose of 0.92 Sv is determined. Similarly, the cumulative dose at solar minimum is 0.32 Sv.

5.5 Mitigation of SPE Radiation Dose to Human Explorers on Mars

The overall radiation risk from SPE's to humans on the surface of Mars is clearly variable and depends on a variety of factors, such as solar cycle, atmospheric shielding that depends on the Martian surface altitude, shielding materials, and time of exposures under different shielding situations. An overview of these considerations and the radiation risk to unshielded humans at an average surface altitude is provided here. Unfortunately, a more detailed atmospheric model than the one used in this study is required to directly assess variations in dose with altitude. However, information in the literature is available to estimate the impacts of changing altitude on radiation risk. There are also ample data on the use of various shielding materials, including Martian regolith, to mitigate radiation dose. These data are also presented here.

5.5.1 Radiation Dose Limits and Risk for Human Mars Explorers

Table 5-11 presents the lifetime radiation dose limits for human space travelers from SPE's and GCR, as established by NASA. Even for the least stringent limits – 4.0 Sv for men with their first radiation exposure after age 55 – one year on the surface of Mars during solar maximum contributes nearly a quarter (0.92 Sv) of the permissible lifetime dose limit. The estimated dose during travel time to Mars is 0.5 Sv in each direction (See Table 5-12). Hence, a standard round trip mission to Mars during solar maximum can deliver a dose of approximately 2.0 Sv -- 50% of the lifetime dose limit for men over the age of 55. For women and younger men, the dose

received could easily surpass the lifetime limits. Of course, NASA can extend its lifetime dose limits beyond their current values, but that adds significant biological risk for human explorers.

According to Letaw (1997), a 2.0 Sv dose can increase the risk of cancer fatality by as much as 20%. As noted previously, radiation risk estimates for human space explorers are particularly uncertain due to the small sample size. Moreover, there is no terrestrial radiation source that compare with the energies and types of radiation found in space. However, the potential for a 20% increase in fatal cancer is an unacceptable increase in risk and highlights the need for proper shielding and mission planning.

The acute radiation risk from a single event is only significant for very large events. Assuming an average spectrum, the cumulative dose from the largest event observed at Mars (September 24, 2001) was approximately 0.5 Sv. This is significant enough to cause some deleterious effects, such as nausea and vomiting, but it is not life threatening. Of course, a slightly harder spectrum for the same event – or a somewhat weaker event – can create a grave physiological threat. A spectral index of 2.7 for the September 24, 2001 event would deliver approximately 4.0 Sv to an unshielded astronaut on the surface of Mars. This is enough to cause death within 30 – 60 days after exposure in half the individuals exposed.

5.5.2 Dose Variations with Martian Surface Altitude

It is reasonable to consider the changes in radiation dose with altitude, because the additional atmospheric protection at low altitudes may provide significant shielding from incident radiation. As discussed previously, the atmospheric model used in this study does not provide a reliable representation of real conditions at lower altitudes on Mars. However, Gurtner et al (2005) conducted an analysis of the flux of GCR and SPE particles at various altitudes, using computer simulations. From this study, an estimate can be determined for the difference in dose between average and low altitudes on Mars.

Figure 5-6 presents the omnidirectional flux of GCR and SPE's at various atmospheric depths on Mars (Gurtner et al 2005). As expected, there is very little variation for GCR protons, because the energy range is very high. SPE proton flux varies by a factor of 3 between the lowest and highest Martian altitudes. Neutron fluxes increase at lower altitudes for both GCR and SPE's, but the increase is much higher for GCR – ~300% increase compared to ~30%, respectively. According to Figure 5-5, the net change in GCR dose is approximately 20% lower between the average surface altitude and the lowest depth of the atmosphere.

Given the steep drop in proton flux for SPE's at low altitudes, it is estimated that the SPE dose decreases by a factor of 2 between the average surface altitude and the lowest atmospheric depth. This a significant reduction in the total radiation dose from SPE's. However, the radiation risk at very low altitudes is still high and contributes significantly to the lifetime dose limits established by NASA. Moreover, the increased risk of cancer fatality remains on order of 10% (Letaw 1997). Even at the lowest altitudes on Mars, additional shielding is necessary to mitigate radiation risk.

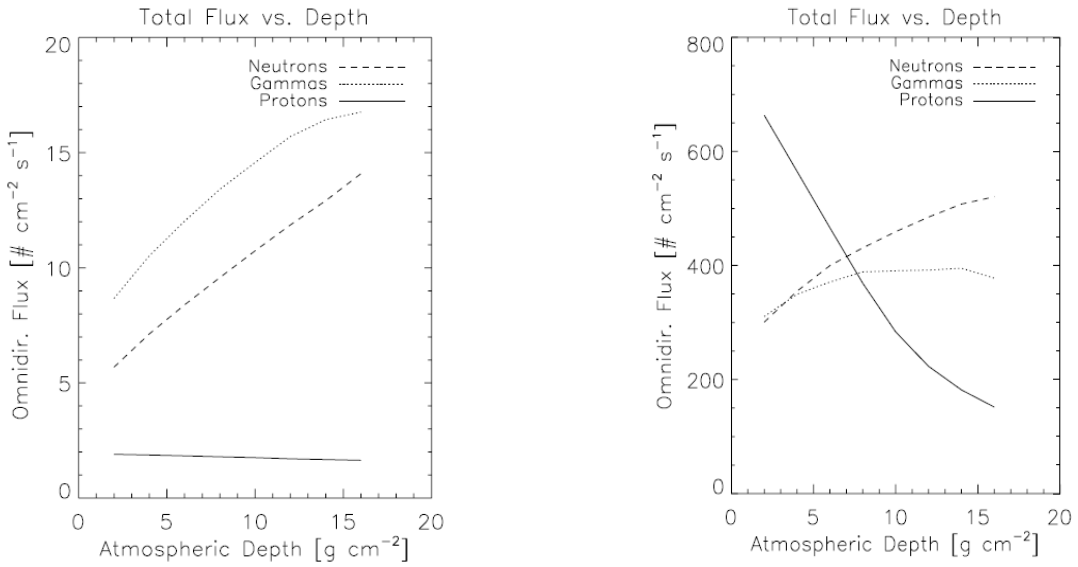

Figure 5-6. Surface flux of protons, neutrons, and gammas at different atmospheric depths on Mars from GCR (left panel) and SPE's (right panel). (Gurtner et al 2005)

5.5.3 Dose Variations with Solar Cycle

It is evident from data presented in Table 5-9 and the discussion in Section 5.4.3 that the annual SPE dose on the Martian surface varies dramatically with solar cycle. In 2001 (near solar maximum), the cumulative SPE and GCR dose was 0.92 Sv. There were no SPE's observed in 2006 (near solar minimum), and there was thus no SPE dose that year. The cumulative SPE and GCR dose in that year was 0.32 Sv. This nearly three-fold decrease in cumulative dose between solar maximum and solar minimum indicates that radiation risk can be reduced by avoiding missions on Mars during times of increased solar activity. Typically, solar minima and maxima last between 2-4 years.

As presented in Chapter 3, there are also variations in the probability of SPE occurrence from one solar cycle to the next. For example, current predictive models suggest the current solar cycle will have 33% fewer SPE's than the previous solar cycle (See Chapter 3). Figure 5-7 presents the predicted SPE probability by month from the previous and current solar cycles. It is not possible to estimate the reduction in radiation dose from the reduction in number of events, because the scale of individual events is unpredictable. However, it is reasonable to expect some reduction in SPE dose during relatively weak solar cycles. Thus, the development of more reliable solar cycle predictive models could provide valuable information in the planning of missions to Mars. It may be possible to time missions near solar maximum without generating a prohibitive radiation risk.

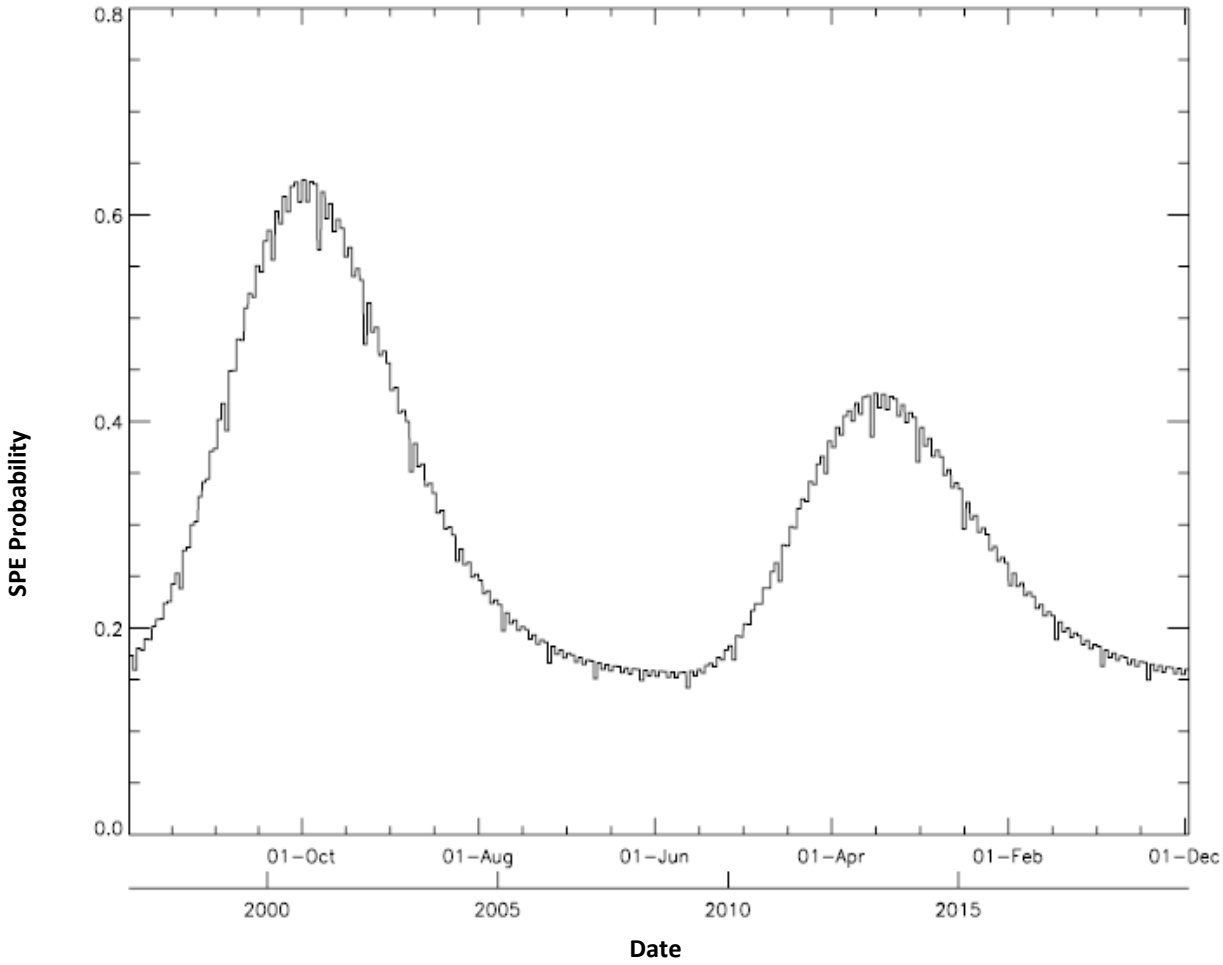

Figure 5-7. Predicted probability of an SPE occurrence, based on predictive model for sunspot activity and modeled relationship between sunspot area and SPE occurrence. (See Chapter 3)

5.5.4 Radiation Shielding Inside a Mars Habitat

Radiation shielding is necessary to mitigate radiation risk for all human space missions. This is particularly true for long-duration space travel, such as a mission to Mars. While the maximum annual GCR dose (0.32 Sv) is significantly lower than the maximum annual SPE dose (0.77 Sv), it is much more difficult to shield human explorers from GCR radiation. This has led some to suggest travel to Mars during solar maximum may be preferable to solar minimum, because it is easier to develop shielding strategies for the lower-energy solar energetic particles. A brief summary of shielding studies found in the literature is provided here.

Figures 5-8 and 5-9 present the dose attenuations behind various thicknesses of aluminum for GCR and SPE's, respectively. The GCR dose attenuation is presented for a variety of nuclear fragmentation and environmental models. As reported by Cucinotta et al. (1996), the hard and soft spectra in Figure 5-9 closely reflect direct observations made on the space shuttle. From these results, it is clear that aluminum is an ineffective shield for GCR. The varying spectra of

SPE's create differences in the dose attenuation from aluminum. As presented in Figure 5-10, some SPE's can be attenuated with relatively little aluminum shielding while others require an impractical amount. This is generally true for all materials, which makes it difficult to assess the relative effectiveness of any material to shield from SPE's.

Materials other than aluminum are far more effective at attenuating dose than aluminum. Figures 5-10 and 5-11 present the dose attenuations of alternate materials, such as water and lithium hydride. Heavier materials, such as lead, can effectively shield SPE's but secondary particles from GCR can cause a higher dose than with no shielding due to spallation. In general, materials with high concentrations of hydrogen are the most effective shields. Typical spacecraft shielding uses a combination of aluminum and a hydrogen-rich material, such as polyethylene.

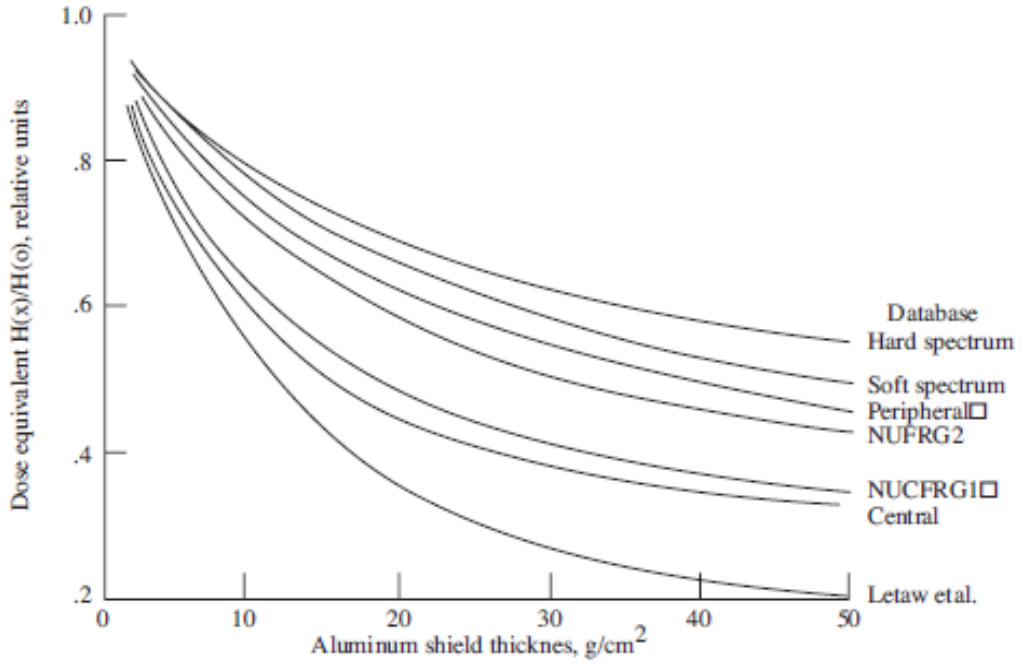

Figure 5-8. Shield attenuation for solar minimum galactic cosmic ray dose equivalent resulting from nuclear fragmentation models. 1 g/cm^2 of aluminum is equivalent to 0.37 cm thickness. (Wilson et al. 1999)

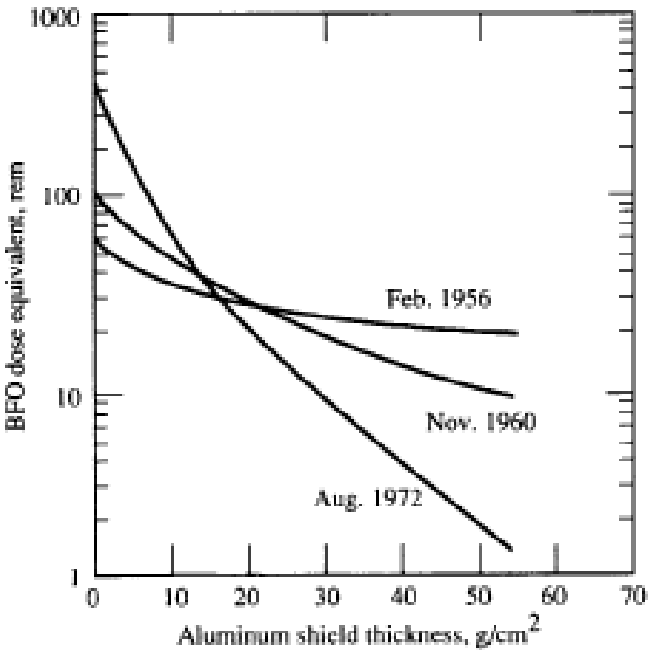

Figure 5-9. Blood forming organ (BFO) dose equivalent as a function of aluminum shield thickness for three large SPE's. 1 g/cm^2 of aluminum is equivalent to 0.37 cm thickness. 1 rem = 10 mSv. (Simonsen and Nealy 1991)

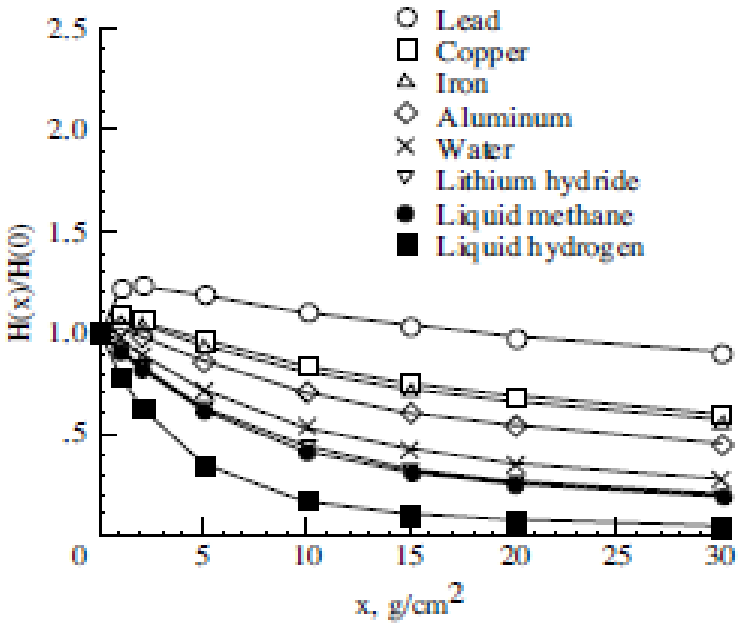

Figure 5-10. Attenuation of dose equivalent for a one-year GCR exposure at solar minimum behind various shielding materials. Material Densities (g/cm^3): Lead = 11.35, Copper = 8.96, Iron = 7.87, Aluminum = 2.70, Water = 1.0, Lithium Hydride = 0.82, Liquid Methane = 0.42, Liquid Hydrogen = 0.07. (Wilson et al. 1999)

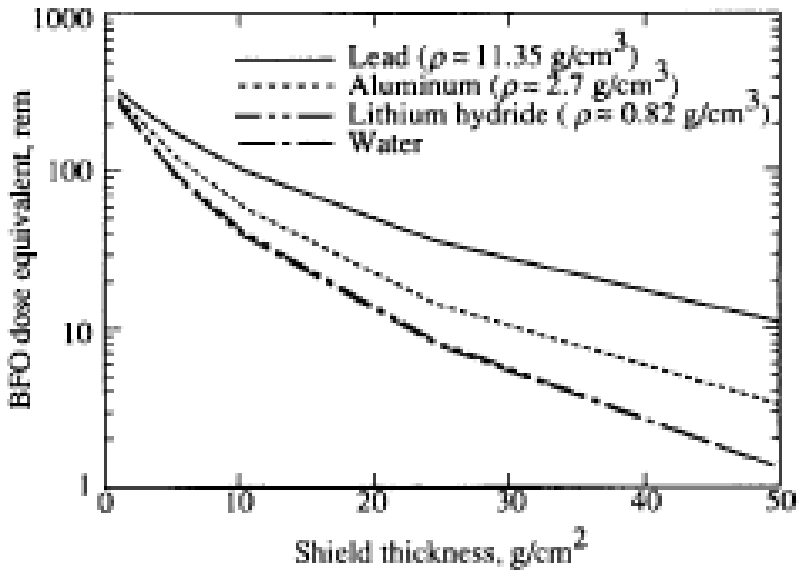

Figure 5-11. Blood forming organ (BFO) dose equivalent versus depth functions for sum of 1989 SPE fluences for four materials. (Simonsen and Nealy 1991)

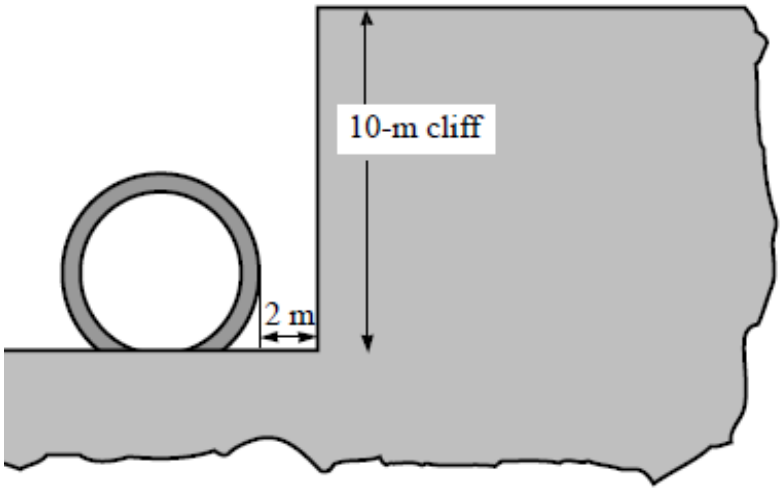

Figure 5-12. Mars module design that uses varying shielding thicknesses of Martian regolith and is positioned next to a cliff for added protection. (Simonsen et al. 1990)

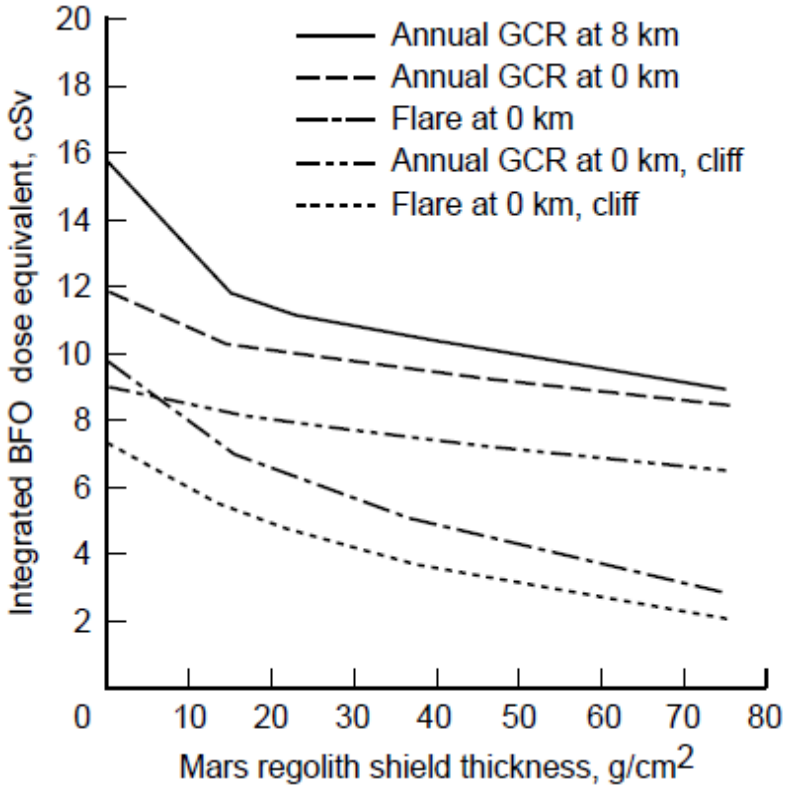

Figure 5-13. Annual dose equivalent behind various thicknesses of Martian regolith and next to a cliff for GCR and a sample SPE. (Simonsen et al. 1990)

The terrestrial environment of Mars provides an additional opportunity to use in situ materials for radiation shielding. Simonsen et al. (1990) examined the shielding properties of Martian regolith against GCR. As displayed in Figure 5-13, the shielding provided by Martian regolith against GCR is minimal. Hence, it was conceived that positioning the habitat next to a cliff would provide significant additional shielding with minimal practical consequences. Figure 5-12 presents a design of a habitat next to a cliff. Approximately 40 g/cm^2 of Martian regolith is necessary to reduce the SPE dose by 50%. However, only 20 g/cm^2 is required if the habitat is also located next to a cliff. Similarly, the GCR dose can be reduced by approximately 50% behind a 20 g/cm^2 regolith shield next to a cliff. Of course, this form of shielding is only available when crew members are inside the habitat. Outside of the habitat, only the space suit or vehicle provides shielding, and space suits provide minimal radiation protection.

5.5.5 Radiation Shielding Outside a Mars Habitat

In Low-Earth Orbit (LEO), Reames (1999) determined that astronauts had a 12 hour period from the onset of an SPE to reach safety in an orbiting spacecraft without receiving a potentially lethal dose. In Chapter 3, it was determined that Earth-based detectors provide poor warning for the occurrence of SPE's at Mars. Thus, a Mars-based space weather monitoring system would appear to be a necessity for human exploration of that planet.

Even with appropriate monitoring, there may be restrictions on the distance an explorer may travel in order to return to the habitat in time to avoid significant radiation exposure from an SPE. Crew members might be provided with a vehicle with significant shielding. In fact, Wilson et al. (1999) examined the radiation dose to vital organs from a large SPE in a variety of shielding conditions on the surface of Mars. This study found that the space suit and a pressurized vessel, such as a reasonably-sized rover, provide minimal shielding to a large SPE. Such and event could result in a dose of approximately 0.45 Sv to the skin or 0.32 Sv to blood forming organs. These results are presented in Table 5-14. The true doses are likely higher than the results reported in Wilson et al. (1999), because this study did not consider the dose delivered by secondary neutrons, which are unlikely to be shielded by a space suit or pressurized vehicle.

	Skin (Sv)	**Ocular Lens (Sv)**	**BFO (Sv)**
Space Suit	0.45	0.44	0.32
Helmet/Pressure Vessel	0.44	0.42	0.31
Equipment Room	0.38	0.37	0.28
Shelter	0.33	0.32	0.25

Table 5-14. Dose Equivalent from "worst case" SPE on the Martian Surface, in Sv. (Wilson et al. 1999)

5.6 Conclusion

Unshielded human explorers on the surface of Mars face significant long-term radiation risks from the absorbed doses due to GCR and SPE's, and they face potential acute radiation sickness from SPE's. Based on the data presented in this report, the cumulative dose to a human explorer on the surface of Mars from SPE's and GCR during solar maximum is approximately three times that at solar minimum. In one year near solar maximum, doses from SPE's and GCR can contribute nearly the entire lifetime dose limit established by NASA, depending on the crew member's age and gender. SPE's with large fluences and slightly harder-than-average spectra can deliver enough dose to cause deleterious physiological effects. These factors are of major consideration in planning a human mission to Mars.

The most significant contributors to radiation dose from an SPE are secondary protons produced in the Martian atmosphere and regolith. Primary protons (energies greater than 200 MeV) also contribute approximately 19% of the total radiation dose. Secondary neutrons contribute approximately 10% of the radiation dose, and roughly half of the neutrons are backscattered from the Martian regolith. Electrons and gamma rays do not contribute significantly to the radiation dose on the Martian surface. The total dose from and SPE is strongly influenced by the energy spectrum of the event.

There are several strategies that can mitigate the radiation risk associated with a mission to Mars. Perhaps the most obvious strategy is to select travel times near solar minimum, when the

probability of an SPE is lower for about a four year period in the eleven year solar cycle than at other times. There are years, such as 2006, when no SPE's are observed at Mars. Moreover, it is possible to select particularly weak solar cycles that have a relatively low probability of SPE's occurring even during solar maximum. The primary problem with traveling during times of low solar activity is that the GCR flux increases during these times. Unlike SPE's, GCR is particularly difficult to shield against. This has led some to suggest that travel to Mars near solar maximum may reduce radiation risk more than at solar minimum.

	Solar Maximum (2001)		**Solar Minimum (2006)**	
	SPE Dose (Sv)	*GCR Dose (Sv)*	*SPE Dose (Sv)*	*GCR Dose (Sv)*
Unshielded	0.77	0.15	0.0	0.32
Cliff-Side Habitat w/ ~10 cm Shielding	0.39	0.09	0.0	0.19
-8 km Altitude & Cliff-Side Habitat	0.26	0.08	0.0	0.16
Total Dose	0.34		0.16	

Table 5-15. Comparison of dose received (Sv) at solar maximum and solar minimum, by shielding crew members with Martian regolith and locating at the lowest altitude possible.

Other mitigation strategies include traveling to low altitudes in order to increase protection from the Martian atmosphere and providing a variety of shielding options. Travelling from an average altitude to the lowest depths of Mars (~8 km below sea level) decreases the GCR dose by approximately 15% and SPE dose by an estimated 150%. However, the SPE dose is strongly tied to the incident spectrum, which varies widely between events. So, there are occurrences (i.e., relative hard spectrum) where an SPE will not be significantly mitigated with increasing depth. The most appealing shielding strategy is to use the in situ geological features of Mars to shield from the radiation particles. One strategy presented in this report is the placement of a Mars habitat beside a cliff. This shields crew members inside the habitat from half or more of the incident radiation. Coupling a cliff-side habitat at an average altitude with approximately 10 cm of additional regolith shielding reduces the GCR dose by approximately 40% and the SPE dose by approximately 50%.

Table 5-15 estimates the radiation dose at solar maximum (2001) and solar minimum (2006), using the mitigation options described above. Data presented in this report do not support the notion that solar maximum is the most appropriate time to stage a Mars mission. With all mitigation strategies in place, the total dose received during solar maximum is more than twice than that received during solar minimum. In fact, the total dose during solar maximum at a low altitude with ~10cm shielding is higher than the unshielded dose received at solar minimum.

Moreover, the potential for a large-scale SPE to occur while surface explorers are away from their habitat creates a significant health risk that could compromise an entire mission. It is difficult to shield astronauts outside of the habitat. Space suits and pressurized vehicles provide minimal shielding from radiation, particularly neutrons. Assuming the time to reach safety during an SPE on Mars is equivalent to that in Low Earth Orbit (approximately 12 hours), activities outside the habitat must allow for an adequate transit time. This limits the range of activities that can occur on a Mars mission and necessitates the use of Mars-based space weather monitors. These data and analyses show there is a significant level of risk from ionizing radiation to explorers on the surface of Mars; however, with choice of mission timing and provision of shielding shelters within about 12 hours transit distance, the potential health effects are minimized.

Acknowledgments

Special thanks to Dr. Thomas Budinger for spending many hours meeting with me to review and comment on the contents of this chapter.

References

E. Alpen. Radiation Biophysics. 2nd Edition. *Academic Press*. 1998.

Cucinotta et al. "Evaluating Shielding Effectiveness for Reducing Space Radiation Cancer Risks." *Radiation Measurements*, 41, 1173-1185. 1996.

F.A. Cucinotta et al. "Space Radiation Cancer Risks and Uncertainties for Mars Missions." *Radiation Research*, 156, 682-688. 2001.

F.A. Cucinotta et al. "Space Radiation Cancer Risk Projections for Exploration Missions: Uncertainty Reduction and Mitiation." *NASA Technical Paper 2002-210777*. NASA, Washington, DC. 2002.

M. Gurtner et al. "Simulation of the Interaction of Space Radiation with the Martian Atmosphere and Surface", *Advances in Space Research,* 36, 2176-2181, 2005.

E. Hall and A. Giaccia. Radiobiology for the Radiobiologist. 6th Edition. *Lippincott, Williams, & Wilkins*. 2006.

C. Hellweg and C. Baumstark-Khan. "Getting Ready for the Manned Mission to Mars: The Astronauts' Risk from Space Radiation." *Naturwissenschaften* .94(7): 517-26. 2007.

http://www.aps.anl.gov/Users/Become_A_User/Before_You_Arrive/Study_Guides/GERT/

http://www.nrc.gov/reading-rm/doc-collections/nuregs/staff/sr1556/v21/1556vol21final/1556vol21final7.gif

J. Letaw. "Radiation Biology." Fundamentals of Space Life Sciences, Volume 1, Chapter 2. *Orbit Foundation Series*. 1997.

National Research Council, Committee on the Biological Effects of Ionizing Radiation. *Health Effects of Exposure to Low Levels of Ionizing Radiation (BEIR V)*. National Academy Press, Washington, DC. 1990.

National Council on Radiation Protection and Measurement (NCRP). "Protection Against Neutron Radiation." *NCRP Report No. 38*. NCRP, Washington, DC. 1971.

National Council on Radiation Protection and Measurement (NCRP). "Limitation of Exposure to Ionizing Radiation." *NCRP Report No. 116*. NCRP, Washington, DC. 1993.

D. Reames. "Solar Energetic Particles: Is there time to hide?" *Radiation Measurements*, 30, 297-308, 1999.

L. Simonsen. “Analysis of Lunar and Mars Habitation Modules for the Space Exploration Initiative.” Shielding Strategies for Human Space Exploration. Chapter 4. NASA CP-3360, 43–77. 1997.

L. Simonsen. “Radiation Exposure for Manned Mars Surface Missions.” *NASA Technical Paper 2979*. NASA, Washington, DC. 1990.

L. Simonsen and J. Nealy. “Radiation Protection for Human Missions to the Moon and Mars.” *NASA Technical Report Paper 3079.* NASA, Washington, DC. 1991.

J. Turner. Atoms, Radiation, and Radiation Protection. 3rd Edition. *Wiley-VCH*. 2007.

J.W. Wilson et al. “Astronaut Exposures to Ionizing Radiation in a Lightly-Shielded Space Suit.” *NASA Technical Paper* 1999-01-2173. NASA, Washington, DC. 1999.

Chapter 6
Summary and Conclusions

6.1 Overview

The International Space Station (ISS) is scheduled for completion in 2010. At that time, NASA will discontinue its Space Transportation System (STS) missions and move toward designing advanced technologies for human space exploration. Future human missions will focus on exploration of the Mars, asteroids, and other deep space targets.

As NASA moves forward in expanding human presence in the Solar System, it is likely to see strong competition from various nations and private industry. China is rapidly advancing its human space program and has stated its intention to place humans on the Moon within the next fifteen years. The Indian Space Agency is also rapidly advancing as a new wave of entrepreneurial spirit has emerged in that country and tremendous amounts of venture capital are driving the expansion of industry. Within the next decade, private corporations will also expand operations to provide the general public with access to space.

As these and other competing interests converge on a common ambition to expand human presence in space, it is not unimaginable that human endeavors to Mars could occur within the next twenty to thirty years. While human exploration of Mars may be decades away, it is important to assess potential risks immediately so that space exploration profiles and vehicles can be designed to minimize these risks. Many of the hazards that humans will face may take decades to resolve.

This project has examined one specific issue facing human explorers at Mars – radiation dose from solar particle events (SPEs). While the issue is specific, the work involved in carrying out this study has been truly multidisciplinary. From space physics to modeling the Martian atmosphere to assessing radiation risk to humans, a lot of ground is covered. At each point along the way, efforts were made to clarify the science and assumptions used to derive quantitative estimates and draw meaningful conclusions. The data and analyses provided in this project represent the most comprehensive study of SPE's at a planetary body other than Earth. The analysis includes dose estimates from galactic cosmic radiation derived from others.

Some of the conclusions drawn from this study include:

- The MCP detector onboard MGS ER (and presumably other spacecraft) can serve as an effective detector for high-energy ionizing radiation.
- Though more work is necessary, it is possible to estimate future solar activity at Earth and Mars based on current solar observations.
- Spectral information from SPE's at Mars is required to thoroughly assess the radiation environment on the Martian surface.

- An unshielded astronaut on the Martian surface may face long-term and acute radiation risk from SPE's, depending on the likelihood of their occurrence.
- Various mitigation strategies can be employed to minimize the radiation risk to human explorers on Mars, though shielding is limited for astronauts outside of a fixed habitat.

In this chapter, the findings from each of the previous chapters are summarized, and a discussion of limitations in the current work and suggestions for future work are provided. Of course, the best way to advance the study of radiation on Mars is to place a high energy radiation detector on the Martian surface, preferably with a corresponding satellite-based instrument in near-Mars space. That said, it is unlikely that such instruments will be deployed for at least a decade. So, options for future work described in this chapter are based on current limitations. Because this project touched on a variety of disciplines, there are also implications for future work beyond the specific focus of this study. These issues are also presented here.

6.2 Detection & Analysis of Solar Energetic Particles at Mars

Chapter 2 deals with what is perhaps the most significant challenge in meeting the goals of this study, which is verifying the viability of the primary data set. There are not instruments at Mars designed to analyze high-energy particle radiation from the Sun. However, data are derived in this project from the Electron Reflectometer (ER) onboard the Mars Global Surveyor (MGS) satellite. The MGS ER instrument is designed to detect low-energy electrons from the Martian atmosphere and solar wind. Energetic particles (e.g. protons with E > ~ 25 MeV) are capable of penetrating the instrument's shielding and registering particle counts. These "penetrating particle" count rates provide the most direct data available to understand the impact of SPEs at Mars.

It is evident from Figure 6-1 that MGS ER, detected solar energetic particles. However, determining the detection efficiency for MGS ER is not trivial. The instrument uses a microchannel plate (MCP) detector, which has not been extensively tested for responses to energetic particle radiation. However, there are key publications in the literature that provide relevant information. Mosher et al. (2001) found ~80% efficiencies for MCP response to 8 MeV alpha particles, and Oba et al. (1981) found a ~60% efficiency for 7 GeV protons.

6.2.1 Findings

This study used a physical analysis to arrive at an estimate of 90% efficiency for the MCP detector on MGS ER. The MARIE instrument onboard the Mars Odyssey satellite collected energetic particle data sporadically for approximately one year. These data were compared with SPE data from MGS ER to validate the 90% efficiency estimate. Both MARIE and MGS ER data were in close agreement during SPE and GCR measurements. The flux and fluence drop-offs for SPEs between Earth and Mars was also examined, and it was found that the decline in particles arriving at Mars is consistent with predictions found in the literature.

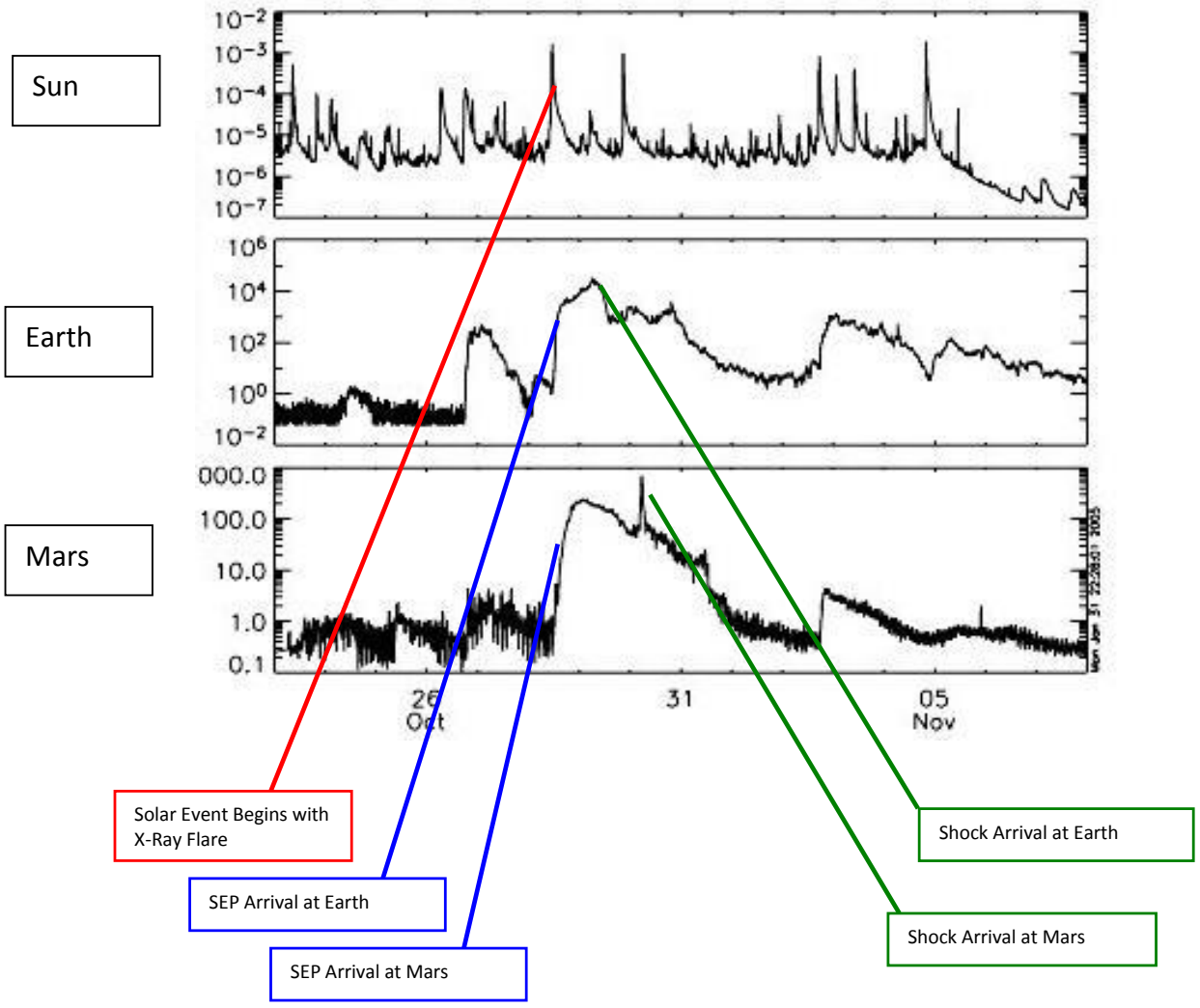

Figure 6-1. Comparison plot of Sun, Earth, and Mars data during a period of intense solar activity. *Top Panel.* X-ray flux measurements made by a GOES satellite (photons/s). *Middle Panel.* Proton Flux measurements for protons with energies > 10 MeV, measurements made by a GOES satellite (protons/s). *Bottom Panel.* Particle Flux measurements for particles with energies > ~25 MeV, measurements made by Mars Global Surveyor (MGS) Electron Reflectometer (ER) (particles/s).

6.2.2 Future Work

While the 90% efficiency estimate provided in this study is well-founded, the glaring dearth of information in the literature regarding MCP efficiencies for high-energy radiation was surprising. In fact, attempts to secure these efficiency data from MCP manufacturers also yielded little, as the manufacturers surveyed had not collected such information. There is a clear need to collect empirical data on the MCP response to high-energy radiation, including the detector response to particles that enter from the back-side of the detector.

This information is important for support of data analysis from MGS ER but is also relevant to a variety of space missions. There are several instruments currently in space that utilize MCP detectors and could provide useful data on the propagation of SPEs through the Solar System. For example, the Lunar Prospector satellite has an ER instrument similar to MGS ER. The three STEREO satellites also have instruments with MCP detectors; the STEREO satellites are placed in three locations orbiting the Sun at 1 astronomical unit (AU) – the distance from the Sun to the Earth. While different satellites have varying physical structures that affect the collection of MCP data, gathering baseline efficiencies for MCPs will provide the fundamental information necessary to rigorously analyze such data on most satellites.

6.3 Characteristics of Solar Particle Events at Mars

Once the efficiency estimates for MGS ER were validated, the full data set of SPEs were entered in the next step of the analysis. Chapter 3 examined various properties of SPEs at Mars and compared them to Earth-based data. These properties include time-intensity profiles, frequency of events, fluences, peak fluxes, and interplanetary shock arrival times. An analysis of predictive models was also presented.

Many SPEs overlap with other events, which makes the distinction between specific events ambiguous. Figure 6-2 presents the uniform criteria that were established to define an SPE. Based on these criteria, 85 SPEs were observed at mars during the nearly eight years of MGS ER operation. Comparison of these events to Earth-based data was further complicated by solar longitudinal variations between Earth and Mars. Figure 6-3 presents the relative positions of Earth and Mars when SPEs were observed.

6.3.1 Findings

A significant finding from Chapter 3 is that 18% of SPEs observed at Mars were not also observed at Earth. In one case, a Mars-only event occurred when Earth and Mars were near opposition. This finding significantly diminishes the ability to use Earth-based data to predict SPE onset at Mars. Similarly, Earth-based models to estimate the CME shock arrival time are not applicable at Mars. The CME shock arrival time is significant, because it typically corresponds to the peak event flux – and presumably the peak radiation dose. The peak flux and fluence for each observed SPE was applied to a power law model to allow for prediction of SPE magnitudes.

An additional attempt was made to apply predictive solar activity models to the occurrence of SPEs at Mars. While these types of predictive models are limited in their capabilities, they did predict the number of events at Mars for the last solar cycle within 22%. More importantly, the model provides some predictive capability for the relative frequency of SPEs during the current and subsequent solar cycle.

6.3.2 Future Work

It may be useful to compare MGS ER data to relevant instruments at other locations in the Solar System, including other Earth-based satellites. These types of comparisons could provide useful information in modeling the propagation of SPEs through the Solar System. This is important not just for understanding the radiation environment at Mars but for all human and robotic space missions. Further work is also needed to improve the reliability of models that aim to predict solar activity. The model developed by Hathaway et al. (2009) and applied in this study is based almost exclusively on sunspot area. There are likely many other factors that influence future solar activity that need to be identified and incorporated into more advanced predictive models.

6.4 Impact of Solar Particle Events on the Radiation Environment at the Martian Surface

SPE data from Mars orbit were applied to the Particle and Heavy Ion Transport code System (PHITS) radiation transport code, which simulated the transport of energetic particles through the Martian atmosphere and regolith. Chapter 4 presented the details of this model, as well as the strategy for estimating the energy spectra of SPEs. MGS ER does not provide spectral data for SPEs. To account for this lack of critical information, the spectra of Earth-based data were examined during the same timeframe of MGS ER operation. This allowed for the determination of a range of spectra and an "average" SPE spectrum. A power law spectrum of the form of Equation 6-1 was assumed for SPEs observed by MGS ER.

$$\Phi(E) = A \times E^{\alpha} \qquad \text{(Equation 6-1)}$$

Here, Φ is the particle flux or fluence, A is a scaling constant, and α is the spectral index. The average spectrum and extreme spectral limits were applied to the PHITS model of Mars, using MGS ER flux and fluence data. The surface fluxes and fluences of protons, electrons, neutrons, and photons were examined.

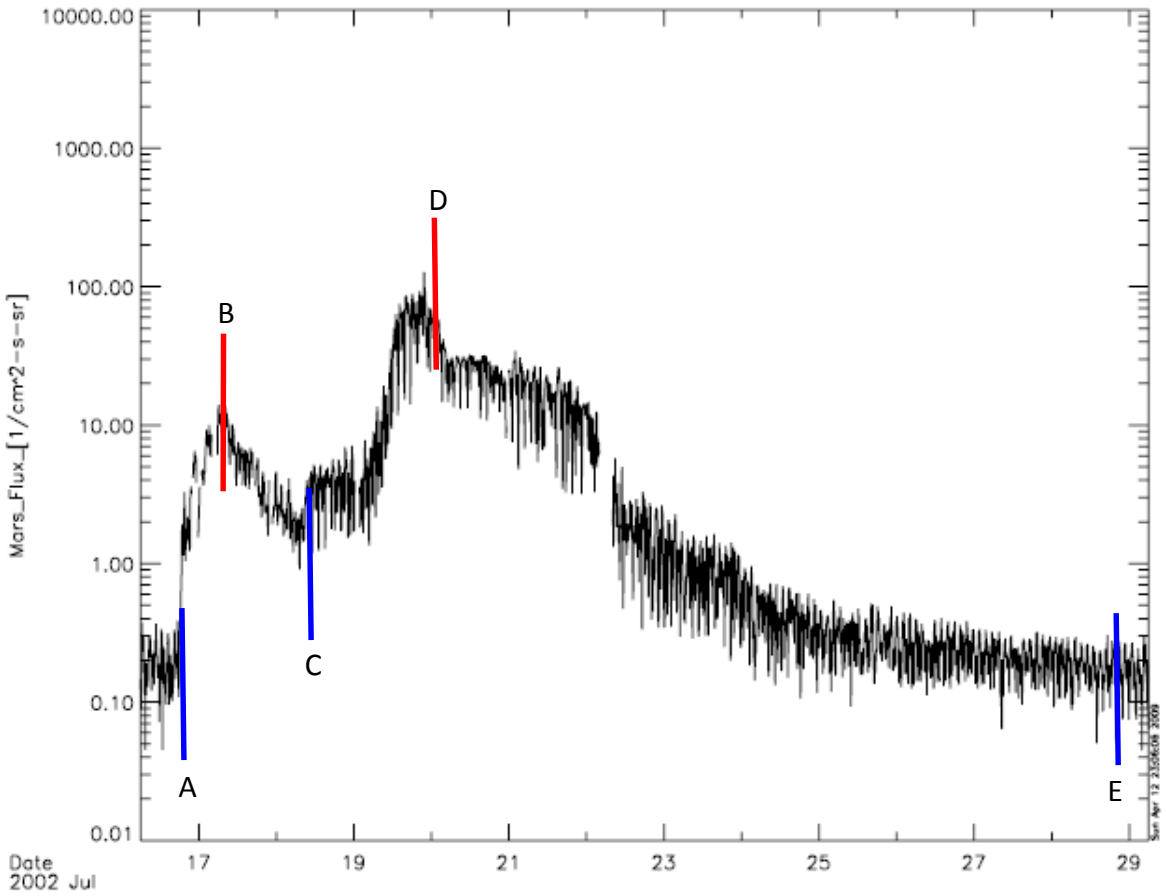

Figure 6-2. Criteria for Identifying Start and End Times for an Overlapping Series of SPE's.

A. The flux exceeds 3σ of the annual background flux for more than one hour, which satisfies Criterion #2. This signifies the start time of both the series of SPE's and the first event within the series.

B. The peak flux of the first event exceeds 1 particle/cm^2-s-sr, which satisfies Criterion #1.

C. The flux decreases by more than one order of magnitude after the first peak and subsequently increases more than one order of magnitude to reach the second peak. This satisfies Criterion #3b and signifies the end of the first event and the beginning of the second event.

D. The peak flux of the second event exceeds 1 particle/ cm^2-s-sr.

E. The flux is smaller than3 times the annual background flux for more than one hour. This signifies the end time of both the series of SPE's and the second event within the series.

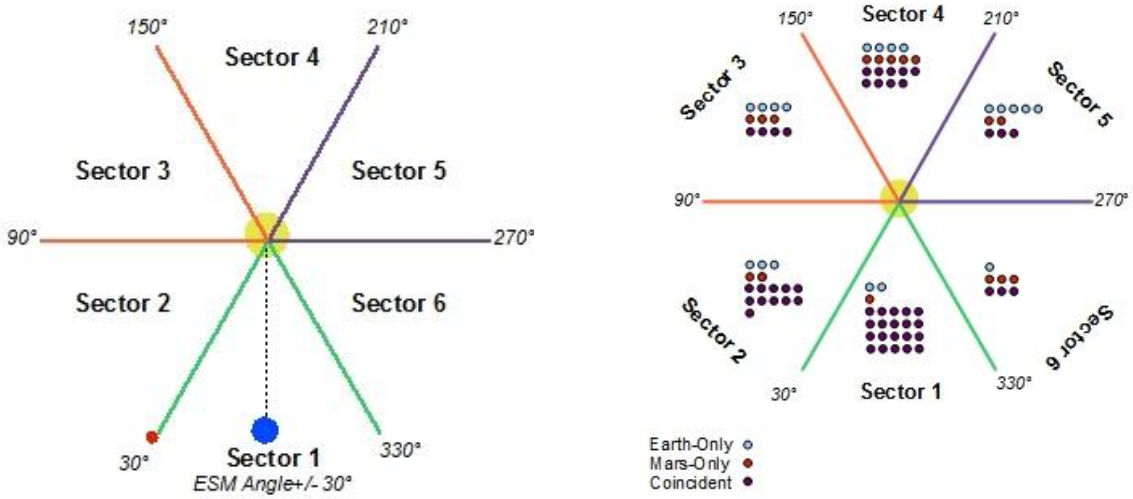

Figure 6-3. (Left Panel) Top-down view of the Solar System, divided into six sectors based on the Earth-Sun-Mars (ESM) angle. (Right Panel) Distribution of Coincident, Earth-Only, and Mars-Only SPE's by Earth-Sun-Mars angle (ESM).

6.4.1 Findings

Not surprisingly, the surface fluences of particles vary by orders of magnitude over the range of SPE spectral indexes, which range from 1.3 to 4.3. The average spectral index is 3.2. Figure 6-4 presents the energy spectra on the surface of Mars for protons, neutrons, electrons, and photons, using an average incident SPE spectrum. Perhaps the most significant finding in Chapter 4 is that the back-scattered neutrons from the Martian surface are equal in fluence to the forward-scattered neutrons. These results are consistent with studies conducted by Clowdsley et al. (2000) and Gurtner et al. (2005). The Clowdsley study used HZETRN as its radiation transport code, and the Gurtner study used the Geant4 code.

6.4.2 Future Work

The primary limitation of this analysis is the lack of direct spectral data at Mars. To the extent possible, it would be useful to generate more rigorous estimates of spectra for each specific event, perhaps by using spectral data from multiple instruments. This study also used a crude model of the Martian atmosphere and surface. As has been done in studying GCR particle fluence on Mars, it would be helpful to use a more detailed Mars model to generate topographical flux and fluence maps for SPEs.

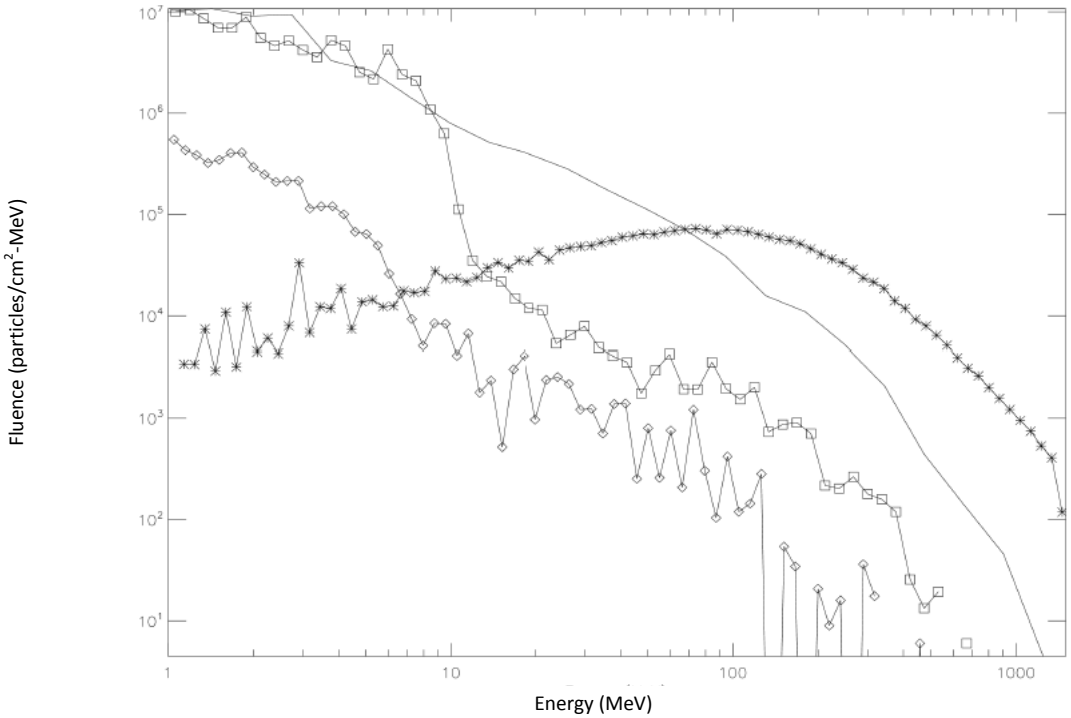

Figure 6-4. Fluence as a function of energy for neutrons (solid line), protons (stars), electrons (diamonds), and photons (squares) at the Martian surface for an incident SEP with flux of 3.0x10^7 protons/cm^2-sr and a spectral index of 3.2.

6.5 Radiation Dose on the Martian Surface from Solar Particle Events

The culmination of work in this study is provided in Chapter 5, which presents an estimate of the radiation doses a human on the surface of Mars would have received from the SPEs detected by MGS ER. SPE doses were compared to estimates of GCR doses on the Martian surface, as well as NASA's lifetime dose limits for astronauts. Various dose mitigation options were also considered, including traveling to lower depths on the Martian surface, planning missions around times of heavy solar activity, and utilizing various forms of radiation shielding.

6.5.1 Findings

Protons contribute approximately 90% of the SPE radiation dose on the surface of Mars, and neutrons contribute nearly all the remaining dose. Electrons and gamma rays contribute a negligible dose to humans. The annual dose in 2001 (solar maximum) to an unshielded human on Mars from SPEs was approximately 0.77 Sv, assuming an average SPE spectrum. This is a significant dose when compared to NASA's lifetime limits, which range from 1.0 to 4.0 Sv depending on gender and age. Moreover, the largest event observed by MGS ER would contribute approximately 0.49 Sv to a human on the Martian surface. This is enough dose to potentially cause deleterious physiological effects. If the spectral index for that event were slightly harder than average, the dose could reach several Sieverts, which is potentially lethal.

In 2006 (solar minimum), there were no SPEs observed at Mars. Hence, there was no SPE dose. However, the annual GCR dose is highest during solar minimum (0.32 Sv, compared to 0.15 Sv at solar maximum). GCR radiation is more difficult to shield against, because the energies are substantially higher. This has led some to speculate that a shielded human may receive a lower dose during solar maximum than solar minimum. The analyses conducted in this study suggest that even with significant shielding at very low altitudes on the Martian surface, it is best to plan human Mars missions during times of minimal solar activity. Table 6-1 summarizes these results.

A major conclusion of this dissertation is that while the radiation hazards exist during transits to Mars and during occupancy of Mars, the hazards are not so great as to endanger space explorers if easily-implemented mitigation strategies are employed.

	Solar Maximum (2001)		**Solar Minimum (2006)**	
	SPE Dose (Sv)	*GCR Dose (Sv)*	*SPE Dose (Sv)*	*GCR Dose (Sv)*
Unshielded	0.77	0.15	0.0	0.32
Cliff-Side Habitat w/ ~10 cm Shielding	0.39	0.09	0.0	0.19
-8 km Altitude & Cliff-Side Habitat	0.26	0.08	0.0	0.16
Total Dose	0.34		0.16	

Table 6-1. Comparison of annual dose received (Sv) at solar maximum and solar minimum, by shielding crew members with Martian regolith and locating at the lowest altitude possible

6.5.1 Future Work

The dose analyses conducted in this study considered only whole-body dose. More advanced modeling could provide dose estimates to specific tissues that would further demonstrate the radiation risk at different times on the surface of Mars. Similarly, more advanced shielding studies would allow optimization of radiation mitigation strategies.

Acknowledgments

Special thanks for Dr. Thomas Budinger for being an outstanding – and very patient – advisor both on this project and a variety of other random activities I have pursued in my time as an undergraduate and doctoral student at UC Berkeley.

The completion of this project also would not have been possible without the many individuals scattered across the globe who have advised me on a wide range of topics. Some are listed here:

Dr. Sukesh Aghara, Texas A&M University, Prairie View

Dr. Stephen Blattnig, NASA Langley Research Center

Dr. Martha Clowdsley, NASA Langley Research Center

Dr. Greg Delory, University of California, Berkeley

Dr. Lawrence Heilbronn, University of Tennessee

Dr. Christian Iliadis, University of North Carolina

Dr. Kerry Lee, NASA Johnson Space Center

Mr. Bill Netolicky, Photonis USA, Inc.

Dr. Koji Niita, RIST, Japan

Dr. Roger Thelwell, James Madison University

Dr. Cary Zeitlin, Southwest Research Institute

Dissertation Committee Members: Dr. Thomas Budinger, Dr. Thomas Lang, and Dr. Robert Lin.

References

M.S. Clowdsley et al, "Neutron Environments on the Martian Surface", *Physica Media*, 17, 2001.

M. Gurtner et al. "Simulation of the Interaction of Space Radiation with the Martian Atmosphere and Surface", *Advances in Space Research,* 36, 2176-2181, 2005.

D. Hathaway et al. "A Synthesis of Solar Cycle Prediction Techniques." *Journal of Geophysical Research*, vol. 104, no. A10, pgs. 22,375 – 22,388. 1999.

J. Mosher, et al. "Nuclear Recoil Detection with Microchannel Plates." *Nuclear Instruments and Methods in Physics Research,* A 459, pages 532-542. 2001.

K. Oba et al. "High Gain Micro-Channel Plate Multipliers for Particle Tracking or Single Photo-Electron Counting." *IEEE Transactions on Nuclear Science*, Vol. NS-28, No. 1, February 1981.

Appendix A: Sample PHITS Input Code

```
[ T i t l e ]
    Test Code for proton spectra on Mars Atmosphere & Soil.

[ Parameters]
icntl = 0            ! Main control parameter.
                     ! 0: normal, 7: 2D-geometry plot, 11: 3D-geometry plot.
                     !
                     ! It requires [t-gshow]  section for icntl=7, and
                     !              [t-3dshow] section for icntl=11
                     !

     maxcas = 434783.  ! Number of calculation in each batch
     maxbch = 23.        ! Number of batch

                      ! Total number of calculation = maxcas * maxbch

     emin(1) = 1.e-6   ! Energy cutoff for proton   (MeV)    (D=1.0)
     emin(2) = 1.e-11   !                   neutron ( MeV)    (D=1.0)
     emin(12) = 1.0e-06    !                   electron  (MeV)   (D=1.d9)
     emin(13) = 1.0e-06    !                   positron  (MeV)   (D=1.d9)
     emin(14) = 1.0    !                   photon    (MeV)   (D=1.d9)
     emin(15) = 1.0    !                   deuteron  (MeV/u) (D=1.d9)
     emin(16) = 1.0    !                   triton    (MeV/u) (D=1.d9)
     emin(17) = 1.0    !                   3He       (MeV/u) (D=1.d9)
     emin(18) = 1.0    !                   Alpha     (MeV/u) (D=1.d9)
     emin(19) = 1.0    !                   Heavy Ion (MeV/u) (D=1.d9)


$    dmax(1) = 150.     ! Maximum E (MeV) of cross section use for p
(D=emin(1))
     dmax(2) = 150.     ! Maximum E (MeV) of cross section use for n
(D=emin(2))
     dmax(12) = 500.0   ! Maximum E (MeV) of electron for transport
     dmax(13) = 500.0   ! Maximum E (MeV) of positron for transport
     dmax(14) = 1000.0  ! Maximum E (MeV) of photon for transport
```

```
     deltm = 1.0e6
     deltc = 1.0e5
     delt0 = 1.0e6

     tmax(1) = 6.e+10
     tmax(2) = 30.e+12

     itall = 1.                    ! Output results after each batch
     file(7) = xsdir~.txt          ! Cross section data file name
     file(6) = spectrum_test.out   ! General output file name
     file(14) = trxcrd.dat

     icrhi = 1          ! Total reac. XS for HI; 0: Shen, 1: Tripathi

     ieleh = 1           !electron transport and energy loss on


     inmed = 2          ! nucleon-nucleon XS 0: free, 1: Cugnon old, 2: Cugnon
new
    eqmdnu = 20.        ! use JQMD instead of Bertini for n, p nuclear reac.
                                ! It is always better to use JQMD but takes
longer time.

                                ! An Example with setting eqmdnu = dmax(2)

                                ! emin(2) ----- dmax(2)
                          !               eqmdnu -----------
                          !         MCNP          JQMD
                          !
                          ! without eqmdnu,
                          !
                          ! emin(2) ----- dmax(2) ----------- eqmdnu ----
                                 !         MCNP           Bertini           JQMD

   eqmdmin = 20.      ! min E of JQMD in MeV/u
      nevap = 3         ! Evap model 0: no, 1: DRES, 2: SDM, 3: GEM

nlost = 100.
```

```
     nspred = 0         ! Coulomb diffusion on
      ndedx = 0         ! dE/dx by 0:SPAR+NMTC, 1: ATIMA+NMTC, 2: SPAR+NMTC
(D=2)
                                !
                                ! Using ATIMA is better than SPAR for lower
energy
                               ! but it takes longer time (2 - 10 times)
                               !
     nedisp = 0         ! E stragg 0: no, 1: Landau, 2: ATIMA



     igamma = 1         ! 0: no gamma emitt 1: with gamma emit
                                  !
                                  ! This option is important if you calculate
                               ! energy deposition in your detector and so on,
                               ! because residual energies in nuclei should be
                               ! also tallied as dE by means of the gamma
emission



     e-mode = 0         ! 0: standard, 1: event generator mode
                                  !
                               ! With this option PHITS does further decay
calculation
                               ! for remaining energy which still exists after
nuclear
                               ! reactions treated by the nuclear data (below
dmax())



      imagnf = 1         ! Magnetic field
     itstep = 0         ! Tally tracks of charged particles under magnetic
field
                        !  (it is only for 2D graphical plots)
```

[S o u r c e]

```
 s-type = 10
 $s-type=9
 proj = proton
 r1 = 3780.87262e5
 r2 = 3780.87262e5
 dir = -all
 $e0 = 100.
 e-type = 5
 eg1 = 25.
 eg2 = 1500.
 nm = 200.
 f(x) = x**(-2.1)


[ Material ]
     mat[1] $ CO2, air density at Mars surface ~ 1.64e-5g/cm3, is ~ 95% of
the Martian atmopheric composition
              gas = 1
              12C.24c   -2.244e-7
              16O.60c    -4.488e-5


     mat[2] $ This is a dummy material for detector and source regions
              14N.60c  4.680E-05  16O.60c 7.943E-06


     mat[3] $ SiO2, density ~ 2.2 g/cm3, is ~ 60% of the Martian Soil
Composition and FeO, density ~5.7g/cm3, is ~20% of the Martian Soil
Composition
            $ Cumulative density is ~3.37g/cm3.
              28Si.24c  -.687   $-1.03
              16O.60c   -1.203   $-1.17
              56Fe.24c  -1.48


 [surface]
  1 so 3779.87262e5    $ sphere just inside source
  2 so 3754.28111e5
  3 so 3728.68960e5
  4 so 3703.09809e5
  5 so 3677.50659e5
  6 so 3651.91508e5
```

```
  7 so 3626.32357e5
  8 so 3600.73206e5
  9 so 3575.14055e5
 10 so 3549.54905e5
 11 so 3523.95754e5
 12 so 3498.36603e5
 13 so 3472.77452e5
 14 so 3447.18301e5
 15 so 3421.59151e5
 16 so 3413.88770e5
 17 so 3409.38126e5
 18 so 3406.18389e5
 19 so 3403.70381e5
 20 so 3401.67744e5
 21 so 3399.96418e5
 22 so 3398.48007e5
 23 so 3397.17100e5
 24 so 3396.00005e5
 25 so 3396.00000e5
 50 so 5.e8 $rest of universe

[cell]
  100   1 -1.64e-19 2 -1  $ Outermost Layer of Martian Atmosphere
  101   1 -1.64e-18 3 -2
  102   1 -1.64e-17 4 -3
  103   1 -1.64e-16 5 -4
  104   1 -1.64e-15 6 -5
  105   1 -1.64e-14 7 -6
  106   1 -1.64e-13 8 -7
  107   1 -1.64e-12 9 -8
  108   1 -1.64e-11 10 -9
  109   1 -1.64e-10 11 -10
  110   1 -1.64e-9  12 -11
  111   1 -1.64e-8  13 -12
  112   1 -1.64e-7  14 -13
  113   1 -1.64e-6  15 -14
  114   1 -3.28e-6  16 -15
```

```
  115   1 -4.92e-6  17 -16
  116   1 -6.56e-6  18 -17
  117   1 -8.20e-6  19 -18
  118   1 -9.84e-6  20 -19
  119   1 -1.15e-5 21 -20
  120   1 -1.31e-5 22 -21
  121   1 -1.48e-5 23 -22
  122   1 -1.64e-5  24 -23  $ Innermost Layer of Martian Atmosphere
  123   2 -1.64e-20 25 -24  $ region inside detector
  124   3 -3.37    -25      $ Martian Surface
  999   2 -1.64e-20 -50 1   $ everywhere else
  9999  -1 50                $ infinite region cut-off


[ Mat name color]
  mat      name          color
   1    Atmosphere       yellow
   2    Space            blue
   3    Soil             gray


[ T -cross]
part = electron
mesh = reg
reg = 2
    r-in r-out area
    122  123   1.45e18
    124  123   1.45e18
e-type = 3
ne = 100
emin = 1.e-1
emax = 1.e3
unit = 1
axis = eng
file = Sphere_test_electron.out
output = flux
x-txt = {\it En} (MeV)
```

```
y-txt = {\it Flux} (1/cm^2)
epsout = 1


[ T -cross]
part = proton
mesh = reg
reg = 2
    r-in r-out area
    122  123   1.45e18
    124  123   1.45e18
e-type = 3
ne = 100
emin = 1.e0
emax = 5.e3
unit = 1
axis = eng
file = Sphere_test_proton.out
output = flux
x-txt = {\it En} (MeV)
y-txt = {\it Flux} (1/cm^2)
epsout = 1

[ T -cross]
part = photon
mesh = reg
reg = 2
    r-in r-out area
    122  123   1.45e18
    124  123   1.45e18
e-type = 3
ne = 100
emin = 1.e-2
emax = 1.e3
unit = 1
axis = eng
file = Sphere_test_photon.out
```

```
output = flux
x-txt = {\it En} (MeV)
y-txt = {\it Flux} (1/cm^2)
epsout = 1

[ T -cross]
part = neutron
mesh = reg
reg = 2
    r-in r-out area
    122  123   1.45e18
    124  123   1.45e18
e-type = 3
ne = 100
emin = 1.e-10
emax = 1.e4
unit = 1
axis = eng
file = Sphere_test_neutron.out
output = flux
x-txt = {\it En} (MeV)
y-txt = {\it Flux} (1/cm^2)
epsout = 1

[ T -track ]
part = proton
mesh = xyz
x-type = 2
nx = 100
xmin = 0.
xmax = 4.e8
y-type = 2
ny= 1
ymin = -10.
ymax = 10.
z-type = 2
nz = 100
```

```
zmin = 0.
zmax = 4.e8
e-type = 3
ne= 1
emin = 1.e1
emax = 1.e4
unit = 1
axis = xz
file = track_Sphere_test_protons.out
gshow = 1
epsout = 1


[ T -gshow ]
mesh = xyz
x-type = 2
nx= 1
xmin = 0.
xmax = 4.e8
y-type = 2
ny = 150
ymin = -10.
ymax = 10.
z-type = 2
nz = 200
zmin = 0.
zmax = 4.e8
axis = yz
file = gshow_Sphere_test.out
resol = 1
width = .5
epsout = 0
angel = noms nofr port
output = 6
```

Appendix B: Sample PHITS Output File

```
[ T - C r o s s ]
    title = [t-cross] in region mesh
     mesh =  reg            # mesh type is region-wise
      reg =    2            # number of crossing regions
      non     r-in    r-out      area
        1     122     123     1.4500000E+18
        2     124     123     1.4500000E+18
   e-type =    3            # e-mesh is log given by emin, emax and ne
     emin =  1.0000000E-02  # minimum value of e-mesh points
     emax =   1000.000      # maximum value of e-mesh points
#    edel =  0.1151293      # mesh width of e-mesh points
       ne =  100            # number of e-mesh points
#    data = ( e(i), i = 1, ne + 1 )
#           1.00000E-02  1.12202E-02  1.25893E-02  1.41254E-02  1.58489E-02
#           1.77828E-02  1.99526E-02  2.23872E-02  2.51189E-02  2.81838E-02
#           3.16228E-02  3.54813E-02  3.98107E-02  4.46684E-02  5.01187E-02
#           5.62341E-02  6.30957E-02  7.07946E-02  7.94328E-02  8.91251E-02
#           1.00000E-01  1.12202E-01  1.25893E-01  1.41254E-01  1.58489E-01
#           1.77828E-01  1.99526E-01  2.23872E-01  2.51189E-01  2.81838E-01
#           3.16228E-01  3.54813E-01  3.98107E-01  4.46684E-01  5.01187E-01
#           5.62341E-01  6.30957E-01  7.07946E-01  7.94328E-01  8.91251E-01
#           1.00000E+00  1.12202E+00  1.25893E+00  1.41254E+00  1.58489E+00
#           1.77828E+00  1.99526E+00  2.23872E+00  2.51189E+00  2.81838E+00
#           3.16228E+00  3.54813E+00  3.98107E+00  4.46684E+00  5.01187E+00
#           5.62341E+00  6.30957E+00  7.07946E+00  7.94328E+00  8.91251E+00
#           1.00000E+01  1.12202E+01  1.25893E+01  1.41254E+01  1.58489E+01
#           1.77828E+01  1.99526E+01  2.23872E+01  2.51189E+01  2.81838E+01
#           3.16228E+01  3.54813E+01  3.98107E+01  4.46684E+01  5.01187E+01
#           5.62341E+01  6.30957E+01  7.07946E+01  7.94328E+01  8.91251E+01
#           1.00000E+02  1.12202E+02  1.25893E+02  1.41254E+02  1.58489E+02
#           1.77828E+02  1.99526E+02  2.23872E+02  2.51189E+02  2.81838E+02
#           3.16228E+02  3.54813E+02  3.98107E+02  4.46684E+02  5.01187E+02
#           5.62341E+02  6.30957E+02  7.07946E+02  7.94328E+02  8.91251E+02
#           1.00000E+03
     unit =    1            # unit is [1/cm^2/source]
```

```
     axis =  eng            # axis of output
     file = Sphere_test_photon.out  # file name of output for the above axis
   output = flux            # surface crossing flux
     part =  photon
# kf/name :  22
    x-txt = {\it En} (MeV)
    y-txt = {\it Flux} (1/cm^2)
   epsout =    1            # (D=0) generate eps file by ANGEL
#    used :        main (  %)        temp (  %)       total (  %)
#  memory :         521 (  0)         502 (  0)        1023 (  0)

#------------------------------------------------------------------------------
--
#newpage:
#   no. =    1   reg = 122 - 123

x: {\it En} (MeV)
y: {\it Flux} (1/cm^2)
p: xlog ylog afac(0.8) form(0.9)
h: n            x            y(photon  ),hh0l  n
#  e-lower      e-upper         flux     r.err
   1.0000E-02   1.1220E-02   0.0000E+00  0.0000
   1.1220E-02   1.2589E-02   0.0000E+00  0.0000
   1.2589E-02   1.4125E-02   0.0000E+00  0.0000
   1.4125E-02   1.5849E-02   0.0000E+00  0.0000
   1.5849E-02   1.7783E-02   0.0000E+00  0.0000
   1.7783E-02   1.9953E-02   0.0000E+00  0.0000
   1.9953E-02   2.2387E-02   0.0000E+00  0.0000
   2.2387E-02   2.5119E-02   0.0000E+00  0.0000
   2.5119E-02   2.8184E-02   0.0000E+00  0.0000
   2.8184E-02   3.1623E-02   0.0000E+00  0.0000
   3.1623E-02   3.5481E-02   0.0000E+00  0.0000
   3.5481E-02   3.9811E-02   0.0000E+00  0.0000
   3.9811E-02   4.4668E-02   0.0000E+00  0.0000
   4.4668E-02   5.0119E-02   0.0000E+00  0.0000
   5.0119E-02   5.6234E-02   0.0000E+00  0.0000
   5.6234E-02   6.3096E-02   0.0000E+00  0.0000
```

6.3096E-02	7.0795E-02	0.0000E+00	0.0000
7.0795E-02	7.9433E-02	0.0000E+00	0.0000
7.9433E-02	8.9125E-02	0.0000E+00	0.0000
8.9125E-02	1.0000E-01	0.0000E+00	0.0000
1.0000E-01	1.1220E-01	0.0000E+00	0.0000
1.1220E-01	1.2589E-01	0.0000E+00	0.0000
1.2589E-01	1.4125E-01	0.0000E+00	0.0000
1.4125E-01	1.5849E-01	0.0000E+00	0.0000
1.5849E-01	1.7783E-01	0.0000E+00	0.0000
1.7783E-01	1.9953E-01	0.0000E+00	0.0000
1.9953E-01	2.2387E-01	0.0000E+00	0.0000
2.2387E-01	2.5119E-01	0.0000E+00	0.0000
2.5119E-01	2.8184E-01	0.0000E+00	0.0000
2.8184E-01	3.1623E-01	0.0000E+00	0.0000
3.1623E-01	3.5481E-01	0.0000E+00	0.0000
3.5481E-01	3.9811E-01	0.0000E+00	0.0000
3.9811E-01	4.4668E-01	0.0000E+00	0.0000
4.4668E-01	5.0119E-01	0.0000E+00	0.0000
5.0119E-01	5.6234E-01	0.0000E+00	0.0000
5.6234E-01	6.3096E-01	0.0000E+00	0.0000
6.3096E-01	7.0795E-01	0.0000E+00	0.0000
7.0795E-01	7.9433E-01	0.0000E+00	0.0000
7.9433E-01	8.9125E-01	0.0000E+00	0.0000
8.9125E-01	1.0000E+00	0.0000E+00	0.0000
1.0000E+00	1.1220E+00	9.5770E-22	0.0182
1.1220E+00	1.2589E+00	9.7593E-22	0.0209
1.2589E+00	1.4125E+00	9.6668E-22	0.0205
1.4125E+00	1.5849E+00	9.8447E-22	0.0201
1.5849E+00	1.7783E+00	1.0237E-21	0.0191
1.7783E+00	1.9953E+00	1.0365E-21	0.0212
1.9953E+00	2.2387E+00	1.0618E-21	0.0190
2.2387E+00	2.5119E+00	1.0555E-21	0.0199
2.5119E+00	2.8184E+00	1.4264E-21	0.0175
2.8184E+00	3.1623E+00	1.2854E-21	0.0178
3.1623E+00	3.5481E+00	1.1426E-21	0.0211
3.5481E+00	3.9811E+00	2.2912E-21	0.0124
3.9811E+00	4.4668E+00	2.7468E-21	0.0124

4.4668E+00	5.0119E+00	1.1220E-21	0.0196
5.0119E+00	5.6234E+00	1.1057E-21	0.0198
5.6234E+00	6.3096E+00	3.1587E-21	0.0117
6.3096E+00	7.0795E+00	1.6832E-21	0.0139
7.0795E+00	7.9433E+00	1.4403E-21	0.0163
7.9433E+00	8.9125E+00	9.0108E-22	0.0210
8.9125E+00	1.0000E+01	5.6244E-22	0.0244
1.0000E+01	1.1220E+01	2.5700E-22	0.0427
1.1220E+01	1.2589E+01	1.5763E-22	0.0521
1.2589E+01	1.4125E+01	1.5656E-22	0.0558
1.4125E+01	1.5849E+01	1.3682E-22	0.0638
1.5849E+01	1.7783E+01	1.4065E-22	0.0672
1.7783E+01	1.9953E+01	1.4666E-22	0.0741
1.9953E+01	2.2387E+01	1.0369E-22	0.0782
2.2387E+01	2.5119E+01	9.0944E-23	0.0761
2.5119E+01	2.8184E+01	8.8786E-23	0.0939
2.8184E+01	3.1623E+01	8.9129E-23	0.0709
3.1623E+01	3.5481E+01	1.0205E-22	0.0983
3.5481E+01	3.9811E+01	9.4485E-23	0.0795
3.9811E+01	4.4668E+01	8.3436E-23	0.0750
4.4668E+01	5.0119E+01	8.6698E-23	0.0781
5.0119E+01	5.6234E+01	9.2554E-23	0.0747
5.6234E+01	6.3096E+01	9.5738E-23	0.0755
6.3096E+01	7.0795E+01	9.9217E-23	0.0880
7.0795E+01	7.9433E+01	9.5577E-23	0.0919
7.9433E+01	8.9125E+01	9.1304E-23	0.0557
8.9125E+01	1.0000E+02	9.3507E-23	0.0549
1.0000E+02	1.1220E+02	9.4530E-23	0.0570
1.1220E+02	1.2589E+02	9.3876E-23	0.0515
1.2589E+02	1.4125E+02	1.0635E-22	0.0622
1.4125E+02	1.5849E+02	1.0365E-22	0.0586
1.5849E+02	1.7783E+02	8.5614E-23	0.0632
1.7783E+02	1.9953E+02	8.1451E-23	0.0736
1.9953E+02	2.2387E+02	6.1932E-23	0.0859
2.2387E+02	2.5119E+02	4.5034E-23	0.0695
2.5119E+02	2.8184E+02	4.0155E-23	0.0807
2.8184E+02	3.1623E+02	3.6798E-23	0.0901

```
   3.1623E+02   3.5481E+02   3.2929E-23  0.1381
   3.5481E+02   3.9811E+02   2.0250E-23  0.1036
   3.9811E+02   4.4668E+02   1.4664E-23  0.1245
   4.4668E+02   5.0119E+02   9.6068E-24  0.1203
   5.0119E+02   5.6234E+02   8.1837E-24  0.1704
   5.6234E+02   6.3096E+02   3.3405E-24  0.2494
   6.3096E+02   7.0795E+02   3.6758E-24  0.3783
   7.0795E+02   7.9433E+02   4.3804E-25  0.4440
   7.9433E+02   8.9125E+02   1.0214E-24  0.4315
   8.9125E+02   1.0000E+03   1.5274E-25  0.7269

#   sum over                 3.0074E-20  0.0037
'no. =    1   reg = 122 - 123'
msuc: {\huge [t-cross] in region mesh}
msdl: {\it plotted by \ANGEL \version}
msdr: {\it calculated by \PHITS  2.14}
wt: s(0.7)
\vspace{-3}
  region surface crossing
  area  &=&   1.4500E+18 [cm^2]
e:

#------------------------------------------------------------------------------
--
 newpage:
#   no. =    2   reg = 124 - 123

x: {\it En} (MeV)
y: {\it Flux} (1/cm^2)
p: xlog ylog afac(0.8) form(0.9)
h: n            x            y(photon  ),hh0l  n
#  e-lower      e-upper         flux     r.err
   1.0000E-02   1.1220E-02   0.0000E+00  0.0000
   1.1220E-02   1.2589E-02   0.0000E+00  0.0000
   1.2589E-02   1.4125E-02   0.0000E+00  0.0000
   1.4125E-02   1.5849E-02   0.0000E+00  0.0000
   1.5849E-02   1.7783E-02   0.0000E+00  0.0000
```

1.7783E-02	1.9953E-02	0.0000E+00	0.0000
1.9953E-02	2.2387E-02	0.0000E+00	0.0000
2.2387E-02	2.5119E-02	0.0000E+00	0.0000
2.5119E-02	2.8184E-02	0.0000E+00	0.0000
2.8184E-02	3.1623E-02	0.0000E+00	0.0000
3.1623E-02	3.5481E-02	0.0000E+00	0.0000
3.5481E-02	3.9811E-02	0.0000E+00	0.0000
3.9811E-02	4.4668E-02	0.0000E+00	0.0000
4.4668E-02	5.0119E-02	0.0000E+00	0.0000
5.0119E-02	5.6234E-02	0.0000E+00	0.0000
5.6234E-02	6.3096E-02	0.0000E+00	0.0000
6.3096E-02	7.0795E-02	0.0000E+00	0.0000
7.0795E-02	7.9433E-02	0.0000E+00	0.0000
7.9433E-02	8.9125E-02	0.0000E+00	0.0000
8.9125E-02	1.0000E-01	0.0000E+00	0.0000
1.0000E-01	1.1220E-01	0.0000E+00	0.0000
1.1220E-01	1.2589E-01	0.0000E+00	0.0000
1.2589E-01	1.4125E-01	0.0000E+00	0.0000
1.4125E-01	1.5849E-01	0.0000E+00	0.0000
1.5849E-01	1.7783E-01	0.0000E+00	0.0000
1.7783E-01	1.9953E-01	0.0000E+00	0.0000
1.9953E-01	2.2387E-01	0.0000E+00	0.0000
2.2387E-01	2.5119E-01	0.0000E+00	0.0000
2.5119E-01	2.8184E-01	0.0000E+00	0.0000
2.8184E-01	3.1623E-01	0.0000E+00	0.0000
3.1623E-01	3.5481E-01	0.0000E+00	0.0000
3.5481E-01	3.9811E-01	0.0000E+00	0.0000
3.9811E-01	4.4668E-01	0.0000E+00	0.0000
4.4668E-01	5.0119E-01	0.0000E+00	0.0000
5.0119E-01	5.6234E-01	0.0000E+00	0.0000
5.6234E-01	6.3096E-01	0.0000E+00	0.0000
6.3096E-01	7.0795E-01	0.0000E+00	0.0000
7.0795E-01	7.9433E-01	0.0000E+00	0.0000
7.9433E-01	8.9125E-01	0.0000E+00	0.0000
8.9125E-01	1.0000E+00	0.0000E+00	0.0000
1.0000E+00	1.1220E+00	1.3802E-21	0.0159
1.1220E+00	1.2589E+00	1.7626E-21	0.0136

1.2589E+00	1.4125E+00	1.3456E-21	0.0150
1.4125E+00	1.5849E+00	1.2303E-21	0.0175
1.5849E+00	1.7783E+00	1.4261E-21	0.0150
1.7783E+00	1.9953E+00	2.5654E-21	0.0122
1.9953E+00	2.2387E+00	1.3243E-21	0.0160
2.2387E+00	2.5119E+00	1.1583E-21	0.0174
2.5119E+00	2.8184E+00	1.4261E-21	0.0155
2.8184E+00	3.1623E+00	1.2895E-21	0.0167
3.1623E+00	3.5481E+00	1.2760E-21	0.0169
3.5481E+00	3.9811E+00	1.5861E-21	0.0134
3.9811E+00	4.4668E+00	1.7544E-21	0.0140
4.4668E+00	5.0119E+00	1.0859E-21	0.0183
5.0119E+00	5.6234E+00	9.4542E-22	0.0199
5.6234E+00	6.3096E+00	1.8538E-21	0.0138
6.3096E+00	7.0795E+00	1.0154E-21	0.0185
7.0795E+00	7.9433E+00	1.5954E-21	0.0119
7.9433E+00	8.9125E+00	4.5825E-22	0.0320
8.9125E+00	1.0000E+01	3.2371E-22	0.0349
1.0000E+01	1.1220E+01	1.3679E-22	0.0593
1.1220E+01	1.2589E+01	9.1105E-23	0.0736
1.2589E+01	1.4125E+01	6.3700E-23	0.0668
1.4125E+01	1.5849E+01	4.9021E-23	0.0799
1.5849E+01	1.7783E+01	3.9744E-23	0.0734
1.7783E+01	1.9953E+01	4.5605E-23	0.0938
1.9953E+01	2.2387E+01	4.4550E-23	0.1132
2.2387E+01	2.5119E+01	2.9983E-23	0.1106
2.5119E+01	2.8184E+01	3.2081E-23	0.1178
2.8184E+01	3.1623E+01	3.3129E-23	0.1568
3.1623E+01	3.5481E+01	2.6204E-23	0.1074
3.5481E+01	3.9811E+01	3.1800E-23	0.1109
3.9811E+01	4.4668E+01	2.2501E-23	0.1013
4.4668E+01	5.0119E+01	3.4587E-23	0.1405
5.0119E+01	5.6234E+01	2.8410E-23	0.0982
5.6234E+01	6.3096E+01	2.7960E-23	0.1153
6.3096E+01	7.0795E+01	3.0341E-23	0.1356
7.0795E+01	7.9433E+01	3.5064E-23	0.0983
7.9433E+01	8.9125E+01	2.7677E-23	0.0981

```
   8.9125E+01   1.0000E+02   2.9160E-23  0.0996
   1.0000E+02   1.1220E+02   2.9660E-23  0.1044
   1.1220E+02   1.2589E+02   1.9908E-23  0.0920
   1.2589E+02   1.4125E+02   3.1121E-23  0.0967
   1.4125E+02   1.5849E+02   2.4872E-23  0.0936
   1.5849E+02   1.7783E+02   1.9326E-23  0.2015
   1.7783E+02   1.9953E+02   1.4976E-23  0.2237
   1.9953E+02   2.2387E+02   1.2673E-23  0.4115
   2.2387E+02   2.5119E+02   6.5528E-24  0.2728
   2.5119E+02   2.8184E+02   4.3909E-24  0.3340
   2.8184E+02   3.1623E+02   5.2845E-25  0.6404
   3.1623E+02   3.5481E+02   1.6157E-24  0.4131
   3.5481E+02   3.9811E+02   2.8322E-25  1.0000
   3.9811E+02   4.4668E+02   0.0000E+00  0.0000
   4.4668E+02   5.0119E+02   0.0000E+00  0.0000
   5.0119E+02   5.6234E+02   0.0000E+00  0.0000
   5.6234E+02   6.3096E+02   0.0000E+00  0.0000
   6.3096E+02   7.0795E+02   0.0000E+00  0.0000
   7.0795E+02   7.9433E+02   0.0000E+00  0.0000
   7.9433E+02   8.9125E+02   0.0000E+00  0.0000
   8.9125E+02   1.0000E+03   0.0000E+00  0.0000

#   sum over                 2.7828E-20  0.0035
'no. =    2   reg = 124 - 123'
msuc: {\huge [t-cross] in region mesh}
msdl: {\it plotted by \ANGEL \version}
msdr: {\it calculated by \PHITS  2.14}
wt: s(0.7)
\vspace{-3}
  region surface crossing
  area  &=&   1.4500E+18 [cm^2]
e:
```

Bibliography

B. Leskovar. “Microchannel Plates”. Physics Today, pages 42-49. November 1977

B. Netolicky. Personal Correspondence. 2009.

C. Hellweg and C. Baumstark-Khan. “Getting Ready for the Manned Mission to Mars: The Astronauts’ Risk from Space Radiation.” *Naturwissenschaften* .94(7): 517-26. 2007.

C. Leroy and P. Rancoita. Principles of Radiation Interaction and Matter and Detection. World Scientific Publishing Company. 2004.

Cucinotta et al. “Evaluating Shielding Effectiveness for Reducing Space Radiation Cancer Risks.” *Radiation Measurements*, 41, 1173-1185. 1996.

D. Curtis. Personal Correspondence. 2009.

D. Hathaway et al. “A Synthesis of Solar Cycle Prediction Techniques.” *Journal of Geophysical Research, vol. 104, no. A10, pgs. 22,375 – 22,388*. 1999.

D. Reames. “Solar Energetic Particles: Is there time to hide?” *Radiation Measurements*, 30, 297-308, 1999.

D.C. Ellison and R. Ramaty. “Shock Acceleration of Electrons and Ions in Solar Flares”. Astrophysical Journal, vol. 298, pages 400-408. 1985.

D.F. Smart and M.A. Shea. “Comment on Estimating the Solar Proton Environment that May Affect Mars Missions”. Advances in Space Research, vol. 31, no. 1, pages 45-50. 2002.

D.H. Crider et al. “A Proxy for Determining Solar Wind Dynamic Pressure at Mars using Mars Global Surveyor Data.” *Journal of Geophysical Research, vol. 108, no. A12*. 2003.

D.L. Mitchel et al, “Intense Solar Activity of Oct-Nov 2003 Observed at Mars with the MGS Magnetometer/Electron Reflectometer”, 2003 American Geophysical Union Conference, San Francisco, California. December 8-12, 2003.

D.L. Mitchell et al. “Probing Mars’ Crustal Magnetic Field and Ionosphere with the MGS Electron Reflectometer”. Journal of Geophysical Research, vol. 106, no. E10, pages: 23, 403-423, 417. 2001.

E. Alpen. Radiation Biophysics. 2nd Edition. *Academic Press*. 1998.

E. Hall and A. Giaccia. Radiobiology for the Radiobiologist. 6th Edition. *Lippincott, Williams, & Wilkins*. 2006.

E.J. Daly et. al. "Space Environment Analysis: Experience and Trends." ESA 1996 Symposium on Environment Modelling for Space-based Applications, Sept. 18-20, 1996, ESTEC, Noordwijk, The Netherlands.

F. Leblanc et al, “Some Expected Impacts of a Solar Particle Event at Mars”, *J. Geo. Res.*, Vol. 107, No. A5, 2002.

F.A. Cucinotta et al, “Analysis of Radiation Risk from Alpha Particle Component of Solar Particle Events”, *Adv. Space Res.*, Vol. 14, No. 10, 1994.

F.A. Cucinotta et al. “Space Radiation Cancer Risk Projections for Exploration Missions: Uncertainty Reduction and Mitiation.” *NASA Technical Paper 2002-210777*. NASA, Washington, DC. 2002.

F.A. Cucinotta et al. “Space Radiation Cancer Risks and Uncertainties for Mars Missions.” *Radiation Research*, 156, 682-688. 2001.

G. Delory. Personal Correspondence. 2009.

G.D. Badhwar et al, “Radiation Measurements Onboard the Mir Orbital Station”, *Rad. Measurements*, 35, 2002.

G.D. Badhwar and P.M. O’Neill, “Long-Term Modulation of Galactic Cosmic Radiation and its Model for Space Exploration”, *Adv. Space Res.,* Vol. 14, No. 10, 1994.

G.J. Taylor et al, “Scientific Goals, Objectives, and Investigations: 2003”, *Mars Exploration Program Analysis Group*, October 2003.

G.M. Lindsay et al. “Relationships between Coronal Mass Ejection Speeds from Coronagraph Images and Interplanetary Characteristics of Associated Interplanetary Coronal Mass Ejections.” *Journal of Geophysical Research,* vol. 104, no. A6, pgs. 12,515 – 12,523. 1999.

http://burro.astr.cwru.edu/stu/media/missions/mgs_diagram.jpg

http://marsprogram.jpl.nasa.gov/MPF/science/apxs_elemental.html

http://nssdc.gsfc.nasa.gov/planetary/image/mars_global_surveyor.jpg

http://phits.jaea.go.jp/expacs/

http://phits.jaea.go.jp/Overview.html

http://physics.nist.gov/PhysRefData/Star/Text/contents.html

http://solarscience.msfc.nasa.gov/images/ssn_predict_l.gif

http://www.aps.anl.gov/Users/Become_A_User/Before_You_Arrive/Study_Guides/GERT/

http://www.igpp.ucla.edu/

http://www.nrc.gov/reading-rm/doc-collections/nuregs/staff/sr1556/v21/1556vol21final/1556vol21final7.gif

http://www.srim.org/SRIM/SRIMINTRO.htm

J. Feynman and S. Gabriel (Eds.). Interplanetary Particle Environment. JPL Publication 88-28, Jet Propulsion Laboratory, California Institute of Technology, Pasadena, CA, 1988.

J. Feynman et al. “Interplanetary proton Fuence Model: JPL 1991.” *Journal of Geophysical Research* vol. 98, pgs. 13,281–13,294. 1993.

J. Letaw. “Radiation Biology.” Fundamentals of Space Life Sciences, Volume 1, Chapter 2. *Orbit Foundation Series*. 1997.

J. Mosher, et al. “Nuclear Recoil Detection with Microchannel Plates.” *Nuclear Instruments and Methods in Physics Research*, A 459, pages 532-542. 2001.

J. Turner. Atoms, Radiation, and Radiation Protection. 3rd Edition. *Wiley-VCH*. 2007.

J.L. Wiza. “Microchannel Plate Detectors”. Nuclear Instruments and Methods, Vol. 162, pages 587-601. 1979.

J.N. Kapur. *Maximum Entropy Models in Science and Engineering*. John Wiley & Sons, Inc. New York. 1989.

J.W. Wilson et al, “Mars Surface Ionizing Radiation Environment: Need for Validation”, *MARS 2001 Workshop*, Houston, Texas, October 2-4, 1999.

J.W. Wilson et al. “Astronaut Exposures to Ionizing Radiation in a Lightly-Shielded Space Suit.” *NASA Technical Paper* 1999-01-2173. NASA, Washington, DC. 1999.

K. Lee. Personal Correspondence. 2009.

K. Niita. “Nuclear Reaction Models in Particle and Heavy Ion Transport code System PHITS”, *1st Workshop on Accelerator Radiation Induced Activation*, Paul Scherrer Institut, Switzerland, October 13-17, 2008.

K. Niita. *Personal Correspondence.* 2009

K. Oba et al. “High Gain Micro-Channel Plate Multipliers for Particle Tracking or Single Photo-Electron Counting.” *IEEE Transactions on Nuclear Science*, Vol. NS-28, No. 1, February 1981.

K.M. Kosev. A High-Resolution Time-of-Flight Spectrometer for Fission Fragments and Ion Beams. Dissertation, Technical University of Dresden. 2007.

L. Katz and A.S. Penfold. “Range-Energy Relations for Electrons and the Determination of Beta-Ray End-Point Energies by Absorption”. Reviews of Modern Physics, vol. 24, pages 28-44. 1952.

L. Simonsen and J. Nealy. “Radiation Protection for Human Missions to the Moon and Mars.” *NASA Technical Report Paper 3079.* NASA, Washington, DC. 1991.

L. Simonsen. “Analysis of Lunar and Mars Habitation Modules for the Space Exploration Initiative.” Shielding Strategies for Human Space Exploration. Chapter 4. NASA CP-3360, 43–77. 1997.

L. Simonsen. “Radiation Exposure for Manned Mars Surface Missions.” *NASA Technical Paper 2979*. NASA, Washington, DC. 1990.

L.S. Pinsky and T.L. Wilson. “Analysis of the Mars Odyessey MARIE Experiment Data”. ISSO Annual Report, Y2002, pages 97-100. University of Houston, Clear Lake. 2002.

M. Gurtner et al. “Simulation of the Interaction of Space Radiation with the Martian Atmosphere and Surface”, *Advances in Space Research,* 36, 2176-2181, 2005.

M.A. Xapsos et al. “Extreme Value Analysis of Solar Energetic Proton Peak Fluxes.” *Solar Physics, vol. 183, pgs. 157-164.* 1998.

M.A. Xapsos et al. “Space Environment Effects : Model for Emission of Solar Protons (ESP) – Cumulative and Worst-Case Event Fluences.” *NASA Technical Paper 1999-209763*. 1999.

M.S. Clowdsley et al, “Neutron Environments on the Martian Surface”, *Physica Media*, 17, 2001.

M.Y. Kim et al, “Contribution of High Charge and Energy (HZE) Ions During Solar-Particle Event of September 29, 1989” , NASA/TP-1999-209320, May 1999.

N. Gopalswamy et al. “Predicting the 1-AU Arrival Times of Coronal Mass Ejections.” *Journal of Geophysical Research.* 2002.

N. Zapp et al, “A Comparison of Quality Factors and Weighting Factors for Characterizing Astronaut Radiation Exposures”, *Adv. Space Res,*, Vol. 30, No. 4, 2002.

National Council on Radiation Protection and Measurement (NCRP). “Protection Against Neutron Radiation.” *NCRP Report No. 38*. NCRP, Washington, DC. 1971.

National Council on Radiation Protection and Measurement (NCRP). “Limitation of Exposure to Ionizing Radiation." *NCRP Report No. 116*. NCRP, Washington, DC. 1993.

National Research Council, Committee on the Biological Effects of Ionizing Radiation. *Health Effects of Exposure to Low Levels of Ionizing Radiation (BEIR V)*. National Academy Press, Washington, DC. 1990.

R.A. Mewaldt et al, “Solar-Particle Energy Spectra during the Large Events of October-November 2003 and January 2005”, *29th Annual Cosmic Ray Conference Pune*, 2005, 00, 101-104.

R.A. Mewaldt, et al. “Proton, Helium, and Electron Spectra During the Large Solar Events of October – November 2003”. Journal of Geophysical Research, vol. 110. 2005.

R.A. Nymmik. “Probabilistic Model for Fluences and Peak Fluxes of Solar Energetic Particles.” *Radiation Measurements*, vol. 30, pgs. 287-296. 1999.

T. Sato and K. Niita, “Analytical Functions of Predict Cosmic-Ray Neutron Spectra in the Atomsphere,” *Radiation Research*, 166, 544. 2006.

T. Sato et al. “Development of PARMA: PHITS-based analytical radiation model in the atmosphere,” *Radiation Research*, 170, 244-259, 2008.

Townsend L.W. and E.N. Zapp, “Dose Uncertainties for Large Solar Particle Events: Input Spectra Variability and Human Geometry Approximations”, *Rad. Measurements*, 30, 1999.

Tylka A.J. and W.F. Dietrich, “IMP-8 Observations of the Spectra, Composition, and Variability of Solar Heavy Ions at High Energies Relevant to Manned Space Missions”, *Rad. Measurements*, 30, 1999.